

Cardiff University



Magnetotransport measurements of connected
and unconnected NiFe artificial spin ice lattices

Doctor of Philosophy

Simon Olivari

September 2016

Abstract

Artificial spin ice analogues formed from hexagonal arrays of individual magnetic nanoislands or connected nanowires have been studied via magnetotransport measurements. Asymmetry in the magnetoresistance data at temperatures below 50K has previously been attributed to long-range order and chiral loop states forming at the edges of the lattice. After capping the magnetic lattice with a nonmagnetic non-conducting layer to avoid oxidation there was no evidence for this asymmetry below 25K. A complex combination of effects due to exchange bias and the onset of a modified magnetisation reversal mechanism are responsible for the observed asymmetry in uncapped samples.

Electrical transport measurements of an unconnected hexagonal lattice of artificial spin ice show an increase in the magnitude of the anisotropic magneto-resistance compared with connected lattices. The switching signal size in an unconnected lattice is 0.1% of the overall measurement resistance, compared to just 0.01% in a connected lattice. This results from magnetic domain walls no longer being free to propagate through the lattice, in comparison to the case of the connected lattice, forcing a domain wall nucleation in each individual nanowire.

Connected artificial spin ice lattices can be made to mimic their unconnected counterparts by reducing the magnetic nanowire width at the vertices. This restricting lattice impedes magnetic domain wall propagation in a manner similar to the unconnected lattice. A lattice with 300nm-wide wires requires 25% restriction to completely prevent the domain wall propagation, compared with just 7% in a 150nm wire.

Finally a two-layer square lattice has been created, in order to produce an artificial spin ice with equivalent magnetostatic interactions between all nanowires across a vertex. This new variant of artificial spin ice has been achieved by vertically offsetting two magnetic sub-lattices via a non-magnetic polymeric spacer layer.

Acknowledgements

I would like to begin by acknowledging my project supervisor, *Dr Dan Read*, first and foremost for having the trust in me and giving me the opportunity to partake in this research project, and for guiding me through the challenges posed by this PhD.

Thanks also to my 2nd supervisor, *Dr Phil Buckle*, always willing to assist both with advice and knowledge but also tangibly through the use of equipment for gathering vital data for my research. I also thank *Dr Sam Ladak* for informative discussions and for his assistance on my research visits to Diamond Light Source.

It has been a challenge to always keep the high morale throughout the days in this project and so I thank *Ifan Williams* for the experiences we shared. I also acknowledge the 3 guys who have had to put up with sharing an office with me during these last few years, *Kane Esien*, *Dr Craig Allford* and *Dr Rob Thomas*, also offering valuable scientific advice both in the making and analysing of my samples. Particularly singling out *Kane Esien* with whom I have shared in our attempts to build up our lab and make head-or-tail of the results we have gathered, along with visits to the synchrotrons and conferences. I would like to thank my family for supporting me, particularly my mother, *Debbie*, and my father, *Stan*, for also giving me the position to pursue these challenges.

I would like to lastly thank my partner *Josie*, who has been by my side to help and support me throughout the last three years and having such patience during my large time inputs to attempt to complete this thesis. I hope you find the fruits of my labour were worth it!

List of Abbreviations

ADW	Asymmetric transverse Domain Wall
AFM	Atomic Force Microscope
AMR	Anisotropic MagnetoResistance
ASI	Artificial Spin Ice
DW	Domain Wall
EBL	Electron Beam Lithography
RRR	Residual Resistivity Ratio
RT	Room Temperature
SEM	Scanning Electron Microscope
TDW	Transverse Domain Wall
VDW	Vortex Domain Wall

Contents

1. Introduction	1
1.1. Overview of chapter content	2
2. Theory of Ferromagnetism and Artificial Spin Ice.....	5
2.1. Fundamentals of the theory of magnetism	5
2.2. An introduction to micromagnetism	7
2.3. Domains in magnetic materials	8
2.4. Summary of the Gibbs free energy	11
2.4.1 Basis of the Exchange Energy	11
2.4.2 Basis of the Magneto-Crystalline Energy & Shape Anisotropy	12
2.4.3 Basis of the Magnetostatic and Magnetoelastic Anisotropy Energy	14
2.4.4 Basis of the Zeeman Energy	15
2.5. Domain Walls (DWs)	15
2.5.1 The conditions for Bloch & Neel Walls	15
2.5.2 The conditions for Transverse & Vortex Walls.....	17
2.6. Origins of Artificial Spin Ice (ASI)	19
2.6.1 Geometric frustration.....	19
2.6.2 Discovery of the frustrated structure of water ice and spin ice	20
2.6.3 Development of Artificial Spin Ice and the ice rules.....	22
2.7. Anisotropic MagnetoResistance (AMR)	23
2.8. Magneto-Optic Kerr Effect (MOKE).....	25
2.9. Outline of Magnetic Imaging Techniques	28
2.10. Conclusions	29
3. Published literature around Artificial Spin Ice (ASI).....	31
3.1. Developments of ASI	31
3.1.1 The first fabrication of ASI samples	31
3.1.2 Recently-developed ASI lattices	38
3.1.3 Measuring the interactions between nanoscale ferromagnetic structures	40
3.2. Theoretically assessing Quasi 3-D ASI	41
3.3. Pinning of DWs within ferromagnetic nanowires	43

3.4.	Simulating the AMR of a ferromagnetic structure	47
3.5.	Conclusions	48
4.	A summary of the experimental techniques and procedures used	49
4.1.	An overview of the procedures for processing samples	50
4.1.1	Clean Room.....	50
4.1.2	Fabrication of new samples.....	50
4.1.3	Electron Beam Lithography (EBL)	53
4.1.4	Designing the lithographic patterns for samples.....	55
4.1.5	Sample development and plasma ashing	56
4.1.6	Adding material to samples through thermal deposition and lift-off.....	57
4.1.7	Summary of fabrication process	59
4.2.	Techniques for measuring samples	60
4.2.1	Magneto-Transport measurement technique	60
4.2.2	Four-terminal measurements	61
4.2.3	Hexagonal Lattice Measurement Orientations	64
4.2.4	ASI Lattice measurement types.....	66
4.2.5	Low-temperature measurements.....	66
4.3.	MOKE (Magneto-Optic Kerr Effect) Measurements.....	67
4.4.	Description of micromagnetic simulations	70
4.5.	Conclusions	71
5.	Investigating the hexagonal lattice of Artificial Spin Ice (ASI)	75
5.1.	Connected Hexagonal Lattice Samples	77
5.1.1	Hexagonal Lattice - Single Vertex	77
5.1.2	Connected Lattice.....	79
5.1.3	NiFe samples capped with AlO _x	80
5.1.4	Samples summary	81
5.2.	Measuring and simulating single nanowire.....	81
5.3.	Analysing a single vertex of the hexagonal lattice	84
5.3.1	Single Vertex measurements	86
5.3.2	Measuring individual bars of the hexagonal single vertex	88

5.3.3	Horizontal Bar of the single vertex	88
5.3.4	Measuring the top diagonal bar in hexagonal single vertex	97
5.4.	A magnetotransport study of the connected hexagonal lattice	99
5.4.1	Studying the effect had by capping the connected lattice	101
5.4.2	Measuring the effect of capping hexagonal lattice ASI	102
5.4.3	Comparing Connected Lattice at RT for different measured orientations	109
5.5.	Conclusions.....	114
6.	Comparison of connected and unconnected Artificial Spin Ice (ASI)	117
6.1.	Outlining the hybrid lattice and the restricting lattice	118
6.1.1	Hybrid Lattice	118
6.1.2	Restricting Lattice.....	120
6.1.3	Summary of investigated samples	122
6.2.	Comparing absolute resistances of different ASI lattice samples	122
6.2.1	Two-terminal resistance measurements.....	123
6.2.2	Four-terminal resistances and Residual Resistivity Ratio	124
6.3.	Magnetotransport measurements of the Hybrid Lattice	128
6.3.1	Measuring different orientations of the hybrid lattice giving evidence of the ice rules	129
6.3.2	Comparing Hybrid Lattice with OOMMF Simulations.....	155
6.3.3	Comparing Hybrid & Connected Lattice	157
6.3.4	Comparison of the hybrid AMR curves for different orientations	163
6.3.5	Hybrid Temperature Dependence.....	164
6.4.	Design and creation of the Restricting Lattice	165
6.4.1	AMR Signal size for different lattice forms.....	167
6.5.	Conclusions.....	175
7.	Studying the interactions of magnetic Domain Walls (DWs) in adjacent nanostructures	177
7.1.	Samples for investigating DW-DW interactions.....	178
7.1.1	DW Pinning in adjacent magnetic nanowire	179
7.1.2	A two-layer variation of the square ASI lattice	179
7.2.	Reproducible pinning and depinning of DW-DW pairs	180

7.2.1	Outline.....	180
7.2.2	Experimental.....	180
7.3.	Quasi 3-D ASI.....	186
7.3.1	Introduction.....	186
7.3.2	Square Lattice Theory.....	187
7.3.1	Experiment Outline	190
7.3.2	Initial PMMA Inversion	191
7.3.1	Preliminary MOKE measurements	192
7.3.2	Square lattice MOKE measurements.....	194
7.3.3	MOKE through photoresist layer.....	196
7.3.4	Simple Two-layer structure.....	198
7.4.	Conclusions	202
8.	Conclusion.....	203
8.1.	Future restricting lattices and quasi 3-D ASI	204
9.	References.....	207

List of Figures

Figure 2.1: Magnetic Force Microscope (MFM) image of a NdFeB material showing the magnetic domain structure of the material, with the different contrasts shown corresponding to different magnetisation directions across the sample, the dimensions are confirmed by the scale bar atop the image [21]	9
Figure 2.2: The process of a magnetic material breaking down into domains, results in an energetically favourable condition for the material – the solid arrows represent the magnetisation in each domain of the material, and the dotted lines show the stray fields outside of the material [20]	10
Figure 2.3: Defining the hard and easy axes of materials, which form the basis of magnetocrystalline anisotropy – the red arrow is pointing in towards the centre of the cube, with the red dotted line showing the direction at which the red arrow is propagating, in the horizontal plane of the cube	12
Figure 2.4: Demonstrating the role played by the creation of magnetostatic charge in the phenomenon of shape anisotropy within rectangular medium, with the positive and negative signs referring to build up of positive and negative charge, and the blue arrows representing the magnetisation direction	13
Figure 2.5: The uniform magnetisation rotation that takes place in a Néel wall – the black arrows show the magnetisation direction within the red and blue domains, while the white arrows show the consistent rotation of the magnetisation within the DW, represented by the black triangle	16
Figure 2.6: Schematic of the different arrangements of neighbouring domains, and the characterisation of the domain walls, represented by the black triangles, that separate them: AW - Anticlockwise rotation, CW - Clockwise rotation – these are the same wires as depicted in Figure 2.5	16
Figure 2.7: OOMMF simulation of the structure of a Transverse Domain Wall within a magnetic nanowire – these simulations saw external magnetic fields applied parallel to the long axis of the nanowire. The red and blue backgrounds represent the direction of the magnetisation at each point along the wire	17
Figure 2.8: OOMMF simulation of the structure of a Vortex Domain Wall within a magnetic nanowire. External magnetic fields were applied parallel to the long axis of the nanowire. The red and blue backgrounds represent the direction of the magnetisation at each point along the wire	18
Figure 2.9: Basic form and example of geometric frustration, with an antiferromagnetic triangular lattice. The arrows depict spin directions at two vertices, and the question	

mark emphasises how, given the two known spin directions, it is not possible to definitively predict the spin direction at the question mark [31]	20
Figure 2.10: A depiction of the tetrahedral structure within water ice, and the two-in, two-out structure of the bonds between the hydrogen (black) and oxygen (white) ions [33]	21
Figure 2.11: A diagram of a bulk magnetic material (grey rectangle) with labelling denoting the angle, θ , between the applied current (red arrow) and sample magnetisation (blue arrow) – these are the properties which give rise to AMR.....	24
Figure 2.12: Comparing the three different geometries used to perform a MOKE measurement – the black arrow labelled “M” represents the applied magnetic field direction, with the red arrow representing the red laser light reflecting off of the sample surface within the incident plane	25
Figure 2.13: A standard hysteresis loop for a hard ferromagnetic material – the arrows on the loop show the manner in which the field is changing at these points. M_s is the saturation magnetisation, M_r is the remnant magnetisation, H_{ci} is the coercive field required to reverse the magnetisation and H_{sat} is the field required to saturate the material. The gradual nature of the magnetisation change is the indicator for the material being a hard ferromagnet [45]	27
Figure 3.1: Image taken from <i>Wang et al.</i> 's paper (2006). The two obtained images are AFM and magnetic contrast scans of an array of nanoislands in a square lattice geometry, and the accompanying graphics outline the potential alignments of magnetic moments around a vertex within this array, and their probabilities of occurring	32
Figure 3.2: SEM image taken from <i>Tanaka et al.</i> 's 2006 paper showing a fabricated hexagonal lattice, with a depiction of a number of the parameters involved in the measurements: J represents the current direction, and θ represents the angle between the current and the magnetic field, H	34
Figure 3.3: Graph taken from <i>Tanaka et al.</i> 's paper with the first measurements of magneto-transport properties of Artificial Spin Ice structures, with the measurement being taken at an angle of 75° as defined in the paper, with 0° having the applied magnetic field parallel to one of the bars of the lattice [48]	35
Figure 3.4: From <i>Branford et al.</i> paper showing the asymmetry which arises in low temperature measurements but has not been observed at higher temperatures – the images on the right show the orientations of the current, voltage and magnetic field relative to the lattice, with the plots to the left of each image showing the resultant data at 100K and 2K temperatures [15]	37

Figure 3.5: Schematic diagram of the short-island (c) and long-island (d) Shakti lattice designs, showing how the nanomagnetic bars are orientated in these two designs – those bars in a darker shade of blue show the effective “unit cell” of the lattice[63].....	39
Figure 3.6: Scanning Electron Microscope image and schematic representation of the setup in <i>O'Brien et al's</i> publication in 2009, showing the DWs within their nanowires, and their propagation directions under specific applied magnetic field conditions. The SEM image shows a physical sample and labels measurement locations with the stars	40
Figure 3.7: Graph from <i>O'Brien et al's</i> 2009 publication showing the depinning field of a pair of DWs in adjacent magnetic nanowires, as a function of the separation distance of the adjacent wires. – the inset figure shows the typical MOKE signal obtained in measuring these structures [71].....	41
Figure 3.8: Simulation of a two-layer square lattice of nanoislands and their associated magnetic moments, shown by the arrows inside the islands [73] – the two different colours represent the two different deposition layers of the magnetic bars, with the blue layer atop the green, separated by a spacer layer not represented in this image	42
Figure 3.9: SEM image in <i>Allwood et al.</i> [46] showing the design of a domain wall diode within a nanowire, with a narrower region and a wider region separated by an area which will restrict DW motion from right-to-left, but not at all from left-to-right.....	43
Figure 3.10: Diagram from <i>Kläui et al's</i> 2003 paper showing the setup used to identify Domain Wall pinning in ferromagnetic nanoring, with image (b) showing a portion of the ring with a narrowed region intended to restrict the propagation of the DW [77]	44
Figure 3.11: Graph from <i>Kläui et al's</i> 2003 paper showing Domain Wall pinning through magnetoresistance measurements of circular nanowire – the five inset schematics showing the position of the DW within the nanoring and at what magnetic fields these instances correspond to [77]	45
Figure 3.12: Diagram showing the design and operation of "racetrack memory" as defined by <i>Parkin et al</i> in 2008 – the red and blue colours in magnetic nanowires represent the two magnetisation directions possible in these wires, analogous to binary bits used for storing data. Images detail the manner in which an array of these wires would be stored and methods by which information can be read and written[1]	46
Figure 4.1: Schematic of the stages of production: 1-Spinning 2-Developing 3-Thermal Deposition 4-Lift-Off, Yellow – PMMA resist, Blue – Silicon substrate, Silver – Permalloy deposition.....	51
Figure 4.2: Schematic showing the scattering processes that are experienced by electrons from an electron beam as they are incident upon a layer of resist (dark) atop silicon wafer (light). The blue arrow denotes incident electrons reflected off of the layer	

of resist, whereas the red arrows are electrons transmitting through the resist and scattering, subsequently reflecting off of the substrate.....	54
Figure 4.3: Screen capture of a typical image on the EBL Pattern Design software – each different colour on the above pattern refers to a separate “layer” of the design; each layer can be explicitly and individually added and excluded from a write – the faint squares represent individual “write fields” into which the overall pattern is broken down. These write fields have areas of 100x100µm.....	56
Figure 4.4: Calibration of the thickness of Permalloy deposited according to the crystal monitor, compared with actual measured thickness – the blue line represents a best fit to the data, while the red line represents a unity relationship between the two thickness readings.....	58
Figure 4.5: Schematic of how four measuring wires are placed on a sample for a 4-terminal resistance measurement. The green region indicates the area of the grey magnetic material which will be measured based on the placement of the gold contacts, and based on the wires chosen for voltage and current being as labelled....	61
Figure 4.6: SEM image of the typical arrangement of the contacts used to electrically measure ASI lattices – the dark rectangles extending out from the edge of the central lattice are the gold contacts used to supply electrical current and detect voltage	62
Figure 4.7: Schematic outlining the four measurement orientations used while performing magneto-transport measurements on hexagonal lattice-based ASI – the surrounding hexagon shape refers to the orientation of the hexagons in the lattice relative to the depicted directions of the current and magnetic field	65
Figure 4.8: Schematic of the relative directions of Current & Voltage in standard AMR and Hall measurements. Here the red arrow represents the current path and the blue arrow is the direction over which the voltage is detected.....	66
Figure 4.10: A normalised average calibration obtained for the intensity detected by the detector for a MOKE experiment as a function of the angle of the quarter wave plate.	69
Figure 5.1: Example of a magnetotransport measurement dataset, with coloured arrows demonstrating the way in which the magnetic field is changing between data points of the corresponding colours	76
Figure 5.2: Scanning Electron Microscope (SEM) image of an example of a single vertex in a hexagonal ASI – the single vertex in the centre is deposited first, and is formed from Permalloy, while the contacts attached to it are made from gold	78
Figure 5.3: SEM image of a connected example of a hexagonal ASI – the network consists of Permalloy of 20nm thickness, wire width 150nm	79
Table 1: Detailing the samples whose data features in the following chapter, and a description of their characteristics.....	81

Figure 5.4: AMR obtained from simulation data (red) of a single magnetic nanowire influenced by the effect of external magnetic field, overlaying the raw data (blue) of a sampled Permalloy nanowire – the red trace is relating to the right y-axis, and the blue data relates to the left y-axis – the resistances quoted in the simulation are not representative and so the overlay is merely indicative of the shape of the resistance change as a function of magnetic field	82
Figure 5.5: Graph from <i>Fert et al</i> showing the AMR data for a single magnetic nanowire of Co [95]	84
Figure 5.6: Annotated SEM image of sample ASI47, which consists of a single vertex of a hexagonal lattice, labelled with the names of the three individual magnetic bars for reference – these bars are named as such based on their orientation relative to the applied magnetic field	85
Figure 5.7: Annotated SEM image of sample ASI47, which consists of a single vertex, showing the current and voltage contacts necessary for measurement of a single bar – the red regions show the current delivering contacts overlapping with the vertex, the yellow regions show where voltage is detected between, and the green region represents an estimate of the volume of the magnetic material which is detected in this measurement geometry	87
Figure 5.8: The AMR from the horizontal bar of a single magnetic vertex of a hexagonal lattice at room temperature, conducted on sample ASI47 – inset is a schematic showing the region (red) of the single vertex (blue) measured in this instance, with the green arrow representing the external field	88
Figure 5.9: OOMMF Simulation of the AMR of the horizontal nanowire of the single vertex when external field is applied - inset is a schematic showing the region (red) of the single vertex (blue) measured in this instance, with the green arrow representing the external field.....	89
Figure 5.10: Schematic of how a smaller fraction of the horizontal bar of a single vertex is measured by the movement of one contact away from the end of the bar - the blue arrow shows the movement of the 2nd contact along the wire	90
Figure 5.11: A comparison of the AMR data for a horizontal bar within the single vertex of hexagonal lattice ASI, as the percentage of the bar measured is varied.....	91
Figure 5.12: The single vertex, showing the increased size of the measured region - the red area represents the region of the initial measurement, with the brown area the region which has been added for the next calculation	93
Figure 5.13: Simulating the single vertex where the larger shaded region of Figure 5.12 is measured for its magnetoresistance, with the measurement exceeding the length of just the parallel magnetic bar	94

Figure 5.14: Schematic diagram depicting how the application of a sufficiently high external magnetic field (Blue arrow) causes the magnetic moments (Grey arrows) within a magnetic nanowire to divert away from the easy axis of the wire and tend towards parallel alignment with the field.....	95
Figure 5.15: Graph showing a simulation of the magnetisation along the easy axis of a single ferromagnetic nanowire as the angle and intensity of the magnetic field is varied, evidencing the idea that the magnetisation is affected more strongly as the size of the angle between the easy axis and the magnetic field is increased	96
Figure 5.17: SEM image of lattice on sample ASI13 for experiment into effect of capping samples on low-temperature AMR – the hexagonal bars are composed of Permalloy, and in the case of this experiment are capped with a thin layer of Aluminium	100
Figure 5.18: Annotated SEM image of hexagonal lattice from sample ASI13, showing the electrical measurements taken relative to the sample orientation – this measurement configuration was completed for both the capped and uncapped samples	101
Figure 5.19: The AMR in the Planar Hall geometry of an uncapped Permalloy lattice from sample ASI7 at 3K – the inset panel showing how the current (red) and the applied magnetic field (blue) are orientated in relation to the hexagons of the lattice	102
Figure 5.20: The AMR of sample ASI7, an uncapped Permalloy lattice of hexagonal ASI, at 25K - the inset panel showing how the current (red) and the applied magnetic field (blue) are orientated in relation to the hexagons of the lattice	104
Figure 5.21: Describing how the asymmetry in the AMR data for the uncapped connected lattice in sample ASI7 is varied as a function of the temperature of the sample – the red dotted line is simply a guide for the eye and does not have physical meaning, and the inset panel shows how the current (red) and the applied magnetic field (blue) are orientated in relation to the hexagons of the lattice	105
Figure 5.22: The AMR of a Permalloy lattice of ASI with Aluminium Cap at 3K – sample ASI13, with a Permalloy thickness of 31nm – the inset panel showing how the current (red) and the applied magnetic field (blue) are orientated in relation to the hexagons of the lattice	106
Figure 5.23: Demonstrating the observed magnetisation reversal in a connected vertex for temperatures under 50K by <i>Zeissler et al.</i> The large blue arrow denotes the applied field direction for both images. The black and white arrows represent the magnetisation direction within the nanowires and the red and green regions are domains	108
Figure 5.24: Schematic of the four measurement orientations used while performing magneto-transport measurements on hexagonal lattice-based ASI – the hexagons	

represent the orientation of the hexagons in the lattice with respect to the other quantities	109
Figure 5.25: The AMR measurement in Orientation 4 for a connected hexagonal ASI lattice - the inset panel showing how the current (red) and the applied magnetic field (blue) are orientated in relation to the hexagons of the lattice	110
Figure 5.26: <i>Tanaka et al's</i> graph showing the AMR of a hexagonal lattice and its dependence on the angle between the measured current and magnetic field applied across the sample.....	111
Figure 5.27: The AMR measurement in Orientation 3 for a connected hexagonal ASI lattice - the inset panel showing how the current (red) and the applied magnetic field (blue) are orientated in relation to the hexagons of the lattice	112
Figure 5.28: The AMR measurement in Orientation 2 for a connected hexagonal ASI lattice - the inset panel showing how the current (red) and the applied magnetic field (blue) are orientated in relation to the hexagons of the lattice	113
Figure 6.1: SEM image of a hybrid lattice with non-magnetic connectors at the vertices - in this case the connectors are of the same shape as the bars being connected. The bars are made out of Permalloy while the vertices are Aluminium.....	118
Figure 6.2: SEM image of a hybrid example of a hexagonal ASI – the narrow bars are fabricated from Permalloy and the connecting triangles are fabricated from Gold	119
Figure 6.3: SEM image of a vertex within a typical restricting hexagonal lattice made out of NiFe – the restricting sections of the lattice at each vertex are constructed as such through the design implemented into EBL during fabrication	121
Table 2: Documenting the samples created and measured as part of the displayed results within Chapter 6.....	122
Table 3: The two-terminal resistances of different hexagonal ASI lattices at both room temperature and 3 kelvin – the average is calculated from 15 different resistance measurements per sample.....	123
Table 4: The four-terminal resistance measurements for different lattice types of hexagonal ASI – this is an average of between 5 and 10 measurements for each sample type	124
Figure 6.4: SEM image showing the relative distances of current paths through the hybrid lattice - the yellow line shows the path through Permalloy for one nanowire, while the red line shows the distance from one Au/Py interface to the next equivalent interface.....	125
Figure 6.5: Evaluating the 4-terminal resistances across different types of samples as a function of sample temperature – the key refers to the type of lattice depicted by the two different colours displayed in the graph	126

Table 5: Detailing the RRR for different types of hexagonal ASI Lattice	127
Figure 6.6: SEM image of a hybrid lattice of 25nm thick Permalloy nanowires, connected by 20nm thick gold triangles at the vertices	129
Figure 6.7: SEM image, highlighting the direction of the applied magnetic field (Blue) and the direction of the current path through the hybrid lattice (Red) during measuring of Orientation 4, flowing from the positive end to the negative end. This is a simplified representation as, given the size of the contacts relative to these wires, there are likely to be several start and end points of the current path	131
Figure 6.8: The AMR of the Orientation 4 measurement for the hybrid hexagonal ASI lattice at RT - the inset panel showing how the current (red) and the applied magnetic field (blue) are orientated in relation to the hexagons of the lattice	132
Figure 6.9: Comparing the AMR data for the hybrid lattice in Orientation 4 with a square of a cosine function, attempting to fit to the background AMR curve – the red data is experimental and runs from -120mT up to +120mT – the blue curve is an attempted fit to the background curve caused by the AMR of the bars not parallel to the field - the inset panel showing how the current (red) and the applied magnetic field (blue) are orientated in relation to the hexagons of the lattice	133
Figure 6.10: The remaining data for the Orientation 4 measurement of the hybrid lattice when the fitted curve is subtracted from the data - the inset panel showing how the current (red) and the applied magnetic field (blue) are orientated in relation to the hexagons of the lattice	134
Figure 6.11: The low-field data from the Orientation 4 measurement for the hybrid hexagonal ASI lattice at room temperature - the inset panel showing how the current (red) and the applied magnetic field (blue) are orientated in relation to the hexagons of the lattice	135
Figure 6.12: Sequence of schematic diagrams explaining the mechanisms of the ice rules – the large blue arrow represents the applied external magnetic field, a blue arrow within the wires signifies the magnetisation pointing out from the vertex, while a red one signifies the magnetisation pointing in towards the vertex	136
Figure 6.13: Simulation of a single vertex with applied magnetic field parallel to the x-axis, with the field of 30mT causing a reversal in the magnetisation of the horizontal magnetic nanowire – the inset shows the scale of the image, with the sideways length of the white bar equating to a 200nm length within the image	138
Figure 6.14: Continuation of the simulation of a single vertex with applied magnetic field parallel to the x-axis, still with applied field of 30mT, causing the DW to reverse the magnetisation of the bottom diagonal magnetic nanowire	139

Figure 6.15: Schematic depiction of Orientation 4 measurement of a hexagonal lattice as a network of individual resistors – the individual resistors represent an individual nanoisland within the lattice, and their intersections are the vertices of the lattice – the two red boxes are the endpoints of the current path, and the blue arrow is the direction of applied magnetic field	140
Figure 6.16: Close-up schematic depiction of Orientation 4 measurement of a hexagonal lattice as a network of individual resistors, outlining why bars parallel to the field do not contribute to resistance in this orientation – the red arrows depict the direction of current flow through the network, and the large blue arrow denotes the applied magnetic field direction	141
Figure 6.17: SEM image, highlighting the direction of the applied magnetic field (Blue) and the direction of the current path through the hybrid lattice (Red) during measuring of Orientation 3 flowing from the positive end to the negative end. This is a simplified representation as, given the size of the contacts relative to these wires, there are likely to be several start and end points of the current path.....	142
Figure 6.18: Low-field AMR data from the Orientation 3 measurement for the hybrid hexagonal ASI lattice at room temperature - the inset panel showing how the current (red) and the applied magnetic field (blue) are orientated in relation to the hexagons of the lattice	143
Figure 6.19: Comparing the AMR data for the hybrid lattice in Orientation 3 with a square of a cosine function, attempting to fit to the background AMR curve – the red data is experimental and runs from -120mT up to +120mT – the blue curve is an attempted fit to the background curve caused by the AMR of the bars not parallel to the field - the inset panel showing how the current (red) and the applied magnetic field (blue) are orientated in relation to the hexagons of the lattice	144
Figure 6.20: The remaining data for the Orientation 3 measurement of the hybrid lattice when the fitted curve is subtracted from the data - the inset panel showing how the current (red) and the applied magnetic field (blue) are orientated in relation to the hexagons of the lattice	145
Figure 6.21: Comparing the magnetisation reversal of the hybrid lattice in Orientation 3 both experimentally and through OOMMF simulation of a single vertex	147
Figure 6.22: The AMR for the Orientation 2 measurement for the hybrid hexagonal ASI lattice at room temperature - the inset panel showing how the current (red) and the applied magnetic field (blue) are orientated in relation to the hexagons of the lattice	148
Figure 6.23: SEM image, highlighting the direction of the applied magnetic field (Blue) and the direction of the current path through the hybrid lattice (Red) during measuring of Orientation 2 flowing from the positive end to the negative end. This is a simplified	

representation as, given the size of the contacts relative to these wires, there are likely to be several start and end points of the current path	149
Figure 6.24: AMR of the Orientation 1 measurement for the hybrid hexagonal ASI lattice at room temperature - the inset panel showing how the current (red) and the applied magnetic field (blue) are orientated in relation to the hexagons of the lattice	151
Figure 6.25: SEM image, highlighting the direction of the applied magnetic field (Blue) and the direction of the current path through the hybrid lattice (Red) during measuring of Orientation 1 flowing from the positive end to the negative end. This is a simplified representation as, given the size of the contacts relative to these wires, there are likely to be several start and end points of the current path	152
Figure 6.26: Fitting a curve to the AMR data obtained for Orientation 1 of the hybrid hexagonal lattice – the blue curve is an attempt to match the background AMR effect but is not physically representative - the inset panel showing how the current (red) and the applied magnetic field (blue) are orientated in relation to the hexagons of the lattice	153
Figure 6.27: The resulting difference when subtracting the curve fitted to the data for Orientation 1 of the hybrid lattice from the data itself - the inset panel showing how the current (red) and the applied magnetic field (blue) are orientated in relation to the hexagons of the lattice	154
Figure 6.28: Base image created and inputted into OOMMF to simulate the AMR of a single vertex of Artificial Spin Ice, with scale bar inset.....	155
Figure 6.29: AMR data extracted from OOMMF simulations of a hexagonal vertex with varying levels of connection and proximity between the bars – an offset has been assigned to the y-axis measurements such that they do not overlap one another and thus readability is improved.....	156
Figure 6.30: SEM image, highlighting the direction of the applied magnetic field (Blue) and the direction of the current path through the hybrid lattice (Red) during measuring of Orientation 4 flowing from the positive end to the negative end. This is a simplified representation as, given the size of the contacts relative to these wires, there are likely to be several start and end points of the current path	158
Figure 6.31: The AMR signal for Orientation 4 measurement of a connected ASI hexagonal lattice at Room Temperature - the inset panel showing how the current (red) and the applied magnetic field (blue) are orientated in relation to the hexagons of the lattice	159
Figure 6.32: The AMR signal for Orientation 4 measurement of a hybrid ASI hexagonal lattice at Room Temperature - the inset panel showing how the current (red) and the applied magnetic field (blue) are orientated in relation to the hexagons of the lattice	160

Figure 6.33: Low-field range data for Orientation 4 of a hybrid hexagonal ASI lattice at room temperature, with two dashed black lines showing the two resistance minima and the fields at which they occur - the inset panel showing how the current (red) and the applied magnetic field (blue) are orientated in relation to the hexagons of the lattice	162
Figure 6.34: Comparing the normalised resistances measured through the hybrid lattice through Orientations 3 & 4 – the offset on the y-axis between the two measurements is deliberate and not significant in the data - the inset panels correspond to the two sets of data, and show how the current (red) and the applied magnetic field (blue) are orientated in relation to the hexagons of the lattice in each instance	163
Figure 6.35: The normalised sizes of the switching signals of a hybrid lattice in Orientation 3 as a function of temperature – the two different colours refer to data sets taken several months apart, although they contribute to one set of data - the inset panel showing how the current (red) and the applied magnetic field (blue) are orientated in relation to the hexagons of the lattice	164
Table 6: List of the switching fields of hybrid lattices at different measurement temperatures	165
Figure 6.36: SEM image of a vertex within the restricting hexagonal lattice, with the two different widths of the lattice channels labelled – W_2 is the width of the normal hexagonal lattice, while W_1 is a reduction on this, in an attempt to obstruct the propagation of DWs across vertices in the lattice	166
Figure 6.37: The AMR signal for a 30% restricting hexagonal lattice of Permalloy nanowires, carried out in the Orientation 4 measurement geometry - the inset panel showing how the current (red) and the applied magnetic field (blue) are orientated in relation to the hexagons of the lattice	168
Table 7: Table showing the signal size of AMR measurements in Orientation 2 for a range of different hexagonal lattices	169
Figure 6.38: The size of the AMR switching signal for hexagonal lattices of different levels of restriction – the blue dotted line is a guide to the eye	170
Figure 6.39: Simulating the competing magnetic fields within a restricting lattice to determine the nature of DW propagation – the red data refers to a lattice of wire width 200nm, the blue data for a lattice of wire width 300nm – the solid horizontal lines are the fields required to nucleate a new DW in a wire with 60° to the applied magnetic field	171
Figure 6.40: How the critical restriction of the hexagonal lattice varies as a result of the width of the wires within the lattices, and the corresponding switching field at the critical restriction – the narrow red rectangle represents the experimentally suggested	

approximate critical lattice restriction for a lattice with width 150nm – the red and blue lines are guides to the eye	173
Table 8: Detailing how the nature of the transitions within a restricting lattice affect the DW propagation and, therefore, the critical restriction.....	175
Figure 7.1: Example of a magnetotransport measurement dataset, with coloured arrows demonstrating the way in which the magnetic field is changing between data points of the corresponding colours	178
Figure 7.2: SEM image of a pair of magnetic nanowires, designed such that two different DW types can be nucleated into the wires and brought together through magnetic field applications – the arrows labelled A and B show the directions of applied magnetic field pulses during the experiment, required to nucleate and then propagate DWs through the wires.....	179
Figure 7.3: Schematic showing the manner in which magnetisation (red) in the sample is directed as a result of the external magnetic field (yellow arrow), resulting in the formation of one head-to-head and one tail-to-tail DW in the two wires.....	181
Figure 7.4: Schematic diagram showing the effect of the external field on the two types of DW, with the red and grey arrows showing the two magnetisation directions, and the black arrows the direction of DW propagation caused by the external field (yellow) ..	182
Figure 7.5: XMCD-PEEM image of a pair of nanowires, showing the magnetic contrast of magnetic domains and highlighting the DWs on the wires – the black and white regions of the wires are opposing directions of magnetic contrast.....	183
Figure 7.6: Image showing the clear separation of two nanowires used in the DW pinning experiment at Diamond Light Source.....	184
Figure 7.7: XMCD-PEEM images of pinning of DWs in the adjacent nanowires, and the strengths of the magnetic pulses at each different image shown above. The lighter and darker contrast within the nanowires show the two opposing magnetisation directions of the material.....	185
Figure 7.8: XMCD-PEEM imaging showing the depinning of a pair of DWs and the fields (magnitude) necessary for this. The lighter and darker contrast within the nanowires show the two opposing magnetisation directions of the material	186
Figure 7.9: SEM image of a connected ASI square lattice produced during a single fabrication process – the bars consist of Permalloy	187
Figure 7.10: Close up of the SEM image of a connected ASI square lattice, with the red lines showing the four bars of a single vertex.....	188
Figure 7.11: Schematic image showing the two varieties of interaction in a square lattice – the red arrow, showing the distance between the ends of a perpendicular pair of bars, is shorter than the black arrow indicating the separation of parallel bars	189

Figure 7.12: Hysteresis loop taken from a MOKE magnetometer measurement of a thin film of Nickel	193
Figure 7.13: Hysteresis loop taken from a MOKE magnetometer measurement of a thin film of Permalloy, with the hysteresis occurring in the measured laser intensity by a detector following the reflection of the laser light off of the magnetic material being exposed to the magnetic field.....	194
Figure 7.14: Scanning Electron Microscope image of the square lattice Artificial Spin Ice, showing the angles that the externally applied magnetic field was directed across the sample, and what these angles refer to in respect to the lattice.....	195
Figure 7.15: Graph showing the hysteresis loop of a square lattice Artificial Spin Ice, for an applied field of angle 45° obtained via MOKE	196
Figure 7.16: Graph showing the size and quality of the MOKE signal obtained from a square lattice of ASI through a layer of inverted PMMA, with the magnetic field at an angle of 0 degrees to the easy axis of the lattice – also taken with the laser’s temperature controller turned off	197
Figure 7.17: Graph showing the size and quality of the MOKE signal obtained from a square lattice of ASI through a layer of inverted PMMA, with the magnetic field at an angle of 0 degrees to the easy axis of the lattice – for comparison, the laser’s temperature controller was turned on.....	198
Figure 7.18: SEM image of a simple two-layer structure with the two layers separated by a transparent layer of inverted PMMA	199
Figure 7.19: SEM image of a larger two-layer structure with the two layers separated by a transparent layer of inverted PMMA	200
Figure 7.20: SEM Image of a Quasi 3D Square lattice - the line across the image along the centre, ending in a black dot, is a row of dead pixels on the image capturing camera.....	201

1. Introduction

The increasingly digital nature of society has placed a huge importance on the availability and efficiency of commercial devices. In particular there is an interest in advancing the capabilities of data storage devices, and computer logic systems [1]–[5], through the further understanding and exploitation of nanomagnetic structures.

Currently, the demand for data storage already exceeds the ability of contemporary storage devices [6], with the amount of data stored being dictated by the available space. One particular avenue being considered as a potential source of an improved data storage technique is through the further exploration of nanomagnetism, and notably domain walls (DWs) in ferromagnetic nanowires [1], [2], [7], [8].

When made from Permalloy (NiFe), the dominant effects within these nanowires can be, in part, controlled by the sample geometry. Having narrow wires ensures that the magnetisation within these structures will lie in one of two orientations, along the “easy axes” of the wires. This is highly suitable to the proposed application of data storage, due to the conventional storage of data in the form of binary bits. [1]

Electron beam lithography (EBL) [9]–[11] is a technique involved in sample fabrication, which has allowed for sufficiently sophisticated and small-scale devices to be realised, with dimensions of as small as tens of nanometres being consistently reproducible. Magnetic structures on this scale have become viable tools to be utilised in these different technological applications.

The aim of this thesis is to investigate novel and previously unconsidered aspects of artificial spin ice (ASI), through magnetotransport measurements of hexagonal lattices with differing amounts of physical connectivity. This will shed light on the manner in which magnetic DWs can affect the interactions within these different ASIs.

The ferromagnetic material used for the magnetic regions of all different structures investigated is NiFe. The reason for its use is due to it having almost no magnetocrystalline anisotropy. [12] Due to the competing effects which determine the magnetisation within these structures, the magnetisation will normally lie along the easy axis of the structures. This changes when the structures are subjected to an external magnetic field. The small amount of magnetocrystalline anisotropy means that the magnetisation is comparatively less hindered in rotating to face the same direction as that field. [12]

1.1. Overview of chapter content

Chapter 2 focuses on the fundamental theory of nanoscale ferromagnetism, with specific focus on the understanding of magnetic domains and DWs and the basic concept of ASI. Different techniques for sample measurement are introduced, in terms of the scientific theory which underlies them and allows for their use as a means to measure samples. These phenomena include the magneto-optic Kerr effect (MOKE) and anisotropic magneto-resistance (AMR), emphasised as these are the techniques I have favoured for my data acquisition. Following this, Chapter 0 discusses relevant published work within the fields of ASI and nanomagnetic DWs, which has shaped the research path taken during this study.

Chapter 4 is a description of the processes involved in designing and fabricating the ASI and magnetic DW-based samples which have been measured during my study. This is alongside the equipment and techniques used to perform those measurements. Different samples within my portfolio require different measuring techniques, such as the aforementioned AMR or MOKE, and which measurement is preferable is dependent on the specific nuances of the samples and what the desired outcome of the measurements is.

After outlining the processes and equipment used in the creation and measurement of the samples, the remainder of the thesis focusses on the measurements completed and the subsequent results and analysis. Firstly, chapter 0 is based on the hexagonal lattice of ASI, initially focussing on examples where the wire widths and thicknesses remain the same throughout the lattice. This is achieved by considering the single vertex of the hexagonal lattice, and the manner in which DWs are propagating through it. [13] The single vertex is assessed for its magnetoresistance properties.

Following this the connected hexagonal lattice was investigated, both to assess the effect of different DW types within the lattice (either transverse (TDWs) or vortex (VDWs)), and also the effect of having a non-magnetic cap atop the magnetic lattice. This has been studied previously [14], as a means of investigating an effect discovered in ASI lattice at low temperatures. [15] The measurements of an asymmetry in the AMR signal at these low temperatures prompted my experiment. I added a non-magnetic capping layer to the magnetic channel to consider whether this affected the behaviour

of the low temperature magnetisation, and whether this previously-seen asymmetry in the measurements would remain present.

Chapter 0 features an in-depth investigation into what we have dubbed the “hybrid lattice”. This is based on a hexagonal lattice of unconnected magnetic nanoislands, but with the addition of a series of non-magnetic, normal metal connectors forming an electrical circuit through this network of unconnected nanoislands. The name derives from being able to combine the unconnected lattice with the ability to still conduct electrical measurements. This measuring of the unconnected ASI via magnetotransport represents the first such measurement on an unconnected ASI, and offers the opportunity to compare the AMR behaviour of the connected and unconnected ASIs.

Following on from the hybrid lattice, the investigation developed to consider other forms of the hexagonal lattice between the two extremes of the fully connected lattice and the unconnected ‘hybrid’ lattice. Between these two extremes can be investigated hexagonal lattices which are connected, but with narrower vertices than the wires connecting them. This type of lattice has been named the ‘restricting lattice’ during this study, so-called because it restricts the propagation of the DWs through the lattice between individual nanowires. The investigation attempted to describe the onset of the level of restriction to these DWs being sufficient to prevent them from propagating, and for it to be favourable for each nanowire to have its own DW nucleated within it.

Chapter 0 looks at the interaction between DWs in adjacent nanostructures in two different contexts: either with both nanostructures on the surface of the substrate, or with one nanostructure vertically displaced from the surface by a non-magnetic layer. The first of these sees pairs of DWs propagated in opposite directions along parallel nanowires, and their interaction is examined. The other investigation sees the separation of nanostructures in a vertical direction atop the substrate, with the introduction of a “spacer” layer between two magnetic layers, and to study the interactions of these nanostructures perpendicular to the area of the nanowires. This vertical displacement between two ferromagnetic layers opens the opportunity for novel two-layer ASI samples, such as a square lattice which has equal interactions between all nanowires at a vertex. This has been the preliminary focus for this part of my study.

2. Theory of Ferromagnetism and Artificial Spin Ice

This chapter will outline the basic theory of micromagnetism as well as structures and phenomena which are to be made use of in the following experimental and results chapters. The chapter begins with a description of micromagnetism and the competing magnetic interactions within structures.

Key to the kinds of investigations seen later in the thesis are the ways in which magnetisation is reversed with different structures, and so there is an introduction to domain structure and magnetic domain walls (DWs).

The main focus of the study is artificial spin ice (ASI), a form of nanomagnetic structure which makes use of and serves to investigate the property of magnetic frustration. The origins of this kind of structure and the theory behind this concept of frustration are outlined clearly in this chapter, before a far greater level of detail into the investigations using these structures is included in Chapter 0.

Measuring the samples created in the course of my investigation requires the use of systems which function through the exploitation of a number of different magnetic phenomena, such as anisotropic magneto-resistance (AMR) and the magneto-optic Kerr effect (MOKE). These phenomena will be described here, before the created systems are to be discussed in Chapter 4. Also explained is the mechanism behind a measurement technique, photoemission electron microscopy (PEEM) and X-Ray magnetic circular dichroism (XMCD) which has been made use of while investigating samples focussed on DW interactions.

The subject of this thesis is nanomagnetic samples, the majority of which are in the form of ASI, with a focus also on DWs and the control and manipulation of these. This chapter attempts to outline the relevant theory which has led to these areas of interest for this project. This includes the origins of the phenomena and how they came to be discovered, thus leading to the creation of such structures as studied thoroughly today.

2.1. Fundamentals of the theory of magnetism

Within magnetism there have been defined two different types of magnetic field, defined **B** and **H**. **H**, the magnetic field strength, is defined as the driving magnetic

component deriving explicitly from external currents in materials. However, these materials can react to the input of this field **H**, and this can result in a different magnetic field ultimately being produced. This is what is denoted as **B** and is known as the magnetic flux density. These two variables are related to each other via:

$$\mathbf{B}_0 = \mu_0 \mathbf{H} \quad (1)$$

where μ_0 is defined as the permeability of free space, and B_0 is defined as the constant and homogeneous magnetic field which creates magnetisation within a material by polarising spins. Another way of expressing the relationship between **B** and **H** is:

$$\mathbf{B} = \mu_0 (\mathbf{H} + \mathbf{M}) \quad (2)$$

Where **M** represents the magnetisation in the material, indicating the prevalent direction of the magnetic moments within that material.

The reaction demonstrated by a magnetic material in response to an applied external magnetic field can be expressed as either the magnetic susceptibility or permeability.

The magnetisation, **M**, of a material being acted on by an applied field, **H**, can be defined by the following relationship:

$$\mathbf{M} = \chi \mathbf{H} \quad (3)$$

where χ is effectively a constant of proportionality and represents the magnetic susceptibility. The permeability, on the other hand, is defined as:

$$\mu = \mu_r \mu_0 \quad (4)$$

where μ_0 is the permeability of free space, essentially the magnetic permeability found inside a vacuum. μ_r is the relative permeability, and compares to the previously defined susceptibility through:

$$\mu_r = 1 + \chi \quad (5)$$

The relative permeability is used to allow for the permeability to be conveyed as a factor of the permeability of free space. Therefore in a vacuum, $\mu_r = 1$, and the relative permeability is also very close to unity in cases where the material is not ferromagnetic. [16]

2.2. An introduction to micromagnetism

This thesis focusses on the field of micromagnetism, namely the study of magnetic materials and their interactions on scales below the micrometre, and particularly ferromagnetic materials.

All materials have a level of magnetisation – typically defined as a measure of the magnetic moment per unit volume. [17] There are a number of different forms of magnetism, [17] and so the manner in which the different materials are magnetic is not consistent across the range. This leads to further sub-categorising of these magnetic materials, into groups such as paramagnetic, diamagnetic and ferromagnetic materials.

Paramagnetism is an effect which causes attraction of the magnetic moments, such that they follow the direction of externally applied magnetic fields, creating an internal magnetic field which follows the direction of the external field. This is in direct contrast with diamagnetism, which sees repulsion when encountering the same magnetic field, and therefore creates a magnetic field inside the material which opposes the external field.

Ferromagnetism is often macroscopic in scale, albeit the individual interactions involved are still each of a microscopic size. The term describes ferromagnets, a group of materials which have their magnetic moments align with an externally applied field, but which can retain their magnetic order even after the removal of the external field, hence obtaining the moniker of “permanent magnets”. This can be misleading however

as, with the application of a suitable applied field, this magnetic state can ultimately be both reversed and reduced.

The alignment with an external magnetic field in a ferromagnet, results also in the alignment of the individual magnetic moments with one another, and a ferromagnetic material therefore favours this kind of alignment. The opposite can be said of antiferromagnetic materials – in this case the magnetic moments order themselves such that a moment has the opposite magnetisation to a nearest neighbour.

In reality, relatively few materials exhibit either ferromagnetic or antiferromagnetic properties. Typically those materials which do not show magnetic properties which pertain to ferromagnetism, are known as normal metals.

This is as a result of their magnetic moments pointing in random directions with respect to one another. Some samples remain in this state as they are affected negligibly by the application of magnetic fields – these samples are considered to be non-magnetic. The remaining materials have a non-zero magnetisation under certain conditions, and thus are characterised as being magnetic, or of having magnetic properties.

Magnetic materials can also be referred to as being hard or soft magnets, and this is in relation to the materials' 'hardness parameters' [18], which in reality is a ratio of the anisotropy of the material and its dipole energy. This measure of the hardness also has implications for the manner in which the magnetisation of the materials changes, and the way in which they respond to interactions from the external magnetic fields.

Hard magnetic materials have a hysteresis loop which is relatively square in profile, which is to say that the top and base of the loop are flat, meaning that the material retains its magnetised state even upon the removal of the applied field. Soft materials however have a fairly small area within the loop, and are likely to quickly lose any magnetisation developed by the external field's presence.

2.3. Domains in magnetic materials

Micromagnetism uses continuum mechanics, which considers materials as continuous masses, as opposed to discrete particles. The modern understanding of ferromagnetism is governed by findings from studies carried out by Landau and Lifshitz in 1935. [19] It was, however, Pierre-Ernest Weiss in 1907 who first coined the concept

of magnetic “domains” and the way in which magnetic materials have their structure determined.

All materials will seek to be in their state of minimum potential energy, and often this state sees these regions of aligned magnetic moments; and these ‘clusters’ are what became known as magnetic domains.[20] While this of course implies a level of order within the individual domains, the sum of the magnetic moments across the sample can still tend to zero for a non-magnetic sample, despite this grouping taking place.

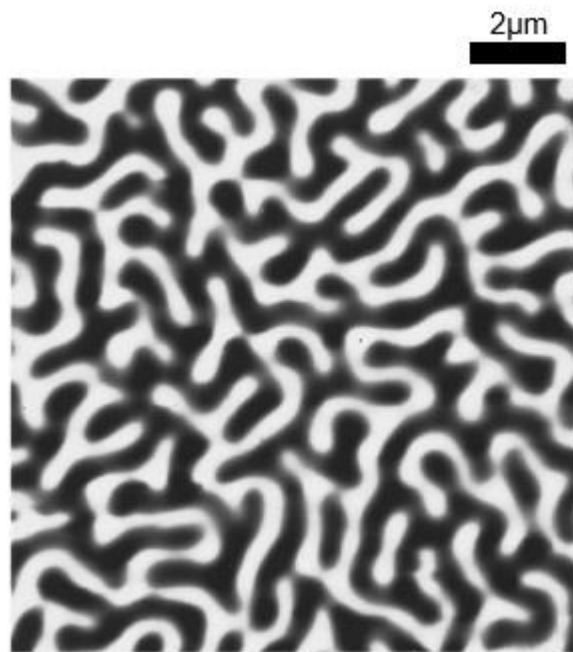


Figure 2.1: Magnetic Force Microscope (MFM) image of a NdFeB material showing the magnetic domain structure of the material, with the different contrasts shown corresponding to different magnetisation directions across the sample, the dimensions are confirmed by the scale bar atop the image [21]

The magnetically-sensitive contrast of the MFM allows for easy identification of the different domains within the structure and their boundaries. The reason for the presence of these domains comes from the principle of the minimum potential energy – the idea that all systems will tend to relax to their lowest energy state. Landau and Lifshitz presented the theory that magnetic domains form within these materials to minimise the total energy of the material. [19]

An important part of the total energy is the stray field energy, also commonly known as the demagnetising energy. This is the energy that originates from the magnetic dipole

interaction. In order to minimise the potential energy, the magnetic field lines maintain closed loops, which, in the event of single-domain bodies, leads to a large distance of field occupying space outside of the body itself.

This energy can be reduced by flux-closure type domains, which are of the form where magnetic flux essentially completes a closed loop in its path through domains. Figure 2.2 below serves to highlight this concept, showing in a simple example how progressing from a single-domain structure to a material with 4 domains, the volume that the inherent magnetic field has to cover outside of the confines of the material is greatly reduced and, indeed, eradicated.

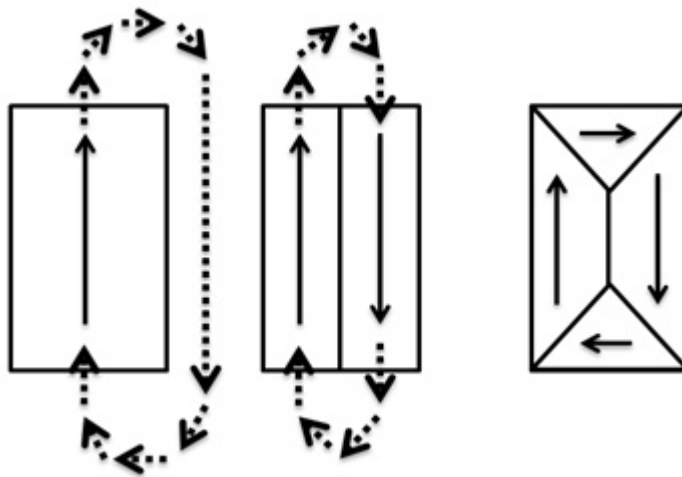


Figure 2.2: The process of a magnetic material breaking down into domains, results in an energetically favourable condition for the material – the solid arrows represent the magnetisation in each domain of the material, and the dotted lines show the stray fields outside of the material [20]

Aside from the manner in which they form a complete and ‘closed’ loop of magnetisation, the use of the nomenclature of “flux closure domains”, also refers to the setup in which there are no net magnetic poles.

Domain structures are also formed as a result of the fact that magnetic bodies have finite dimensions. The size of these domains also increases with the size of the overall structure. In theory, if there was a uniform magnetic material of infinite size, then it could have no domain structure in equilibrium.

2.4. Summary of the Gibbs free energy

The concept of reducing the overall energy of the system to determine the domain structure was realised elegantly and more completely by Landau and Lifshitz, who expressed the minimising of the Gibbs free energy through the summation of five different energy sources. It is the way in which the domain structure can best minimise all of these energies which will ultimately determine the state of the material.

2.4.1 Basis of the Exchange Energy

In the Landau and Lifshitz model of the Gibbs free energy, the first term in the equation responsible for the domain structure, E_{ex} is the idea of exchange interaction between neighbouring moments.

The exchange interaction is an effect seen through quantum mechanics, and relates to a situation where the wave functions of identical and indistinguishable particles overlap one another. In a ferromagnetic material, the interaction affects the Coulomb interaction and makes the interaction between the neighbouring particles such that the moments prefer to be aligned parallel to one another – whereas in an antiferromagnetic material, the opposite is the case.

The total exchange energy for a group of magnetic moments can be expressed quantum mechanically in terms of the Hamiltonian of the system:

$$H = \sum_{i,j=1} J_{i,j} S_i S_j \quad (6)$$

where S_i and S_j are the spin angular momenta of pairs of nearest neighbour moments within the material, and $J_{i,j}$ is known as the exchange constant, and refers to the way in which the spins of each particle will interact with its nearest neighbours. If the constant J is positive, then the spins will favour to be aligned to their nearest neighbours, and the material will tend to be ferromagnetic. If negative, then this leads to the favouring of anti-parallel alignment and the onset of antiferromagnetism.

2.4.2 Basis of the Magneto-Crystalline Energy & Shape Anisotropy

The second term in the equation for Gibbs free energy, E_k is due to the property of magnetocrystalline anisotropy.

Magnetocrystalline anisotropy [22] is the way in which a material's magnetic properties are dependent on the direction within the material. When there is no externally applied magnetic field, the magnetic moment of an isotropic non-ferromagnetic material is completely random – that is to say there is no inherent preference for any particular direction. That is not the case in an anisotropic material.

In this case, the magnetic moment will be aligned with what is known as an “easy axis” of the material, a direction of spontaneous magnetisation which is deemed to be energetically favourable – these favourable directions being borne out of several different types of anisotropy, such as magnetocrystalline, shape, magnetoelastic and exchange anisotropy. These anisotropy contributions compete against one another, with some contributing more strongly in particular materials, while not being a significant factor at all in others. For instance, in Permalloy, a compound of Nickel & Iron, there is no magnetocrystalline anisotropy and as such it is not a factor when considering the energy in this material.

Magnetocrystalline anisotropy is a property of a material where the energy required to saturate the magnetisation in a sample varies depending on the direction the energy is applied relative to the sample, commonly that the lower energy corresponds to directions along the easy axes of the crystal structure of the materials.

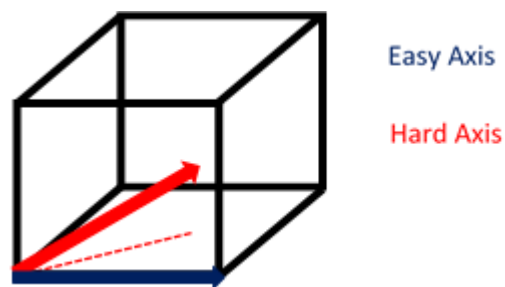


Figure 2.3: Defining the hard and easy axes of materials, which form the basis of magnetocrystalline anisotropy – the red arrow is pointing in towards the centre of the cube, with the red dotted line showing the direction at which the red arrow is propagating, in the horizontal plane of the cube

As depicted above in Figure 2.3, in the case of a simple cubic lattice, the easy axis of the material lies along the bonds within the lattice, with the hard axis traversing layers of the lattice. This is what creates the offset in the magnetic fields required to switch the sample magnetisation, depending on the direction of this applied field.

The picture is simpler for a larger, bulk material, but quickly becomes complicated as structures become smaller and more complex in their geometries. The phenomenon of shape anisotropy can be engineered through the careful design and manufacture of a magnetic material, and sample geometry plays an important role in determining the characteristics of the magnetic behaviour.

By defining dimensions in particular ways, an easy axis within a sample can be created. This is because the design of the geometry can be such that different directions of the magnetisation within the material can lead to different levels of magnetostatic charge, thus creating a favoured magnetisation direction.

The magnetostatic charge builds up along the axis of magnetisation such that the magnetisation points from a negative region to a positive one, as shown below in Figure 2.4.

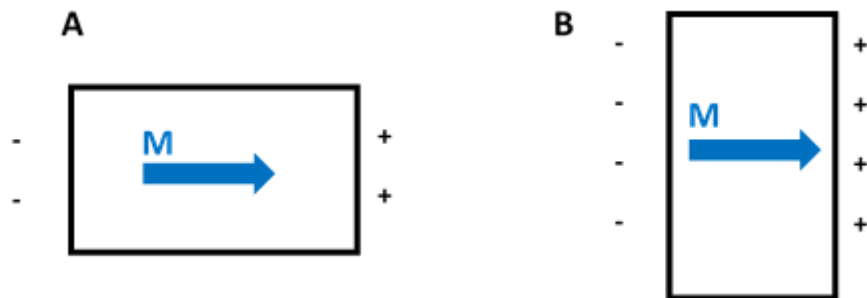


Figure 2.4: Demonstrating the role played by the creation of magnetostatic charge in the phenomenon of shape anisotropy within rectangular medium, with the positive and negative signs referring to build up of positive and negative charge, and the blue arrows representing the magnetisation direction

Figure 2.4 shows a rectangular magnetic thin film with sides of different length. Due to the direction of the magnetisation within the sample at this moment, a magnetostatic charge builds up as a result. In diagram A, the magnetisation is pointing parallel to the side of the sample with the greater length. This results in a smaller build-up of charge in comparison to B. In the case of B the charge build-up is greater, due to the charge building up along the longer side of the rectangular film, as dictated by the offset in the

magnetisation at both edges of the sample. This disparity is the cause of the easy axis in the sample, where diagram A shows the more energetically favourable situation, and correspondingly the magnetisation will tend to align like this when not under any externally applied conditions.

This can be further explained by referring back to the description of flux-closure domains. These are formed in a material to reduce and limit the stray field outside of the boundaries of the sample itself, such is the unfavourability of that arising. So considering the preference for the field remaining inside the structure, it can be seen that scenario A is more preferable, as the amount of stray field outside of the confines of the material is significantly larger for scenario B.

As the lengths of the two sides become more and more unequal, the favour towards the easy axis continues to increase. This trend extends onwards to the extent that in the case of a typical nanowire, the shape anisotropy is essentially the dominant factor in controlling the magnetic moments in the sample, and the wire can have one of two magnetisation states, pointing in either direction parallel with its long axis.

This shape anisotropy, of course, can also become a dominant factor in more complicated systems – as has been shown in previous studies, such as repeating lattices [23] – and it is this property which is of more pertinence to my study.

2.4.3 Basis of the Magnetostatic and Magnetoelastic Anisotropy Energy

The magnetostatic energy is reduced by the process outlined previously, through the formation of flux closure domains.

Magnetostatic energy is created by the internal magnetic field of a material being forced to pass through a region outside the material. Therefore in most cases, due to the existence of the flux-closure domains, this energy term can be successfully reduced.

Magnetoelastic anisotropy is a phenomenon brought about by the rotation of magnetic moments in the material as the magnetisation changes. This rotation forces a minor change in the lattice structure of the material, resulting in its dimensions changing on a small scale, but also therefore changing its magnetic properties. This is also known as magnetostriction. [24] The phenomenon was able to inform scientists about features of the interatomic interaction that takes place within ferromagnets.

This concept is not something which is explored during my thesis.

2.4.4 Basis of the Zeeman Energy

The Zeeman energy is an energy relating to the interaction between a magnetic material and an externally applied magnetic field. This energy tends to oppose the magnetostatic energy, as its mechanism ensures that its formation is the opposite of the interaction between nearest neighbour moments.

The Zeeman energy is minimised when magnetic moments are orientated parallel to the external field, and therefore this leads to the favouring of a single-domain material. This is at odds with the magnetostatic energy because it will lead to a large stray field outside of the material's boundaries in order to close the loop, which is usually avoided through the more complex multi-domains.

2.5. Domain Walls (DWs)

Separating neighbouring domains from one another are Domain Walls (DWs). Within these regions, the direction of the magnetisation is uniformly rotated from the direction of one neighbouring domain to that of the other. Depending on the directions of the neighbouring domains and other properties relating to the shape of the material, there are a variety of different domain walls which are to be found. Related to this, the size of the domain walls is also partly determined by the geometry of their surroundings.

2.5.1 The conditions for Bloch & Néel Walls

The most prevalent DW is one which separates two domains which are 180° apart from one another. For this category of DW, there are two distinct types of rotation seen within these regions, giving rise to Bloch walls, and Néel walls. [25], [26]

The difference between the two opposing DW types is the plane of rotation in which the magnetisation direction is altered. In large, bulk materials and structures, Bloch walls are more prominent. However, in structures where a number of the dimensions of a body are restricted, such as long, thin structures, rotation in this same plane would come at a large demagnetising energy cost. This ensures that such a rotation is not

favoured, leading to the prevalence of Néel walls. [27] Bloch walls see no change in the magnetisation perpendicular to the DW, and this leads to the fact that no demagnetising fields are generated at this boundary.



Figure 2.5: The uniform magnetisation rotation that takes place in a Néel wall – the black arrows show the magnetisation direction within the red and blue domains, while the white arrows show the consistent rotation of the magnetisation within the DW, represented by the black triangle

DWs are characterised in a variety of forms, with their names offering an insight into the respective directions of the magnetisations in the neighbouring domains, and the direction of rotation within the DW. Tail-to-Tail and Head-to-Head walls arise as a result of the manner in which the magnetisation is created and the geometry of the structure they are within, a mechanism which will be shown to have been intentionally exploited in an experiment later in this thesis.



Figure 2.6: Schematic of the different arrangements of neighbouring domains, and the characterisation of the domain walls, represented by the black triangles, that separate them: AW - Anticlockwise rotation, CW - Clockwise rotation – these are the same wires as depicted in Figure 2.5

Figure 2.6 shows four different types of DW, depending on the alignment of the magnetic moments on either side of the boundary, and the direction the magnetic moments rotate within it. Which DW is present at any particular point within the material is again determined by magnetic anisotropy. The width of the DW is also a result of the level of anisotropy of the material: a material of higher anisotropy would see a narrower DW.

2.5.2 The conditions for Transverse & Vortex Walls

Within the typical long, thin structures that contain Néel Walls, a further pair of structures for the rotation of the magnetisation are known to exist. These are known as Transverse Domain Walls (TDW) and Vortex Domain Walls (VDW). Their names are almost wholly derived from their structures, as illustrated in the following diagrams.

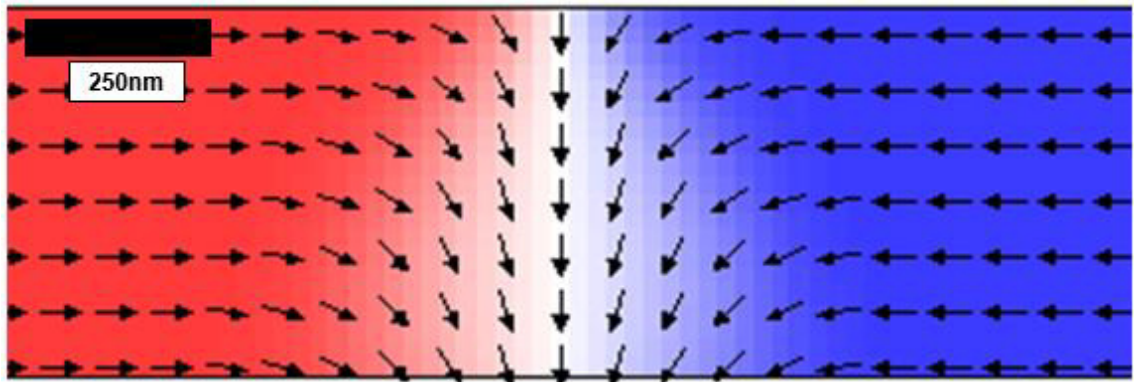


Figure 2.7: OOMMF simulation of the structure of a Transverse Domain Wall within a magnetic nanowire – these simulations saw external magnetic fields applied parallel to the long axis of the nanowire. The red and blue backgrounds represent the direction of the magnetisation at each point along the wire

A TDW consists of a rotation in the magnetisation around a point on the edge of a structure. The TDW shown in Figure 2.7 is an example of a head-to-head DW, as seen by the magnetisations of the two domains on either side of the wall pointing towards each other, and is defined as having clockwise rotation of the magnetisation.

Depending on the geometry of the wider sample, there can also be present DWs with anticlockwise rotation and being in the tail-to-tail setup.

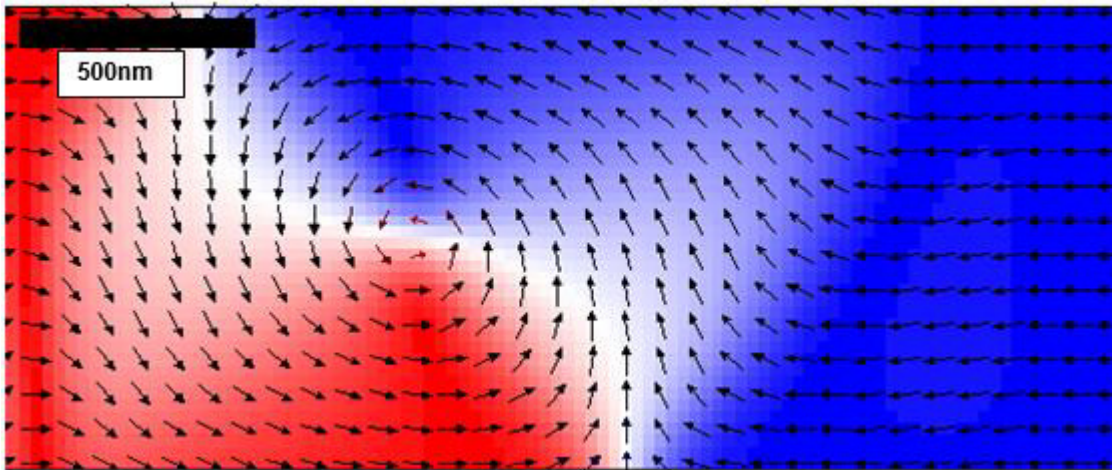


Figure 2.8: OOMMF simulation of the structure of a Vortex Domain Wall within a magnetic nanowire. External magnetic fields were applied parallel to the long axis of the nanowire. The red and blue backgrounds represent the direction of the magnetisation at each point along the wire

Whereas a TDW consists of a rotation in the magnetisation around a point on the edge of a structure, a VDW sees the centre of rotation situated in the centre of the structure. As with the TDW, the VDW can be shown to have its magnetisation rotate in either a clockwise or anticlockwise direction, in the above case this is an anticlockwise head-to-head VDW.

To identify which kind of DW to anticipate again depends on the specific size of the structure. Typically if a wire is not suitably thin or suitably narrow, then it is likely that a VDW will be present between two neighbouring domains. If however these two dimensions in question are suitably narrow then a TDW will be favoured.

Several different experiments have, both theoretically and experimentally, presented a boundary for the transition from TDW to VDW. [28] *Nakatani et al* has also discovered evidence of a third type of DW [29], which can be found in certain conditions of wire dimensions to be between the TDW and VDW. This is known as the Asymmetric Transverse Wall (ADW).

These transitions, and the dimensions of the wires at which they arise, are broadly similar for different materials but will be subtly different and, particularly around the boundary line between TDW and VDW, there will be variations for different materials, in terms of exactly at what width or thickness the transition between the two wall types occurs. *Nakatani et al* also find that the DWs themselves are also vastly different in appearance and size [29], with their wire widths differing largely: a TDW has a wire width equal to:

$$w = \pi\Delta \quad (7)$$

and in the case of the VDW

$$w = \frac{4\Delta}{3} \quad (8)$$

where Δ is a wire-width parameter which has been derived from simulations. [29]

2.6. Origins of Artificial Spin Ice (ASI)

Water- and spin-ice highlighted the potentially fascinating phenomenon of frustration, and this gave rise to the concept of creating new structures, designed in such a way as to include the frustration seen in the natural systems.

2.6.1 Geometric frustration

Geometric frustration arises in structures whose geometry determines that there is no distinct and unique lowest energy state. It is a concept which stretches as far as 1950, when Wannier discovered that a series of Ising spins set up into a triangular or hexagonal lattice had a non-zero entropy at zero temperature. [30] There are conflicting inter-atomic forces, which can lead to complex arrangements and structures. As suggested above, this can result in there being many distinct ground states to a system at zero temperature.

Figure 2.9 serves as a good illustration of the concept of frustration and how it can arise.

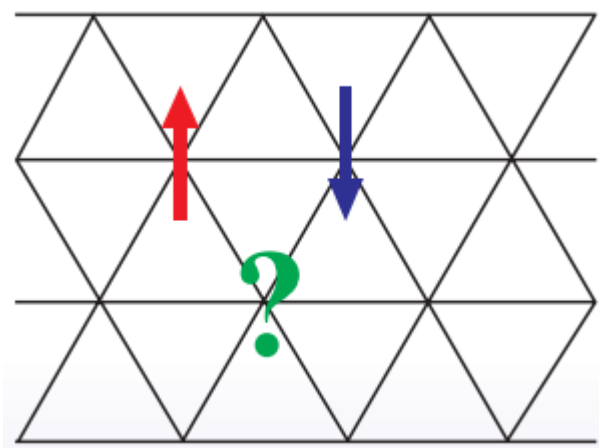


Figure 2.9: Basic form and example of geometric frustration, with an antiferromagnetic triangular lattice. The arrows depict spin directions at two vertices, and the question mark emphasises how, given the two known spin directions, it is not possible to definitively predict the spin direction at the question mark [31]

Here, it is known that two of the spins are aligned antiparallel to one another, but the question of the orientation of the third spin is impossible to definitively determine, as there is an equal likelihood that it could be found in either the up or down position.

The important point of this is that, with there being a guarantee that two of the spins will align with a nearest neighbour, in spite of this being an antiferromagnetic system, then there will not be a conventional zero energy state; there will be an amount of what is termed residual entropy at zero temperature. This residual entropy is an inherent property of a system in which there is no unique ground state, and so therefore there will always be some level of disorder within the structure, as not all interactions can be satisfied to the lowest energy level. [31], [32]

As alluded to in the above figure and descriptions, the simplest evidence of the concept of frustration can be found in spin systems, and within this field a common example is that of spin ice – the arrangement of spins in a structure similar to that found in water ice. The tetrahedral structure of both water-ice and spin-ice means that there are a large number of possible lowest-energy states within both of those materials.

2.6.2 Discovery of the frustrated structure of water ice and spin ice

Linus Pauling discovered the phenomenon that water ice possesses finite entropy at zero temperature, through the competing interactions in its bond structure.

Each oxygen ion is surrounded by, and ‘feels’ interaction from, four hydrogen ions. The lowest energy state for this structure is when it will best conform to its standard H_2O molecular structure. The way for this to be apparent across a large-scale structure like water ice, is for two of the four hydrogen ions to interact strongly with the oxygen ion, and for the other two to act weakly with it, and to act strongly with a different neighbouring oxygen ion. In fact, as shown in Figure 2.10 below, each hydrogen ion interacts with two oxygen ions – one strongly, one weakly – and the water ice bonds in a tetrahedral structure.

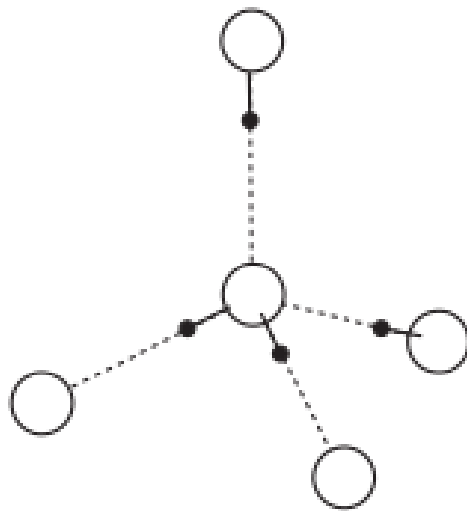


Figure 2.10: A depiction of the tetrahedral structure within water ice, and the two-in, two-out structure of the bonds between the hydrogen (black) and oxygen (white) ions [33]

But of course, among any group of one oxygen and four hydrogen ions, there will be several valid combinations in terms of which hydrogen ions are strongly interacting with which oxygen ion. Considering simply one oxygen ion, there are six different possible combinations of two hydrogen ions which could be the strongly interacting pair. This leads to the terming of this as a “2-in, 2-out” structure. [33]

This fact regarding the tetrahedron structure, extrapolated over a large-scale array within a water ice structure, serves to highlight the myriad of possible lowest-energy states of the water ice, and why it is such a clear example of a frustrated system.

A spin ice is a system composing of spins which does not have a single minimum energy state. It has a structure that is mathematically analogous to that of water ice,

and, like water ice, does not have a single minimum-energy state, but rather several. It is also a structure which retains 'residual entropy' at zero temperature.

Spin Ice sees a group of spins arranged in a tetrahedral structure. In a style mirroring that seen in the water ice, the lowest energy state would see two spins pointing towards the centre of the tetrahedron, and two spins pointing directly away from the centre, and rather pointing towards the centres of different tetrahedra within a lattice, not depicted in the above diagram. [33]

2.6.3 Development of Artificial Spin Ice and the ice rules

With research developing rapidly into these frustrated systems, the results borne out of this encouraged the conception of the idea of artificially creating such frustrated systems. The immediately apparent advantage to these structures over the naturally discovered alternatives is the freedom to design and create structures with enhanced interactions, or to be able to determine how many competing interactions there are at any given point in a structure. [32] These structures are also subject to the ice rules, governing the nature of competing magnetisation directions around a vertex. [34]

These artificial structures can be created through electron beam lithography, which can fulfil the creation of ferromagnetic nanoislands – these can be arranged into a large variety of configurations, allowing, as mentioned above, for a much greater level of freedom in terms of structure design. [35] One challenging aspect is that of producing a truly frustrated system, and attempting to ensure that all pairs of interactions in a lattice are equivalent, as is the case in water ice, and therefore ensuring that the ground state of the structure is not readily determinable.

This has extended to the design of lattices of both connected and unconnected magnetic islands, with both forms of lattice providing different interesting features. Attempting to discern patterns and order within these structures has been at the forefront of recent investigations.[36]

When considering these structures in terms of their magnetic charge, each individual island or bar can be described as having magnetic charges of $+q$ and $-q$ at its opposing ends, where q is the ratio of the magnetisation in the bar with its length. [37]

In a hexagonal lattice, the main focus of my study, each vertex sees the meeting of three of these bars, and as such there can be a maximum charge at vertex, Q , of $+3q$ and a minimum of $-3q$. However due to the energetic favourability of other states, this

$\pm 3q$ is seen incredibly rarely in hexagonal lattices. It is more common to see what is referred to as a 2-in, 1-out state or 2-out, 1-in state, where “out” and “in” refer to the direction of the magnetisation along each of the three magnetic bars which make up the vertex.

The way in which the magnetisation in these structures is reversed is dependent on the type of structure; the connected lattices have different switching mechanisms to those seen in lattices of unconnected nanoislands. In connected lattices the magnetic reversal is controlled and governed by domain wall propagation through the lattice, while in unconnected arrays the mediating factor is a coherent rotation within each of the individual nanoislands, due to the impossibility of domain wall motion between the separate bars in these types of structures.

All of the above examples of frustrated systems see their interactions governed by a set of limits imposed by the nature of the interactions between neighbouring ions/spins/moments. The term for this is the ice-rules.

The ice rules restricts the number of moments that are able to be pointing inwards to the centre of a vertex, and similarly the number which can be pointing away from a vertex.

In reality the reason for the limitations placed on the structure is as a result of the charge which would build up at the vertex as a consequence of particular structures being realised.

2.7. Anisotropic MagnetoResistance (AMR)

AMR is an interesting property of ferromagnetic materials, with quite a wide variety of strength observed across the range of materials. Permalloy (compound of Nickel and Iron) is an example of a material with a high level of AMR.

The resistance of a structure is measured as being determined by the resistivity of its material, and also the shape and form of the structure. The resistance, R , can be calculated using the following equation:

$$R = \frac{\rho L}{A} \quad [2]$$

Where ρ is the resistivity of the material, L is the length of the current path, and A is the cross-sectional area of that material.

AMR arises from a combination of the magnetisation in the material and spin-orbit interaction. When the magnetisation of the material aligns with the current path, it creates a larger probability of the current-carrying electrons being scattered, and so the obstruction to the flow of current is more significant. Ultimately this causes the electrical resistance in a material to vary, and to be a maximum when the magnetic field applied across the material is parallel to the current path within it.

So AMR is essentially the dependence of the resistance on the angle between the electrical current passing through the material, and the magnetisation direction the material. The magnitude of the resistance varies with $\cos^2(\theta)$, where θ is the angle between the current direction and the prevalent magnetisation direction. [38]

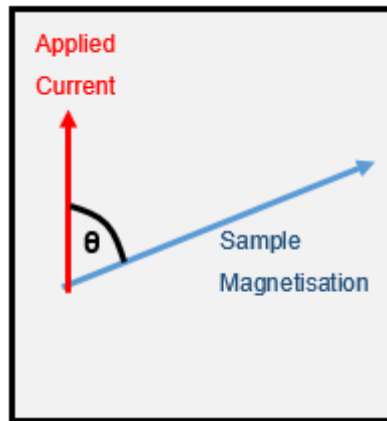


Figure 2.11: A diagram of a bulk magnetic material (grey rectangle) with labelling denoting the angle, θ , between the applied current (red arrow) and sample magnetisation (blue arrow) – these are the properties which give rise to AMR

In practice, due to the shape of the cosine function, this results in the resistance being at a maximum when the current and magnetisation are either parallel or antiparallel to one another, and then at a minimum when the two quantities are perpendicular to each other. [39]

Measurement and detection of the AMR proves to be a useful tool in nanomagnetism, not purely for ASI but also in areas such as domain wall motion and pinning. [40]

The AMR of a system can also be modelled and calculated from other simpler measurements, for instance through the normalised output from a MOKE magnetometer [41], and this presents opportunities to analyse the switching mechanisms within structures in greater detail in a quite straightforward manner.

2.8. Magneto-Optic Kerr Effect (MOKE)

The effect of MOKE is commonly used in the study of magnetic materials. The effect is essentially the effect experienced by polarised light when it reflects off of the surface of a magnetic sample. [42]

In the event of linearly polarised light reflecting off of a magnetic sample, the polarisation of the light can be changed, from linearly polarised to elliptically polarised, in a manner which depends on the magnetic state of the surface off which it reflects.

There are three different optical and magnetic setups which can be used to measure MOKE, namely polar, longitudinal and transverse MOKE. [43][44] These setups differ from one another in terms of the relative directions of light propagation and magnetisation direction.

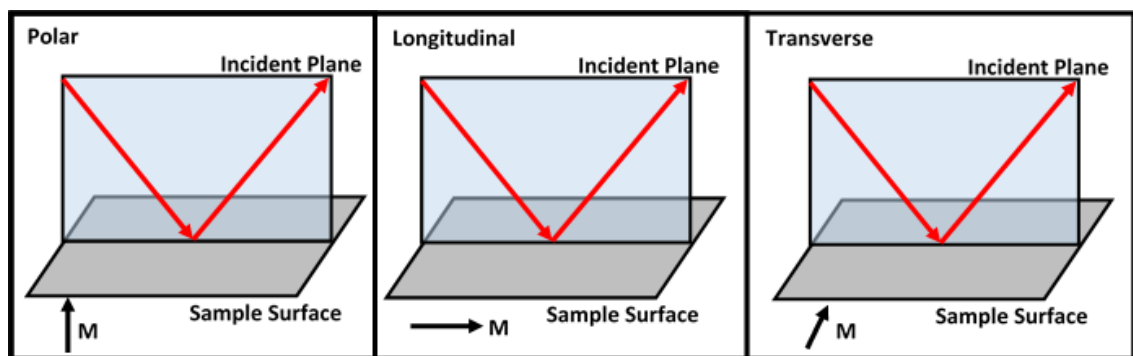


Figure 2.12: Comparing the three different geometries used to perform a MOKE measurement – the black arrow labelled “M” represents the applied magnetic field direction, with the red arrow representing the red laser light reflecting off of the sample surface within the incident plane

Polar MOKE is the term for a measurement of magnetisation perpendicular to the sample surface, and while it can be performed at a variety of incident angles, it is common to perform this at normal incidence. By contrast, longitudinal and transverse

MOKE both measure and detect a magnetisation vector parallel to the sample surface, and only operate at large angles of incidence. Where these two differ is in the magnetisation vector relative to the optical plane of incidence: parallel in the case of longitudinal MOKE, and perpendicular in the case of transverse. During my investigations using MOKE in this thesis, I will be measuring in the longitudinal MOKE geometry.

When linearly polarised incident light impacts on the sample surface, both the polar and longitudinal effects generate an orthogonally polarised component of the light when it reflects back off the surface, whereas in the case of transverse MOKE, only the amplitude of the light is changed, not the polarisation.

Through the use of a polariser after the light has been reflected off the sample, the intensity of the light in a certain polarisation direction, before and after the application of an external magnetic field, can be analysed and compared.

The intensity of the light in the measured polarisation direction is affected when the external magnetic field is applied in one direction. When the magnetic field direction is reversed, the intensity of the light will undergo an equal and opposite change.

The difference in intensity between these two extremes is known as the MOKE signal. This difference can allow for the plotting of varying external magnetic field, against the intensity of the detected light reflected off the sample. Through this, a hysteresis loop of the magnetic sample can be obtained.

If the applied magnetic field is being varied from negative to positive, the point at which the magnetisation switches direction is different, when compared to if the magnetic field is varied from positive to negative.

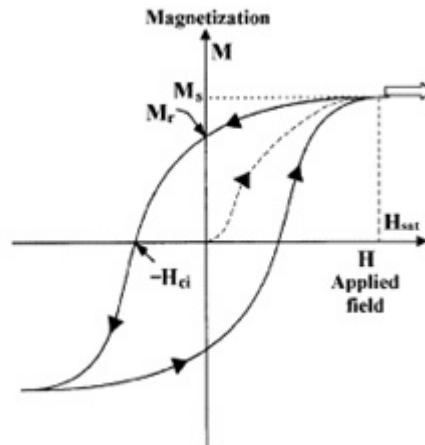


Figure 2.13: A standard hysteresis loop for a hard ferromagnetic material – the arrows on the loop show the manner in which the field is changing at these points. M_s is the saturation magnetisation, M_r is the remnant magnetisation, H_{ci} is the coercive field required to reverse the magnetisation and H_{sat} is the field required to saturate the material. The gradual nature of the magnetisation change is the indicator for the material being a hard ferromagnet [45]

Figure 2.13 shows the relationship between applied magnetic field H , proportional to the applied voltage used to probe the material, and the magnetisation M , which is proportional to the intensity of the light detected post-reflection. The steepness and suddenness of the transition from saturation in one direction, to saturation in the opposite direction, is a property of the specific material in question – namely the hardness parameter of the material. [18] In the case above of Figure 2.13, the trend shows a gradual transition from one saturation point to the other. In the case of a particularly soft magnetic, the transition between these two points is very abrupt, as nearly all magnetic moments are reversed simultaneously. This is not the case here, and suggests that the material shown in Figure 2.13 is not as soft as other ferromagnets.

The size of the MOKE signal, the difference between the magnetisation values of the two saturation points, also varies with each different material, and can also vary dependent on the amount of magnetic material being sampled at any one time – that is to say the fraction of the laser spot which is reflecting onto magnetic material at that time.

2.9. Outline of Magnetic Imaging Techniques

A common challenge of magnetic structures is the difficulty of understanding the mechanisms of the magnetisation in some of the magnetic phenomena, and this is as a result of the difficulty in imaging magnetic contrast on a small length-scale. This has been overcome in a variety of ways including Magnetic Force Microscopy (MFM), which allows for the measurement of a magnetic image of a sample. This proves to be highly effective at detailing a sample at a given moment in time as a result of a previous magnetisation.

Of far greater interest, however, is the ability to study a magnetic sample's progression as a known parameter is changed during imaging, for instance through the application of a variable magnetic field, without the need to remove the sample from a vacuum chamber between measurements. This is the main benefit of an experimental setup housed on a beamline of the Diamond Light Source synchrotron, in Oxfordshire.

Through the creation of a small cartridge for samples, within which is a small magnet positioned to supply a magnetic field to the samples, it is possible to perform a series of images for a series of applied magnetic field steps. This is made use of through two complementary features, namely the technique of PEEM and the effect of XMCD.

PEEM is a surface technique which is able to display contrast in an image of a material through detecting different intensities of secondary electrons, after the excitation of a sample surface through the exposure to usually either Ultraviolet light or X-ray sources, a process known as the Photoelectric Effect.

The limitation of PEEM is that it requires a suitably effective vacuum in order to provide a well-resolved image of the sample. The vacuum needs to be good enough for the mean free path of the electrons to be sufficiently high as to reach the detection equipment, to enable the image to be produced.

XMCD is a difference spectrum which can be gained from the use of X-ray absorption spectra in a magnetic field. Taking two spectra, using left and right circularly polarised light, analysis of this allows for the obtaining of information pertaining to the structure of the material, such as spin.

Differences in the absorption intensity between the two types of polarised light at different photon energies within the X-rays, can be obtained to identify the material involved and its properties, such as the relative proportions of different elements

contained within it. This is of particular interest for this investigation as the ability to image the magnetisation allows for the images produced of samples to display magnetic contrast.

It is the combination of these two techniques and their resulting outputs which produce a clear opportunity to measure the magnetic contrast of nanomagnetic structures such as the ones central to this study.

2.10. Conclusions

This chapter has introduced the scientific field of micromagnetism and the outlining theory which has led to the current interest in nanomagnetism as a means to improve technologies in the immediate future [1], [3], [46]. It works through the manner in which the basic underlying theory of nanomagnetism has been shaped throughout the twentieth century, with the introduction of Domain Theory, and the work of Landau and Lifshitz in discovering the rules governing micromagnetism [19].

Magnetic domains and DWs, and the control and manipulation of these, plays a huge role as to the motivation for the overall study in this thesis, and so the understanding of these, along with how this has developed, is discussed. The different forms of domain wall are introduced, as are the conditions under which different DWs are observed.

The main subject of this thesis is the field of ASI, which has been borne out of the discovered phenomenon of frustration inherent in the atomic structure of water ice, and the latterly discovered spin ice, both of which are natural materials where the lattice structure is such that they do not have a unique lowest energy ground state. The principles of frustration and the so-called “ice rules” governing the magnetisation ordering within ASI lattices are introduced and discussed.

There are measurement techniques included in the evaluating of magnetic samples which exploit particular aspects of magnetic theory, such as MOKE and AMR. The magnetic theory of the origins of these effects is described to enable a better appreciation of the techniques being used to analyse the samples.

3. Published literature around Artificial Spin Ice (ASI)

This chapter is a review of the published literature within nanomagnetism, artificial spin ice (ASI) and magnetic domain walls (DWs) which directly influences aspects of my research, and which has relevance to the decisions taken and samples produced during my project, as well as the analysis of data obtained.

3.1. Developments of ASI

3.1.1 The first fabrication of ASI samples

The main focus of my thesis, and the subject of the majority of my data and discussions, is ASI. ASI has come to be seen as a rich playground for understanding the nanoscale interactions of complex magnetic systems, and has been the subject of an extensive study, particularly over the last decade [32], [47]. It still, however, possesses high potential for further investigation.

Arguably the greatest asset of ASI systems in comparison to the naturally occurring spin ices is their complete tunability. They present the ability to focus in on a specific aspect of a system and assess the characteristics of this aspect and its role in the interactions of the system, and therefore to directly control the type of interactions seen.

ASI had been considered and discussed extensively as a way in which to mimic and measure the characteristics of spin ice systems, by way of creation of a ferromagnetic network in a two-dimensional lattice. Such a lattice was created and measured by Wang *et al.* [35], who presented work relating to a lattice of individual nanoislands, arranged in a square lattice geometry and consisting of Permalloy.

They were able to outline the favourable magnetisation combinations of neighbouring nanowires. They achieved this through characterisation of the vertices, by considering each vertex as consisting of the four nanoislands directly adjacent to it. Analysis of a magnetic force microscope (MFM) image and assessing the variety of configurations seen at different vertices across the entirety of the lattice, showed that there is a strong prevalence of vertices which are more balanced in terms of their net charge.

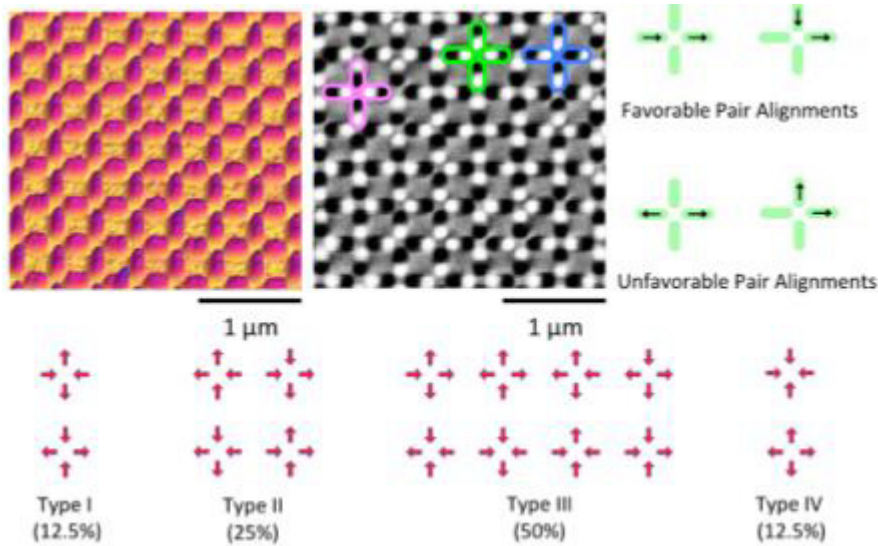


Figure 3.1: Image taken from *Wang et al.*'s paper (2006). The two obtained images are AFM and magnetic contrast scans of an array of nanoislands in a square lattice geometry, and the accompanying graphics outline the potential alignments of magnetic moments around a vertex within this array, and their probabilities of occurring

Considering each individual island as having a charge relative to the vertex of $\pm q$, (where $+q$ has the magnetisation pointing inward to the vertex, and $-q$ has it pointing away), limiting the build-up of charge will result in the 2-in, 2-out arrangement, which is analogous to the ice-rules seen in the water ice and spin ice systems. Conversely, should there arise a 4-in or 4-out vertex, the net charge accumulation at that vertex would be $\pm 4q$.

As seen in the figure taken from *Wang et al.*'s paper, only 12.5% of all the vertices sampled across the lattice are of the 4-in or 4-out configurations, showing a strong prevalence where 87.5% of the vertices have charge accumulation of $\pm 2q$ or smaller in magnitude.

It was also shown that pairs of bars which are perpendicular to one another, have a stronger interaction than a pair of parallel wires, as a result of the different distances between different pairs of bars in this lattice – those pairs of bars which are closer together have stronger interactions than those with larger separations.

Wang et al repeated the lattice investigation for a variety of different lattice parameters, and identified that the interaction between the bars in the array as a whole diminishes as the lattice parameter increases, to the point that there is little-to-no interaction at a lattice parameter of 700nm.

Also in 2006, *Tanaka et al.* produced another ASI sample but with a few differences. [48] This study looked into the interactions found in a Permalloy honeycomb lattice. This lattice has taken on various names across the literature, from honeycomb [15], [49] as well as “hexagonal”, or “kagome” [14], [50]–[53].

In this instance the sample is a connected network of bars, as opposed to the unconnected nanoislands studied by Wang. The hexagonal lattice also introduces the three-vertices, where each vertex connects three magnetic bars. Unlike the square lattice, the hexagonal lattice has no inherent imbalance of interactions between different pairs of nearest neighbour bars at a vertex, and this can make the hexagonal lattice a more ideal candidate to investigate the frustration.

The three-vertex structure means that there are four different combinations of magnetisation around the vertex: “3-in”, “3-out”, “2-in, 1-out” and “1-in, 2-out”, referring again to the magnetisation directions of the bars around the vertex, relative to the vertex. Whereas as shown in *Wang’s* work into the square lattice, there has been observation of all possible vertex types, *Tanaka’s* work shows a lack of any of the 3-in or 3-out type vertices. This is further endorsed via imaging completed by *Qi et al.* in 2008 [54], and also by other publications, [55] such as *Mengotti et al.* in 2008, who focussed on an unconnected lattice of islands, but retaining the hexagonal lattice geometry.

This lack of presence of any 3-in or 3-out vertex in the lattice is due to the highly unfavourable condition that would arise from having an abrupt change in magnetisation at the vertex that would come as a result of all the bars at the vertex opposing one another in terms of magnetisation direction. The only sign of the 3-in or 3-out vertex appears as a monopole defect. [56] Qi also commented the strong agreement between the experimentally observed data of the sample, and the Monte Carlo simulation data previously acquired on this subject, while also emphasising that the particular geometry of the hexagonal lattice made it an ideal and simple-to-understand ASI variation.

As mentioned above, in terms of the interactions between the bars within the vertices, the honeycomb lattice is unique, out of the lattices which have been physically measured, in that it offers the benefit that interactions between all pairs of bars at a vertex are equivalent. This is because the angles between all pairs of bars around a vertex are equal in size. This compares with other lattices, including the square lattice, where there is a difference in the size of the interaction between perpendicular pairs and parallel pairs, due to perpendicular pairs being separated by an angle of 90° and parallel pairs by 180° , by definition.

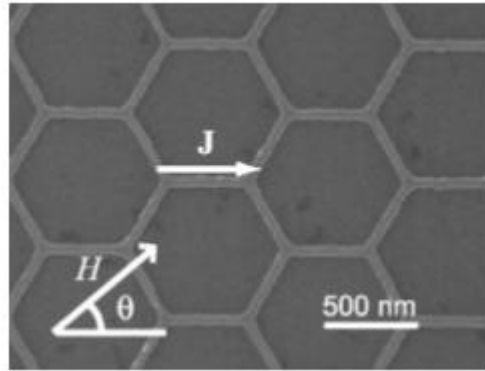


Figure 3.2: SEM image taken from *Tanaka et al.*'s 2006 paper showing a fabricated hexagonal lattice, with a depiction of a number of the parameters involved in the measurements: J represents the current direction, and θ represents the angle between the current and the magnetic field, H

Another difference I alluded to in a comparison of the work of *Tanaka et al.* with that of *Wang et al.*, clearly seen above in Figure 3.2, is that the lattices were all connected nanowires, as opposed to the physically isolated nanoislands of the square lattice. This led to the possibility of performing magneto-transport measurements, to interrogate these lattices electrically, which represented a first in the study of these frustrated systems, one which has since become a commonplace technique for their examination.

The magneto-resistance curves presented by *Tanaka et al.* revealed a sharp spike in the resistance measured, corresponding to the switching of the magnetic bars. These measurements were completed for several different angles between the magnetic field and one of the magnetic bars of the lattice.

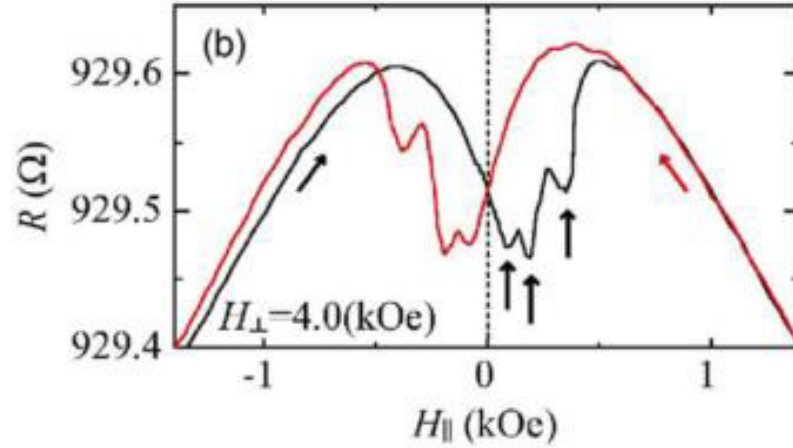


Figure 3.3: Graph taken from *Tanaka et al.*'s paper with the first measurements of magneto-transport properties of Artificial Spin Ice structures, with the measurement being taken at an angle of 75° as defined in the paper, with 0° having the applied magnetic field parallel to one of the bars of the lattice [48]

The above figure from Tanaka's work shows how the resistance is changed as a result of the changing magnetisation caused by the external magnetic field. There were a range of data sets taken for angles between 0° and 90° , with the resistance decreases associated with the magnetisation reversal differing both in terms of their magnitude and the applied field at which they occur.

The ease with which the connected lattice can be measured in a variety of different ways, and the inherent symmetry in the interactions of the hexagonal lattice, has ensured that this form of ASI has been very heavily studied, and it has been used to investigate not simply properties pertaining to the hexagonal lattice, but which can also be easily applied to all other lattices of ASI.

Later work by *Daunheimer et al.* [50] has suggested that the connected lattices are more predictable in their switching behaviour, in terms of the magnetic field at which their magnetisation reverses, than the unconnected ones. The unconnected lattices display a variability in the coercive field of four times that observed in the connected lattice. This difference was found to be true for both simulation and experiment.

However, there has been evidence found through the simulation of unconnected square ice systems that ASI lattices actually show memory effects, [57] that is to say that during repeated cycles of the same applications of external magnetic field, the lattice returns to an exact state very similar to that of the previous identical field application.

This occurs irrespective of the size of the magnetic field. However, the reproducible pattern of magnetisation does occur within fewer magnetic field cycles at some field magnitudes than others – at most fields the cycle reproduces after as few as one field cycle, whereas when the magnetic field is equal to that of the coercivity of the lattice, the reproducible magnetisation pattern does not arise before several iterations of the field application have been completed.

What is apparent is that for one set of researchers, and a connected hexagonal lattice [37], the control and carrying out of magnetic reversal is governed by propagation of DWs through the material, whereas for the other group, with an unconnected square lattice [58], the main effect causing the switching of the bars is coherent rotation.

A series of publications from the group at Imperial College London have focussed on the hexagonal or kagome lattice, and have described a number of interesting phenomena to have been observed within their data, measured both optically and electrically.

A paper from the group from 2012 [37] discusses a situation where the ice rules, which predominantly restrict the manner in which the magnetisations can align around vertices within the ASI lattices, are broken down and cease to govern under certain situations, creating monopole defects, where isolated bars and their vertices are disobeying the ice-rule. [37] This can be modelled using merely the “ice-rule violation field” and the distribution of individual magnetic bar coercivities.

The paper links these monopole defects to those which the group previously identified as being formed at the edges of lattices and propagating inwards, for a similar experiment using cobalt nanowires. [59] These monopole defects and variations from the ice-rule ground state of spin ice samples has been observed by several other groups as well both prior and subsequent to the above publications. [58]

What is apparent is that for one group, and a connected hexagonal lattice [37], the magnetisation reversal mechanism is governed by propagation of domain walls through the material, whereas for the other group, with an unconnected square lattice [58], the main effect causing the switching of the bars is dipolar interaction. This is a significant and important basis for the investigations I have carried out later in the thesis.

Another piece of published work from the Imperial group discussed and presented evidence for a low-temperature asymmetry observed in different measurement orientations. [15] The data revealed symmetric traces in the Anisotropic MagnetoResistance (AMR) data of hexagonal spin ice for all temperatures upwards of

50 kelvin, but decreasing below that temperature saw the onset of an anomalous Hall signal. This led to the prediction of an asymmetric state in ASI which only forms at these low temperatures below 50K.

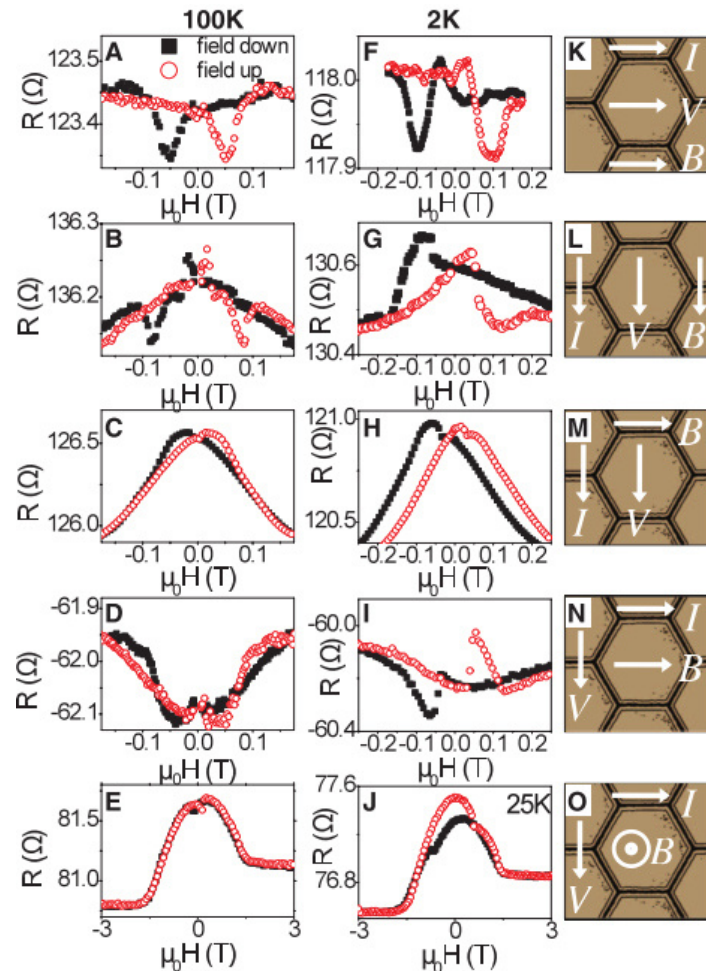


Figure 3.4: From *Branford et al.* paper showing the asymmetry which arises in low temperature measurements but has not been observed at higher temperatures – the images on the right show the orientations of the current, voltage and magnetic field relative to the lattice, with the plots to the left of each image showing the resultant data at 100K and 2K temperatures [15]

This explanation, however, was questioned by a publication in early 2015 [14], in which the hexagonal lattice produced is capped by a thin layer of aluminium, with the basic purpose of preventing the magnetic NiFe layer oxidising, and attempting to clarify if the previous free oxidation of the ferromagnetic layer had in some way affected the results.

It was observed that the low-temperature asymmetry was drastically reduced when the sample was capped. The paper claimed therefore that the low-temperature asymmetry

was simply the result of exchange bias manifesting itself in the electrical transport measurements of this ASI.

This latter publication did, however, admit that these measurements [14] had been carried out with the magnetic material of choice being Cobalt, as opposed to the Permalloy used in the earlier investigation. Therefore it could be possible that the same effect would not be observed in the Permalloy as was in the Cobalt, and so therefore it couldn't be conclusive to rule one way or the other on the similarities of the two measurements.

A lot of study has been dedicated to the analysis of samples when temperatures are significantly reduced, but there have also been studies of temperature effects in the other extreme, including to above the Curie temperature [53], the temperature at which a magnetic material loses its permanent magnetic properties.

These measurements of ASI lattices have generally been accrued with external magnetic fields applied across a lattice consistently. However, there can be interesting properties regarding the dynamics within these lattices, resulting from the application of locally applied magnetic fields. *Burn et al* [60] have recently shown dynamics of DW propagations through applying pulsed magnetic fields at local points within a lattice, in conjunction with a global externally applied field.

The samples discussed here are also of a similar nanowire length within the lattice, however studies in this field do not just pertain to this scale, as can be seen in *Sendetskyi et al* [61], where a soft X-Ray scattering measurement has detected magnetic correlations within their network of sub-70nm nanowires, from which they conclude that they are observing a kagome ice I phase correlations, analogous to bulk spin ice [61].

3.1.2 Recently-developed ASI lattices

As the understanding of the different ASI lattices, particularly the hexagonal and square bases, has increased considerably, so this has encouraged the creation of more complicated lattices, owing to the freedom afforded by the concept of ASI to explore lattices and structures not often naturally observable. This new series of different lattices includes the Shakti lattice, theoretically [62] and experimentally [63] created and modelled.

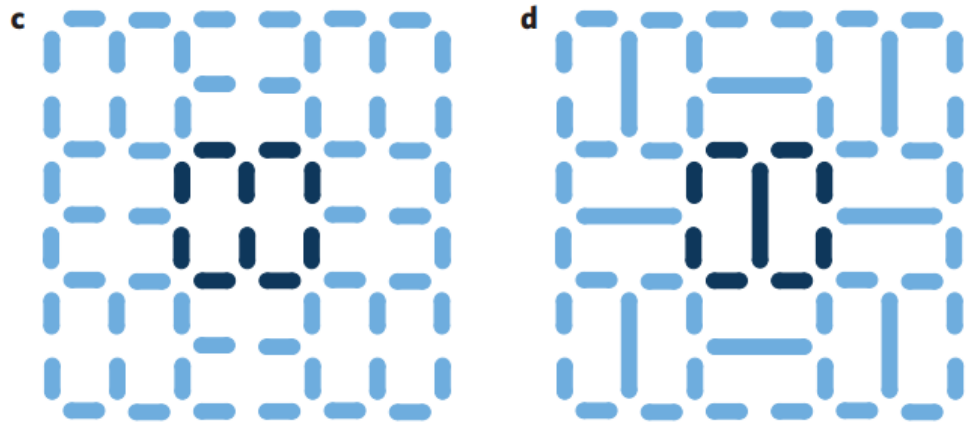


Figure 3.5: Schematic diagram of the short-island (c) and long-island (d) Shakti lattice designs, showing how the nanomagnetic bars are orientated in these two designs – those bars in a darker shade of blue show the effective “unit cell” of the lattice[63]

The lattice is described as having “mixed coordination”, referring to the fact that there are a variety of different vertices within the lattice, including points at which two, three or four bars of the lattice will meet one another, a factor which had yet to be observed in such materials as the square lattice or the hexagonal lattice.

The interest in this lattice was that its design ensures that none of the individual nearest-neighbour interactions are themselves frustrated, but the topology of the lattice frustrates the interactions, which leads to a high level of degeneracy. The same group has also considered other novel lattices, including the “tetris” lattice, previously discussed theoretically, recently created and measured [64] using Scanning Electron Microscopy (SEM).

There are also more complicated variations of ASI such as quasicrystals, including this work by *Bhat et al.* [65] who produced quasicrystals with eightfold rotational symmetry to their lattice. Within the complex structures were observed up to 10 modes, different behaviours observed due to the variety of possibilities with such a complex geometry. A “dipolar dice lattice” has also been conceived and fabricated – this lattice has a mixture of two different types of vertex: ones where 3 nanowires meet, and those where 6 nanowires meet [66].

3.1.3 Measuring the interactions between nanoscale ferromagnetic structures

With the direction of my project demanding a knowledge of the distance of interaction between two magnetic regions, it was a key interest of mine to appreciate the previously-obtained research surrounding DW interactions and the wider interactions between close-proximity sections of magnetic material.

There has been a wide range of publications surrounding this particular issue, notably also in terms of DW propagation, and of pinning domain walls through the proximity of other magnetic “stubs” – narrow, short bars orientated perpendicular to the main domain wall carrying channel of magnetic nanowires.[7], [67]–[70]

A particularly key paper, published by *O'Brien et al* in 2009, [71] showcases the interaction between neighbouring magnetic DWs in adjacent Permalloy nanowires.

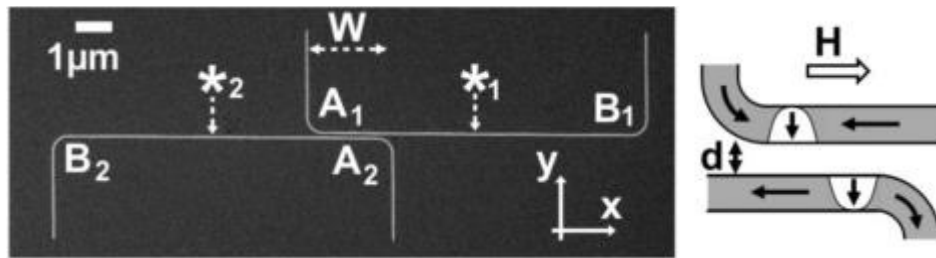


Figure 3.6: Scanning Electron Microscope image and schematic representation of the setup in *O'Brien et al's* publication in 2009, showing the DWs within their nanowires, and their propagation directions under specific applied magnetic field conditions. The SEM image shows a physical sample and labels measurement locations with the stars

Included is a detailed study of how the depinning field (the field require to separate two interacting DWs) varies with increased wire separation. The interaction (and therefore the depinning field) is shown to be particularly strong for very small separations, but dramatically falls away to register only the standard depinning field of the nanowires themselves, when the wire separations are of approximately 90nm and above.

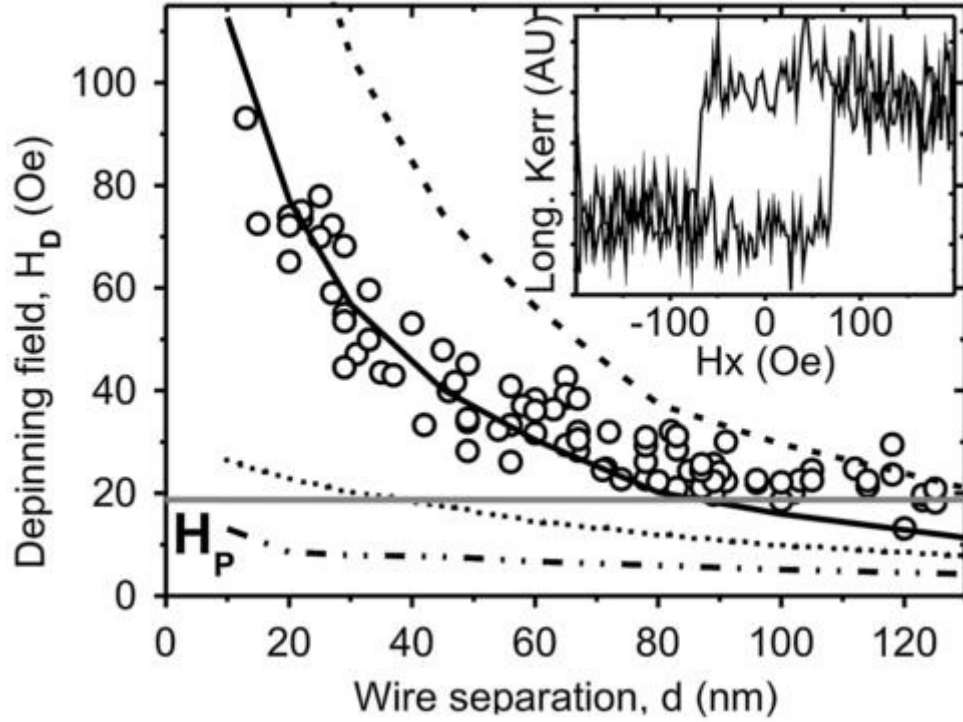


Figure 3.7: Graph from O'Brien *et al*'s 2009 publication showing the depinning field of a pair of DWs in adjacent magnetic nanowires, as a function of the separation distance of the adjacent wires. – the inset figure shows the typical MOKE signal obtained in measuring these structures [71]

This publication is of high interest to a number of my planned investigations during the remainder of my thesis, as they seek to make use of the interaction between different nanomagnetic structures.

3.2. Theoretically assessing Quasi 3-D ASI

Thönig's paper [72] demonstrates a theoretical assessment of the potential to measure a square lattice across two deposition layers. This was as an attempt to create a series of vertices in a square lattice containing equal interactions, and achieving degeneracy in the ground state of the lattice, thereby removing the main drawback of the square lattice over the hexagonal lattice. [73]

If this would be achieved then the four-vertex base of the square lattice means it represents a far closer resemblance to the pyrochlore lattice in the water ice and bulk spin ice than previous lattices have managed to. It also opens up more possibilities as

to the orientations of the magnetic bars at the vertex: whereas in the 3-vertex systems, only 2-in, 1-out and 1-in, 2-out vertices have been shown to be present due to the unfavourability of others.

Thonig's paper also documents useful theoretical parameters, such as the separation distance between two nanoislands such that they no longer interact with one another. This provides an immediate theoretical upper limit on the lattice parameter required for such a lattice to succeed in practice.

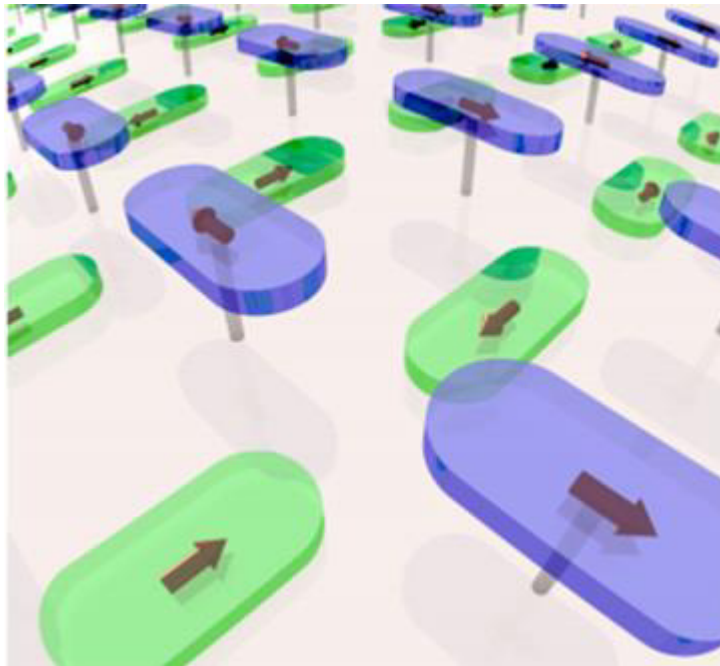


Figure 3.8: Simulation of a two-layer square lattice of nanoislands and their associated magnetic moments, shown by the arrows inside the islands [73] – the two different colours represent the two different deposition layers of the magnetic bars, with the blue layer atop the green, separated by a spacer layer not represented in this image

Figure 3.8 shows the layout of the two-layer structure, clearly highlighting how the blue magnetic bars are situated vertically higher than the green ones. The magnetisations are depicted by the black arrows, with the geometry of the magnetic regions determining the direction of the magnetisation within them.

3.3. Pinning of DWs within ferromagnetic nanowires

Magnetic DWs in nanoscale systems have often been considered to have a number of highly interesting and potentially profound uses for the advancement of current technologies. Some such aspects are in their potential to be incorporated into computer logic systems, and for their ability to act as diodes. Publications have already shown their suitability for such an application, [3], [46] through the creation of triangular regions within nanowires, an example of which is shown below in Figure 3.9.

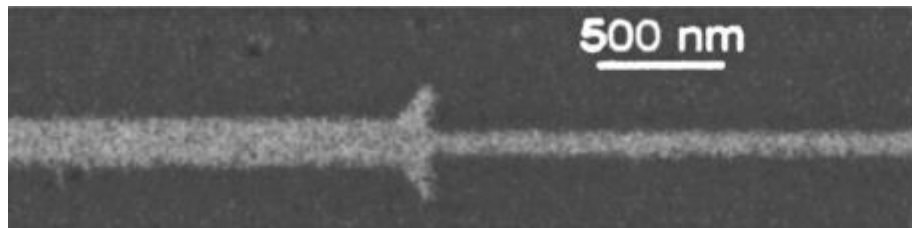


Figure 3.9: SEM image in *Allwood et al.* [46] showing the design of a domain wall diode within a nanowire, with a narrower region and a wider region separated by an area which will restrict DW motion from right-to-left, but not at all from left-to-right.

The DWs which propagate along the nanowire are treated differently, with DWs which arrive at the apex of the triangle able to propagate further along the wire, but those arriving at the base of the triangle being unable to overcome the pinning potential at that point in the wire. The careful design of the nanowire profile has also been considered for use in sensor applications. [74]

Another strong potential application is in the area of data storage, an area which has certainly been publically shown to be one which requires improvements on the current situation, as we are currently in a society whose demand for data storage is outweighing the present supply. The current devices in use can be bettered in terms of the density of data storage in physical space, by the use of DW devices.

DW pinning is an area which has been of keen interest for a variety of research groups – the importance of being able to control the location and propagation of domains could be invaluable in creating working data storage structures. It is also of priority to understand what effects are had on the structure of DWs when they are pinned, either

by geometry or by interaction with external magnetic volumes, or even by other DWs. Should the magnetic domains between these walls be used as a means of representing data, then this will have the potential to corrupt the data within the domains.

The pinning of DWs can be achieved in a variety of ways, as briefly outlined above, and one such method already mentioned previously is through the interactions of DWs in adjacent nanowires causing each other to pin [75], [76], as in *O'Brien et al's* paper of 2009 [71]. As this involved two magnetic regions contributing to pinning with one another, this was of direct relevance to me in terms of my planned investigations into ASI structures. This was, however, far from the first investigation into the pinning of DWs, either through magnetic pins, or through the restriction of the geometry of the materials housing the DWs.

In 2003, Kläui led an experiment in which a narrow Permalloy ring, containing a notch to restrict the width at a point around the ring, was measured using magnetoresistance techniques. It was possible to identify the pinning of a DW at the notch through these measurements [77].

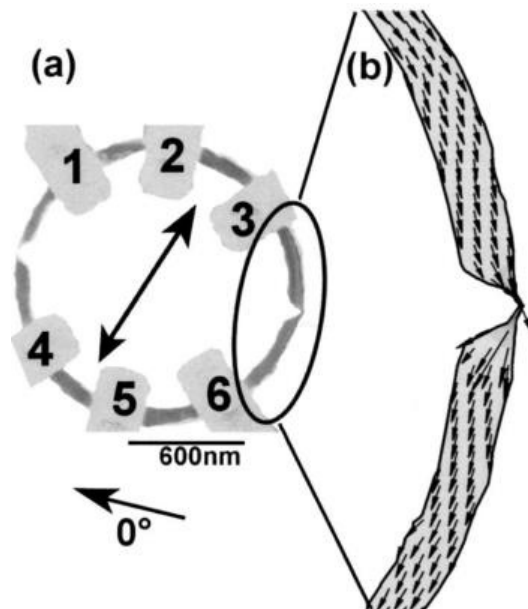


Figure 3.10: Diagram from *Kläui et al's* 2003 paper showing the setup used to identify Domain Wall pinning in ferromagnetic nanoring, with image (b) showing a portion of the ring with a narrowed region intended to restrict the propagation of the DW [77]

Figure 3.10 above shows the geometry of the measurement, with the six numbered regions of Image (a) being the six non-magnetic contacts used to perform the magnetoresistance measurements. The applied field direction, shown below for a case of 0° , is defined as such based on the position of the two notches seen at opposite sides of the ring. Image (b) shows an enlarged version of the region between the magnetic contacts 3 and 6, and the arrows represent the direction and density of the current at each respective place along the ring's path.

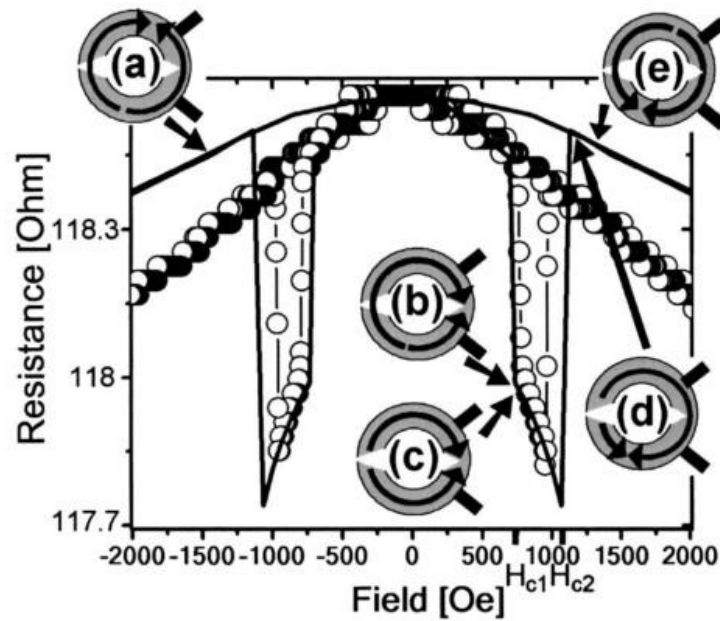


Figure 3.11: Graph from Kläui *et al*'s 2003 paper showing Domain Wall pinning through magnetoresistance measurements of circular nanowire – the five inset schematics showing the position of the DW within the nanoring and at what magnetic fields these instances correspond to [77]

This graph shows the magnetoresistance data obtained from the setup shown in the previous figure. The region between Fields H_{c1} and H_{c2} is where there has been pinning of the DW. The sharp decrease in the resistance shows the initial changing of the magnetic state as the necessary applied field has been reached, however the complete reversal of the wire magnetisation has not fully been completed due to the pinning, and between H_{c1} and H_{c2} the only change to the resistance is through the rotation of the magnetisation caused by the angle of the field, and is not a result of the DW propagating along the wire.

This is only changed when such a large field is achieved at H_{c2} , and the DW becomes depinned and passes through the restriction caused by the notch in the wire. Kläui

furthered his study into the pinning of DWs, including direct observation of the pinning in a similar structure. [78] In 2004 *Faulkner et al.* conducted an experiment where they created “nanotraps” in their nanowires through the design of notches removed from the uniform width, to create a section of narrower wire. [79] This is an approach which is commonly used in the attempt of pinning DWs [80].

Creative and novel ways of controlling the nature of DW pinning have been imagined and realised, including the use of a transverse magnetic field to determine the magnetic structure of a DW, thus affecting how effectively it is pinned by structures such as notches. [8], [81], [82]

DWs in magnetic nanowires have been viewed as potential tools for the development of data storage into physically smaller devices in a bid to improve on the efficiency of current data storage methods. One potential implementation of this idea was outlined in a paper by Parkin et al. in 2008, proposing a technology which they call Magnetic Domain-Wall Racetrack Memory. [1]

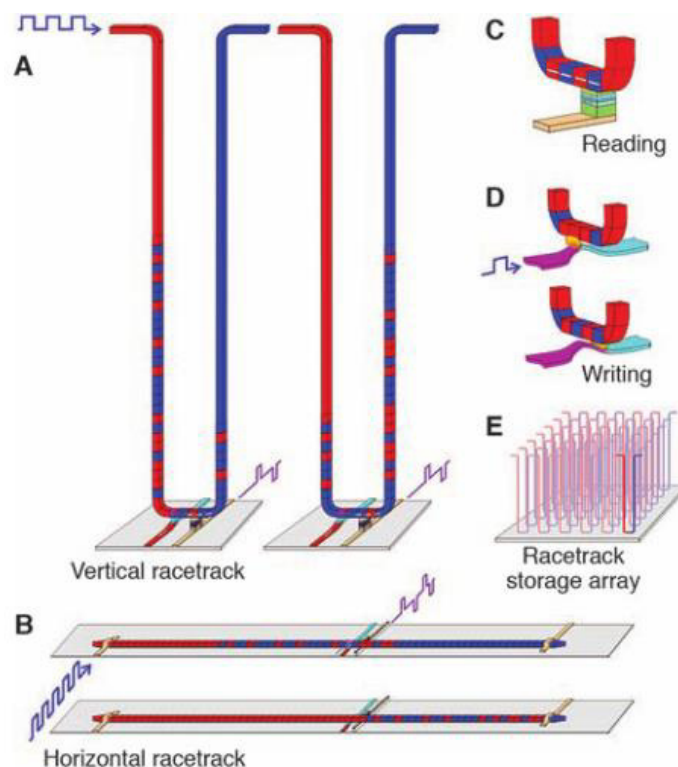


Figure 3.12: Diagram showing the design and operation of "racetrack memory" as defined by *Parkin et al* in 2008 – the red and blue colours in magnetic nanowires represent the two magnetisation directions possible in these wires, analogous to binary bits used for storing data. Images detail the manner in which an array of these wires would be stored and methods by which information can be read and written[1]

The above figure shows the two different potential configurations of such a device, through the vertical racetrack and horizontal racetrack designs. Discussions also included the practical methods of reading and writing data from and onto the racetrack respectively, suggesting the use of fringing fields of DWs in secondary nanowires to alter the magnetisation of domains within the racetrack.

Numerous aspects which need to come together to facilitate the functioning of the racetrack memory are discussed, including the controlled movement of DWs along a nanowire through the application of short spin-polarised current pulses. It was shown that not only could a DW be propagated along a wire in a controlled fashion, but two DWs – even of opposite magnetic charge – can be propagated in the same direction along the nanowire simultaneously. This has also been shown in other work, in which a “domain-wall shift register” has been created and demonstrated. [2] This demonstrates the feasibility of moving a long chain of magnetic domains along the racetrack for reading or writing purposes. [1]

3.4. Simulating the AMR of a ferromagnetic structure

In 1998, Wegrowe et al [41] presented a piece of work where they have generated a representation of the AMR of thin films and wires, using hysteresis data as the basis for these traces. The curves could be then compared to actual AMR data of the same samples acquired experimentally. When performing this simulation on simple structures such as the aforementioned thin films and single wires, the model performs strongly as a valid predictor of the behaviour of the sample during measurements of the AMR.

This model does have significant limitations, however, particularly in light of what my project was intending to achieve. The more complicated networks of the hexagonal ASI lattice require a more elaborate method of converting a MOKE hysteresis loop into its respective AMR form. This is because of the fact that different parts of the lattices will reverse their magnetisation at different fields, therefore it is certain that at various field values, different parts of the sample will be fully magnetised in different directions, depending on the angle of the bars relative to the magnetic field.

The model used in Wegrowe’s paper is based around the idea that the entirety of the sample will switch magnetisation at the same magnetic field, and so the hysteresis loop can easily be considered that the two saturation conditions correspond to when the

magnetisation is parallel or antiparallel to the applied field, and the transition between these two states is a gradual reversal of the magnetisation. This becomes far less simple in the case of an array and so this model will not suffice for the needs of my study.

There have been a myriad of other publications from groups attempting to suitably model the AMR of nanomagnetic structures, introducing and combining a variety of other parameters in order to more and more accurately mimic the experimental data. [83], [84]

3.5. Conclusions

This chapter has presented a review of the literature in the areas within the field of nanomagnetism which this thesis focusses on. ASI has been the subject of intense interest over the past decade, since the first physical examples were created lithographically in 2006 [35], [85]. Through magneto-optic measurements, magnetic imaging techniques, and through magneto-transport measurements, these basic ASI samples have become increasingly well characterised.

The level of understanding of the more simple geometries such as the hexagonal and square lattice, has also led to the quest for more complex geometries to attempt to unearth greater understanding of the complex interactions [62], [63], [65].

Domain walls of course play a huge role in the behaviour of the Artificial Spin Ice lattices, and their importance and potential is being considered in many other technological applications.[1], [46] Therefore studies into the structure and integrity of DWs under certain external conditions have proven useful in evaluating their suitability for these forecast roles. [7], [71], [86]

Through the use of different methods for simulating the AMR of a sample, [41] it has become possible to ever more accurately predict the behaviour of complicated samples, which are currently challenging to lithograph appropriately.

4. A summary of the experimental techniques and procedures used

This chapter will outline the various procedures included in the creation and measurement of samples for the entire study. The ability to reproduce samples of a near-identical form to be able to afford reasonable comparisons is essential to allow for valid conclusions to be drawn. This makes the processes described in this chapter highly integral to the success of the project.

Initially the method for creating a new sample from scratch will be outlined through the various steps taken in this process. Explanations will be given for the decisions made in terms of the materials involved in the samples, and the facilities and machinery used in their production, and why these are of benefit over alternative choices.

The samples made have been measured using several different techniques, making use of equipment and machinery designed and constructed during this project to allow for analysis that suits the requirements of the experiments. Magnetic measurement techniques which make use of magnetic effects such as the Anisotropic Magneto-Resistance (AMR) effect, and the Magneto-Optic Kerr Effect (MOKE) have been implemented to characterise and measure the samples. These have been used alongside Atomic Force Microscopy (AFM), X-Ray Magnetic Circular Dichroism (XMCD) and PhotoEmission Electron Microscopy (PEEM) which have enabled the imaging of samples, helping to correlate the data to the reality of the samples. These techniques will be described in detail.

Also introduced will be measurement conventions which have been consistently employed throughout this experiment, such as the naming of particular and repeated measurement geometries, for ease of conveyance of results in the ensuing chapters following this one.

4.1. An overview of the procedures for processing samples

4.1.1 Clean Room

The devices being created and tested during this study feature complex geometries, with sub-micron features which play an important role in the function of the device. This being the case, it is imperative that the structures are produced in a clean environment, free from any contaminants.

This leads to the fabrication of samples taking place in a cleanroom facility. The cleanroom at Cardiff University is designated a Class 1000 cleanroom [87], which refers to the number of particles with size greater than 0.5 micrometre within a cubic foot of air in the room. This cleanliness of the air serves to greatly reduce the probability of any such damage to samples.

Further to that, there is a smaller booth within the cleanroom which operates as a Class 100 cleanroom, representing a tenfold improvement again in the air quality. This smaller booth houses some of the more sensitive sample preparation apparatus and techniques, such as “spinners”, where samples are prepared for the different lithographic techniques, which will be described more fully in Section 4.1.3.

Cleanroom users are required to wear clothing which attempts to minimise the number of rogue particles like pieces of human skin that can jeopardise the quality of the cleanroom environment.

4.1.2 Fabrication of new samples

The process of preparing and creating samples is crucial for the success of the study, and is outlined in the following section, which covers the entirety of the sample production. It can be initially summarised by four main stages, displayed in Figure 4.1:

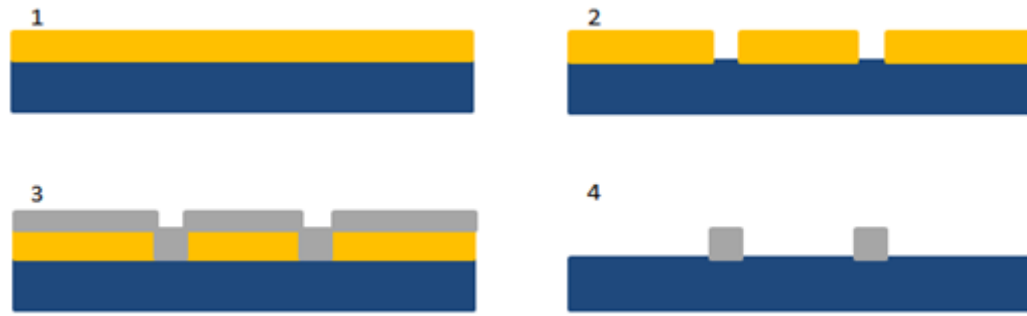


Figure 4.1: Schematic of the stages of production: 1-Spinning 2-Developing 3-Thermal Deposition 4-Lift-Off, Yellow – PMMA resist, Blue – Silicon substrate, Silver – Permalloy deposition

Samples are created on top of thin, flat base wafers with a polished surface, referred to as substrates. The substrate of choice for the experiments undertaken has been wafers of silicon. This was chosen due to silicon being an inert material, and so ideally suited to the tasks required. It is also relatively straightforward to produce thin wafers of this material. In addition to this, some of the electrical measurements being undertaken require the use of an oxide, to provide a layer of insulation which isolates individual elements of a sample atop the substrate. Many of the experiments carried out subsequently in this study are electrical measurements of samples deposited atop this substrate, so isolating them from the substrate electrically is a crucial step.

These wafers then require several stages of preparation, detailed in the following paragraphs, in order to be ready for the deposition of a patterned layer of metal onto their surface.

The first stage of this preparation process is for the wafer of silicon to be cleaved into small pieces. Typically wafers are cut into 10mm x 10mm squares. This stage of the process can actually take place at the outset, or at the conclusion – depending on the manner of pattern writing chosen by the user. For instance, were it the intention to create a large array of numerous copies of a structure, perhaps with one parameter being slowly varied across the array, then it would be beneficial to write a series of patterns onto one large wafer, with the separation into individual samples taking place at the end of the development process.

Be it a larger piece of wafer, or one of the smaller cut pieces, it then needs to be thoroughly ‘cleaned’; for it to have any impurities on its surface removed, including small fragments of the wafer which may have been left from the scribing process. Some of the dimensions of the structures which will later be written onto the surface of the wafer are no more than hundreds of nanometres wide.

The silicon wafers are placed firstly into acetone, for two minutes. This is followed by the wafer being immediately placed in Isopropanol (IPA), another solvent used for further cleaning purposes, for another couple of minutes. It is necessary for this to be carried out immediately so as not to allow for the Acetone to evaporate and leave behind a remaining residue layer on the surface of the wafer. Finally with the use of an air-gun, the IPA is removed from the surface of the wafer, again before it can dry onto the surface.

During these two stages, the beakers containing these chemicals and the silicon wafer are placed in an ultrasonic bath. This bath's vibration aids in the removal of some pieces of dirt which are resolutely stuck onto the surface, and this process will help to make the surface as clean as possible.

Following the drying with an air-gun, the silicon wafer is baked on a hotplate at temperature 100°C for 3 minutes, as a precautionary measure to ensure that any moisture from the solvents does not remain on the wafer.

This preparatory stage is to ready the silicon wafer for the application of a layer of polymethyl-methacrylate (PMMA) 'resist'. PMMA is formulated with either 495, 000 or 950, 000 molecular weight, and in the case of this study, the 950, 000 molecular weight was used. It has been formulated in a resin within Anisole. [88]

This resist is a thin layer applied to the surface of a substrate, and its use is to allow the pattern or design of the structure to be transferred onto the wafer. PMMA is an organic resist and is the conventionally used resist for electron beam lithography, a technique used later in the development process for structures of this kind.

The reason for the suitability of the polymer PMMA as an item used in the spin-coating of these wafers is due to the properties of the polymer and the process that occurs on exposure to a beam of electrons during the structure production process.

Through the lithography stage, the resist can be made to form a temporary mask for the surface of the material below, to limit its exposure to subsequent steps in the production process. Traditionally, these resists are made up of a mixture of polymers, formulated for the specific form of lithography involved in each specific instance.

The substrate is placed into a "spinner", at which time the resist layer is applied across its surface. The spinner then spins the substrate round at typical speeds of 1000s of rpm (revolutions per minute). [88] The purpose of this is to leave the surface of the substrate coated in as uniform a layer of resist as possible, which would ultimately yield the highest quality structures later on in the production process.

The spin speed also dictates the thickness of this layer of resist, also varying with each different solvent and molecular weight, and the percentage of the solution which consists of PMMA. Different applications and lithographic methods require different thicknesses of resist and therefore it is a valuable resource to be able to tune the thickness of this resist so readily.

4.1.3 Electron Beam Lithography (EBL)

Following the completion of the sample preparation and pattern design stages, the sample is placed within a vacuum chamber wherein a pattern can be placed on it through Electron Beam Lithography (EBL). EBL is the technique of scanning a focussed beam of electrons onto a surface covered in a layer of resist, 'exposing' the resist in the previously designed pattern. [11]

The smallest possible precision of the Electron Beam is of the order of 10nm. [89] This is as a result of the resolution of the resist and not the optical systems used, which can resolve down towards 0.1nm. [90] The use of the PMMA resist actually limits the precision to somewhat larger than this. In this study, the smallest feature required has been approximately 80-100nm in a single dimension, and so the limitations of the machinery and resist have not been a factor in the consideration of the measurements.

The exposure to the electrons experienced by the PMMA resist causes a fundamental change to the structure of the polymers. The exposure creates a polymer chain-scission, where the long-chain backbone of the polymers will separate and allow for these parts to react with one another, altering the structure of the polymers. This increases the solubility of those fragments of the PMMA which have been exposed. After sufficient exposure the PMMA is able to be dissolved in the following development process - and so the pattern design alone can be removed from the resist layer on the surface of the substrate.

The different molecular weights play a role in the level of contrast and sensitivity afforded by the resist, with a greater molecular weight resulting in better contrast but a worse level of sensitivity. Interestingly, at lower development temperatures, this offset between the results of different molecular weights diminishes and at a temperature of -20°C (253K), the difference becomes negligible. [91]

PMMA is described as a positive photoresist, meaning that the areas that undergo exposure are the areas that will be removed from the surface of the substrate, whereas a negative resist removes all except for the regions which have been exposed. The

electrons experience random scattering upon incidence with the layer of resist atop the surface, which introduces a wider spot size than just the diameter of the beam.

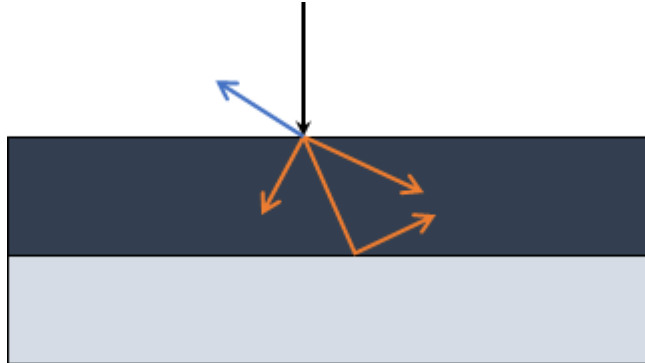


Figure 4.2: Schematic showing the scattering processes that are experienced by electrons from an electron beam as they are incident upon a layer of resist (dark) atop silicon wafer (light). The blue arrow denotes incident electrons reflected off of the layer of resist, whereas the red arrows are electrons transmitting through the resist and scattering, subsequently reflecting off of the substrate

Due to the ability of an electron beam to be precise down to a very small scale – normally of the order of tens of nanometres – the size of the region over which this pattern production is at its most effective is quite low. Conventionally this results in the creation of a “writing field”, within which the electron beam can scan across the surface. These writing fields tend to be of the order of between 100μ and 1mm in width and length – any pattern of a larger size than this would require the stage to translate and to continue scanning from the new position one write-field’s distance away from where previously located.

Some structures are required to be larger than the size of that write-field. The alignment of the stage, and therefore the write-fields, is incredibly important to avoid overlaps or gaps in the pattern, which could significantly damage the integrity of the final structures.

In order to negate this threat to the accuracy of the write, a Write Field Alignment procedure can be carried out, whereby 3 images are taken of a particular feature on the sample substrate. The user is required to centre each image onto the same point of the feature, and if done accurately, this will allow the software to determine the scale and orientation of the sample.

Potential pitfalls of the use of EBL can result in some minor defects being produced across the structures at various places. A typical write of a pattern on an electron beam can take several hours, so over the course of a write and on the scale of the structures typically produced, random defects are likely to occur at various stages.

Problems can arise owing to the fact that the design software allows for a greater degree of precision in its designs than the hardware producing the patterns can provide. One reason for this is the proximity effect, which can be damaging, and so must be accounted for. Due to the scattering processes that occur with the electrons when they are incident upon the surface of the resist, an electron beam still has a finite width of exposure. [9] This means that if there are a set of structures designed in very close proximity to one another, then an area can be accidentally exposed to a dose of electrons at a moment not intended, due to this scattering effect of the electrons. This in turn can lead to the dimensions of the patterns, which are on such a small scale as to be affected by any inaccuracies such as this, being potentially ruined, and therefore even potentially the function of the structure being compromised.

4.1.4 Designing the lithographic patterns for samples

Accompanying the electron beam lithography hardware is a piece of Computer-Aided Design (CAD) software allowing the user to design the pattern. This pattern will be written into the resist on the surface of the substrate. The effects outlined earlier, such as the proximity effect, lead to the fact that the patterns can be designed to a more precise scale than can be achieved in practice.

The software also allows for the breaking down of the pattern into “layers”, enabling for two separate patterns to be written at different times, and for the insertion of a “spacer”, a layer between the two patterns to prevent them from being in direct contact with one another. This provides the opportunity for significantly more complex structures to be produced, with multiple layers of thermal deposition, of which more will be described later in this chapter.

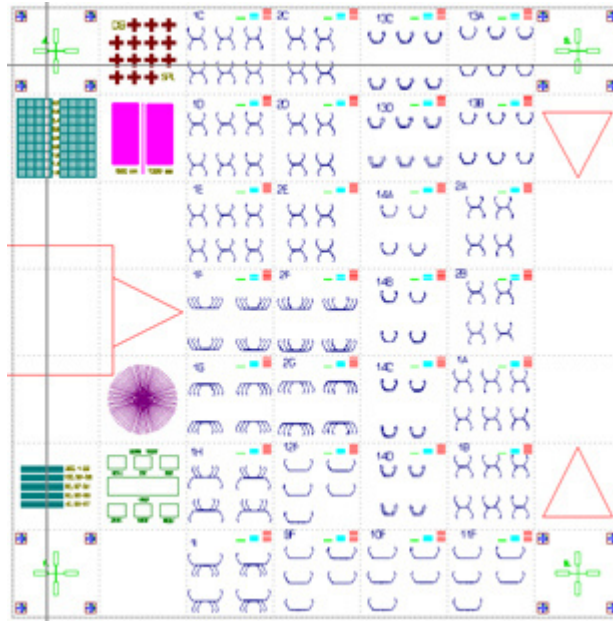


Figure 4.3: Screen capture of a typical image on the EBL Pattern Design software – each different colour on the above pattern refers to a separate “layer” of the design; each layer can be explicitly and individually added and excluded from a write – the faint squares represent individual “write fields” into which the overall pattern is broken down. These write fields have areas of 100x100µm

Figure 4.3 shows a typical file on the software package within which it is possible to design the patterns to then be written onto the wafers. The faint squares shown with a dashed line within the pattern are the individual 100µm writing fields described during the Electron Beam Lithography section.

4.1.5 Sample development and plasma ashing

When the sample is removed from the vacuum chamber in which the EBL is carried out, the substrate is still completely coated in the layer of resist – however, some of it will have become more soluble in certain chemicals (the developer) as a result of the exposure to the beam of electrons.

The wafer is therefore placed into a beaker of MIBK (Methyl Isobutyl Ketone), mixed together with IPA in a ratio of quantities of 3:1. MIBK is another solvent, and is manufactured from Acetone. The now soluble areas of the resist are removed in this stage, leaving only the unexposed resist on the surface of the substrate. The sample is kept in the MIBK:IPA mixture for 45 seconds.

Following this the wafer is placed into another beaker of IPA, much like in the cleaning stage at the outset of the whole process, also for 45 seconds. The sample is then removed from the IPA and blown dry immediately so as to prevent any of the IPA from drying onto the wafer and jeopardising the device.

Following the exposure and development stage where the resist has been exposed and therefore made more soluble, then the soluble regions removed during the development, the sample is ready for the next stage, called Plasma Ashing. This stage involves the removing of any residue resist from the regions of the wafer which have been exposed to the electron beam.

After the resist has undergone development, it is placed inside the Plasma Asher. Using a source of plasma, a reactive species is created – the most typically employed species are Oxygen and Fluorine. The reactive species combines with the exposed resist to form an ash. This ash is then removed by a vacuum pump within the Asher, leaving behind the silicon substrate and the unexposed resist on its surface.

4.1.6 Adding material to samples through thermal deposition and lift-off

At this stage of the sample production process, still no material has been deposited atop the silicon substrate, as the previous steps were in preparation for the addition of a layer of Permalloy (Nickel-Iron). Through the use of a thermal evaporator, the thickness of the layer of the deposited metal can be carefully controlled.

A small amount of the material to be deposited is placed inside a crucible within the thermal evaporator. This crucible is then heated via an electrical current passing through wires inside it. This causes the material within it to heat dramatically to the point that it glows a bright white colour. The material then evaporates onto the surface of the silicon wafer (positioned such that it will become coated in the evaporating material, but also as uniformly as possible).

The equipment is all contained within a sealed vacuum chamber – the reduction of the pressure essentially means a drop in the number of particles between the source material for the evaporation, and the sample onto which material is to be deposited. As individual particles evaporate, the distance they are able to travel towards the sample is limited by the number of particles in the atmosphere within their path. The reduction in pressure then, results in an increase in the “mean free path” of the particles and

allows for significantly more of the source material to reach the sample being evaporated onto.

The thermal deposition process leaves a layer of material evenly coated across the surface of the substrate, although large areas of the surface remained covered in the initial layer of resist, so this lies between the substrate and the metal layer. The thickness which has been deposited is recorded by a crystal monitor – this uses inputted properties of the deposition material such as density and Z-factor, to use the weight deposited onto the monitor and convert this into the thickness of the deposited layer of material. Through several Permalloy evaporations, a calibration was able to be compiled as a way of identifying the reliability of the crystal monitor in the evaporator – with independent measurements via an Atomic Force Microscope providing the accurate results alongside which the crystal monitor readings could be judged.

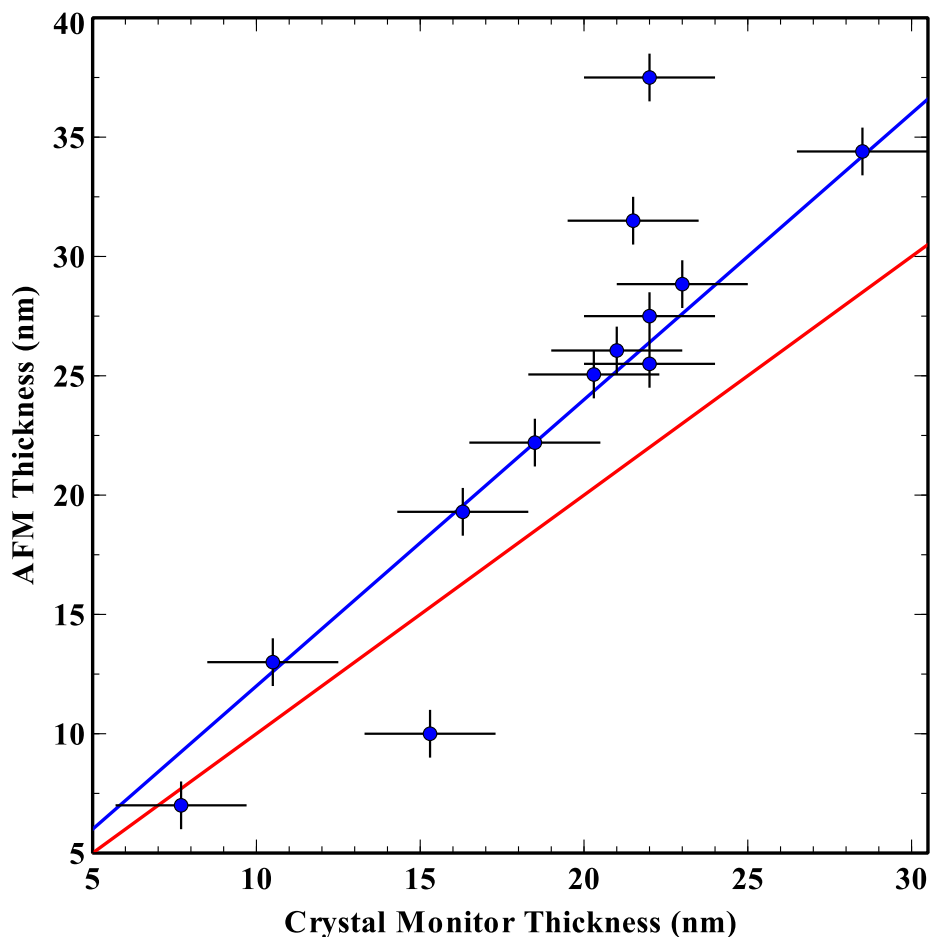


Figure 4.4: Calibration of the thickness of Permalloy deposited according to the crystal monitor, compared with actual measured thickness – the blue line represents a best fit to the data, while the red line represents a unity relationship between the two thickness readings

The above graph shows the calibration data obtained for the deposition of Permalloy within the thermal evaporator that I worked on the construction of, and the required adjustment necessary to obtain samples of the required thickness through the use of the crystal monitor contained within the vacuum chamber.

There are two lines plotted on the graph: the red line has a gradient of 1, where there is a perfect relationship between the two thicknesses, and it is clearly evident that there is a considerable discrepancy between this ideal situation and the reality of the measurement.

The blue line is a fit to the data, with a gradient of 1.3, the restriction of a zero intercept imposed on the trend line due to the fact that no deposited material would automatically ensure no reading present on the crystal monitor. The best possible fit to the data would require for a non-zero intercept, which would of course be unphysical.

The calibration data in the graph was continuously updated as more evaporations were completed, and this graph was used to more effectively create samples of the desired thicknesses based on previous experience.

The final stage involves the removal of the remainder of the resist – and with it the excess metal which has been deposited onto the layer of resist – leaving just the metal deposited straight onto the silicon substrate, in the shape of the pattern designed and written using electron beam lithography.

The silicon wafer is left in a beaker of Acetone overnight, and during this time the remaining PMMA resist is removed from the surface of the silicon. This also causes the metal atop the PMMA resist to be lifted-off with it, leaving only the metal in the shape of the pattern deposited directly onto the surface of the silicon.

This process needs to be repeated several times, in different beakers of acetone. During each iteration of this process, it is possible for some of the removed material to settle back onto the substrate, and so repeating this step several times reduces the possibility of the sample being destroyed or damaged by any debris from the lift-off process. Therefore a fresh beaker of acetone needs to be ready to minimise the risk of producing an unsuccessful sample and ensure the lift-off procedure runs smoothly.

4.1.7 Summary of fabrication process

The process of sample production is one of the most challenging of this study, and arguably the most important – perfecting the processes such that devices can be

reliably and repeatedly produced to a high standard is imperative if a high standard of data and results are to be obtained.

4.2. Techniques for measuring samples

The samples created for the entirety of my investigation were produced in the manner outlined in Section 4.1. Following successful completion of the sample development process, the samples were analysed in a variety of ways – numerically through Magneto-Transport measurements, and through use of the Magneto Optic Kerr Effect (MOKE), and also imaged by the imaging techniques of Atomic Force Microscopy (AFM) and Scanning Electron Microscopy (SEM).

4.2.1 Magneto-Transport measurement technique

The majority of the data that has ultimately been accrued for this study has been through the technique of magneto-transport measurements.

These are measurements which observe the resistance of electrically-conducting regions of samples, and which are of interest due to the property known as Anisotropic Magneto-Resistance (AMR). As was described in the theory chapter, this effect results from the resistance of a magnetic region being directly related to the alignment between the magnetisation direction and the current path through the material when being measured electrically.

Therefore the considered electrical measurement of the samples would provide the opportunity to better understand their magnetic properties. The same basic technique would be employed for the magneto-transport measurements of all samples.

The sample pattern would be lithographed and deposited onto the substrate as outlined in this chapter already, as would a secondary layer of "contacts", wider channels of conducting, non-magnetic material to allow a manner for current to be applied and voltage detected from within the pattern.

These contacts can be connected to separate gold wires, through the use of a silver paint. This paint provides a highly conductive bond between the contacts on the sample substrate and the physical wires, which can then be connected up to measuring devices, creating a complete and measurable path through the samples.

These samples, once wired up correctly, are tested to ensure the connection is valid in both two- and four-terminal configurations which will be described more fully in the following sections. Assuming that the resistances are suitably low - typically, a two-terminal resistance measurement is several 100 ohms, and a four-terminal several 10s of ohms - the sample is positioned into the field centre of an electromagnet.

4.2.2 Four-terminal measurements

There are two types of electrical measurement which can be conducted, namely a two-terminal measurement and a four-terminal measurement. The number of terminals refers to the number of wires physically attached to the sample which are involved in the measuring of the sample.

The two-terminal measurement uses the same pair of electrical wires to carry current and to detect a voltage. In the case of four-terminal measurements these two tasks are completed by separate pairs of wires.

For a two-terminal measurement then, this results in the wires connecting to the sample and the non-magnetic contacts on the substrate being included in the measurement path, and therefore the important information about the sample itself can become masked behind the extra unwanted measurement acquired simultaneously.

This means that in the case of a four-terminal measurement, the lead resistance and the contact resistance are not measured, and as such, solely the sample region is measured, leading to a more accurate reading of the salient data.

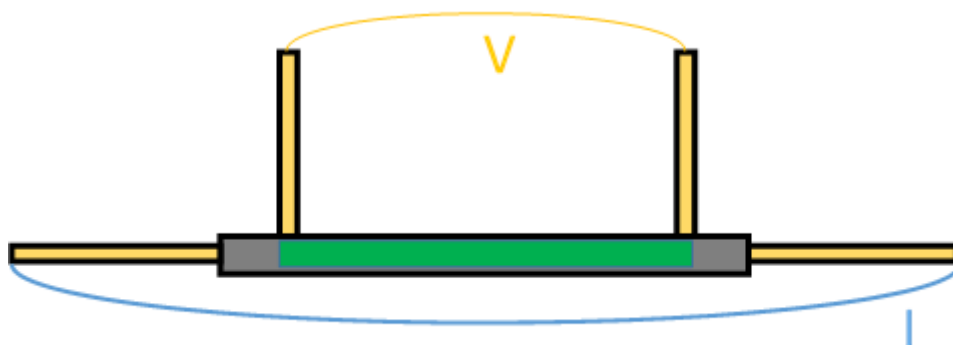


Figure 4.5: Schematic of how four measuring wires are placed on a sample for a 4-terminal resistance measurement. The green region indicates the area of the grey magnetic material which will be measured based on the placement of the gold contacts, and based on the wires chosen for voltage and current being as labelled

Figure 4.5 shows the position of the voltage-detecting probes, within the path of the current carrying outer wires. This setup results in the area of the sample over which the measurement is taken, being as depicted by the green region of the sample in the diagram.

With some more aggressive positioning of the voltage-detecting wires, the vast majority, if not all, of the sample itself can be measured while still maintaining no measurement of the extra wires, yielding a more precise and sensitive measurement in comparison to a 2-terminal measurement setup.

Of course the potential pitfall is that in attempting to measure the entirety of the sample, there is the risk of contacts merging at either end of the sample, and this leads to the possibility of measuring part of the contacts along with the sample, and jeopardising the overall measurement. It is therefore imperative that adequate spacing is included in the design of the sample to account for the proximity effect and its effect on the contacts.

The majority of the samples measured were ASI lattices, and all maintained the same arrangement of the contacts through which electrical measurements could be made.

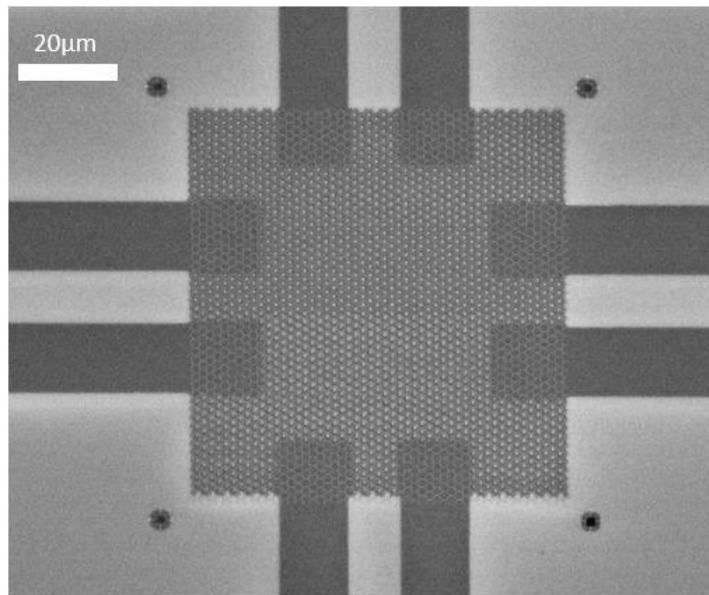


Figure 4.6: SEM image of the typical arrangement of the contacts used to electrically measure ASI lattices – the dark rectangles extending out from the edge of the central lattice are the gold contacts used to supply electrical current and detect voltage

Figure 4.6 shows an SEM image of the hexagonal lattice with eight electrical contacts deposited from the edges of the lattice. The contacts are written in a single pattern and so the alignment between them is always the same, albeit as seen there is minor asymmetry in terms of how centred the contacts are on the lattice. The design ensures that this does not affect the measuring of the different lattices as a result of the contact location.

Commonly employed techniques for contacting to samples for electrical measurements include Hall Bar and van der Pauw methods. The Hall bar method sees an arrangement of contacts in a rectangular shape, with a contact at either end of the longer dimension, through which current is supplied. On the other edges of the material are attached numerous extra contacts for detecting voltage. The geometry is ideal for measuring and investigating materials through Hall Effect measurements. The van der Pauw method is powerful in that it has the capability of measuring the properties of any approximately two-dimensional object – that is to say an object with a third dimension which is significantly smaller in scale than its other two. The van der Pauw method is able to generate an average resistivity for the whole material being measured.

These two methods were overlooked in favour of the solution shown above in Figure 4.6, and the reason this solution was chosen is due to the opportunity it allows for all desired measurement configurations to be achieved with a single set of contacts. It allows for conventional AMR measurements to be achieved, simultaneously alongside planar Hall measurements.

What is also shown in this image of the contacts is how many hexagons are directly connected to each contact. This means that immediately the input current is being split through a number of different channels, rather than a simplistic model which could consider the current path to begin and end at two single points on the sample. This means that when coming to the analysis of data measurements obtained for the different lattices, it is less guaranteed to be a like-for-like comparison.

The magneto-transport measurements conducted during this study were performed on a new measuring setup which was created during the course of this investigation. A large electromagnet was connected in parallel and calibrated to understand the strength and uniformity of the generated magnetic field.

Magnetic samples were mounted onto an electrical probe, and connections made between electrical wires on the probe, and the contacts lithographically placed on the edges of the magnetic devices. This created complete circuits and allowed for the passing of a current across the samples, and therefore the resistance of the magnetic

region could be evaluated. Once the probe was placed inside the magnetic field, the resistance of the sample would be affected by the strength and orientation of that field. The current delivered to the sample, and the voltage range measured, could be adjusted depending on the sample, as each individual sample had different resistances based on design properties such as their width and thickness.

4.2.3 Hexagonal Lattice Measurement Orientations

The large proportion of measurements in this study consist of magneto-transport measurements through a hexagonal lattice of ASI. Therefore a system was devised for the naming of the different magneto-transport measurements that could be carried out, based on the different permutations of the current and voltage directions relative to each other and the sample, and the direction of the applied magnetic field.

In total there were 8 types of measurement carried out, in 4 different orientations of magnetic field and current directions relative to the easy axis of the hexagonal lattice. Within these 4 orientations there were 2 measurements for the different regions over which the voltage was being detected: the standard AMR measurement where the detected voltage is parallel to the current, and a planar Hall geometry, where the voltage is detected perpendicular to the applied current.

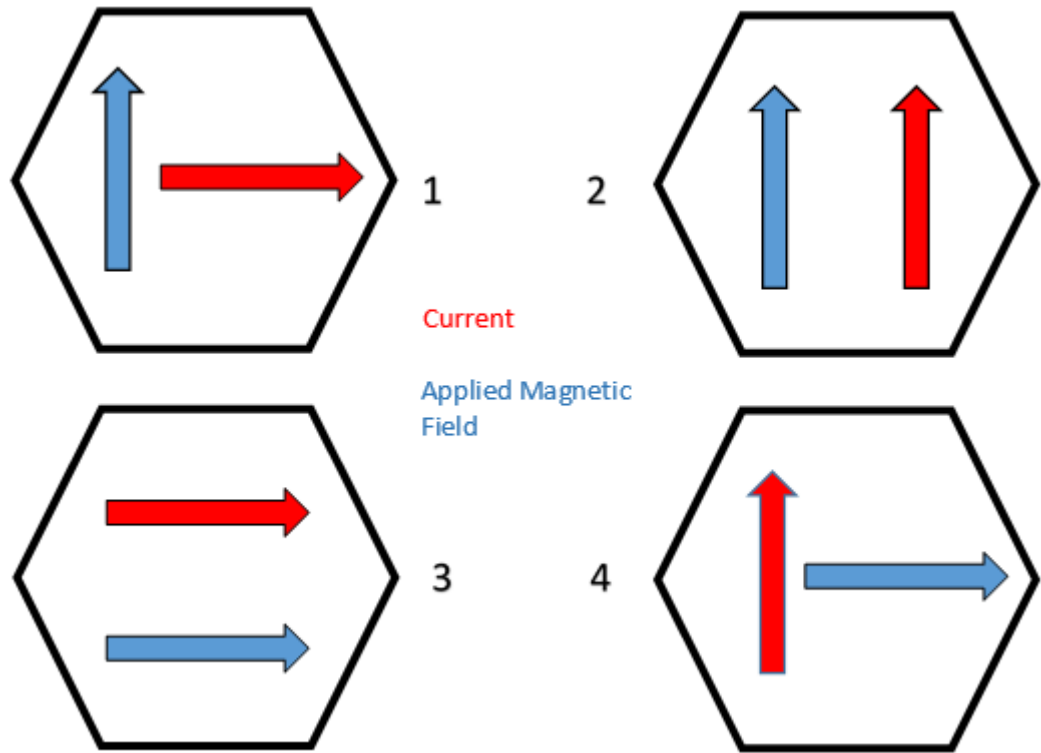


Figure 4.7: Schematic outlining the four measurement orientations used while performing magneto-transport measurements on hexagonal lattice-based ASI – the surrounding hexagon shape refers to the orientation of the hexagons in the lattice relative to the depicted directions of the current and magnetic field

Above in Figure 4.7 is a schematic depiction of these four measurement orientations, showing the directions of the current and the applied magnetic field, relative to both each other and to the orientation of the lattice.

These four orientations were measured collectively across different samples, and can be combined to intentionally probe specific characteristics of the lattices, where perhaps simply measuring a single of these orientations could yield an inconclusive result. It is also interesting to note that different orientations result in different portions of the structure being sampled in each measurement.

In the literature of other AMR measurements on the hexagonal lattice, these four measurements have been categorised into two types, based on the path through which the current flows in the lattices. [15] The two types are referred to as the Armchair geometry and the Zigzag geometry. Considering Figure 4.7, the red arrows denoting the current have two different potential paths. In images 2 and 4, the current is flowing along a diagonal path of bars, almost entirely ignoring one of the bar orientations. This

is referred to as the zigzag geometry due to the shape of the current path along this diagonal series of bars.

The other two measurements shown in the figure, in images 1 and 3, have a mixture of all three types of magnetic bar in their current path and due to the shape that these bars make, this is referred to as the armchair geometry.

4.2.4 ASI Lattice measurement types

Within the four orientations outlined above, there are two types of measurement which can be performed. These differ from each other by the alignment of the supplied current and the detected voltage. The two measurements are conventional AMR from magneto-transport, and the planar Hall geometry measurement.



Figure 4.8: Schematic of the relative directions of Current & Voltage in standard AMR and Hall measurements. Here the red arrow represents the current path and the blue arrow is the direction over which the voltage is detected

In a standard magneto-transport measurement, the supplied current and the detected voltage are parallel to one another across the lattice. In the Hall geometry the voltage detected is perpendicular to the direction of the supplied current.

The AMR measurement is a symmetric measurement but there is an inherent asymmetry to the Hall geometry measurements, and this can occasionally become present in the data acquired in this form, as has been mentioned in my literature review regarding potential temperature-dependent effects of ASIs.

4.2.5 Low-temperature measurements

As with many of the interesting investigations into nanomagnetism and particularly ASI of recent times, it was considered that in order to extract as much useful information as possible about my samples, a considerable amount of temperature-dependent measurements should be carried out, as often it has been shown that the variations of a structure's behaviour across a temperature range can be among the most informative details about a material. These measurements were carried out using a low-temperature pulse tube, onto which had been mounted an electrical measurement device with the potential to carry out both longitudinal and Hall geometry measurements simultaneously.

The pulse tube had been stationed onto a custom-made stand, such that the sample holder was situated precisely in the middle of the field produced by two large copper solenoids wrapped around iron cores, generating a magnetic field in excess of 0.5T.

4.3. MOKE (Magneto-Optic Kerr Effect) Measurements

Aside from evaluating samples using Anisotropic Magneto-Resistance, another primary tool used to measure and investigate my samples was a MOKE magnetometer, which utilises MOKE to determine the magnetic state of samples by examining the polarisation change of laser light reflected off their surface. This machine was built during this project from the outset, which involved the necessary learning about these pieces of equipment and the physics being made use of in their function. The system uses a solid state laser diode, emitting a laser light of wavelength 633nm. The laser has its temperature stabilised by a Peltier cooler, a device which uses the Peltier effect to transfer heat from one side of a device to the other in order to equalise and regulate the overall heat of the device, in this case the laser diode. This ensures the power output of the laser remains as stable as possible, an important requirement of the system being stable enough to obtain reliable data about the samples.

This laser light is directed at the surface of the magnetic sample. Prior to the incidence on the surface however, the light is passed through a linear polariser, so that the light interacting with the sample is linearly polarised. The collimated beam is focussed down to a spot a few microns wide, on the sample surface by a focussing lens, in order to achieve the greatest possible level of sensitivity and to sample individual regions of structures. After being reflected the light is then passed through another focussing lens where it is returned to being collimated light as before the initial focussing lens.

The reflected and re-collimated light passes through a quarter wave plate, the purpose of this being to negate the elliptically polarising effect of the magnetic material on the laser light. Finally the light travels through what is known as the Analyser, but which is essentially another linear polariser, angled perpendicular to the orientation of the incident linear polariser, but with a two-degree shift away from perfectly perpendicular, with reference to the two degree maximum mentioned during the earlier section outlining MOKE.

I worked alongside fellow members of my group and played a major role in the construction of the MOKE magnetometer used in my measurements. The system is measured through a Lock-in Amplifier, which reliably detects a signal of a known frequency from within a noisy background environment, successfully improving the quality of information about the laser light, in this case. Both the laser diode and the detector are connected to the Lock-in amplifier, thus allowing both for the input laser light to be of a specific frequency, and for the measurement to focus explicitly on this frequency.

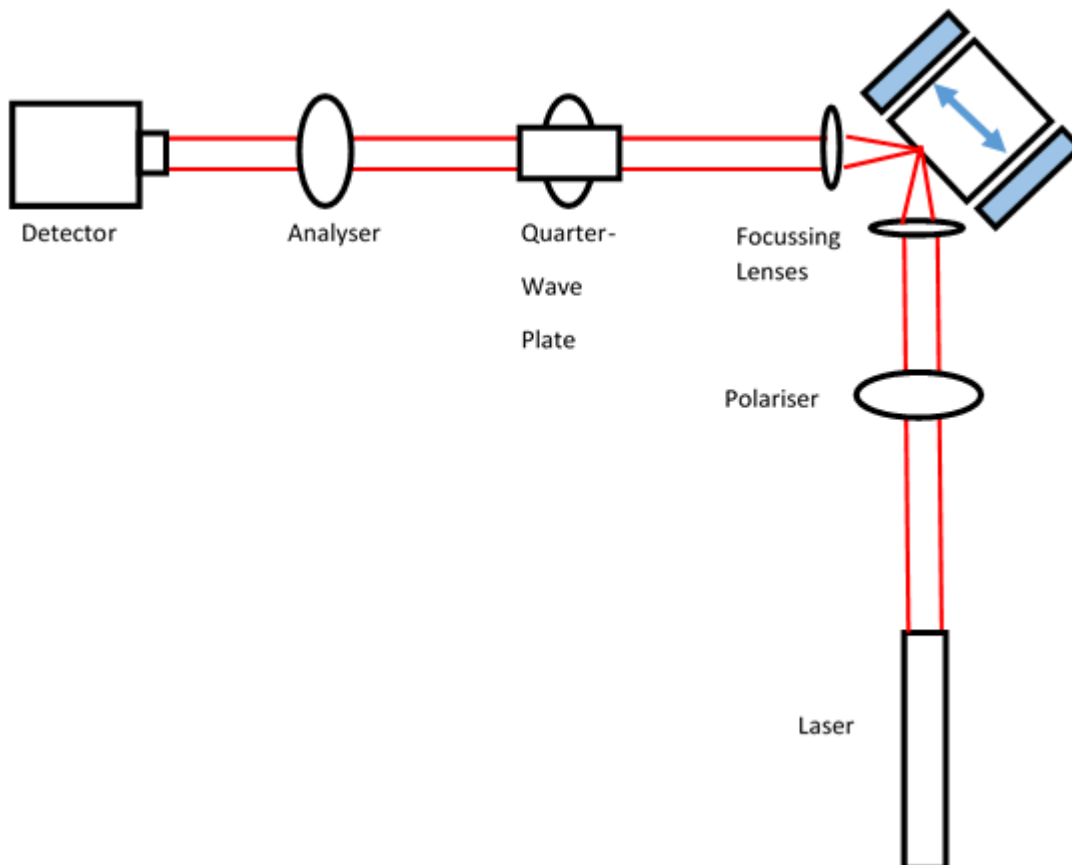


Figure 4.9: Schematic of the setup of the MOKE magnetometer produced to measure samples using MOKE. The blue rectangles represent the two coils of an electromagnet which magnetises the sample, through field applied in the blue arrow direction

A number of calibration steps were taken to ensure the respective components were not only functioning correctly but were also optimised to yield the best data for my study. One such measurement concerned the quarter wave plate, the data for which is shown below.

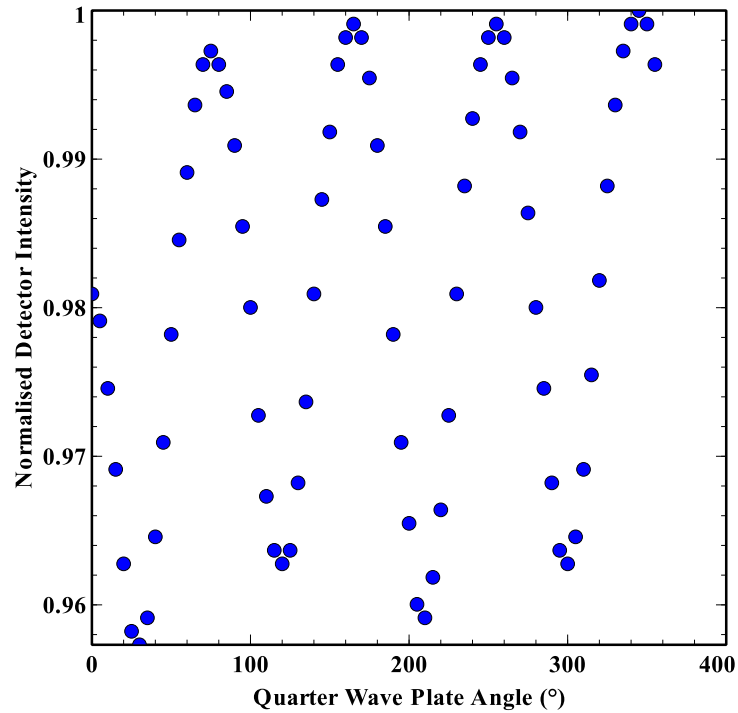


Figure 4.10: A normalised average calibration obtained for the intensity detected by the detector for a MOKE experiment as a function of the angle of the quarter wave plate

The above graph shows the average, normalised detector intensities for different angles of the quarter wave plate – the “angle” referred to on the x-axis relates to the arbitrary labelling of the waveplate itself. This allows for the intensity that reaches the detector to be moderated within this range by the positioning of the wave plate.

The wave plate, of course, whose function is to convert the elliptically polarised light which reflects off of the magnetic surface back to linearly polarised light, can only be truly optimised in conjunction with the other optical components involved in the system.

4.4. Description of micromagnetic simulations

Simulations provide the opportunity to assess and give further validation to experimentally obtained results on a short timescale and without the necessary sample construction, and as such are a highly useful tool for the improved understanding of the physical results being compared.

Object Orientated MicroMagnetic Framework (OOMMF) [92] is a commonly used tool for simulating the behaviour of nanoscale interactions in magnetic structure. It uses a form of finite-element modelling, where a simulated structure is broken down into equally-sized regions of the structure. Each of these individual elements is evaluated independently, and the resulting magnetic properties of the elements are summed together to produce an overall value for the magnetisation of the entire structure. The size of the elements measured is available to be determined by the user, in accordance with their particular needs from the simulation – some uses will require a far more precise simulation than others, which comes at the cost of the amount of time the simulation takes to completed. In the case of this study, the cell size chosen was 5nm x 5nm x 10nm – the thickness of the sample being 10nm. Making the z-component equal to the sample thickness simplifies the analysis of the simulation.

The data obtained from OOMMF was to be adopted and adapted during this study. The values of the magnetisation of the material within each of the elements it is broken down into, were extracted from the simulation and manipulated, such that it would become possible to compare to the experimental AMR data obtained during this study.

The values of the vector field in x and y were acquired for the separate cells and in each case, these could be converted into a resistance through the calculation of their magnetisation direction based on these values. The samples were evaluated and an expected direction for the current path was assigned to the cells. Given its importance to the determination of the size of the AMR, the angle between this assigned current direction and the simulated magnetisation could be estimated.

The individual cells were considered to have a minimum resistance when the simulated magnetisation was perpendicular to the current direction, and maximum resistance when these two quantities were parallel to one another. This mimics the results observed for experimental measurements of the AMR.

One big advantage from the use of finite-element modelling is that it allows for the mechanisms in these systems to become visible down to a very small scale. The ability to observe these nanoscale interactions is particularly key in understanding the way in which these magnetic systems develop. The fact that these processes, such as a DW propagating along a wire, which normally take place over hundreds of nanoseconds, can be observed appreciably in a simulation taking place over a macroscopic time period, allows for far more extensive analysis than is possible simply from assessing experimental data.

Given that location of the attached magnetic contacts in reality, the current path can be determined and therefore the size of the AMR can be identified at each cell within the structure. Considering the geometric locations of these cells in relation to one another, a resistor network analysis can lead to the determination of the overall resistance of the structure, as a function of externally applied magnetic field.

For simple structures like the single wire this can be an approximation of the profile of the magneto transport measurement, however in reality for an accurate indicator of the level of resistance expected from a structure, each cell will need to be considered also in terms of its current density. Particularly when considering the current path through a structure where the channel width is varying, or where the current can split into two paths out of one initial path, then the resistance levels at different points in the sample will vary significantly, giving more weight to some cells than others. So, clearly as the structure is becoming more complicated, so the importance of the current density is increased.

4.5. Conclusions

This chapter has outlined the importance to the study of the conditions within which physical samples can be created and measured, and the implementation of the techniques through which they are measured. The cleanroom facilities within Cardiff University have allowed for the reproduction of high quality magnetic samples, enabling for two similar samples created under the same conditions to represent a valid comparison when judging their associated data.

The different stages of the process of creating these samples have been described, from the initial stages of preparing a silicon-oxide capped silicon wafer for use as the

substrate, through to the process of thermal evaporation to deposit the materials included in the structures. The different materials have been discussed and justified in terms of their inclusion in the devices in preference to other materials.

After the successful creation of the samples for the study, there have been different magnetic measurement techniques employed to characterise and measure these samples, several of which are making use of experimental setups created from scratch during this study. These structures which have been created make use of a combination of a number of existing pieces of equipment.

The measurements included are described in terms of how they are implemented, for which samples they are used and also the advantages to be gained from using each of the different techniques. There are also naming conventions which have been adopted for the measurement geometries employed through the magneto-transport data acquisition.

5. Investigating the hexagonal lattice of Artificial Spin Ice (ASI)

This thesis has thus far outlined the relevant theory for this study, and the facilities and equipment used to create and measure the experimental samples. The following three chapters will discuss the specific experiments conducted, and results obtained from the project. The focus of the work is Artificial Spin Ice (ASI) and the interactions between Domain Walls (DWs) in magnetic nanowires and nanostructures.

In this first results chapter, investigations are carried out into the hexagonal lattice of ASI. This is completed via both a large lattice, and also a single magnetic vertex - essentially a unit cell of the hexagonal lattice. The motivation behind the measurements is to acquire a comparison of the behaviour of a single vertex to that of a large lattice of these vertices. The intention is to determine whether the phenomena seen in these samples can be considered as simply an accumulation of the effects seen in the data for single vertex samples.

The simple connected version of the hexagonal lattice is also investigated, with a view to this being a useful comparison for studies performed in subsequent chapters. It is being investigated in terms of the anisotropic magnetoresistance (AMR) it exhibits during electrical magneto-transport measurements, for all different combinations of current and voltage electrical contacts, and all considered alignments of external magnetic field. The connected lattice is also investigated in terms of its behaviour given the expected presence of particular types of DW, be it either transverse (TDW) or vortex (VDW) - by choosing different thicknesses of the magnetic structures - and the difference in the AMR signals for these different lattices is assessed. Finally, the presence in previous research findings of an asymmetry in the AMR of some samples at low temperatures [15] is considered again and attempts are made to further consider the origins of this effect.

Throughout my experiments I have focussed on the ferromagnetic material Permalloy, due to its characteristic of having almost no magnetocrystalline anisotropy.

The practical work outlined has been supplemented by micromagnetic simulations carried out using OOMMF (Object-Orientated MicroMagnetic Framework), and with this simulated data being adapted into a comparison of the magnetotransport measurements performed. Attempts are made to use the simulations to provide

explanations for some of the details discovered within the experimental data, for instance the nature of the magnetisation reversal.

In the majority of my studies I have conducted and displayed measurements of how the resistance of the sample varies with applied magnetic field, for two opposite directions of magnetic field. In all of the figures shown in this and the following chapters, the same colours will be used to denote the same change in the magnetic field, as illustrated in Figure 5.1:

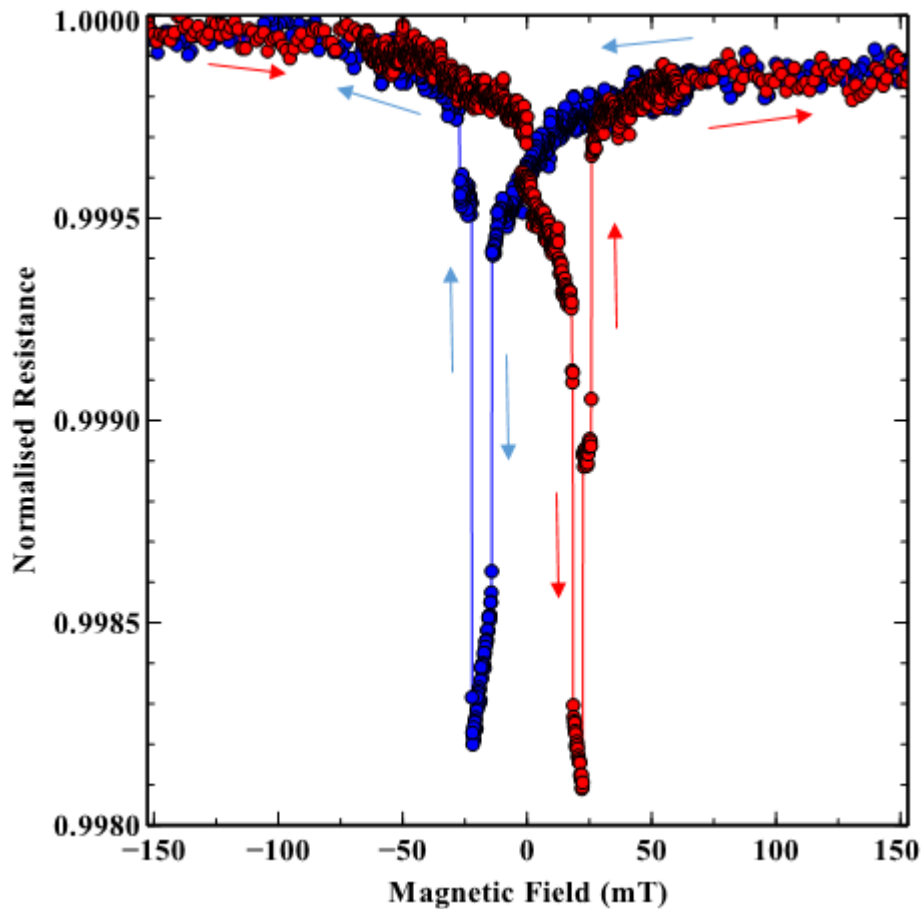


Figure 5.1: Example of a magnetotransport measurement dataset, with coloured arrows demonstrating the way in which the magnetic field is changing between data points of the corresponding colours

This is an important aspect to keep in mind, as whether features in data appear before or after an applied magnetic field passes 0mT in magnitude will determine the nature of the effect being observed.

5.1. Connected Hexagonal Lattice Samples

This chapter centred on samples of a hexagonal lattice structure. That structure can be considered as a collection of 3-vertices, with each 3-vertex being surrounded by three magnetic bars. The base lattice parameter and structure remains the same for all hexagonal lattices, both in this chapter and in subsequent chapters, with the bars being of length $1\mu\text{m}$, and a width of 100-200nm. From this design, alterations are made to the design in order to create the different lattice types to be measured, but the above basic parameters remain consistent throughout.

5.1.1 Hexagonal Lattice - Single Vertex

While the majority of this study focusses on full lattices of ASI, a useful investigation is to consider the case of a single vertex from within a hexagonal lattice. This case, which is essentially the base element, the single building block of the large array of vertices that make up the hexagonal lattice, would potentially provide an interesting insight into how the resistance signal develops as a result of a large array of these structures being combined.

An interesting study can be conducted of the switching properties of a single vertex, and attempt to ascertain whether the resistance of a large network can be as simple as a summation of a large number of these vertices in sequence. Given that the array of these vertices will have a large number of parallel routes through which the current path can travel, the resistance of the array should be lower than the single vertex – this despite the current paths being far longer for an array.

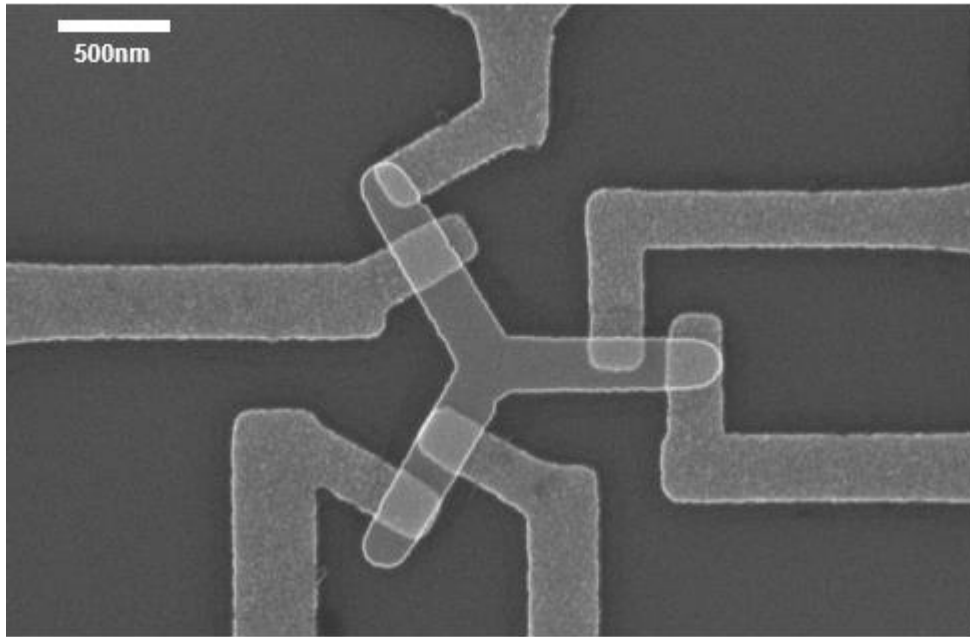


Figure 5.2: Scanning Electron Microscope (SEM) image of an example of a single vertex in a hexagonal ASI – the single vertex in the centre is deposited first, and is formed from Permalloy, while the contacts attached to it are made from gold

Figure 5.2 shows a single vertex after fabrication using Electron Beam Lithography (EBL), and the positioning of the gold contacts to best perform the electrical measurements required. The reason and key benefit of designing the gold contacts' positions on the vertex in such a way, is that it is possible to individually measure any 1 of the 3 bars around the vertex, or any pair of 2 bars, depending on the choice of contacts for voltage and current. This means a full study of the vertex can be completed via a combination of these measurements.

One measurement that can be obtained in this way and would hopefully provide useful information, is to investigate the field range over which the magnetisation reversal occurs. This could be of great importance as a comparison with the field range over which the larger lattices reverse their magnetisation. This is because in those cases a far larger quantity of vertices are being investigated, and there lies the possibility that the magnetisation at all vertices won't reverse direction at the same applied magnetic field. So the field range over which the single vertex switches could provide interesting insight into behaviour of the larger lattices measured.

A useful benefit of the single vertex is that, while it is the simplest base unit of the hexagonal lattice ASI, it will still obey the ice rules, in the same way that the hexagonal lattice does, such that the 3-in or 3-out state of the magnetisation in the bars is still highly energetically unfavourable [54].

5.1.2 Connected Lattice

A connected lattice of nanowires in the hexagonal arrangement is a commonly-studied form of ASI. This is due to the symmetry of the hexagonal lattice, while the connected wires provide paths for electric current to be passed through the connected networks. These open up a variety of potential techniques for the measurement of these devices, as they are now suitable for both optical and electrical measurements. Figure 5.3 below displays an SEM image of a sample fabricated and measured during these investigations.

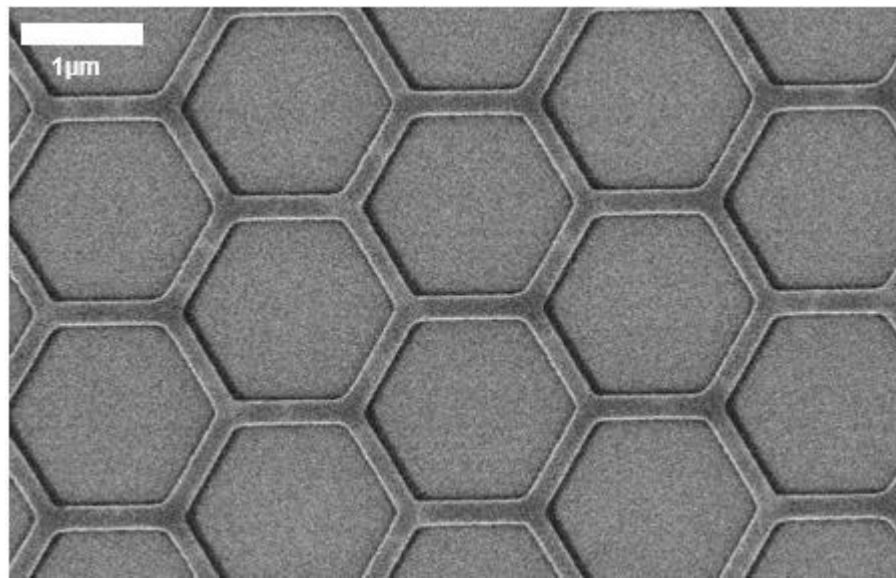


Figure 5.3: SEM image of a connected example of a hexagonal ASI – the network consists of Permalloy of 20nm thickness, wire width 150nm

These connected lattices allow not just the current, but also the DWs, which can form at the edges of the network of bars, to propagate freely through the structure, aiding the process of magnetisation reversal for the bars when interacted with through the addition of a sufficiently large external magnetic field. The DWs can then also remain pinned at these vertices following their propagation through the lattice [49].

This lattice, then, has the process of magnetisation reversal being possibly attributable to both the propagation of DWs through the material, and also the dipolar interaction taking place between the different bars of the lattice. It is believed that the DWs ensure a transition of lower energy change and as such would produce the dominant effect due to the requirement for less applied energy.

These hexagonal lattice ASIs, as a frequently-used and measured sample in various recent publications [14], [15], [36], [37], [48], [59], form the basis for my initial experiments, with them offering a comparison from which I can tailor more varied samples for my investigations.

5.1.3 NiFe samples capped with AlO_x

A potentially key finding in the field of ASI concerns the identification of a low-temperature asymmetry in the magnetotransport data gathered from lattices at low temperatures, in the region of below 50K. [15] This is seen as a breakthrough in the identifying of a new physical state in these ASI systems, and one which is directly brought about by the nature of the ASI. It is considered to have been brought about by the inherent frustration and non-zero entropy at low temperatures.

There have been previous studies into other magnetic structures and the effect of exchange bias [93] on the behaviour of the magnetisation within the magnetic material, regularly being noticed as responsible for a shift in the coercivities of materials.

Exchange bias can be observed in a bilayer structure combining a ferromagnet with an antiferromagnet. In the case of the samples of this study, [14] it arose through the creation of a thin, naturally forming antiferromagnetic oxide layer atop the measured ferromagnetic layer. In the case of the Permalloy structures in this study, an Iron oxide layer will form on the surface of that Permalloy [94]. This antiferromagnetic layer interacts with, and causes a shift in the magnetisation behaviour of the ferromagnetic layer. This manifests itself as an asymmetry in the standard hysteresis loop of the bilayer.

A conventional method of limiting the effect of exchange bias is to reduce the level of oxidation experienced by the magnetic portions of the nanostructures. This can be achieved by the deposition of a thin capping layer. This will be deposited immediately atop the magnetic layer following the deposition of the magnetic layer, while the sample remains under vacuum conditions. This process was recently applied to ASI, with successful results in challenging the previously held theory for the origins of this low-temperature asymmetry [14].

Therefore this part of my study focuses on the confirmation of these results through the creation of a range of both capped and uncapped samples, using thin layers of aluminium as the capping, protective layer atop the magnetic channel. The samples measured in this part of the investigation were all connected hexagonal lattices.

5.1.4 Samples summary

A number of samples were created and measured as part of the investigation into the single vertex and connected lattice, and Table 1 shows a list of the particular samples which have data included in this chapter.

Table 1: Detailing the samples whose data features in the following chapter, and a description of their characteristics

Sample Name	Sample Type	Materials ($\pm 0.5\text{nm}$)	DW Type
ASI7	Connected Uncapped	Py 34nm	Vortex
ASI13	Connected Capped	Py 31nm + Al 2nm	Vortex
ASI14	Connected Capped	Py 7nm + Al 2nm	Transverse
ASI47	Single Vertex Uncapped	Py 22nm	Vortex

Note that in the cases here I have refrained from including information as to the contact material and thickness. This has been maintained and consistent throughout the process, and has always made use of Gold for the material in the contacts, with a thickness of 80nm.

5.2. Measuring and simulating single nanowire

Simulations, outlined previously in Section 4.4, were carried out on a variety of different micromagnetic structures, and it was decided to begin with a simple structure, in order to confirm the suitability of the simulation routine for accurate modelling of the experimental data. The first measurement therefore was of a single magnetic nanowire of Permalloy, with a width of 200nm and a thickness of 10nm. Nanowires have been the subject of investigation through the measurement of AMR previously. [95]

Electrical measurements allowed for the AMR behaviour of the wire to be investigated. This was considered alongside the simulation, which makes use of magnetisation data gathered from OOMMF. Gaining information about the samples magnetisation variation allowed for a value of a form similar to that of AMR to be calculated. The magnetisation is considered as the sum of individual magnetisation elements which the full structure has been broken down into, divided by the volume of the structure. Through the

resistor network analysis it has been possible to show how closely the OOMMF simulations of a structure can mimic the AMR of a real structure of equivalent dimensions.

The magnetic field was applied parallel to the sample's easy axis, from 0mT to 50mT, at which point the simulation ceased. The data from this and the physical measurement of the same sample specification are shown below in Figure 5.4.

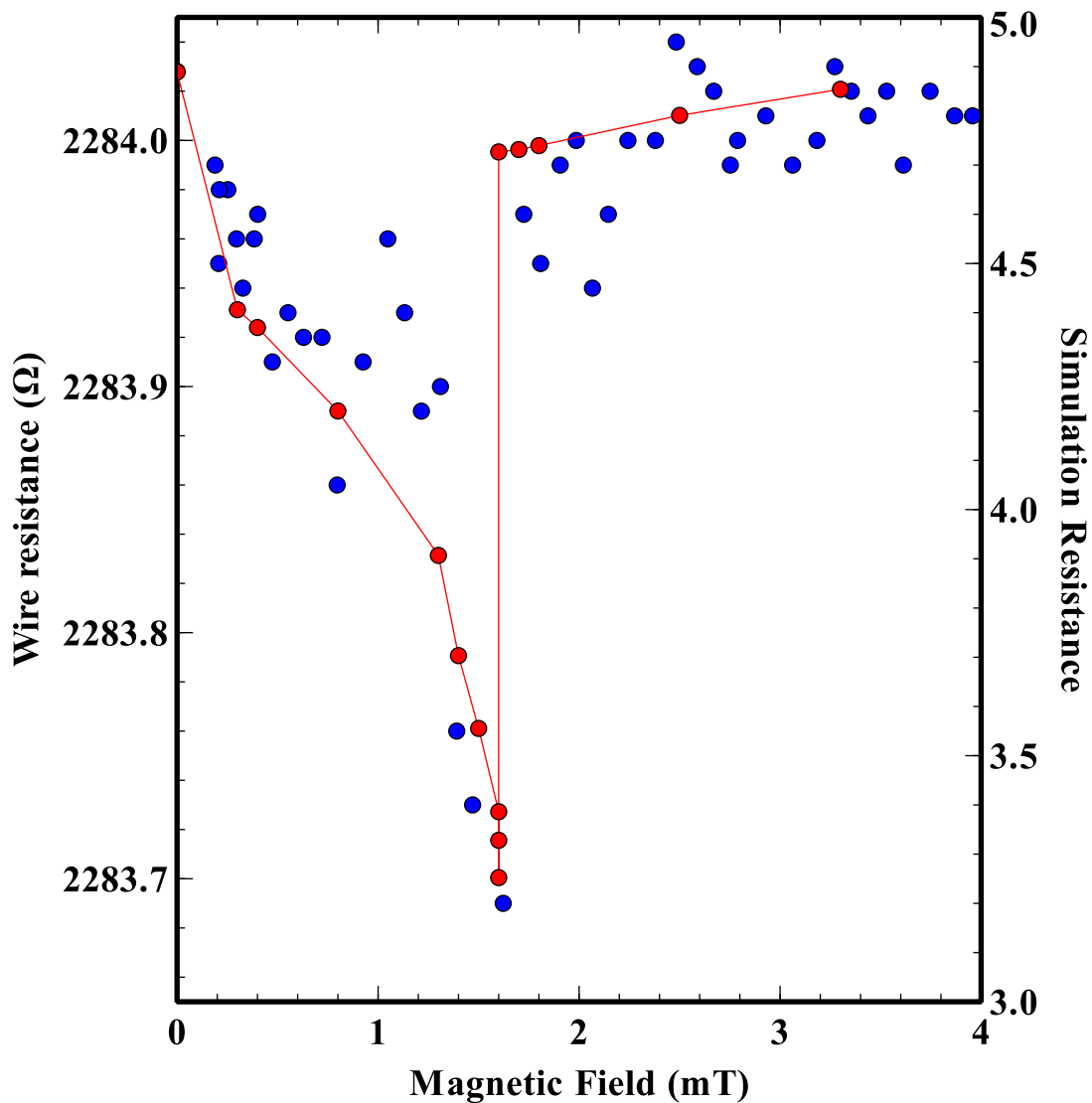


Figure 5.4: AMR obtained from simulation data (red) of a single magnetic nanowire influenced by the effect of external magnetic field, overlaying the raw data (blue) of a sampled Permalloy nanowire – the red trace is relating to the right y-axis, and the blue data relates to the left y-axis – the resistances quoted in the simulation are not representative and so the overlay is merely indicative of the shape of the resistance change as a function of magnetic field

The simulation does not take into account current density and therefore the most useful thing to be able to discern from this data is the how the resistance of the sample changes with applied field, as opposed to the particular magnitudes of the resistance within the measurement. Although in this case as the sample is a single rectangular wire the current density is not as complex as it can become, and therefore a simple analysis can still prove useful. The data from the OOMMF simulation shows the progressive decrease in resistance down to a minimum. This is the slow rotation of the magnetisation caused by the magnetic field opposing that magnetisation. The magnetisation reversal requires a stronger field in order to occur, and the initial drop in resistance is caused by the process of nucleating a DW. The abrupt increase in resistance that follows is a nucleated DW propagating across the wire and reversing the magnetisation.

Due to the resistance in a ferromagnetic structure such as this being equal whether the magnetisation and current are parallel or antiparallel to one another, the reversal of the magnetisation might be considered to not have an effect on the resistance, and therefore no change in resistance could be observed on the AMR data trace. However, another contributing factor to the magnetoresistance is that there is some converging of the vector field at the extreme ends of the nanowires. This remains present when the magnetic field opposes the general direction of the magnetisation, however after the magnetisation reversal, the magnetic field being parallel to the magnetisation direction reduces the effect of the convergence. This produces the offset in the resistances before and after the magnetisation reversal, giving the sharp increase in the resistance.

This data also has a strong similarity to the data acquired in previous experiments of single nanowires, including that shown in Figure 5.5.

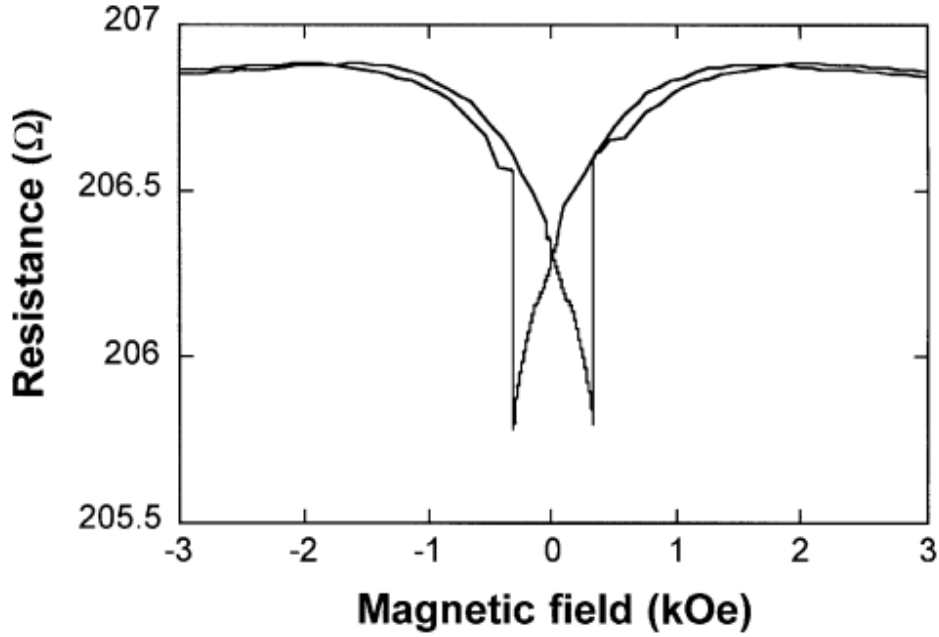


Figure 5.5: Graph from *Fert et al* showing the AMR data for a single magnetic nanowire of Co [95]

While this data is for cobalt, and the data from the simulation and experiment of this thesis is for Permalloy, there are definite similarities in the shape of the data which can be attributed to the nucleation and propagation of the DW within the nanowire.

Of importance though is the general agreement in Figure 5.4 between the different sets of experimental data and the data acquired from the simulation. This seems to endorse the strength of the model created through use of the OOMMF simulation data, and can certainly be applied later to more complicated structures.

5.3. Analysing a single vertex of the hexagonal lattice

Progressing on from the single nanowire, the understanding of the magnetisation reversal and interactions of the bars within the lattices can be advanced by measuring and assessing the data obtained from a single magnetic vertex of an ASI.

This was an avenue I pursued, where a design of the samples and contacts allowed for the measurement of each bar of the vertex individually, and also pairs of bars simultaneously, in an attempt to gain as much and as precise information as possible, to build up a picture of the interactions prior to investigating larger lattices. For the

measurements the magnetic field would be applied with the sample always orientated in the same way, and the bars named as per their orientation relative to that field.

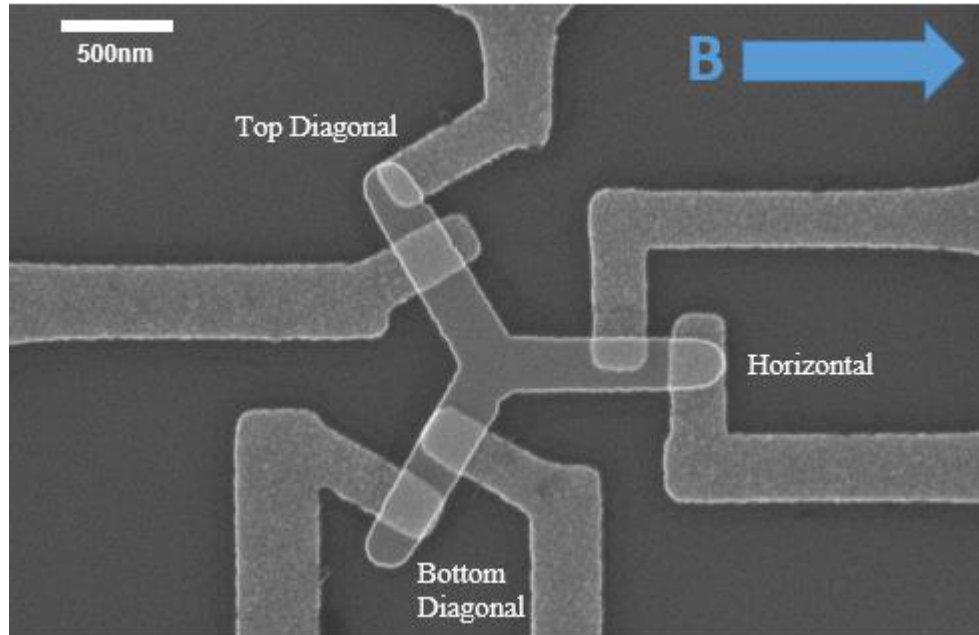


Figure 5.6: Annotated SEM image of sample ASI47, which consists of a single vertex of a hexagonal lattice, labelled with the names of the three individual magnetic bars for reference – these bars are named as such based on their orientation relative to the applied magnetic field

An example of the structure created can be seen in Figure 5.6. The labelled SEM image shows the names of the three individual bars which make up the single vertex. The names are based on the angle to the magnetic field and are not fixed to the specific physical bar – they would change for each bar, if the sample were to be rotated through 120 degrees in the plane of the field. For this study I have retained the bars in the same relative positions for all measurements.

Through the lithography of the two layers, non-magnetic contacts were placed in such a way as to be able to perform various measurements through the selecting of which of the six electrical contacts will supply current and which will detect voltage. Individual magnetic bars can be measured, alongside pairs of bars.

The orientation used means that a new DW will nucleate at the end of the horizontal wire, as a result of an external magnetic field being applied. It will propagate along the horizontal wire, reversing its magnetisation. Which bar it propagates along next can be determined by the chirality of the DW within the wire, as has been shown by *Burn et al.*

[96] If the DW has “up” chirality, it will propagate along the top diagonal wire, and a “down” chirality sees it propagate along the bottom diagonal.

5.3.1 Single Vertex measurements

The possibility exists with the set of magnetic contacts positioned on the single vertex, as seen in Figure 5.6, to measure either one or two bars in any single measurement. One minor imperfection arises from the fact that each contact needs to be separately attached to the structure, to avoid short circuits, where current could flow through the contacts exclusively and not need to flow through the ferromagnetic channel. Due to the varying resistivities of the gold in the contacts and the Permalloy in the ferromagnet, this outcome would certainly be possible. As a result of this, the contacts are relatively conservatively placed, and therefore not all of each wire can be measured.

Due to the fact that the geometry of the structures means they are defined as wires (having one large length and two shorter lengths), they have been considered previously as regions of a single magnetisation domain [97]. However when reaching the level where fractions of wires is measured, rather than the usual sum of whole wires, this may not apply. It might produce unexpected results, as at this level the domain structure might be more complex than previously predicted. There is also, though, the potential for this design to have no impact on the state of the measurement signal, rather that the signal will simply be smaller in absolute terms, due to a smaller current path being measured.

The single bar has been the focus of these measurements, and it can be measured by the contacts being selected as in Figure 5.7.

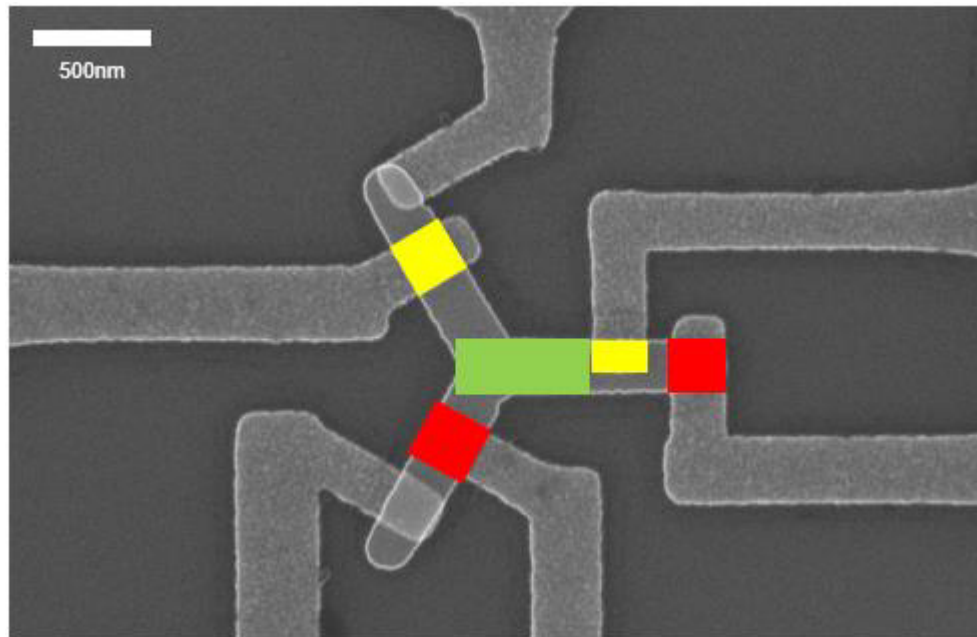


Figure 5.7: Annotated SEM image of sample ASI47, which consists of a single vertex, showing the current and voltage contacts necessary for measurement of a single bar – the red regions show the current delivering contacts overlapping with the vertex, the yellow regions show where voltage is detected between, and the green region represents an estimate of the volume of the magnetic material which is detected in this measurement geometry

The diagram shows an estimate of the region which can be measured using the contacts as shown. The green region is where there is both a current flowing and a voltage being detected. One extra challenge shown by the diagram is that it is quite unclear as to exactly the region which is measured in this setup. This means it is possible that around the vertex, the current path might stray away from the anticipated measurement region, and other bars might be sampled to some minor extent, and play a role in the shape of the measured signal. This is something that needs to be considered when analysing the data.

One other possibility in this particular sample is that some of the contacts do not extend over the entire width of the wires when contacting to them, and in particular the yellow-labelled voltage-detecting contact on the horizontal wire extends little more than 50% across the wire width. What effect this has on the uniformity of the measurement across the bar is unclear – if the current is not evenly distributed across the width of the wire at the source then this might lead to the current distribution throughout the wire being more unpredictable than usual.

5.3.2 Measuring individual bars of the hexagonal single vertex

Using the described arrangements of magnetic contacts, all three of the magnetic bars were measured. A key point of interest in this research was to ascertain the viability of considering the hexagonal lattice to be equivalent to the summing of a large number of these individual single vertices.

5.3.3 Horizontal Bar of the single vertex

The first measurement taken was for the horizontal bar, which is parallel to the applied field. The two effects usually seen in different magneto-resistance measurements of these nanomagnetic samples, are a switching signal from the reversal of the magnetisation, and a high-field decrease in resistance, caused by the rotation of the magnetisation to align with the magnetic field.

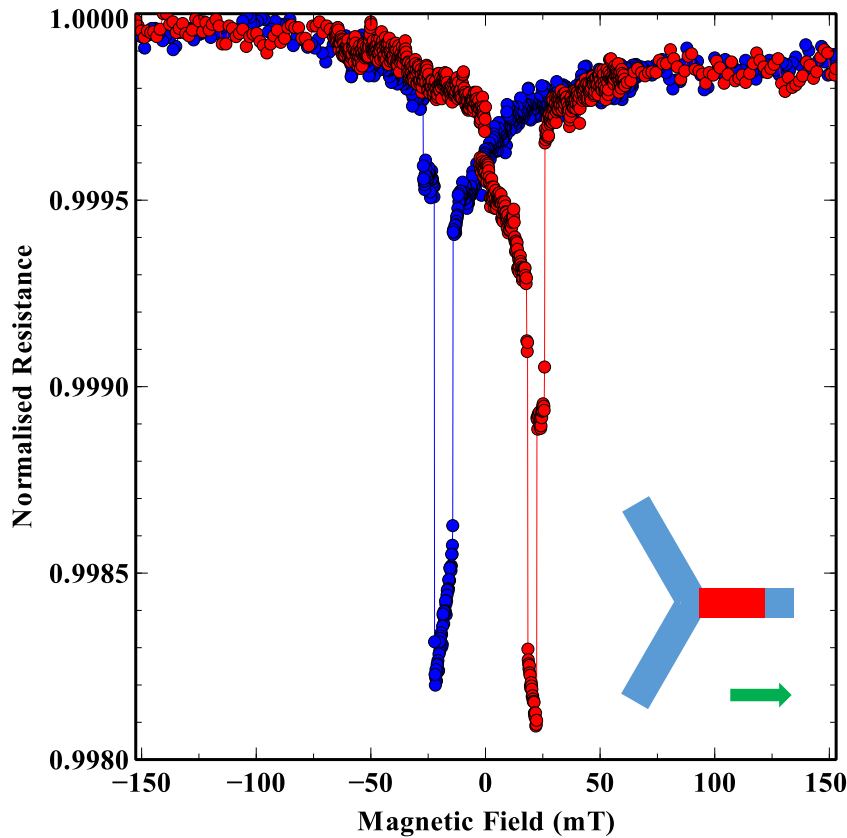


Figure 5.8: The AMR from the horizontal bar of a single magnetic vertex of a hexagonal lattice at room temperature, conducted on sample ASI47 – inset is a schematic showing the region (red) of the single vertex (blue) measured in this instance, with the green arrow representing the external field

A switching signal is a term which will be repeated throughout the analysis of the magneto-transport data, and it refers to the features on the graphs which correspond to the magnetisation being reversed by DWs within the nanowires, and on the figures, as seen in Figure 5.8 above, this can result in a discernible change in the resistance during the reversal event. This is what is referred to in this thesis as the switching signal. Using the AMR simulation derived from the OOMMF software, the associated experimental data could be evaluated properly. The simulation ran from a starting point of zero applied field and incrementally increased the field to saturation in one direction, so this will be compared with the red data upwards of zero field shown in Figure 5.8. Figure 5.9 shows the data from the simulation from 0mT, increasing to 50mT application.

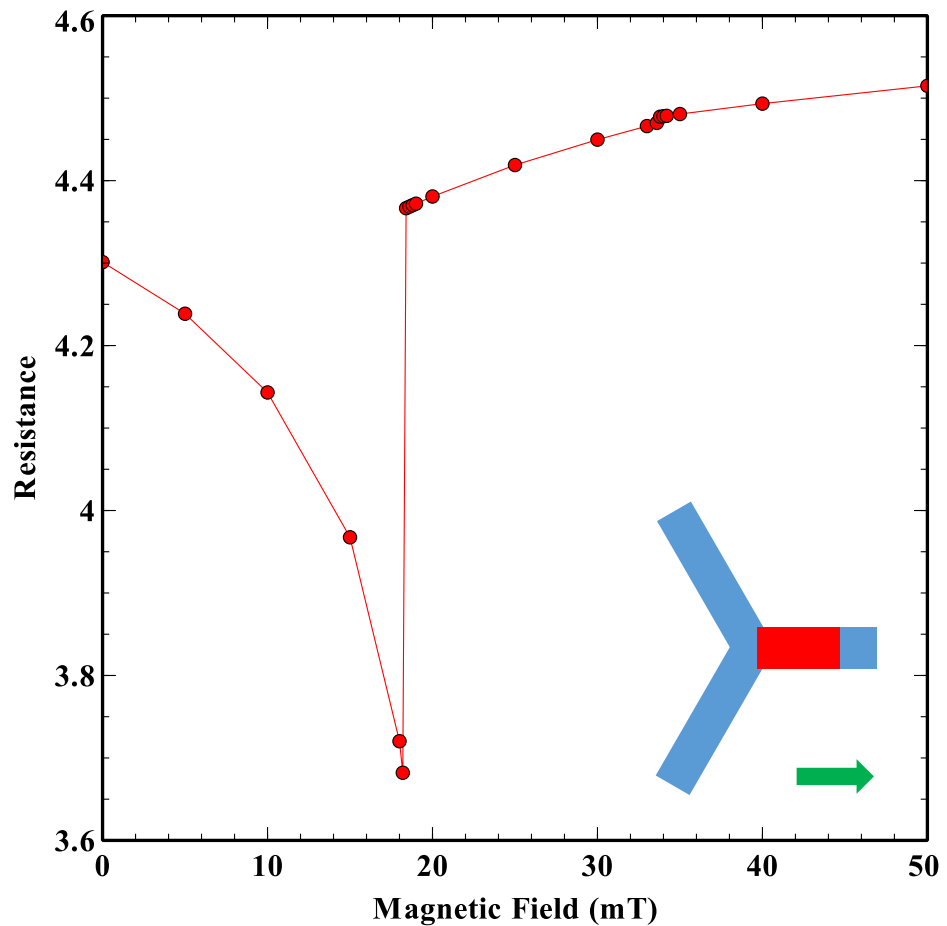


Figure 5.9: OOMMF Simulation of the AMR of the horizontal nanowire of the single vertex when external field is applied - inset is a schematic showing the region (red) of the single vertex (blue) measured in this instance, with the green arrow representing the external field

There is a difference between the shape of the simulated data and the respective data for the experimented sample. This can be explained by considering the amount of the bar which is being sampled, and also the specific region of that bar.

In the OOMMF simulation the calculation of the AMR takes place over the full length of the wire, whereas the experimental sample, due to the positioning of the contacts, sees the edge of the wire being exempt from the measurement. It is at this location that the DW is slowly being nucleated with increased field, and this is what results in the gradually increasing decline in the simulated resistance seen in Figure 5.9 at fields below 18mT. As this DW nucleation is not measured in the nanowire, the only measureable data comes when the nucleation is almost complete, corresponding to the sharp decrease seen in the resistance of the experimental data.

To assess the validity of this claim the data from the simulation was re-examined, in each case considering a smaller percentage of the overall nanowire length, by ignoring data from the end of the wire, as is the case in the experimental data of the single vertex:

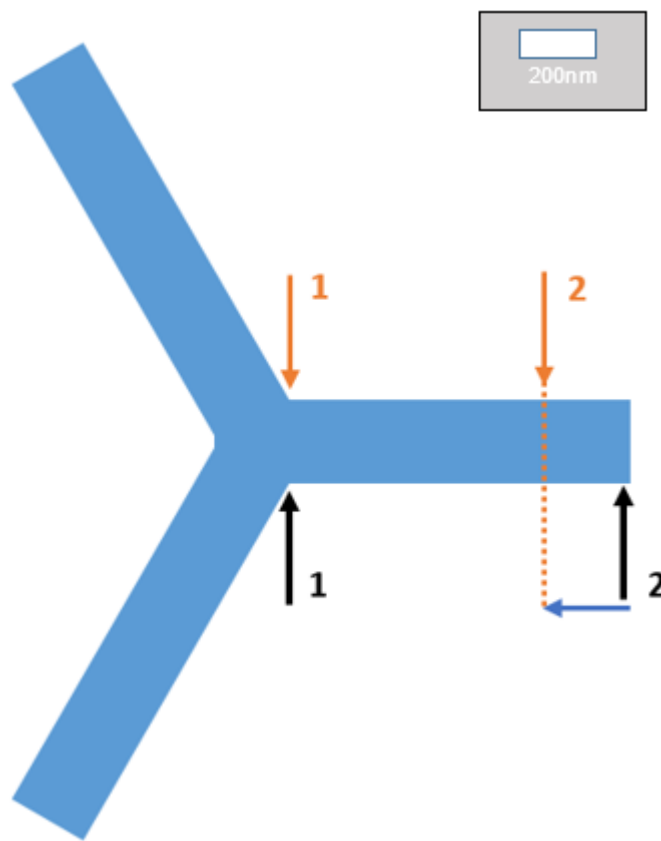


Figure 5.10: Schematic of how a smaller fraction of the horizontal bar of a single vertex is measured by the movement of one contact away from the end of the bar - the blue arrow shows the movement of the 2nd contact along the wire

As can be seen from the illustration, the end of the wire, where the DW nucleation takes place, is not included in the measurement. The further the second contact is moved along the wire, the more reduced the impact of the nucleation will have on the resistance measurement, to the point that ultimately it will not register on the measurement.

The simulation data was therefore analysed for when different fractions of the wire are included in the measurement. Below in Figure 5.11 is the AMR data when considering 100% of the wire, and also 78% and 53% of the wire. 53% is included due to it being similar to the fraction of the wire measured experimentally, taking the midpoint of the contact location as the basis for the approximation.

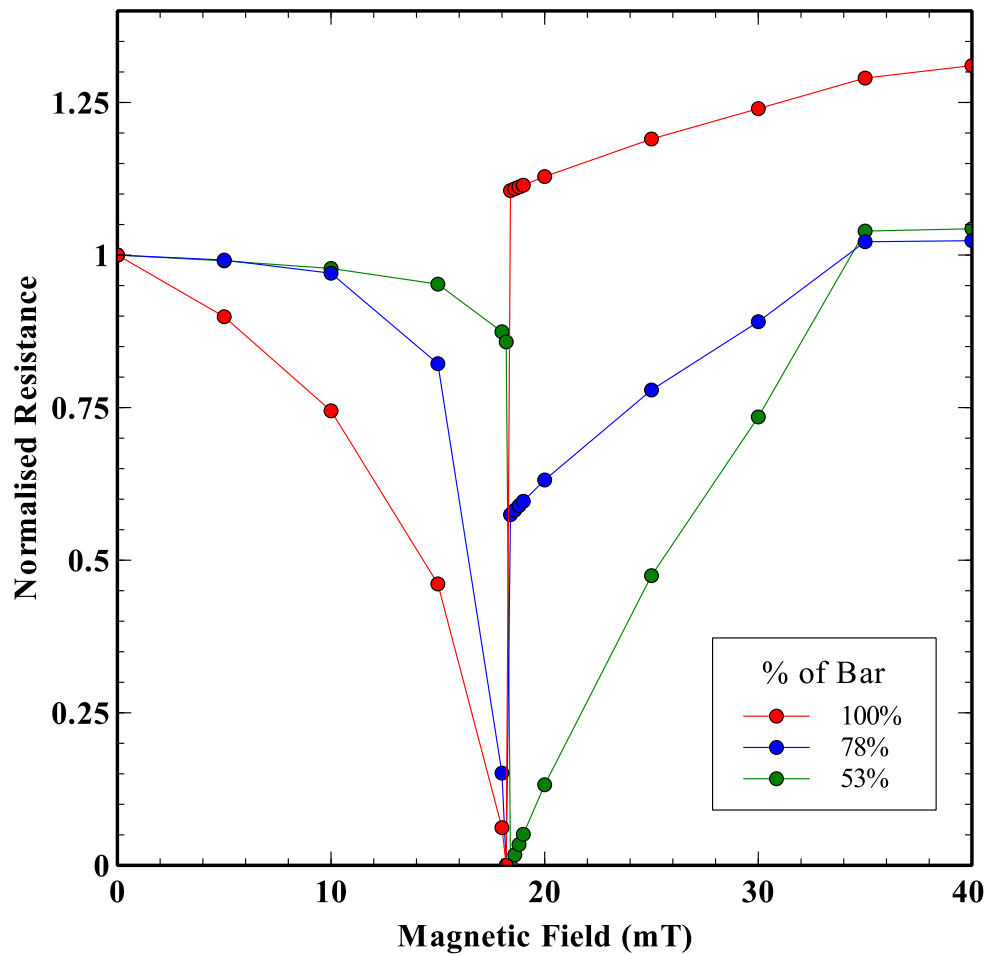


Figure 5.11: A comparison of the AMR data for a horizontal bar within the single vertex of hexagonal lattice ASI, as the percentage of the bar measured is varied

Noticeable from Figure 5.11 is the way in which the data is affected at fields below the 18.2mT coercive fields, where the magnetisation reversal is observed in the lattice. As the fraction of the wire measured is decreased, it requires a larger applied field for there to be an appreciable decrease in the resistance of the measurement. The nucleation of the DW has to have progressed further for this to become evident on the AMR data. This then results in the resistance decrease being sharper when the field is large enough for there to be a noticeable effect apparent on the measurement. This is a key outcome as it mirrors the situation in the experimental data where there is a sharp decrease in the single vertex data, not seen in the other lattices which see a more gradual decrease. It verifies that this sharp decrease, rather than being a feature of the single vertex, is a feature of the way in which the single vertex is measured.

Returning to the experimental data, there is evidence to suggest more than one magnetisation reversal process within the data, unexpected for a single magnetic bar such as here. There is a secondary switching signal appearing at a slightly higher field – 30mT compared to the 24mT of the larger signal – with a similar overall signal size of approximately 0.07% of the total resistance in both cases. This suggests that part of another of the three bars in the vertex is being inadvertently sampled.

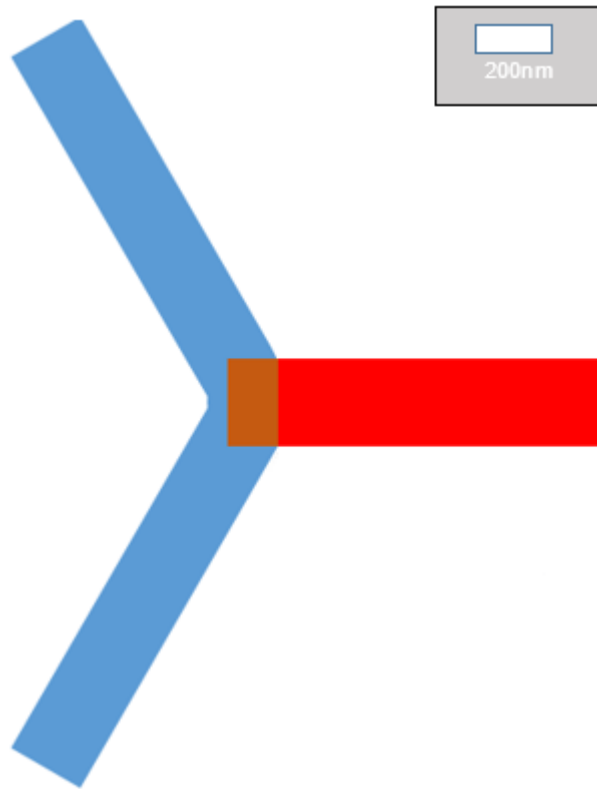


Figure 5.12: The single vertex, showing the increased size of the measured region - the red area represents the region of the initial measurement, with the brown area the region which has been added for the next calculation

This hypothesis can also be tested via further assessment of the simulation data for the single vertex. By sampling slightly more of the vertex to include small fractions of the other two bars, and not simply the horizontal one, which is the hypothesis that this is what is occurring to cause the secondary reversal data.

The brown region in the above vertex in Figure 5.12 shows the increased area included in the AMR measurement, to attempt to show the effect that sampling portions of the other bars of the vertex would have.

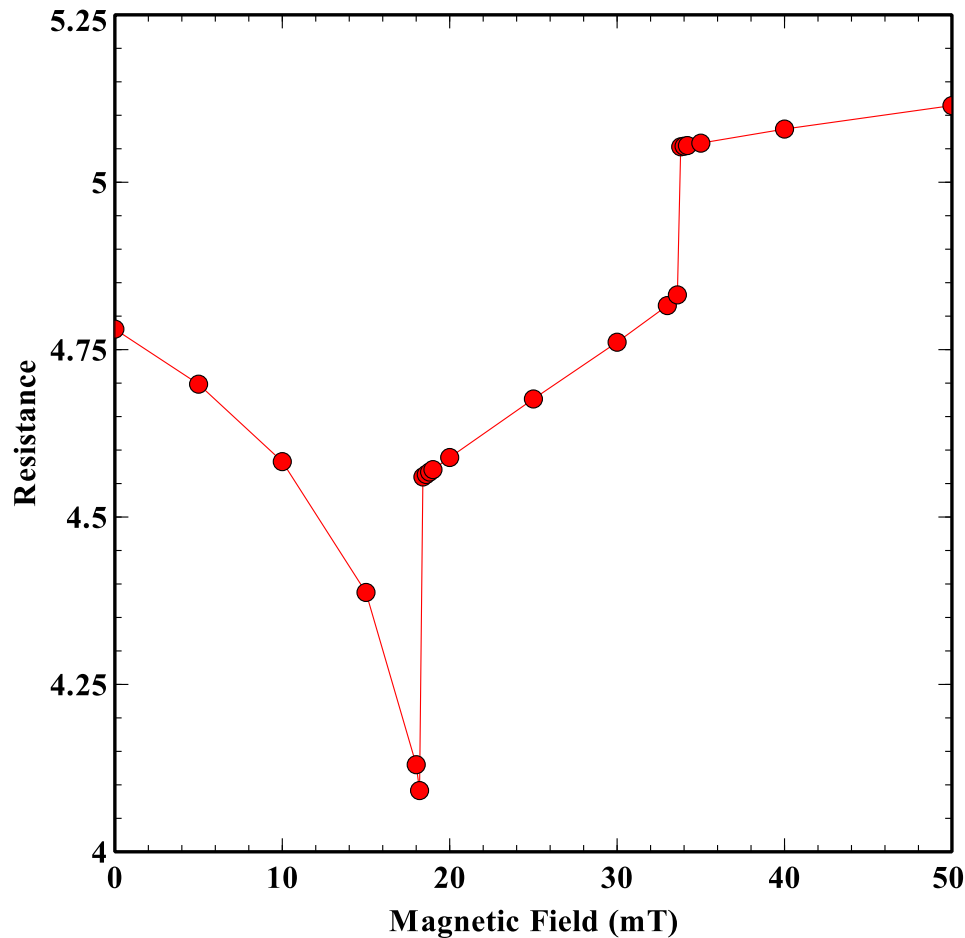


Figure 5.13: Simulating the single vertex where the larger shaded region of Figure 5.12 is measured for its magnetoresistance, with the measurement exceeding the length of just the parallel magnetic bar

The graph from this calculation of the simulation reveals the same magnetisation reversal at 18.2mT from the parallel bar, but also a second magnetisation reversal at 34.2mT. This does not follow the conventional shape from the reversal of the decrease in resistance from the DW nucleation, followed by the increase as the DW has nucleated and reverses the magnetisation along the bar. The reason for this is the small amount of the bar which is being sampled, and that this is far away from the area of the bar within which the DW will be nucleated. Between the two reversals, the trend is a gradual increase in the resistance, as the increasing of the field results in the magnetisation at the edges and corners of the parallel bar being pushed to lie increasingly parallel to the field, the bar's easy axis and, therefore, the current in the bar.

This, then, echoes the experimental data observed for the horizontal bar measurement – the only noticeable difference being the difference in the coercive field of the two

reversal events in each case. In the experimental data the coercive fields are much closer together than in the simulation – a situation which has repeatedly arisen when comparing experiment to simulation of these samples.

Returning to Figure 5.8, there is a flat resistance profile at higher fields, which means there is no evidence of a high-field AMR effect in the horizontal bar. The reason for this is that there is no rotation of the magnetisation in the wires when they are initially orientated parallel to the external magnetic field.

In all bars, the magnetisation at zero field will follow the easy axis of the bar of the hexagon, putting it parallel with the path of the current flowing through the lattice, and therefore this will contribute the maximum level of resistance possible, through the AMR relationship with the angle between the magnetisation and the current.

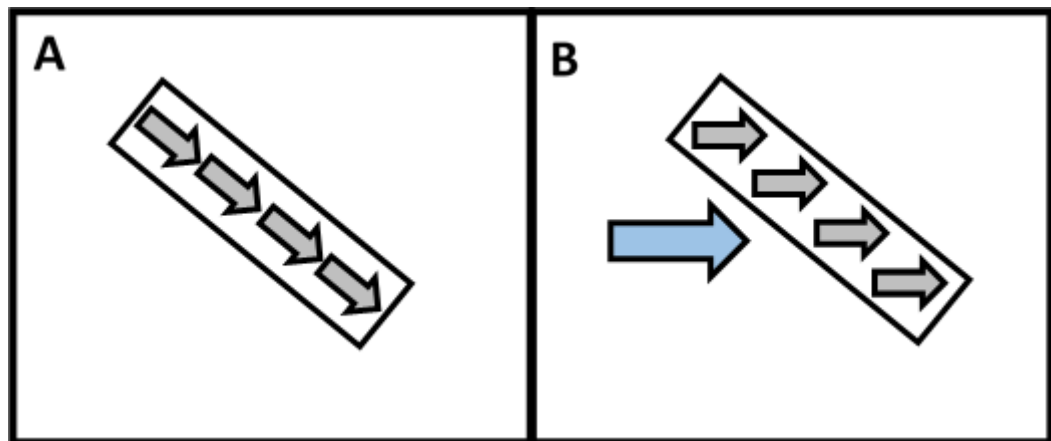


Figure 5.14: Schematic diagram depicting how the application of a sufficiently high external magnetic field (Blue arrow) causes the magnetic moments (Grey arrows) within a magnetic nanowire to divert away from the easy axis of the wire and tend towards parallel alignment with the field

When the field is increased, the individual magnetic moments in bars at a finite angle to the field will gradually favour to be orientated more in line with that field, and stray from the easy axis due to the shape of the nanomagnet. This will decrease the resistance as the current and magnetisation will no longer be parallel, as depicted in Figure 5.14.

Image A in Figure 5.14 shows the scenario of zero applied field, and image B would be the case at a particularly high externally applied field – in the case of measurements conducted during my thesis, the field required to cause this level of rotation in the magnetisation has been shown to be in excess of 0.3T. This is the maximum value measured, and up to this point, the saturation of the high-field AMR has yet to be

reached, so the applied field will have to exceed 0.3T to achieve the saturation of the magnetisation rotation. At field values between these two extremes, the magnetic moments will have rotated between the two orientations depicted in Figure 5.14.

This can be validated with a simple simulation using OOMMF.

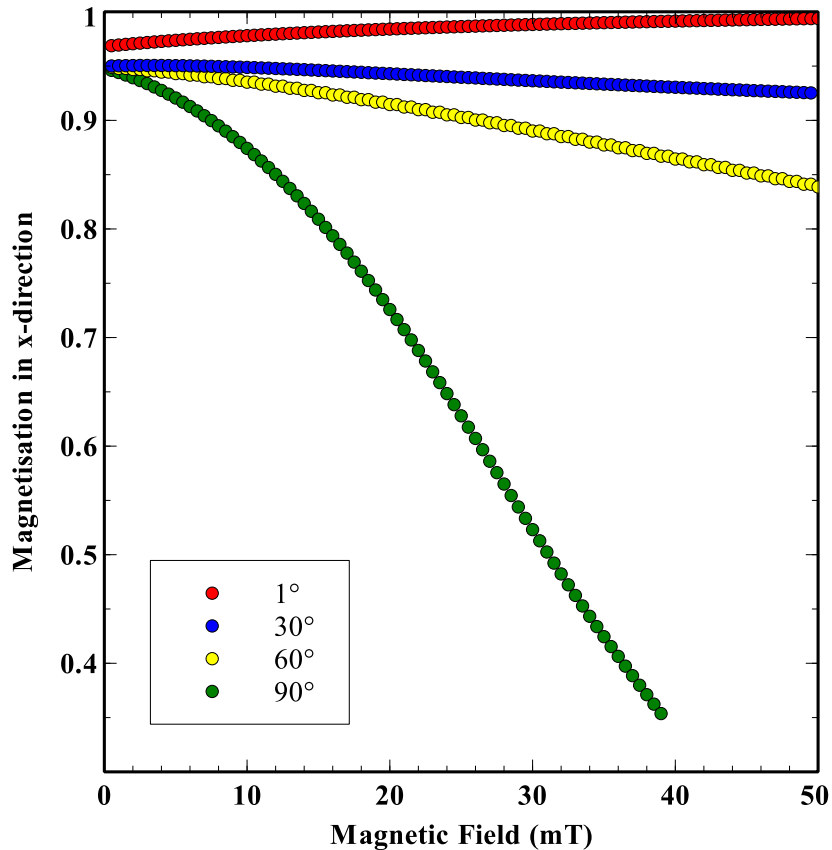


Figure 5.15: Graph showing a simulation of the magnetisation along the easy axis of a single ferromagnetic nanowire as the angle and intensity of the magnetic field is varied, evidencing the idea that the magnetisation is affected more strongly as the size of the angle between the easy axis and the magnetic field is increased

In the course of the study of the hexagonal lattice, the four angles that the bars will be orientated with respect to the field are: 0, 30, 60 and 90 degrees. Therefore these were the focus of the simulation, however to ensure the simulation gives expected results, I have simulated an angle of 1° as an approximate comparator to 0°. When simulations were completed using an angle of zero, the way in which the magnetisation was pre-defined caused it to relax into an unnatural state. This caused the results for a simulation at an angle of 0 to be unrealistic.

A single bar was simulated in OOMMF with the field at these four angles to the easy axis of the bar. In the case of the data shown here, there will not be a reversal in the magnetisation and associated feature present, as the simulation was carried out with the magnetisation already pointing to some extent in the same direction as the applied field.

By considering only the x-axis, and having the simulated nanowire's easy axis aligning with the x-axis, the way in which the magnetisation is changing in Figure 5.15 is the way in which the AMR will change in the physical systems. Returning to the simulation as a means of examining the AMR data in the single vertex, a key reflection is that, as can be seen, when the angle between field and easy axis is exactly or almost 0° , there is minimal change in the magnetisation as the field changes. This suggests that the physical data shown in Figure 5.8 is behaving as expected at high fields. This is encouraging, due to the fact that there was concern as to whether some of the other bars of the vertex might be unintentionally sampled. This would yield some amount of resistance decrease at higher fields. Therefore from this initial assessment of the measurement it appears that this unintentional measurement is minimal at most and potentially negligible.

In conflict with these findings however, is the presence, in the experimental data, of a secondary switching event observed at a higher field to the first. This suggests a small amount of one of the diagonal bars is being sampled in the magnetic measurement. The diagonal bar is at an angle of 60 degrees to the field and so the coercive field of the bar at that angle is increased in comparison to the parallel bar. Also only sampling a small fraction of that bar corresponds to the reduced signal size.

While the positioning of the contacts is such as to attempt to measure solely the single magnetic bar, this is not a guarantee when the vertex is connected as such. Were the single vertex such that the bars were unconnected, it is possible that the measured path would only include the single bar.

Figure 5.8 also shows a minor asymmetry in the data, both in terms of the AMR effect at high fields in the positive and negative field directions, and the size of the magnetisation reversal signal.

5.3.4 Measuring the top diagonal bar in hexagonal single vertex

Following the horizontal bar, the measurement was taken of one of the two diagonal bars, in this case the top diagonal bar. This was done by rotating each of the

measurement contacts to the corresponding one on the next nanowire, compared with those used in the horizontal bar measurement. The data accrued from this measurement is shown in Figure 5.16.

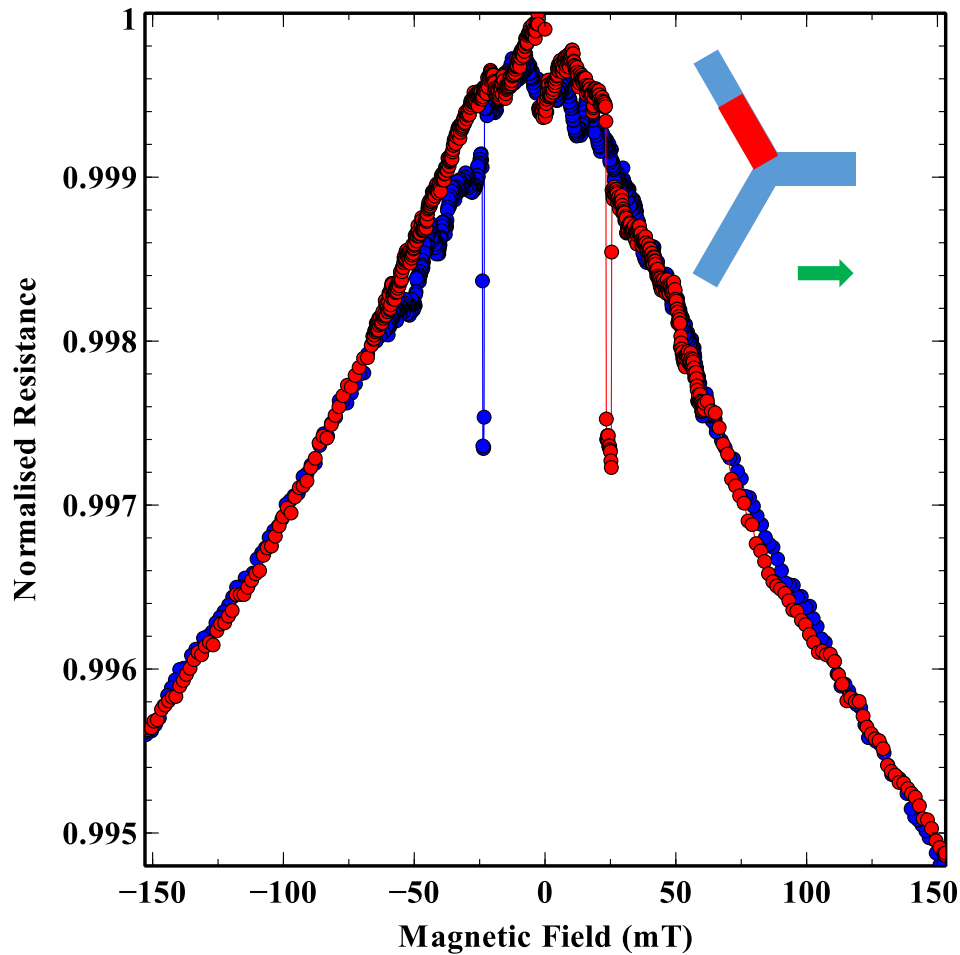


Figure 5.16: AMR of the top diagonal bar of a single magnetic vertex of a hexagonal lattice, conducted on sample ASI47 - inset is a schematic showing the region (red) of the single vertex (blue) measured in this instance, with the green arrow representing the external field

The difference between this measurement and the previous measurement for the horizontal bar is clear, as both main features of the data are transformed.

The high-field AMR is present, when it had been missing from the measurement of the horizontal bar. This is as had been expected as a result of the easy axis of the bar not being parallel to the external field, meaning the high field AMR is expected to have an effect. This therefore confirms that the single vertex behaves as would be expected of both a lattice and an individual nanowire.

Interesting in this data is that the signal for the magnetisation reversal appears to have occurred over a narrower field range in this instance for the top diagonal bar, with the decrease in resistance at 23.3mT and the following increase at 25.3mT, so occurring over a range of 2mT, compared with the 4mT range of the horizontal bar measurement. This is again caused by the amount of the bar that is actually being measured given the precise contact positions, and therefore how much of the DW nucleation is actually being observed in the measurement. This narrower field range implies that less of the bar was being sampled in this measurement compared with the horizontal bar, which is confirmed when analysing the SEM image of the single vertex sample.

There is also little evidence of the sampling of a second bar, like that which was observed for the horizontal bar data. This highlights the challenge of measuring the single vertex reliably and evenly for the different magnetic bars, as the horizontal bar measurement has been affected slightly by sampling the extra magnetic region, while in this measurement it is not the case.

Again, like the horizontal bar, there also appears to be an asymmetry to this measurement, in both the high-field AMR effect and the magnetisation reversal. The differences appear to be more pronounced in this graph than for the horizontal though. When considering the change in resistance from zero field to at $\pm 150\text{mT}$, the high-field AMR causes an overall resistance drop of 0.40% in the negative field direction, and a 0.45% resistance decrease in the positive field direction. The switching signals also vary in both their magnitude and the field range over which the effects occur.

5.4. A magnetotransport study of the connected hexagonal lattice

Following on from the initial investigation into the single vertex of the hexagonal lattice, the next part of the study focussed on a full ASI lattice of connected hexagons. This represents preliminary investigations, which were carried out in order to ensure that the techniques necessary for my central investigations were able to produce results in agreement with data already published for similar samples [14], [15]. It was therefore important that this preliminary investigation is completed over a sample geometry which has been investigated thoroughly previously, so that a reliable comparison is available and in order to ensure reliable and valid results.

The connected lattice was investigated for two main reasons, and with two main goals. The first of these was to have an appreciation of the magnetotransport data that could be obtained from the basic lattice. This way, further investigations into more innovative forms of the lattice would have a reasonable comparator created and measured under the same conditions and in the same manner.

The second intention, and the first to be discussed here, was to establish the origins of the low-temperature asymmetry shown previously to appear in the Hall geometry AMR data [14], [15]. Through the introduction of a capping layer atop the magnetic layer within a ferromagnetic lattice, the investigation looked to reproduce this effect. The capping eliminated the possibility that the exposure of the ferromagnetic layer to the air would cause an antiferromagnetic oxide, and jeopardise the quality of the results due to an exchange bias effect. A series of hexagonal lattices of connected bars was created for this investigation, of sample geometry as defined in Section 5.1. The geometry chosen compares very closely with that of the related research. [15]

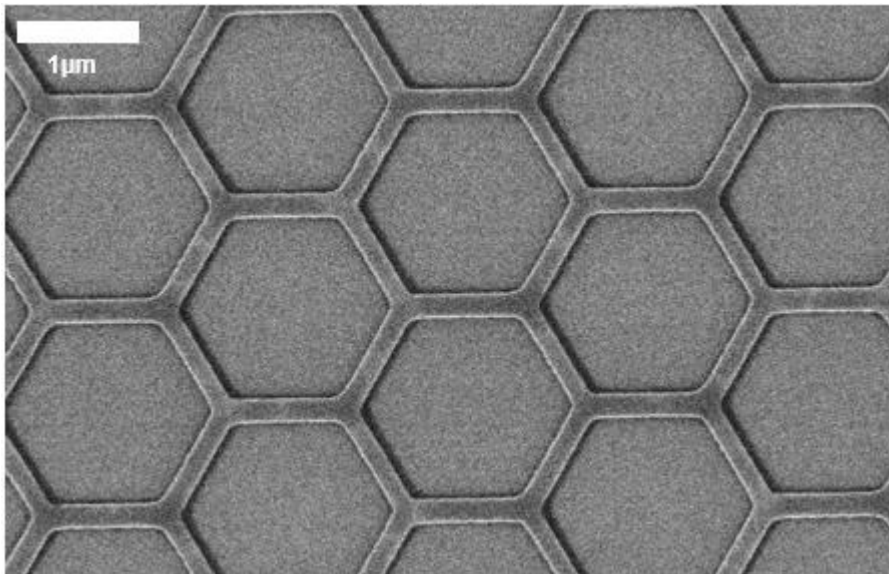


Figure 5.17: SEM image of lattice on sample ASI13 for experiment into effect of capping samples on low-temperature AMR – the hexagonal bars are composed of Permalloy, and in the case of this experiment are capped with a thin layer of Aluminium

Figure 5.17 shows a region of the array of hexagons, created using the processes outlined in Section 4.1. The honeycomb structure is the magnetic layer deposited atop the Silicon Oxide coated Silicon substrate, and the material chosen for the magnetic layer was Permalloy.

The experiment involved the deposition of a second, non-magnetic, non-conducting material atop the magnetic layer, immediately following the magnetic deposition and prior to the opening of the vacuum chamber. This would prevent the Permalloy gaining an antiferromagnetic oxide layer, which has the potential to alter the form of the magnetisation reversal in these measurements, as well as the field magnitudes at which they occur. The material chosen for this was Aluminium, as this layer on the top of the sample will form Aluminium Oxide when exposed to the oxygen present in the atmosphere, which should not affect the behaviour of the ferromagnetic layer underneath.

5.4.1 Studying the effect had by capping the connected lattice

For each set of measurements into the assessment of the low-temperature behaviour of these ASI structures, two samples were created, each with a relatively thick deposited layer of Permalloy of 30nm. The phase boundary for DW types based on structure geometry [28] was used to ensure that the samples would clearly contain only vortex domain walls. Of each pair of samples, one was also coated in a 2nm thin-layer of Aluminium following the Permalloy deposition.

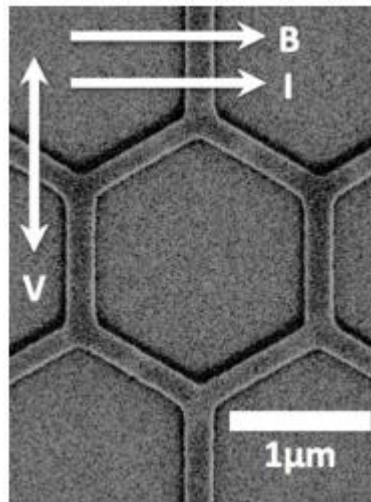


Figure 5.18: Annotated SEM image of hexagonal lattice from sample ASI13, showing the electrical measurements taken relative to the sample orientation – this measurement configuration was completed for both the capped and uncapped samples

The samples were subject to AMR measurements within a cryostat, with the measurement being repeated at temperatures between room temperature and 3 kelvin.

Figure 5.18 shows the measurements taking place perpendicular to the easy axis of the hexagonal lattice, and with the field, current and voltage in a Planar Hall geometry, whereby the voltage detected is perpendicular to the direction of flow of the current and the applied field direction. The Planar Hall geometry was chosen due to the asymmetric nature of the measurement, as this would present the opportunity to witness any asymmetry from either the low-temperature effects or exchange bias seen previously in the uncapped sample [14], [15]. The conventional longitudinal measurement is a symmetric measurement and therefore it would not be expected to reveal any asymmetry within its data.

5.4.2 Measuring the effect of capping hexagonal lattice ASI

The uncapped Permalloy lattice was measured first, and immediately the asymmetry at low temperatures seen in the previous literature [15] was present again.

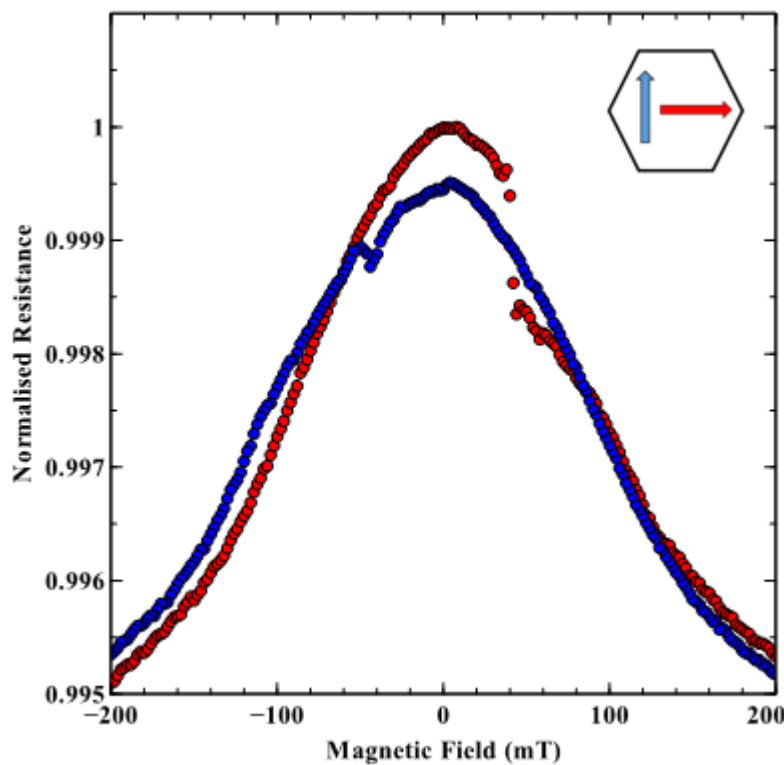


Figure 5.19: The AMR in the Planar Hall geometry of an uncapped Permalloy lattice from sample ASI7 at 3K – the inset panel showing how the current (red) and the applied magnetic field (blue) are orientated in relation to the hexagons of the lattice

A study was completed of the lattice at different temperatures, starting with the sample cooled down to 3 kelvin.

Figure 5.19 shows the normalised resistance at 3 kelvin, with the blue line indicating the decreasing field sweep, and the red line the increasing field sweep. What is immediately apparent is that both main features of the graph (the switching event and the high-field AMR) differ significantly in either field direction. The high-field AMR's presence is in agreement with the single vertex measurements shown previously.

What is clear though, is that with no applied field, the magnetic moments should be aligned with the easy axis of the bars. This would ensure that the resistance of the sample at zero field should be identical in both field sweep directions. However, as can be seen, this is not the case. In fact, the negative field sweep direction yields a resistance 0.05% smaller than the data for the positive field. This does not conform to what is expected of these systems with no applied field, and immediately implies an asymmetric behaviour.

Secondly, the switching of the magnetisation of the bars of the hexagons is exhibited on the graphs in a very different fashion for both sweeps. In the negative field sweep, there is a clear dip in the resistance where it drops dramatically as the magnetisation briefly sits perpendicular to the current and so the resistance drops, before, at -44mT applied field, the magnetisation reversal is completed by the propagation of nucleated DWs through the network. This means that the current and the magnetisation now sit anti-parallel which, as when they are parallel, results in peak resistance.

In the positive field sweep, however, the initial drop in resistance, at +42mT, is far greater in size -0.01% of the total resistance, compared with 0.002% in the negative direction - before the return to the standard AMR curve actually features a further drop in resistance, due to the combination of the two resistance contributors (rapid reversal and the pulling of the moments away from the easy axis) sums to still force a resistance drop. This appears to be a further sign of the asymmetry, as present in the previous work. [15]

Importantly, as also stated in said earlier work, the asymmetry observed appears to be exclusively a low-temperature effect, as measurements from 25K and above exhibit much more symmetric data for the same sample. This is endorsed, in

Figure 5.20, taken at 25K, in which both of the asymmetric features discussed for 3K have become symmetric.

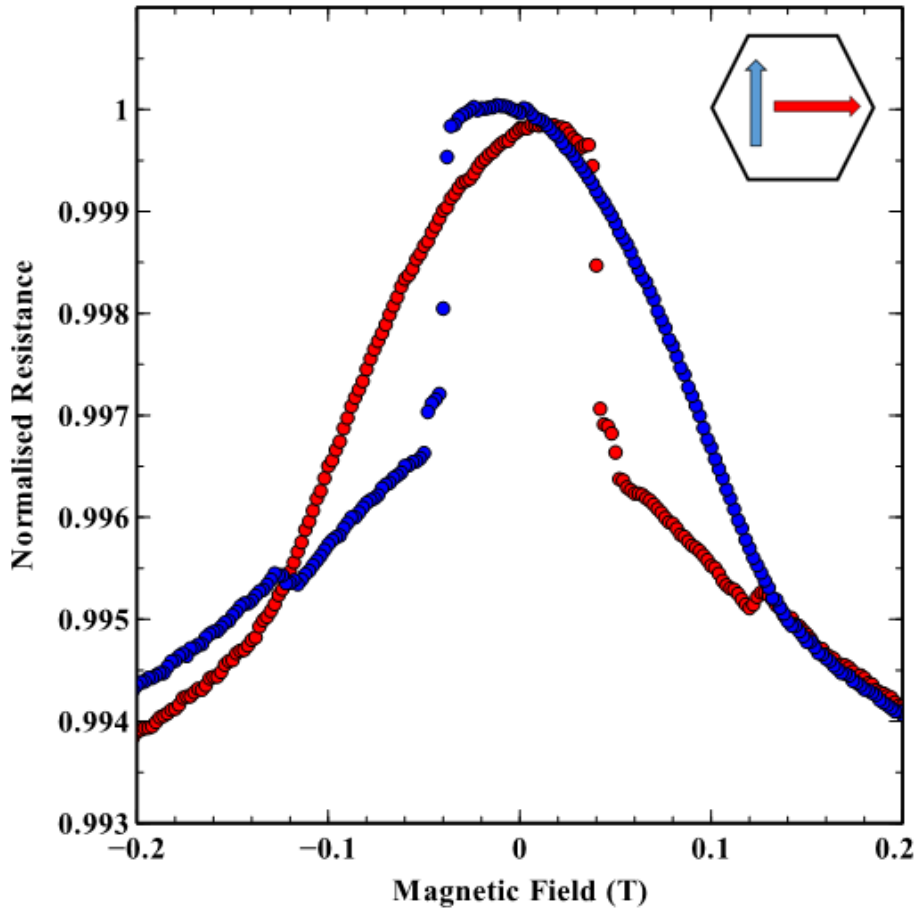


Figure 5.20: The AMR of sample ASI7, an uncapped Permalloy lattice of hexagonal ASI, at 25K - the inset panel showing how the current (red) and the applied magnetic field (blue) are orientated in relation to the hexagons of the lattice

Figure 5.20 are nearly mirror images of each other in the line $x = 0$, and certainly the general shape of both traces is the same, with the rapid decrease in resistance seen in both field application directions appearing at $\pm 38\text{mT}$. It can be seen fractionally in the data at fields lower in magnitude than this, that there is a minor asymmetry in terms of the absolute values, with the negative field data having a slightly larger resistance. However, the shape is the same in both directions, which cannot be said of the previous data at 3K, where not only were the values different but the general shape of the data in both field directions was markedly different.

This suggests that, at least down to as low as 25 kelvin, there is symmetry in the manner in which the sample behaves. That symmetry is lost, however, at temperatures below this, culminating in the high level of asymmetry displayed in the measurement obtained at 10 kelvin. Further measurements are required to ascertain the exact temperature of the beginnings of asymmetry.

The progression of the size of the asymmetry can be considered as a function of temperature. This was completed by looking at the differences in the two resistance values at zero field for different temperatures. As the difference in the resistance should be zero, any variation from this can be considered a measure of the asymmetry.

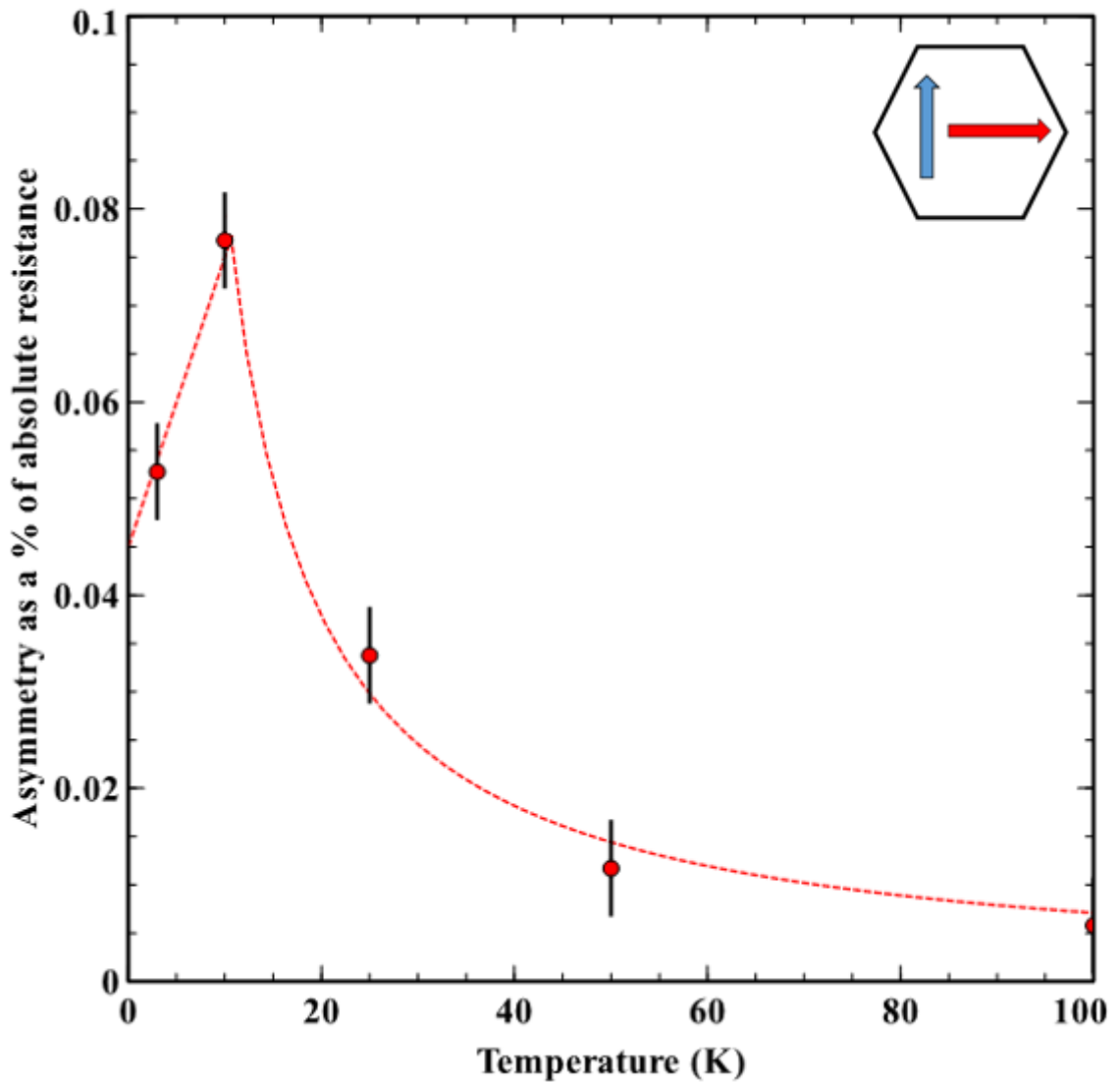


Figure 5.21: Describing how the asymmetry in the AMR data for the uncapped connected lattice in sample ASI7 is varied as a function of the temperature of the sample – the red dotted line is simply a guide for the eye and does not have physical meaning, and the inset panel shows how the current (red) and the applied magnetic field (blue) are orientated in relation to the hexagons of the lattice

It can be seen that the asymmetry is significantly greater in the measurements at low temperatures, and the measurements at 50 and 100 kelvin have asymmetries of less than 10% the size of the asymmetries at the lower temperatures.

So this definitely serves to confirm the low-temperature effect as witnessed before, albeit possibly the exact temperature below which the effect occurs has been defined more precisely. This also meant that the focus of interest could remain on the low temperature effects, and to this end the next investigation uses the sample which has an aluminium cap, to discern whether these low temperature asymmetries remain, or if they are in fact a manifestation of exchange bias.

The measurements at temperatures of 25 kelvin and higher were unsurprisingly very symmetrical, as this had been the case previously in all instances of the capped and uncapped samples. This meant therefore that the focus moved swiftly to the low temperature measurements.

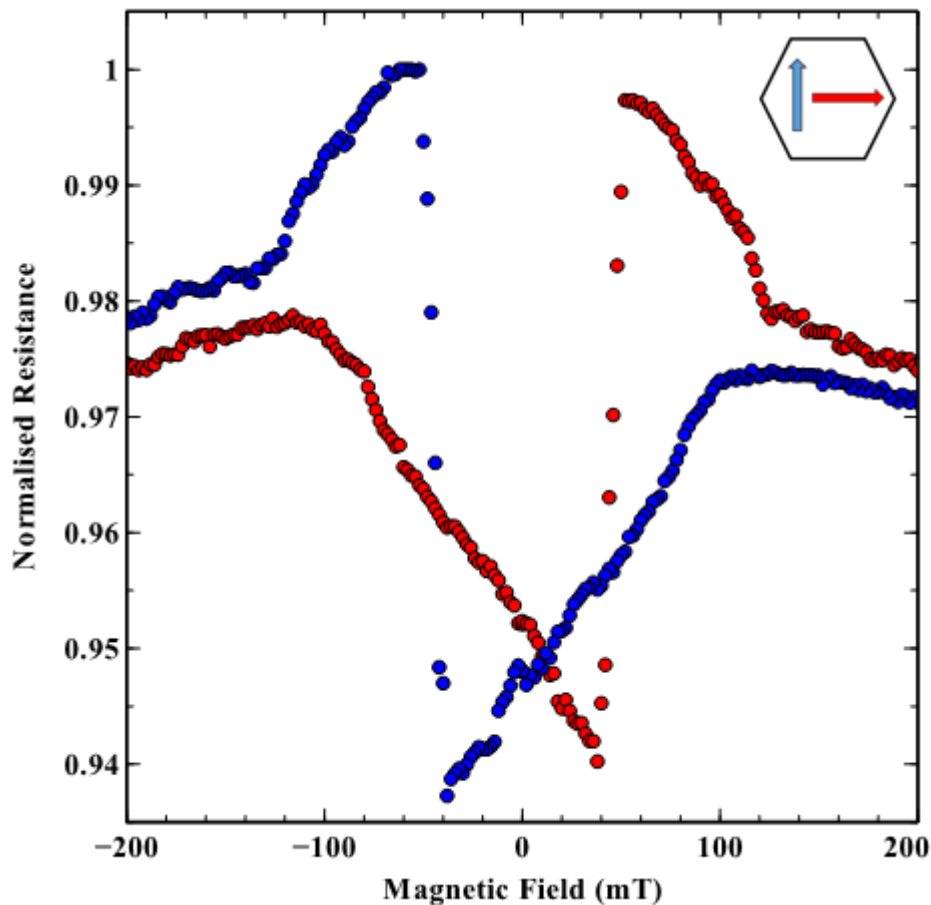


Figure 5.22: The AMR of a Permalloy lattice of ASI with Aluminium Cap at 3K – sample ASI13, with a Permalloy thickness of 31nm – the inset panel showing how the current (red) and the applied magnetic field (blue) are orientated in relation to the hexagons of the lattice

The signal here is unusual by comparison with those seen previously, but similar studies including *Le et al*'s have obtained a similar signal for these measurements, with

the resistance seeing both an increase and a decrease, in effect an oscillation before relaxing at higher fields. [14]

Figure 5.22 contains the set of data for the capped sample at 3K, the lowest temperature measured during the investigation. This is a strong candidate for evidence of the same asymmetry seen in the uncapped sample. This however is far less prominent in Figure 5.22, with the basic progression of the resistance in both field directions appearing to be near identical, with minor differences in the heights of the peaks and features, but not on the scale of those seen with the uncapped sample. In the blue data, the large increase in resistance is 6.25% of the size of the maximum resistance, whereas in the red data it is 5.75%.

This lack of asymmetry can be attributed to the presence of the aluminium cap, which has prevented an oxide layer from forming on the Permalloy magnetic channel. The attribution of this as the reason for the lack of asymmetry in the capped sample, and the ways in which this leads to the conclusion of exchange bias being the basis for the asymmetry seen otherwise, is discussed and evidenced in the paper by Le *et al.* in 2015 [14]. The findings seen in the experimental data in that paper are in agreement with that observed in this study. This is with the same ferromagnetic material, Permalloy, being used, and also similar sample geometries and characteristics. The data produced in these two studies for the asymmetric AMR is very similar – the findings of Le *et al.* show the appearance of this asymmetry at below 20K.

Applying external magnetic fields across the sample during the cooling process results in a changing of the polarity of the asymmetric features in the data, as depending on the direction of the field. This effect shows similarities with the effect seen on hysteresis loops of thin films, where the loop is shifted due to the antiferromagnetic oxide, and the direction of the shift results from the direction of the field applied during cooling. All of which points to the conclusion that previous asymmetries were indeed merely a manifestation of exchange bias in the magnetic channel.

The cap on the sample has not removed all asymmetry, however, as seen in the minor peak differences in Figure 5.22. This could be attributed to the fact that the Aluminium cap only covers the top of the magnetic channel and not the side-edges, as a result of the thermal deposition process. So this leaves the sides exposed and a small oxide layer can still be produced, hence the small amount of asymmetry remaining on the results. In reality, the width of the wire is approximately 150nm, and the thickness is 30nm, so approximately 60% of the sample surface is no longer exposed to the air.

A subsequent publication by *Zeissler et al* [98] proposed that low temperature observations of asymmetry can be as a result of both exchange bias and the emergence of a new correlated reversal of adjacent nanowires within the lattice. At RT the magnetisation reversal for a connected lattice sees a single DW propagate along a lengthy path through numerous vertices, causing the reversal of the wires in this path, described as a chain of vertices. [98]

There is evidence, obtained through Magnetic Force Microscopy (MFM) that the DW behaviour at vertices changes as the temperature drops below 50K. Here when a first bar of the vertex is reversed, instead of consequently reversing one of the two exit wires, determined by the chirality of the DW, there will be a correlated reversal of the magnetisation in both of the diagonal bars, termed a “branching-like reversal”. [98]

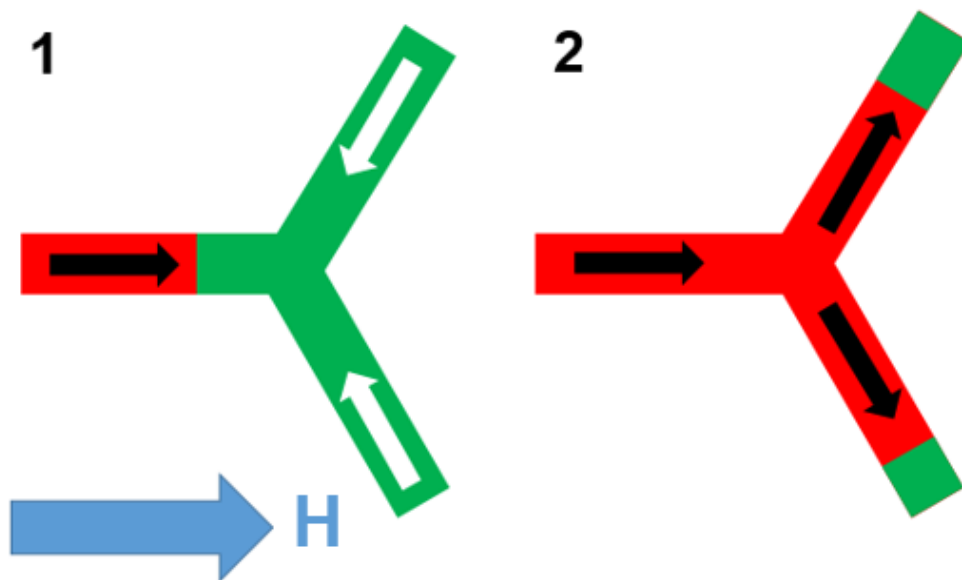


Figure 5.23: Demonstrating the observed magnetisation reversal in a connected vertex for temperatures under 50K by *Zeissler et al*. The large blue arrow denotes the applied field direction for both images. The black and white arrows represent the magnetisation direction within the nanowires and the red and green regions are domains

This is displayed in Figure 5.23, where the wire which is parallel to the applied field is having its magnetisation reversed in Image 1. This causes the subsequent reversal of both of the diagonal wires across the vertex in Image 2. The number of vertices involved in the usual chains of magnetisation reversal is in excess of 60% at RT but as the temperature decreases, this number decreases significantly, down to a mere 4% at 30K and cooler.

The onset of this effect occurs at a different temperature to that caused by the exchange bias, and so both can be identified. As shown by the data measured in this thesis, the onset of the exchange bias caused by the antiferromagnetic oxide in the uncapped samples happens at temperatures below 25K. Meanwhile the change in the magnetisation reversal behaviour is observed as high as 50K, suggesting this is independent of any effect caused by an antiferromagnetic oxide.

5.4.3 Comparing Connected Lattice at RT for different measured orientations

The hexagonal connected lattice has been studied using magnetotransport before [15], [48], however it is still a useful series of measurements to evaluate once again. They will also be valuable for comparison with further measurements in subsequent studies in this thesis. This lattice was measured in all four different orientations, in the AMR geometry.

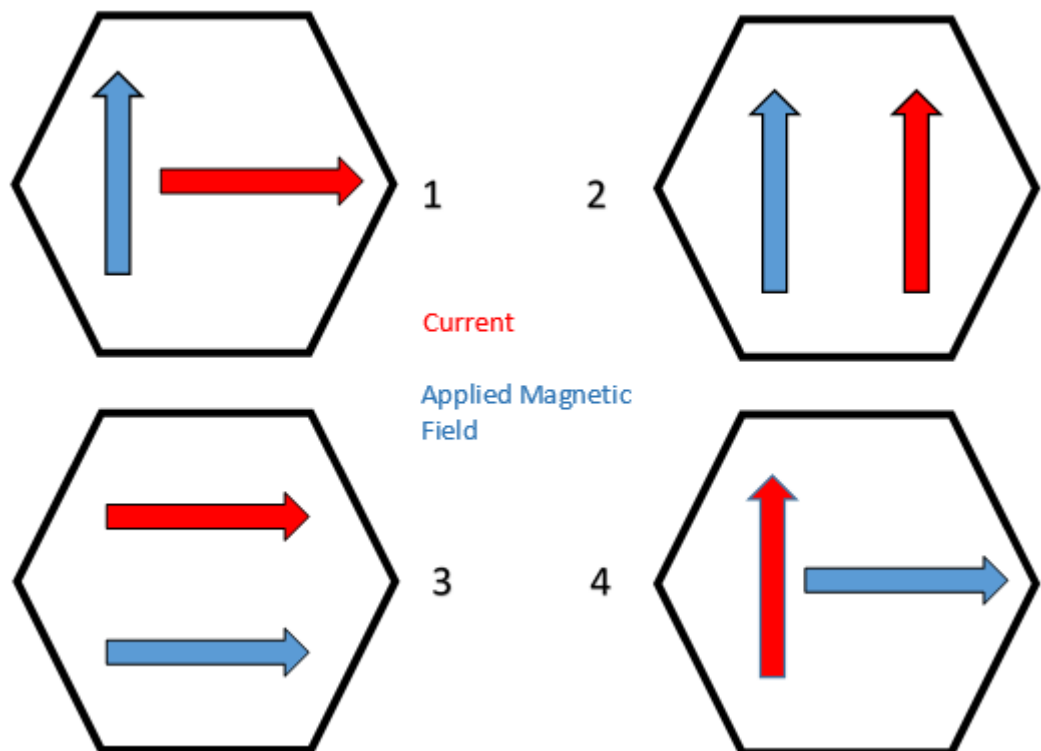


Figure 5.24: Schematic of the four measurement orientations used while performing magneto-transport measurements on hexagonal lattice-based ASI – the hexagons represent the orientation of the hexagons in the lattice with respect to the other quantities

All reveal similar properties of high-field AMR and a small switching signal. The expectation was that the switching signal would be relatively small as the switching is governed by the propagation of DWs through the lattice. The propagation of a single DW would result in the switching of a chain of magnetic wires through the lattice.

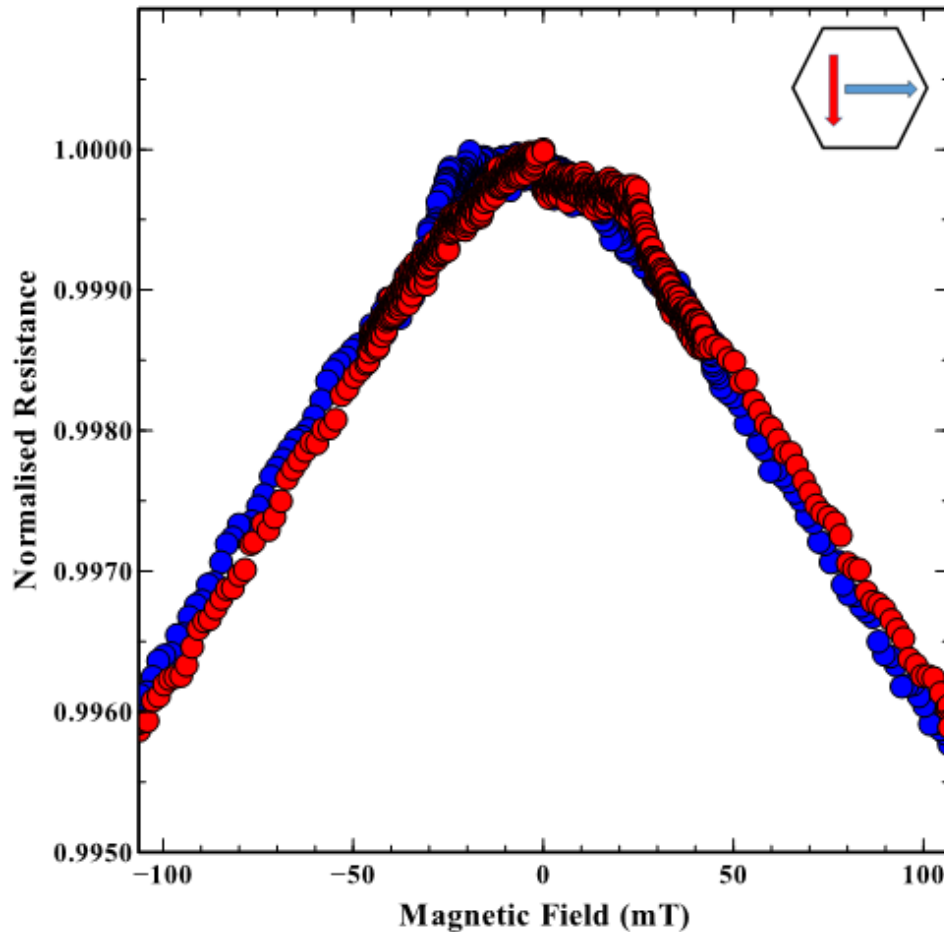


Figure 5.25: The AMR measurement in Orientation 4 for a connected hexagonal ASI lattice, sample ASI46 - the inset panel showing how the current (red) and the applied magnetic field (blue) are orientated in relation to the hexagons of the lattice

The feature at low fields in both directions atop of the background AMR effect is unusual in that the resistance is greater than simply the background AMR at these field values. This feature is brought about by the fact that the current and the applied magnetic field are perpendicular to one another. It has also been seen in a publication by *Tanaka et al* [48], featuring the first magnetotransport measurements of an ASI, where the feature develops up to a maximum when the angle between the two variables is 90° . At an angle of 0° between the two, there is no increase in resistance

above the background AMR and only present is the dip in resistance associated with the magnetisation reversal. Gradually this varies as the angle is increased, up to at 90° where there is no dip below the line observed at all, merely the rise above the background AMR at low fields, before a sharper decrease in resistance back to the background AMR. Figure 5.26 shows a range of graphs from *Tanaka et al's* publication, with the manner in which the AMR is affected by this angle between the current in the sample and the applied magnetic field.

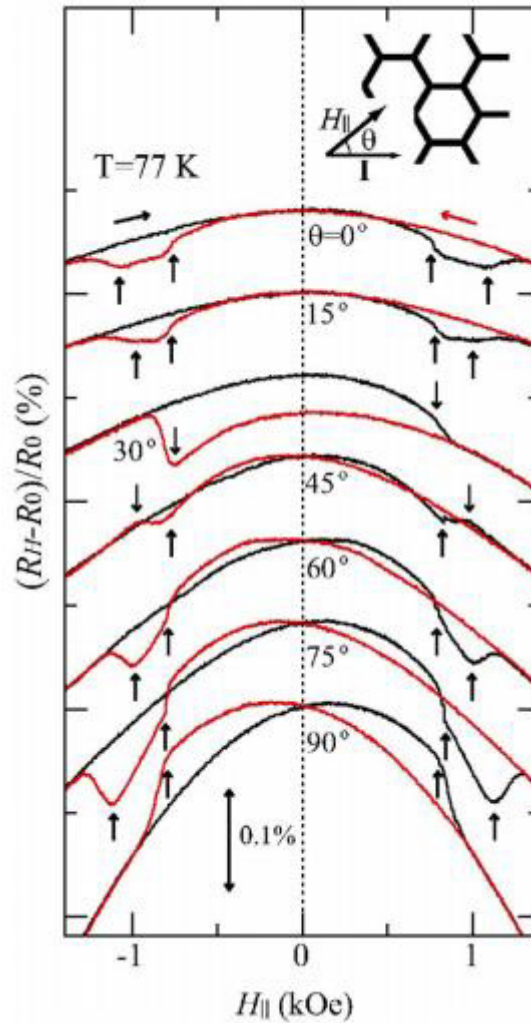


Figure 5.26: *Tanaka et al's* graph showing the AMR of a hexagonal lattice and its dependence on the angle between the measured current and magnetic field applied across the sample

The data obtained by Tanaka shows that the angle between magnetic field and current has a large effect on the extent to which the resistance decreases at higher fields. The high-field AMR in both my data, and Tanaka's data when the field is 90° from the current, is very large in comparison to the field effect of the switching of the bars – the switching effect, seen at $\pm 30\text{mT}$, is barely perceptible on the graph with a percentage

decrease in the resistance of about 0.05%. This is due to the relatively low change in resistance brought about by the DW propagation through the lattice which causes the magnetisation reversal of the bars. By contrast the high-field AMR effect at 100mT is of the order of a 0.4% decrease in the resistance, so the difference is approximately eightfold, although this ratio of 1:8 is relatively meaningless due to the arbitrary choice of $\pm 100\text{mT}$ for the endpoints of the x-axis.

Orientation 3, by contrast, features a much smaller change in resistance at high-fields, with a decrease in normalised resistance of 0.01% contrasting to the same field in Orientation 4 causing a drop in normalised resistance of 0.04%, shown in Figure 5.27.

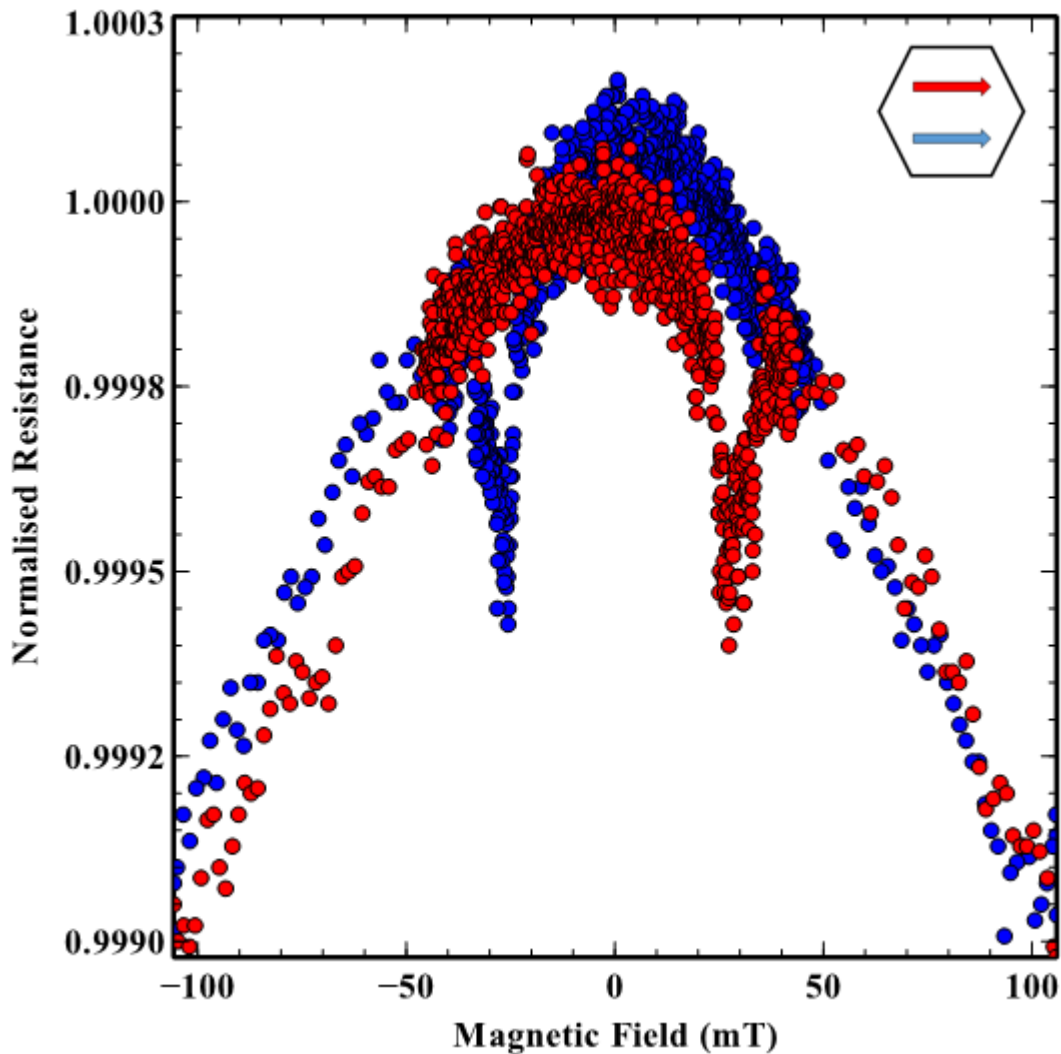


Figure 5.27: The AMR measurement in Orientation 3 for a connected hexagonal ASI lattice, sample ASI46 - the inset panel showing how the current (red) and the applied magnetic field (blue) are orientated in relation to the hexagons of the lattice

In terms of the consideration of what is being measured in each Orientation, Orientation 3 features a mixture of all of the magnetic bars, whereas Orientation 4 consists of mostly diagonal bars. This means that the vast majority of Orientation 4 is on bars which can be subject to the rotation of the magnetisation away from the easy axis, the basis of the high-field AMR, so this leads to the fourfold larger effect in Orientation 4 than 3. This dramatic difference in effect is consistent with the findings of the angular dependence measurements completed by *Tanaka* [48], which show the measurement where the current and the magnetic field are parallel has a noticeable resistance dip caused by the reversal of the magnetisation.

This difference in the two Orientations is similarly apparent in the following data concerning Orientations 1 & 2, with Orientation 1's measurement path ensuring a much larger effect on the AMR from the rotation of the magnetisation in the bars not parallel to the field than seen in Orientation 2.

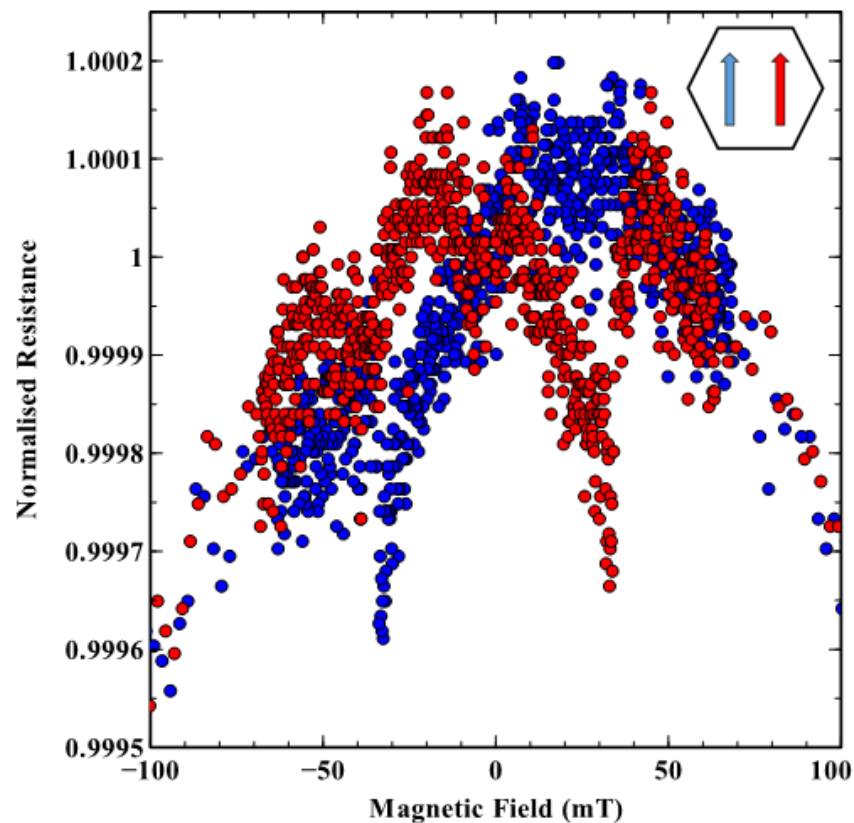


Figure 5.28: The AMR measurement in Orientation 2 for a connected hexagonal ASI lattice, sample ASI46 - the inset panel showing how the current (red) and the applied magnetic field (blue) are orientated in relation to the hexagons of the lattice

Figure 5.28, showing the data for the measurement of Orientation 2, shows another relatively small switching signal in terms of its absolute magnitude, however one that appears significantly larger when set against the high-field AMR than can be seen in Orientation 4. There appears to be a slight amount of asymmetry in this measurement, albeit the general manner in which the magnetisation is changing in both field directions is very similar – it is the sizes of some effects which vary, not the basic nature of their resistance changes.

5.5. Conclusions

This chapter begins the discussion of the results obtained during this study, and therefore deals with the more simple structures investigated during this thesis, in a way as to lay the foundations for the results in the coming chapters, which feature work completed on samples which are less well characterised and understood than those in this chapter. The hexagonal lattice is a common form of ASI and has formed the basis for this first results chapter, both as a complete lattice of hundreds of vertices, and also in the form of a single instance of a vertex from this lattice.

The magneto transport measurements completed in this chapter have presented key information regarding the manner in which a lattice can be considered to approximately be a sum of the individual vertices, or whether the interactions between these vertices make that view over-simplistic. It was discovered that while there are clear similarities between the single vertex AMR and that of the larger lattice, there are distinct differences, most notably the range of magnetic fields over which the switching signal is present. In the larger lattice the switching signal is over a wider magnetic field range, implying a variation in the switching of the different bars, instead of each bar of the same orientation switching at the same field.

The absolute resistance of the two samples is interesting, as the resistance of the lattice measurement is only a quarter that of the single vertex. With the summation of resistances in different configurations, this result shows how the current path in the lattice spreads out across multiple channels, and with the sum of parallel resistors being the sum of the inverse resistance, this corresponds to a lower resistance overall in the lattice, despite the current path being far longer. If the current was simply flowing down one or two different paths through the lattice, then the resistance of the larger lattice would be significantly greater than the single vertex. How much greater is not

straightforward to determine, as there are so many variables regarding the current path.

An attempt has also been made to measure the hexagonal lattice consisting of Permalloy, with an aluminium cap layer so as to prevent the oxidation of the ferromagnetic, and attempt to see the effect this has on the magneto-transport data acquired. One target of this is low temperature measurements, where the anomalous Hall signal observed in the literature previously [15] has been questioned in terms of its physical origins. [14] It was shown that the presence of the anomalous Hall signal at low temperatures was again present in samples which did not have an Aluminium cap, but disappeared upon application of that cap, with which the data becomes symmetrical for all temperatures.

The behaviour of the lattices was also investigated in cases where there were different DW types present, with a comparison between transverse and vortex domain wall lattices. The AMR of the connected lattice has been investigated for the different possible orientations allowed, given the placement of the electrical contacts. These measurements have shown the effect that the free propagation of DWs through the structure has on minimising the magnitude of the effect associated with the magnetisation reversal. This was of importance due to the intention to measure the AMR of more complicated lattices in the following chapters, and so a benchmark of the behaviour from a well-studied lattice was useful for comparisons to be made.

6. Comparison of connected and unconnected Artificial Spin Ice (ASI)

Following the results pertaining to the standard connected hexagonal lattice of Artificial Spin Ice (ASI), the investigation progresses to investigating a new system not previously seen in the literature. The aim of this was to be able to evaluate the interactions within forms of ASI containing physically disconnected nanomagnetic elements.

This chapter considers a lattice that, within this thesis, is termed the 'hybrid lattice', which consists of an unconnected hexagonal lattice of nanomagnetic islands. These islands are linked by a series of normal-metal, conducting connectors. The importance of their conductivity is that it allows for electrical current to be passed through the network, and therefore a magneto-transport measurement to be taken – something which cannot be achieved in a conventional unconnected ASI.

A direct extension of this can be made by considering the lattices to have a level of 'restriction'. For example, considering the hybrid lattice, there is no physical path for a Domain Wall (DW) to propagate from one bar to the next with the lattice, and so this represents a lattice of 100% restriction. Conversely the conventional hexagonal lattice, with its channels of consistently the same width at the vertex as in the DW-carrying wires, has zero restriction to the magnetic propagation.

Using this definition of the two lattices, an extension of this study has brought about the design of a new experiment. This considers the switching mechanisms involved in lattices with different levels of restriction, achieved through lattices whose bars are physically connected, but with the wire width at the vertices reduced in comparison to the width of the wires themselves. A consideration of how the switching signal changes across this range of lattice geometries is conducted, in order to identify the physical geometry at which the propagation of the magnetisation-reversing DW through the lattice becomes prohibited.

As with Chapter 0 the data for the resistance measurements followed the same illustrative order, with all of the field applications colour coded for consistency. The benefit of this was again to ensure ease of like-for-like comparison of all effects which occur either above or below the zero field.

6.1. Outlining the hybrid lattice and the restricting lattice

6.1.1 Hybrid Lattice

The nature of the magnetisation reversal in conventional ASI is well documented and understood to a large extent, and particularly so for the case of the connected lattice. It is accepted that the reversal is dominated by domain wall motion through the lattices [15], [36]. Less, though, has been reliably confirmed in the case of the unconnected array of nanoislands, with characterisation, imaging and magneto-optical work the previous extent of the research completed. [35]

However, this section outlines a method for a design of ASI lattice which can open the door for the direct electrical investigation of the switching mechanisms in this type of lattice. This lattice will produce an ASI where the DWs are unable to propagate through the network, instead confined to the individual nanowire in which they are nucleated. This has been added to with non-magnetic connections to create the Hybrid Lattice, one which allows for electrical measurements while still eliminating the domain wall propagation throughout the sample, and therefore forces each magnetic bar to have its own domain wall nucleate and reverse the magnetisation.

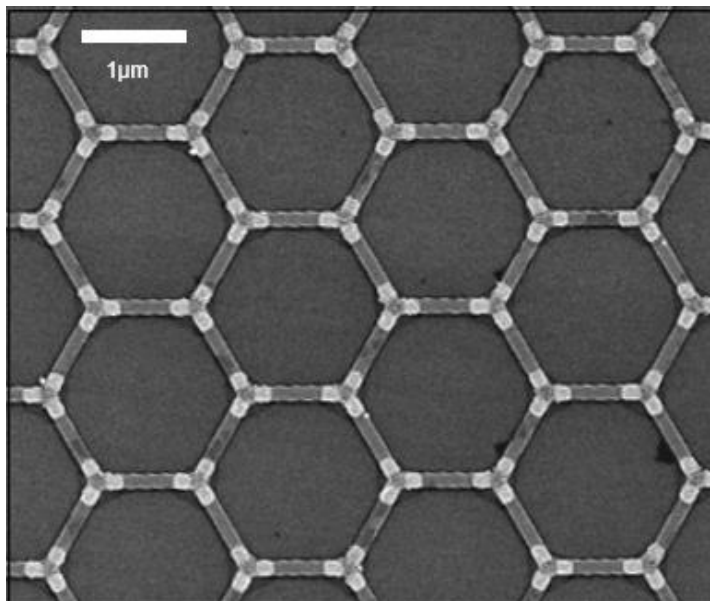


Figure 6.1: SEM image of a hybrid lattice with non-magnetic connectors at the vertices - in this case the connectors are of the same shape as the bars being connected. The bars are made out of Permalloy while the vertices are Aluminium

Figure 6.1 shows an example of the first form of hybrid lattice to be created. In this form, the non-magnetic connecting regions are shaped to be as similar as possible to the magnetic bars they are connecting. This was considered initially to be the best way to connect the bars up without jeopardising the manner of the magnetisation reversal, when compared to the conventional connected lattice. However, other simple forms of interconnect were also implemented, most notably seen below in Figure 6.2.

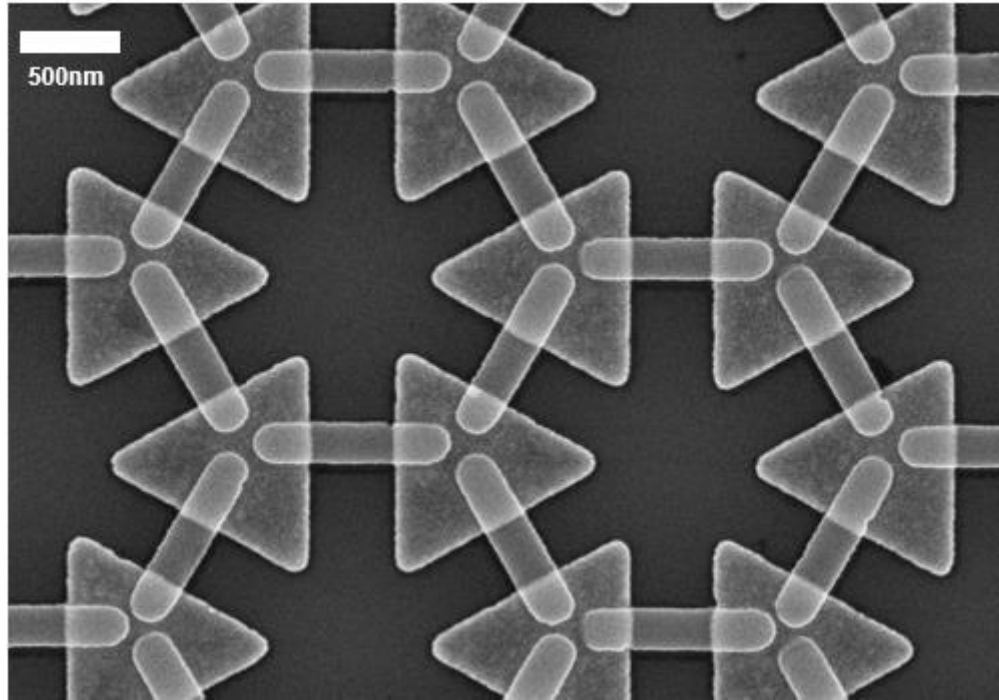


Figure 6.2: SEM image of a hybrid example of a hexagonal ASI – the narrow bars are fabricated from Permalloy and the connecting triangles are fabricated from Gold

In terms of the connection between the normal metal and the ferromagnet in this sample, the current path within a nanomagnetic element is more likely to be predictable in this case, as the interface between the two materials is a straight line, whereas in the case of the initial sample design, a small offset in the alignment between the two stages of lithography can result in only a small contact between the two materials. It can also see the interface not being orientated uniformly across the wire, raising problems about the predictability of the current direction through the bars. From the consideration of the lithography this requires less precision in the alignment of the two layers.

This design is intended to maintain the close proximity of the magnetic bars, as is necessary for the dipolar interaction between them to occur, highlighted by the obeying

or not of the ice rules, and for the system not to become merely a series of isolated bars. This of course can happen in instances where the ferromagnetic nanoislands are separated by too great a distance, as previous literature on the subject has confirmed. [70], [73]

Determining the proximity required in order for the sample to behave as desired was not trivial, however a number of studies on the subject have been completed, notably work by *O'Brien et al*, who studied the interactions between DWs in two parallel nanowires. [71] The information gathered in that investigation determined that at a separation of in excess of 80nm, the interaction between the DWs has diminished such that it is negligible. So this was considered the reference point when producing samples within this study.

The techniques previously used for investigating these unconnected lattices as a whole, have only been non-invasive such as imaging and use of magneto-optics. While these still offer interesting results, electrical measurements of the AMR can present a more detailed picture, through such explicit information as the resistances of the different samples at different magnetic field applications. This was the main motivation behind the study, as an opportunity to further the overall appreciation of the different ASI forms, and shedding light on the nature of unconnected lattices.

Throughout the thesis, there has been an endeavour to maintain the same materials for the different investigations, to aid ease of comparison. The normal-metal regions, whose role it is to electrically connect the magnetic islands and ensure a path for electrical measurements, were made from gold for my investigation. This was due to their high conductivity and their non-magnetic property, as it was imperative to maintain the magnetic isolation of the individual bars. The gold of thickness 20nm was attached to the substrate via an adhesion layer of chromium, of thickness 5nm. The magnetic bars once again consisted of Permalloy with a thickness of 30nm.

6.1.2 Restricting Lattice

As the investigation into the mechanisms of the hybrid lattice developed, the measurements taken revealed noteworthy differences between this and the conventional connected lattice. This led to the inspiration arising for another form of hexagonal lattice. This was intended to provide a link between the two extremes of the connected lattice and the hybrid lattice, and this will be referred to in this thesis as the 'Restricting Lattice'.

The restricting lattice includes the same Permalloy nanowires featured on both the connected and hybrid lattices. In this instance, the wires are connected, however the width of the wire is reduced around the vertices.

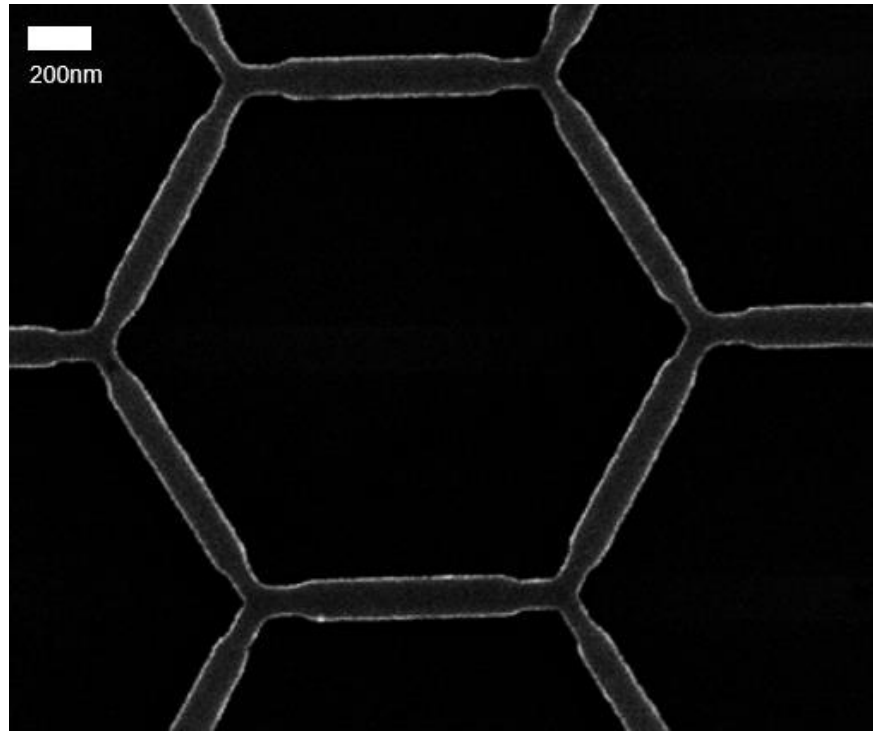


Figure 6.3: SEM image of a vertex within a typical restricting hexagonal lattice made out of NiFe – the restricting sections of the lattice at each vertex are constructed as such through the design implemented into EBL during fabrication

The intention was to limit the DW propagation through the connected lattice to various degrees, such as to be able to see restricting lattices which show one of the switching mechanisms observed in the connected or hybrid lattice, and to identify at what level of restriction the transition between the two mechanisms occurs. Contained within the above aim, it was also intended to be able to show that a structure mimicking the behaviour of the disconnected lattice of nanoislands could be produced, while avoiding the required two-layer lithography of a hybrid lattice.

The restricting lattice could be used to characterise the hexagonal lattices investigated here in terms of a parameter defined as the “level of restriction” at vertices – where a conventional connected lattice had zero restriction, and a hybrid lattice, or unconnected lattice, had a level of complete restriction, with a scale between 0 and 1. The nature of

the transition between the two switching mechanisms was a source of interest. Measurements would be used to consider whether the properties of the magnetisation reversal, such as the rate of reversal, would slowly be changed alongside restriction, or whether there would be more of an abrupt change between two distinctly different types of behaviour.

6.1.3 Summary of investigated samples

The samples are described below in Table 2. Once again, the length of all bars in the lattices of all different samples is $1\mu\text{m}$.

Table 2: Documenting the samples created and measured as part of the displayed results within Chapter 0.

Sample Name	Sample Type	Materials ($\pm 0.5\text{nm}$)	DW Type
ASI43	Hybrid Uncapped	Py 48nm / Au 20nm	Vortex
ASI46	Connected Uncapped	Py 20nm	Vortex
ASI51	Restricting Uncapped	Py 20nm	Vortex
ASI59	Restricting Uncapped	Py 18nm	Vortex
ASI61	Restricting Uncapped	Py 20nm	Vortex

The samples all fall within the vortex DW regime in order to best provide ease of comparison between the different types of lattice geometry. The percentage quoted for the restricting lattice varieties are representative of the percentage decrease in the width at the vertices compared to the width of the bars of the lattice.

6.2. Comparing absolute resistances of different ASI lattice samples

During the work completed in this chapter and chapter 0, a study into the absolute resistances of samples was also compiled. This saw a comparison of the resistance at pre-determined magnetic fields and compared for different sample conditions or conditions of the local environment.

Of particular focus, the temperature dependence of the resistance at a suitably high externally-applied field was obtained for a range of different temperatures across examples of both the connected and hybrid lattice. The reason for basing this on the high-field resistance is due to the fact that at low field, the switching events of different samples can jeopardise the reliability of comparing the different resistances. The magnetisation reversals occur at lower fields, typically below 50mT, and therefore it was considered that this was a more reliable field strength to compare the resistances. In this case the resistance was considered when the applied field was 0.3T.

6.2.1 Two-terminal resistance measurements

Characterisation of the samples was a necessary step when intending to assess the different lattice varieties comparatively. Therefore, as a preliminary measurement prior to the obtaining of AMR and Hall data for these samples, a series of two-terminal resistances were acquired for all possible combinations, for both a hybrid and a connected lattice, and taken at room temperature (RT) (295K) and at 3K.

Table 3: The two-terminal resistances of different hexagonal ASI lattices at both room temperature and 3 kelvin – the average is calculated from 15 different resistance measurements per sample

Sample Lattice Type	Connected	Hybrid
RT Average (Ω)	603	744
3K Average (Ω)	384	541

The table shows that the effect of the decrease in temperature is broadly similar on the two types of lattice. The connected and hybrid lattices behave as was anticipated, with their temperature dependences being similar, albeit constantly observing the resistance of the hybrid lattice being higher in both conditions. The potential cause of this is the number of interfaces that the current will propagate through within the hybrid lattice, repeatedly moving between the gold regions and the Permalloy regions, as well as through the gold contacts. This contrasts with the connected lattice, where there are no interfaces within the lattice and so the measurement is made across just the Permalloy and the gold contacts.

6.2.2 Four-terminal resistances and Residual Resistivity Ratio

Similar to the two-terminal resistances outlined above, each four-terminal magnetotransport measurement was evaluated not just in terms of its AMR but also, simply, of the magnitude of its resistance.

Table 4: The four-terminal resistance measurements for different lattice types of hexagonal ASI – this is an average of between 5 and 10 measurements for each sample type

Sample Lattice Type	Resistance at 0mT (Ω)
Connected	13.1
Hybrid	12.3
Single Vertex	58.0

The results, shown above in Table 4 that the single vertex, while being a far shorter current path than the whole lattice, has a resistance of nearly 5 times that of the two lattices. These two lattices have such low resistances due to the current dividing across the lattice, and with the summation of resistors in parallel, this leads to a lower resistance for the lattices, despite the far larger size of the measured region in the full lattices.

The table of resistances above shows a comparable resistance for both the connected and hybrid lattices, equal to within 0.8 Ohms of one another. Considering the resistivity of the Permalloy region of the sample and that of the gold, a calculation was performed to assess the viability of these results relative to one another.

Given the comparison of the two resistivities of the materials, with Permalloy being approximately 25 times more resistive than the gold, it is to be assumed that in the regions where the materials overlap, the majority of the current will flow through the gold. From Figure 6.2 it was calculated that on average through a potential current path, the current path through a hybrid lattice consisted of at least 41% Permalloy, with the remainder being through the gold. This is shown in Figure 6.4.

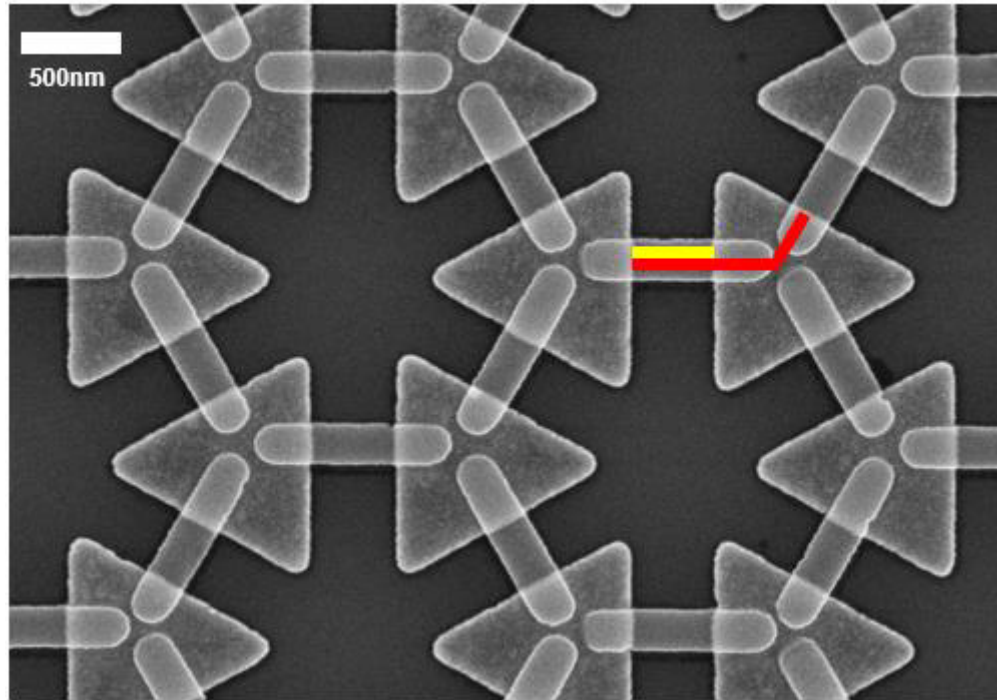


Figure 6.4: SEM image showing the relative distances of current paths through the hybrid lattice - the yellow line shows the path through Permalloy for one nanowire, while the red line shows the distance from one Au/Py interface to the next equivalent interface – image taken from sample ASI40

From this a calculation can be made based on the resistivities, to determine what resistance deficit would be expected between a connected and hybrid lattice. The calculation is performed on the assumption that the current flows immediately into the gold from the Permalloy, meaning that the current path in a hybrid is 41% Permalloy and 59% gold. Calculating for a length of $1\mu\text{m}$, and using resistivity values of $\rho_{\text{Au}} = 2.3 \times 10^{-8}\Omega\text{m}$, and $\rho_{\text{NiFe}} = 5.8 \times 10^{-7}\Omega\text{m}$, the hybrid lattice measurement's resistance should actually be only 0.443 times that of the connected lattice. In reality it is shown to be actually 0.939 times in terms of resistance.

Considering this in another way and assessing the case where the measured resistance of the hybrid is indeed 93.9% of the connected lattice, and the approximation that the interfaces between the two materials contribute no extra resistance. In this case, for the measured percentage of 93.9% to purely arise from the difference in the current paths, then this would mean that the current would flow 92-93% through Permalloy, and only 7-8% through the gold. Based on the resistivities of the two materials this is unrealistic, as the Permalloy is so much more resistive than the gold.

The other factor which can cause the resistance to increase in a hybrid lattice is the interface resistance whenever the current is passing between the Permalloy and the gold layers. Data presented later in this chapter on the hybrid lattice should yield the possibility of considering the size of the effect of the interfaces on the overall resistance of the hybrid lattice. This closeness in the absolute resistance of the measurements is not the case for the single vertex measurement, which yields a resistance of nearly 5 times the magnitude of those other two lattices.

As far as the overall sample resistance at room temperature, it has been observed that the resistance of the hybrid lattice and the connected lattice is broadly the same. The relationship was investigated further to see how these resistances would develop as a function of temperature once again. This investigation allows the assessment of interesting sample properties such as sample purity, and the competing resistivity levels and the number of interfaces within different samples.

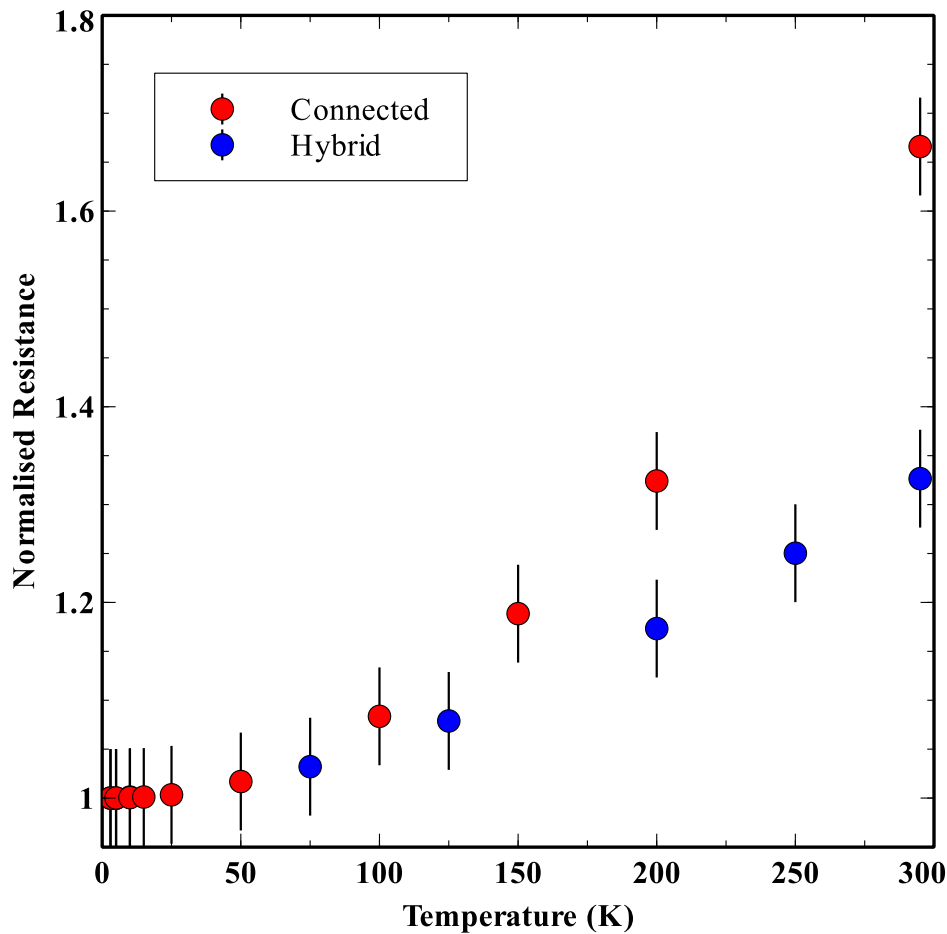


Figure 6.5: Evaluating the 4-terminal resistances across different types of samples as a function of sample temperature – the key refers to the type of lattice depicted by the two different colours displayed in the graph

Figure 6.5 shows how the overall resistance of the spin ice measurements is affected by a change in the sample temperature. In the instance of a connected lattice, there is an increase in the resistance of more than double that which is seen in a hybrid lattice, when the sample has been heated to room temperature.

The data above allows for the calculation of each sample's respective Residual Resistivity Ratio (RRR) as an indicator of sample purity – the purest samples will have a large RRR as the resistance varies greatly with the change in temperature. The RRR is defined as the ratio of the resistance at room temperature with that at close to absolute zero, although typically 4.2K has been used as a benchmark. [99] The determined RRRs for the measured samples is shown below in Table 5:

Table 5: Detailing the RRR for different types of hexagonal ASI Lattice

Structure Type	RRR
Connected	1.666
Hybrid	1.326

The RRR factor is determined by the amount of electrons which are scattered via impurities, lattice defects and the surface of materials. The hybrid lattice has a smaller RRR in comparison to the connected lattice, owing to the large number of interfaces between ferromagnet and normal metal through which the electrical current has to travel within the lattice.

A consideration I had made prior to the measurement was whether any benefit and increase to the RRR could be gained in a hybrid lattice by the fact that some of its path was in a pure metal such as gold, rather than the relatively impure compound Permalloy. This however, was still vastly outweighed by the reduction in the RRR which is brought about by the increase in the number of interfaces encountered within the hybrid lattice.

6.3. Magnetotransport measurements of the Hybrid Lattice

It was Wang *et al.* in 2006 [35] who first demonstrated a fabricated ASI lattice of unconnected nanoislands interacting with one another. This took the form of a square lattice, and exhibited properties such as non-zero entropy. They have since been complemented with a large number of similar lattices of both unconnected and connected structures, in a variety of geometries. [36], [48], [57], [66], [100]

Whereas it is now commonplace to use electrical measurements of the AMR of connected lattices, this is not possible in conventional unconnected lattices due to the lack of a conducting path through the structure. Here I show an important development, enabling access to the electrical signal from an unconnected lattice, and furthering the level of understanding of these samples extensively.

One reason why I believe this area of potential study has such potential is that in ASI lattices, it has been observed that at room temperature (RT) in a connected lattice, the magnetisation reverses across a sample via DWs propagating along paths through the lattice. This motion of the DWs has been observed in connected lattices frequently and it is believed to be understood quite well. However in an unconnected lattice, there are no connected paths for the DWs to propagate along, so this chain of reversing nanowires from a single DW will not occur. Due to the challenges of electrically measuring the disconnected nanoisland-based lattices, the effect of this fact on the AMR has yet to be appreciated.

This study features an attempt to make a connected lattice from two materials: one magnetic and one non-magnetic, in such a way as to get an electrical measurement of only one of these two contributions. Specifically, the creation of a hexagonal lattice of similar dimensions to my previous work, but with vertices made of a non-magnetic material.

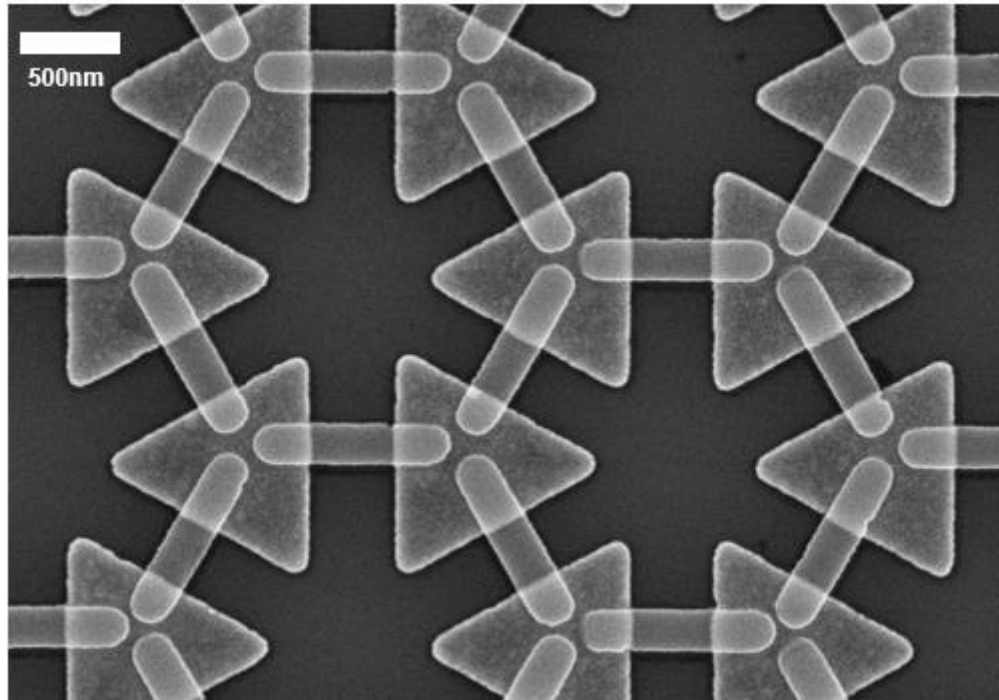


Figure 6.6: SEM image of a hybrid lattice of 25nm thick Permalloy nanowires, connected by 20nm thick gold triangles at the vertices

Figure 6.6 shows a section of a finished sample, which derives from the same base lattice as those used during the investigations of the connected lattice, with a deposition thickness of in excess of 25nm. These are connected by gold triangles at the vertices, of thickness 20nm, and the measurements are completed along gold contacts, of 80nm thickness. The two most important aspects of the design were to ensure that the Permalloy bars were not physically connected to one another directly, and that the separation between neighbouring bars was sufficiently small as to still allow for interactions between the neighbours. The separation was important to allow for interactions like unconnected ASI lattices measured previously.

6.3.1 Measuring different orientations of the hybrid lattice giving evidence of the ice rules

As with the connected lattice, all possible orientations of measurement were carried out over the hybrid lattice, to give the widest range of measurement permutations. This was initially carried out in the longitudinal AMR measurement, as opposed to a planar Hall geometry. There are large differences in the signals produced by all four orientations for the hybrid lattice, and these also differ significantly from their

equivalent measurements of the connected lattice in Section 5.4.3. In most cases a large switching signal features prominently in the hybrid lattice. Using the knowledge of each measurement's field and current directions, it is possible to identify the causes of each of these respective signals.

The hybrid lattice, when viewed as a whole, was designed to have sides of equal length, and the design of the fabrication was such that electrical contacts are also positioned symmetrically on each side of the lattice, each side of the lattice having two electrical contacts connected to it. All of which means that the measurements take place over a very similar number of bars, so it is valid to compare all of the orientations in this manner.

The two main features evident in these hybrid measurements, as also seen in the connected measurements, are a high-field decrease in the resistance and a sharp decrease in the resistance followed by an abrupt increase, which takes place at a lower field, and is caused by the reversal of the magnetisation within the lattice.

The orientations containing proportionately more wires which are not parallel to the applied field, namely orientations 1 and 4, will be expected to show a larger high-field AMR effect. The orientations also affect the magnetisation reversal. Orientation 3 and 4 see the applied field runs parallel to one of the bars of each vertex, and where the other two diagonal bars are at an angle of 60 degrees to the field. By comparison, in Orientations 1 and 2, of the three bars at each vertex, one is angled perpendicular to the applied field, and other two are set 30 degrees to the field. These different combinations will change the fields required to reverse the lattice in different orientations.

Figure 6.7 gives a representation of the path of measured bars across the lattice when a measurement is taken in Orientation 4.

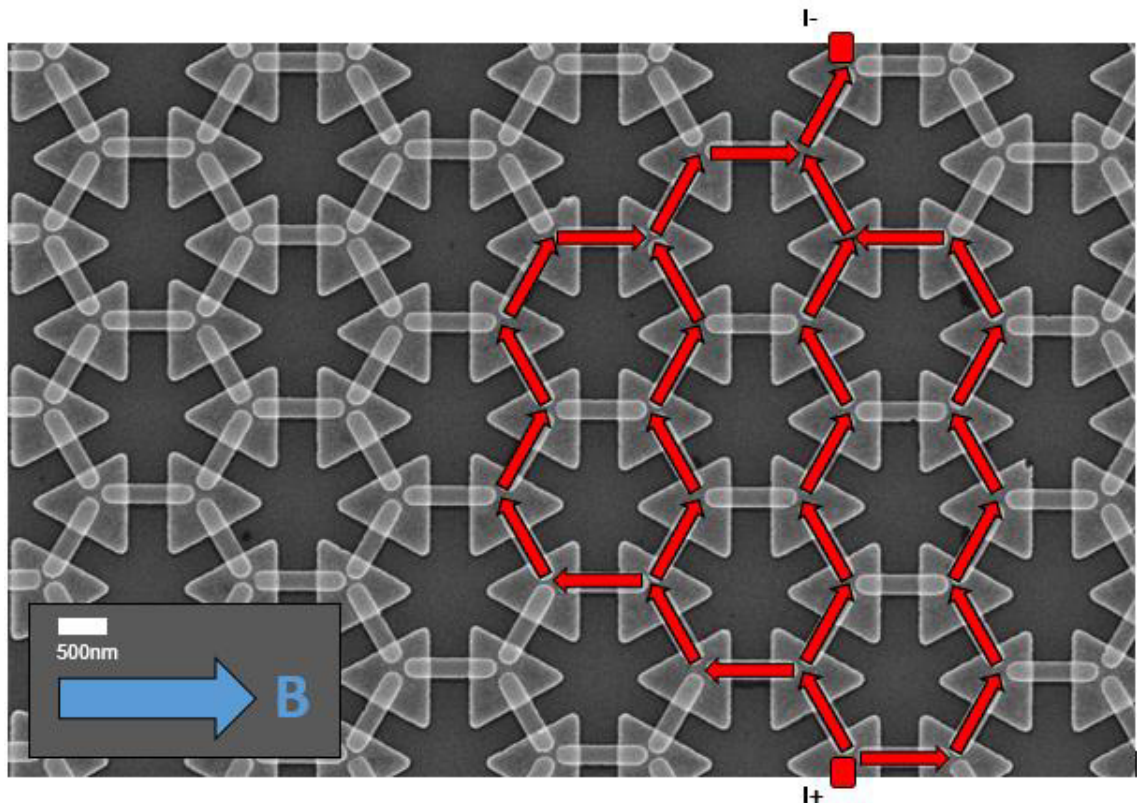


Figure 6.7: SEM image, highlighting the direction of the applied magnetic field (Blue) and the direction of the current path through the hybrid lattice (Red) during measuring of Orientation 4, flowing from the positive end to the negative end. This is a simplified representation as, given the size of the contacts relative to these wires, there are likely to be several start and end points of the current path

In reality there will be more parallel current paths than depicted in this figure, and there will be an amount of current transferring between these current paths. It is also an oversimplification to show that current path beginning and ending from single points, as the electrical contacts will actually overlap four or five magnetic bars normally, so the current is already split into parallel paths from the edges of the lattice. It does show, however, the relative proportions of the current path which are contained within bars diagonal to the external magnetic field and those parallel to it.

The measurement sees Orientation 4 having a very pronounced signal, with two distinctive features, shown from a wide perspective in Figure 6.8.

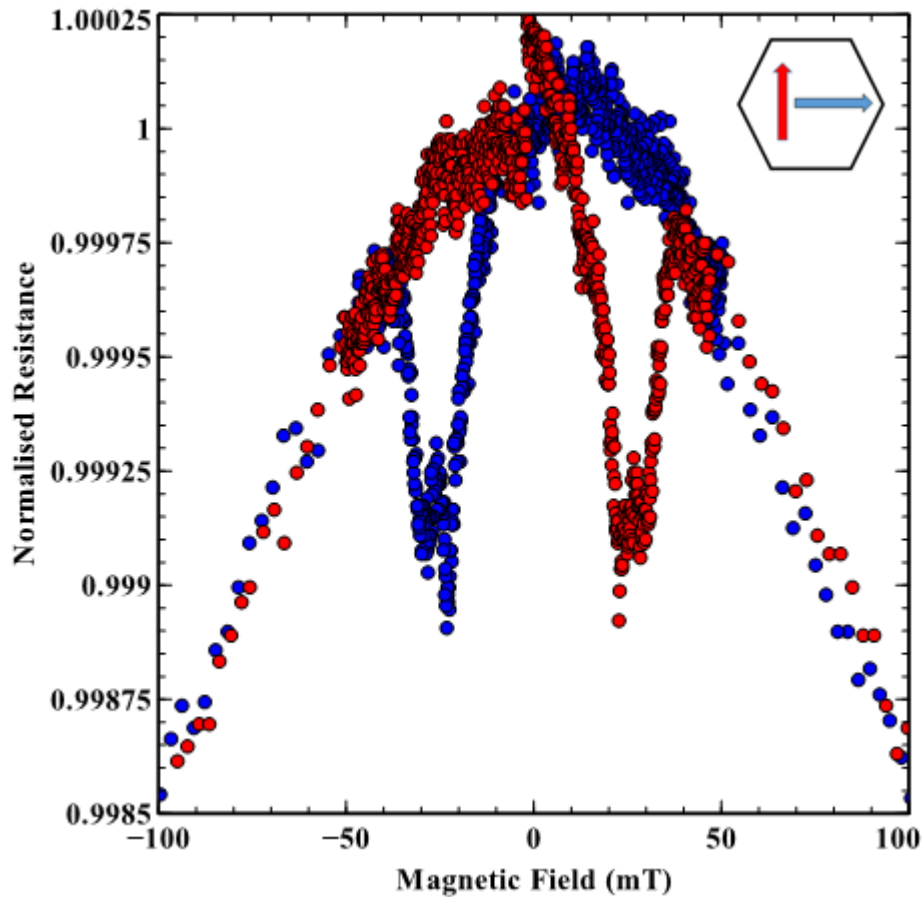


Figure 6.8: The AMR of the Orientation 4 measurement for the hybrid hexagonal ASI lattice, sample ASI43 at RT - the inset panel showing how the current (red) and the applied magnetic field (blue) are orientated in relation to the hexagons of the lattice

There is a very large decrease in the resistance as the field increases, in both field directions, which increases in rate at higher fields, attributable to the large quantity of diagonal bars which are sampled in the measurement, and also the fact that they lie at 60 degrees to the magnetic field, both factors which ensure a large rotation away from the bars' easy axes which drives this resistance change.

Attempting to separate this AMR background from the other features of the data, can be achieved by fitting a curve to the data, in the form of a squared cosine function. This curve is chosen due to this being the relationship between the current and the magnetisation within a magnetic material which governs AMR. Figure 6.9 displays the attempt of fitting this curve to the data.

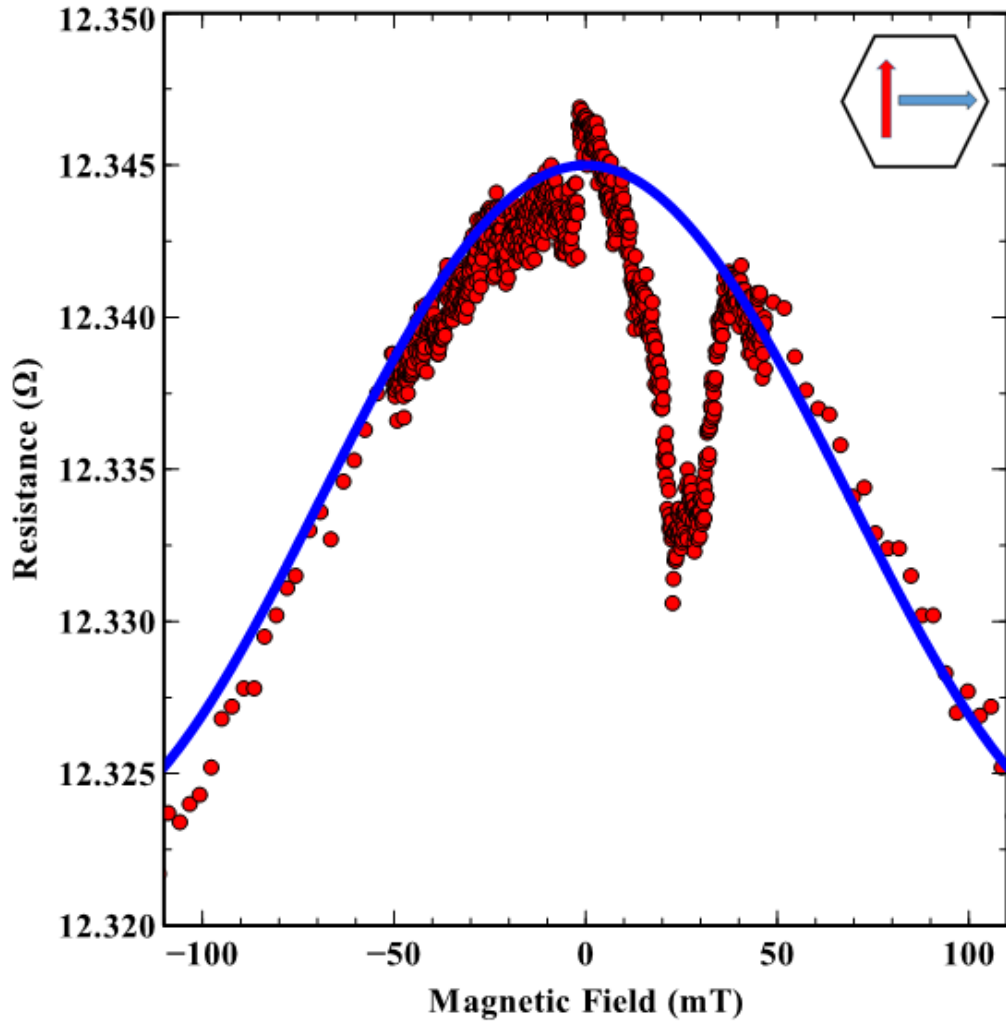


Figure 6.9: Comparing the AMR data for the hybrid lattice in Orientation 4 of sample ASI43 with a square of a cosine function, attempting to fit to the background AMR curve – the red data is experimental and runs from -120mT up to +120mT – the blue curve is an attempted fit to the background curve caused by the AMR of the bars not parallel to the field - the inset panel showing how the current (red) and the applied magnetic field (blue) are orientated in relation to the hexagons of the lattice

The quality of the curve fit is quite high for the majority of the data set, with the most noteworthy discrepancy occurring as the field is high in the negative direction. Attempting to subtract this curve from the data would potentially remove the effect of the diagonal bars and convert the data to become more akin to those data sets concerning only bars parallel to the applied field. This has been attempted and is shown in Figure 6.10.

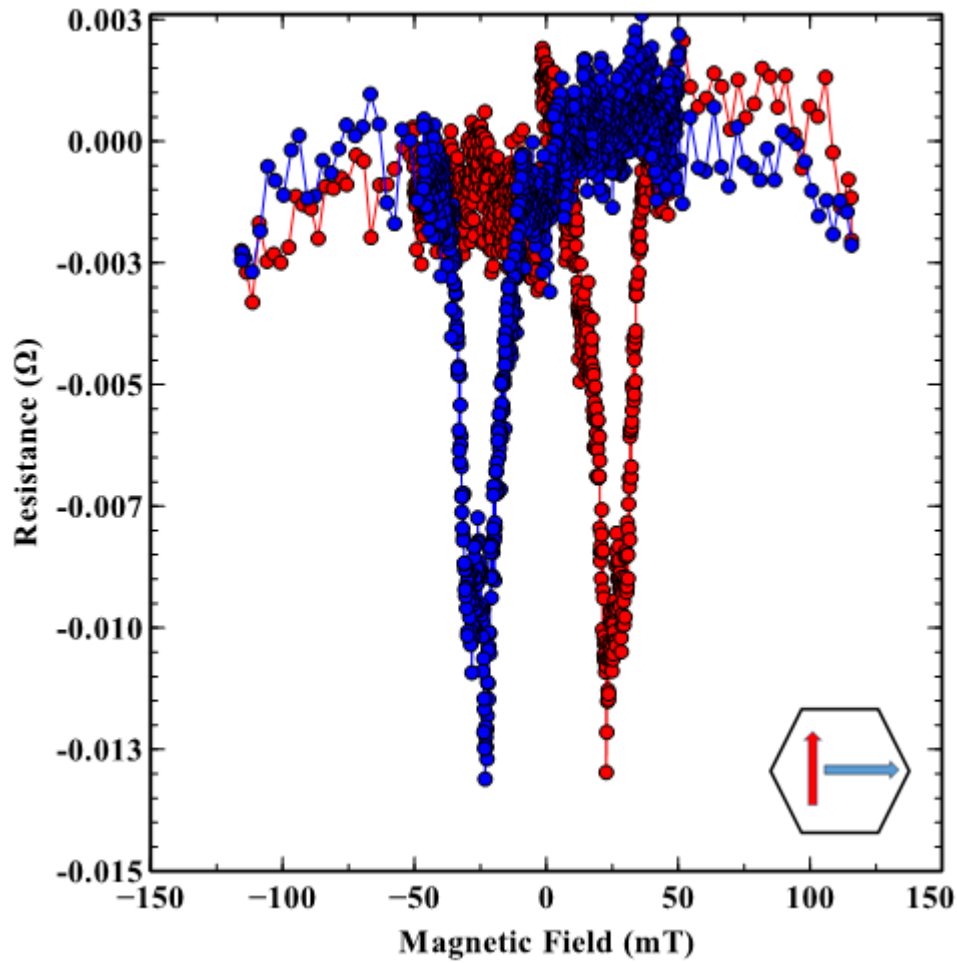


Figure 6.10: The remaining data for the Orientation 4 measurement of the hybrid lattice on sample ASI43, when the fitted curve is subtracted from the data - the inset panel showing how the current (red) and the applied magnetic field (blue) are orientated in relation to the hexagons of the lattice

It is shown that the data remaining following the curve fit has a strong resemblance to the data when the measurement is along bars parallel to the applied field direction. At higher fields in the negative direction there is some discrepancy away from zero, which is caused by the fit not being so ideal in this direction compared with that seen in the positive direction.

The other feature is the pair of large and sharp features in the signal at lower fields - namely at 22mT and 28mT – this can be seen more clearly in the low-field graph in Figure 6.11. These two dips correspond to the two reversals of the magnetisation associated with the diagonal bars, with only a minor switching signal associated with the bars which are parallel to the applied field.

The reason for the diagonal bars contributing two different switching signals in the AMR data is due to the interactions taking place between the bars across the vertices. Figure 6.11 shows the same measurement of Orientation 4, only with a reduced x-axis to focus on the magnetisation reversal.

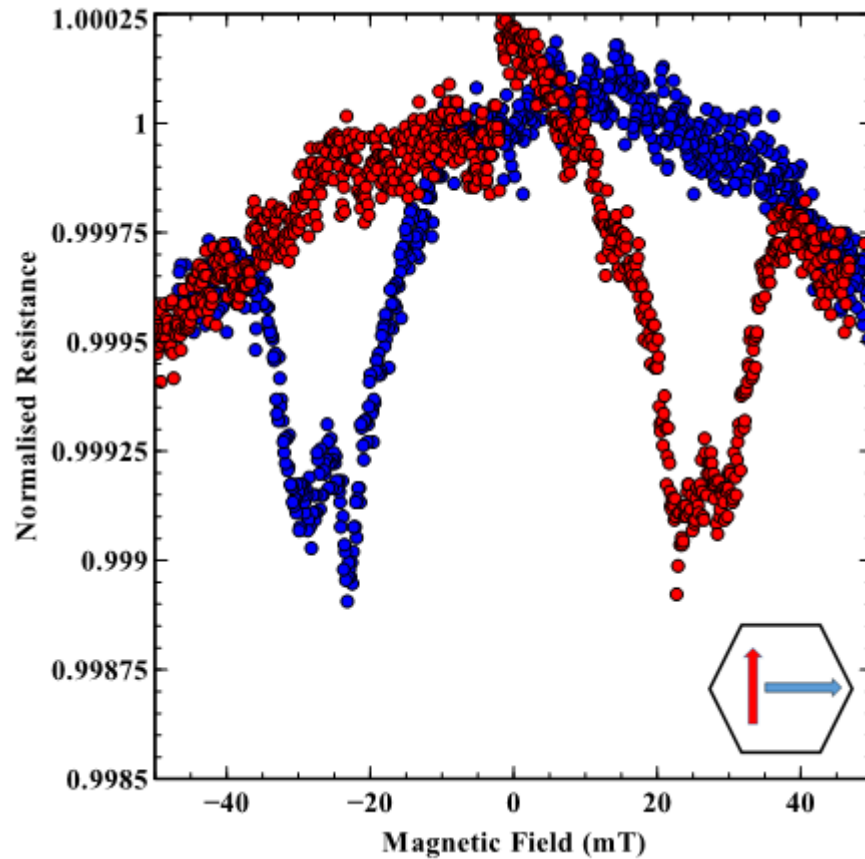


Figure 6.11: The low-field data from the Orientation 4 measurement for the hybrid hexagonal ASI lattice on sample ASI43 at room temperature - the inset panel showing how the current (red) and the applied magnetic field (blue) are orientated in relation to the hexagons of the lattice

In Figure 6.11, assuming the presence of no interaction and therefore no ice rules, there should be only one major switching event happening on the graph, with a single minimum at one applied magnetic field strength, corresponding to domain walls nucleated in all of the bars. This is because almost entirely diagonal bars are being sampled, and these being both at an angle of 60 degrees to the external magnetic field, all of these bars should reverse their magnetisation at the same field. The few parallel bars being sampled should produce a switching signal at a lower field, but it should be very small in comparison to the switching signal of the diagonal bars.

However, present in the graph are two major switching events, and their signal sizes in the AMR data are similar. What the measurement actually shows is that half of the diagonal bars are reversing at a field lower than they would reverse in a non-interacting system, and can be explained in the following way:

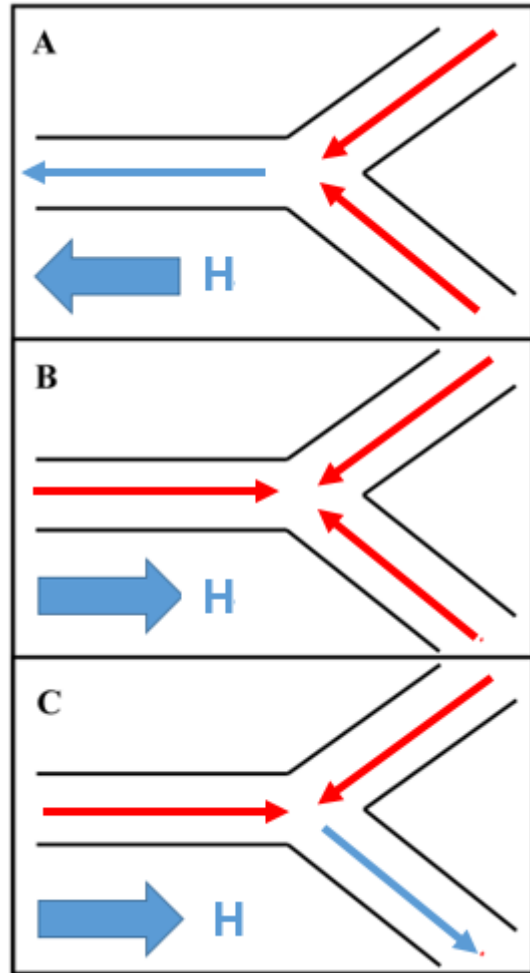


Figure 6.12: Sequence of schematic diagrams explaining the mechanisms of the ice rules – the large blue arrow represents the applied external magnetic field, a blue arrow within the wires signifies the magnetisation pointing out from the vertex, while a red one signifies the magnetisation pointing in towards the vertex

Figure 6.12 above shows a series of diagrams focussed on a single vertex within the hexagonal lattice, and the arrows represent the magnetisation direction within each of the three bars around that vertex. Image A shows the situation where the vertex is saturated in one direction, with a 2-in, 1-out vertex, as a result of the applied magnetic field parallel to the one bar which is pointing out from the vertex.

As the field direction is reversed, and then increases, the bar parallel to the field will have its magnetisation reversed at the lowest field, as seen in image B. This, however, would lead to the situation of a 3-in vertex, as seen by the three red arrows on image B. The result of this is that it forces the magnetisation in one of the two diagonal bars to reverse, even though the applied magnetic field is not yet high enough for it to normally reverse the magnetisation. This can be seen in image C where the top diagonal has reversed to now have its magnetisation pointing away from the vertex, leaving the vertex in a 2-in, 1-out state. It should be stated that due to the two diagonal bars being at identical angles to the applied field, it is not clear which of the diagonal bars would switch early in the process, so the depiction of the top bar is just an example of the type of scenario occurring.

The second diagonal bar will switch at the magnetic field expected given its orientation to the field, but with the first diagonal bar switching at the lower field, this explains why Orientation 4 has an AMR measurement with two distinct switches, even though it is only measuring these diagonal bars, and in a system of isolated bars, the measurement would only have one signal, of double the magnitude. This theory can again be shown via modelling and simulation in OOMMF, which allows for the modelling of a single magnetic vertex with the same parameters as the vertices and surrounding bars have in these physical systems.

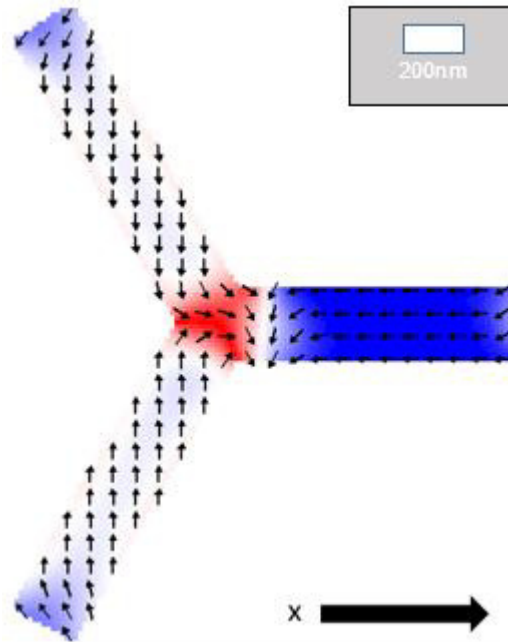


Figure 6.13: Simulation of a single vertex with applied magnetic field parallel to the x-axis, with the field of 30mT causing a reversal in the magnetisation of the horizontal magnetic nanowire – the inset shows the scale of the image, with the sideways length of the white bar equating to a 200nm length within the image

The simulation was completed with finite element dimensions of 5nm, and a magnetic field applied parallel to one of the three bars of the vertex. The initial status saw the system fully magnetised in the positive x-direction. Upon the simulation beginning, the magnetisation in the two diagonal wires relaxed to follow their easy axes towards the vertex.

Following this relaxation of the system, a magnetic field is applied in the negative x-direction, which is incrementally increased, and then ultimately causes the nucleation of a DW and the subsequent reversal of the magnetisation in wires, to align more with the direction of this applied field.

An observation of note is that when the field is applied parallel to one of the nanowires in this vertex of three different nanowire orientations, then the wire which is parallel to the field has its magnetisation reverse first, before the other two wires. The DW which has nucleated then propagates along the wire, and continues to propagate along one of the two diagonal nanowires, as seen below in Figure 6.14.

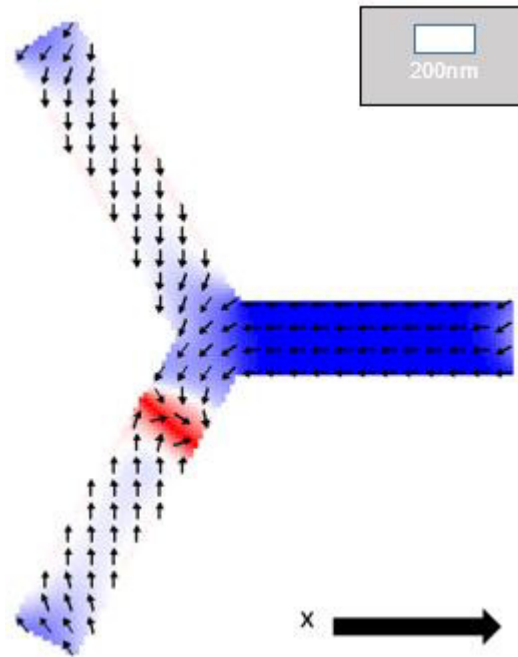


Figure 6.14: Continuation of the simulation of a single vertex with applied magnetic field parallel to the x-axis, still with applied field of 30mT, causing the DW to reverse the magnetisation of the bottom diagonal magnetic nanowire

The DW propagates across the vertex and reverses the magnetisation of the bottom diagonal bar in this case, although in other scenarios it would cause the reversal of the top diagonal bar instead.

As was mentioned previously, in Orientation 4 the parallel bars are almost ignored from the measurement trace by the current path. The reason for this exclusion concerns the path being travelled by the current, which for Orientation 4 includes very few of the parallel bars.

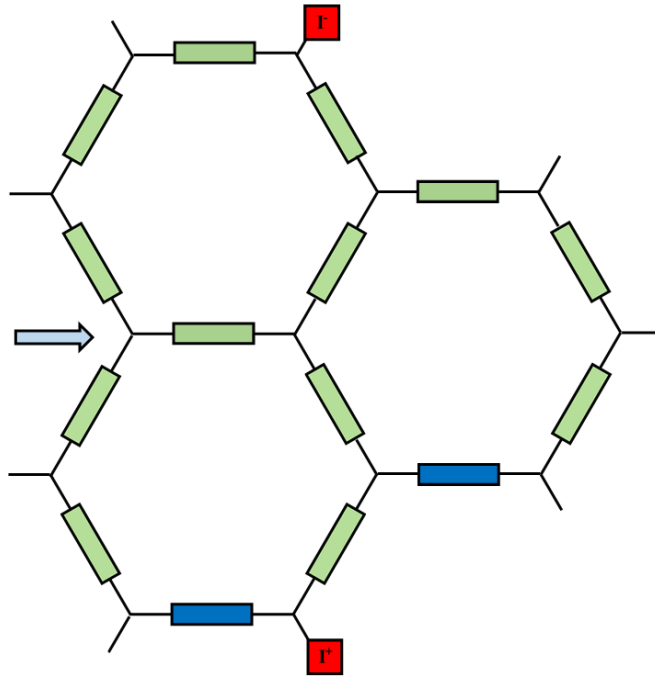


Figure 6.15: Schematic depiction of Orientation 4 measurement of a hexagonal lattice as a network of individual resistors – the individual resistors represent an individual nanoisland within the lattice, and their intersections are the vertices of the lattice – the two red boxes are the endpoints of the current path, and the blue arrow is the direction of applied magnetic field

In Figure 6.15, the blue arrow denotes the applied magnetic field, the red boxes the beginning and end points of the current path, and the green and blue rectangles symbolise resistors, which represent the resistance contributions of each individual nanoisland in the hybrid lattice.

The two blue rectangles are coloured as such as they are the focus of my following analysis. Due to the path of the current through the network, these bars may be parallel to one another but will experience current flow in opposite directions, as shown below.

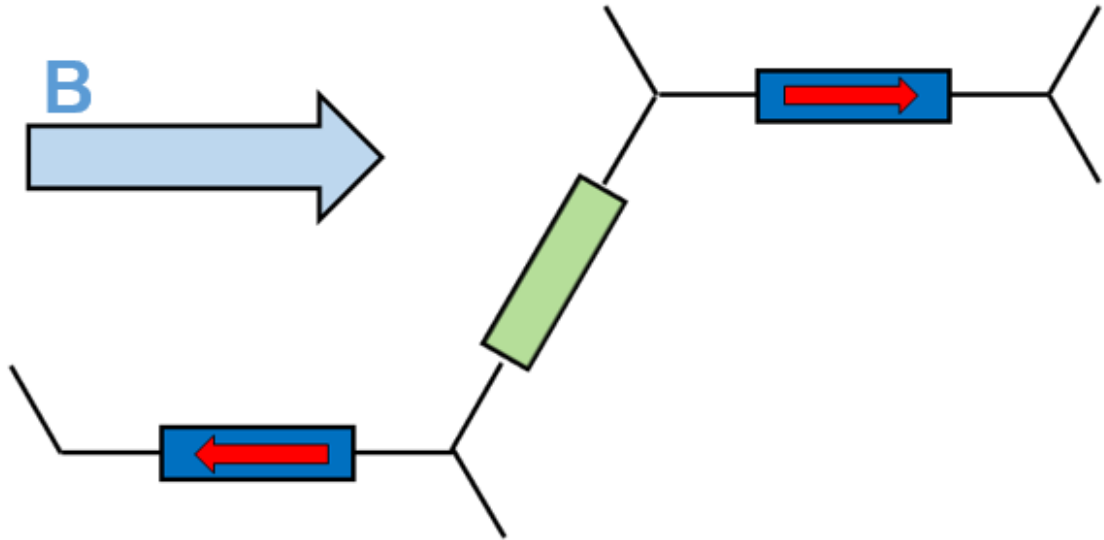


Figure 6.16: Close-up schematic depiction of Orientation 4 measurement of a hexagonal lattice as a network of individual resistors, outlining why bars parallel to the field do not contribute to resistance in this orientation – the red arrows depict the direction of current flow through the network, and the large blue arrow denotes the applied magnetic field direction

The red arrows in the figure above depict the direction of the current through the network at different points. If the AMR were calculated using simply the cosine of the angle between current and magnetisation, then these two bars experiencing opposite currents would in fact cancel each other out. However, due to the relationship actually involving the square of the cosine, the direction of the current has no impact and so the resistances felt by the two bars are equivalent, even during switching events, provided the switching occurs and behaves identically at the same field.

Due to the path of the current across the lattice involving predominantly the diagonal bars, seldom few of the parallel bars register, only when the path is initially diverging and ultimately converging do they feature.

Aside from the switching events, the fact that the diagonal wires are at an angle of 60 degrees to the field means that there is a very appreciable high-field AMR. This compares with an angle of only 30 degrees for the measurements in Orientations 1 & 2, although the angle is still 60 degrees in Orientation 3, so both of these will have a larger rotation of the magnetisation in these diagonal bars than Orientations 1 & 2.

These bars which are parallel to the field do, however, result in the switching signal from the lower magnetic field contributing a larger resistance change. Were it not for

these few bars which are parallel to the field registering on the switching signal, then the size of the two signals would be equal from the contributions of the two different diagonal bars.

By contrast with Orientation 4, Orientation 3 contains a large quantity of all three kinds of bar, roughly equating to 50% of the bars being parallel to the field and 50% being diagonal, of which again the split is approximately 50-50 between the two different diagonal bars.

This can be broadly appreciated in the figure below which outlines an example of a potential current path for Orientation 3, which is much more along the same direction as the applied magnetic field, in contrast with Orientation 4 where current and field were essentially perpendicular. Again it should be stated that the current is highly likely to flow through a far wider network of the lattice than depicted in this diagram.

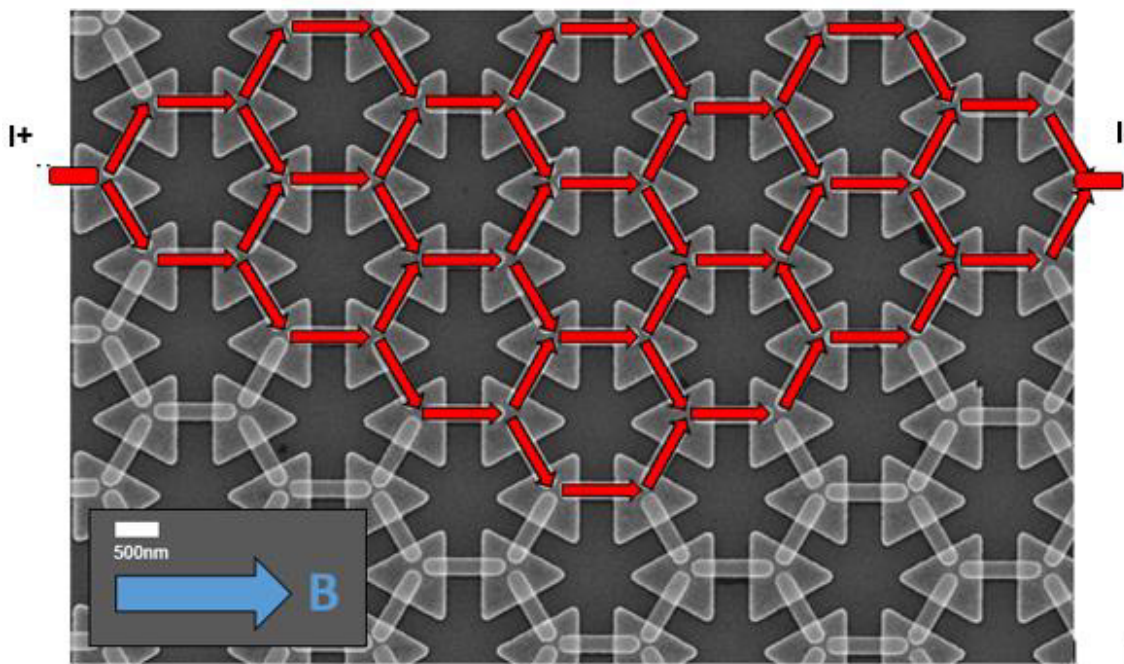


Figure 6.17: SEM image, highlighting the direction of the applied magnetic field (Blue) and the direction of the current path through the hybrid lattice (Red) during measuring of Orientation 3 flowing from the positive end to the negative end. This is a simplified representation as, given the size of the contacts relative to these wires, there are likely to be several start and end points of the current path

Figure 6.18 below shows that the measurement for Orientation 3, like Orientation 4, has two switching events, although here, one of the switching events causes a significantly larger shift in the resistance than the other.

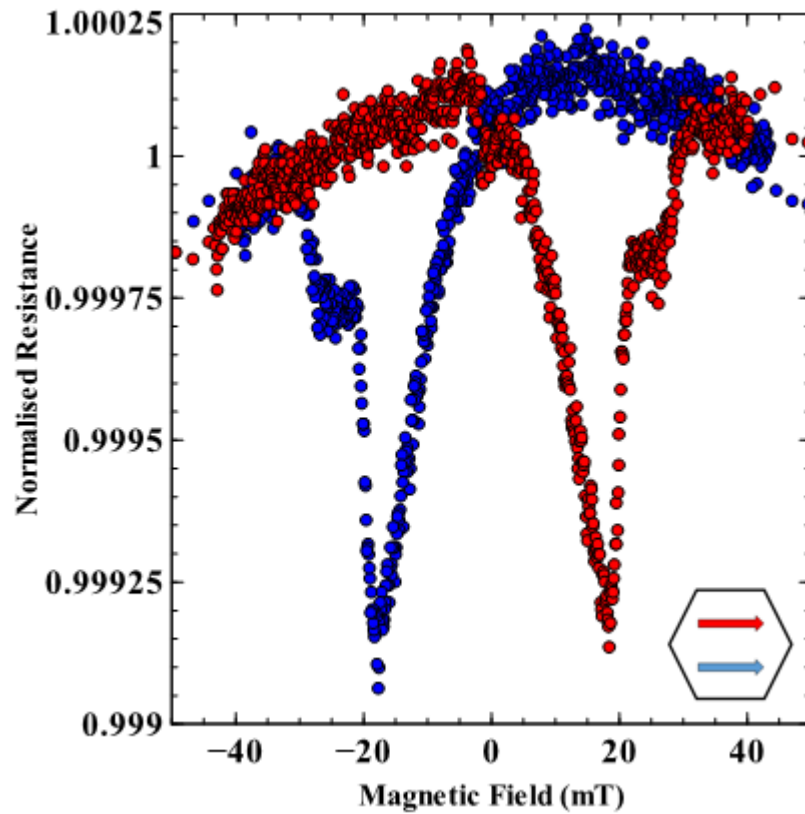


Figure 6.18: Low-field AMR data from the Orientation 3 measurement for the hybrid hexagonal ASI lattice, on sample ASI43, at room temperature - the inset panel showing how the current (red) and the applied magnetic field (blue) are orientated in relation to the hexagons of the lattice

The data can be analysed further in the same way as has previously been done for Orientation 4 measurements, with the plotting of a curve to mimic the profile of the AMR caused by the diagonal bars, and the subtraction of this curve from the data, with the intention of isolating the effect caused by the magnetisation reversal.

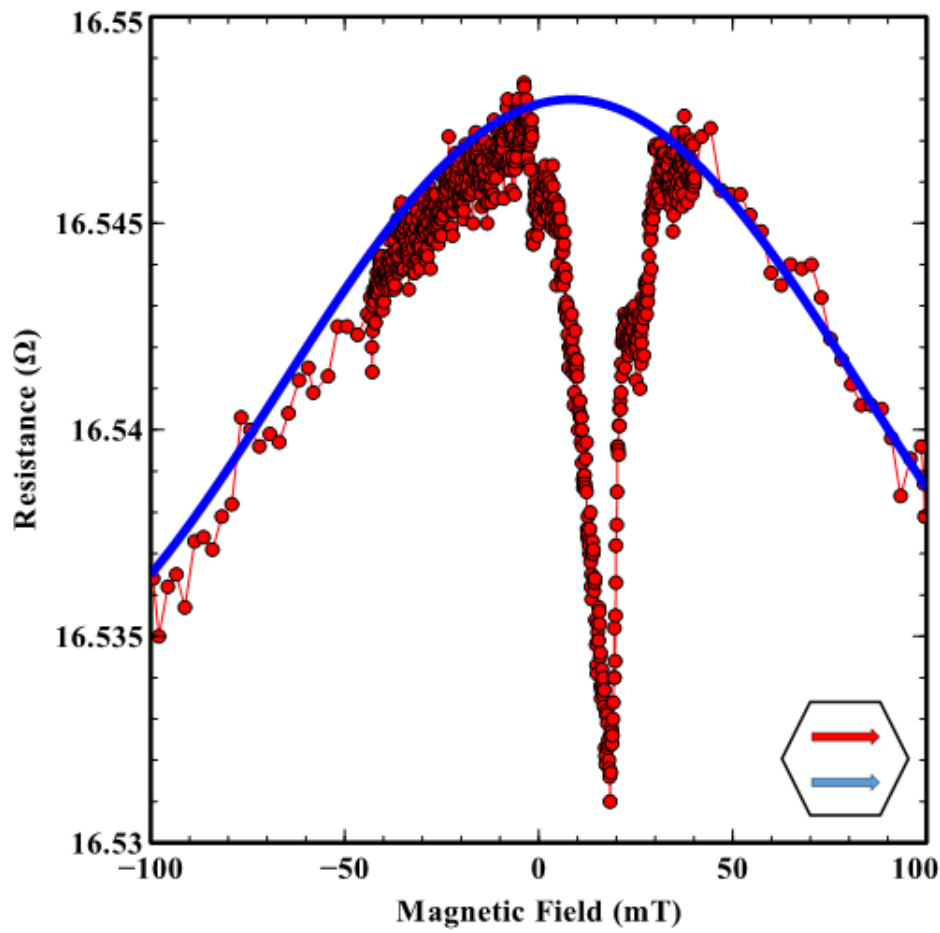


Figure 6.19: Comparing the AMR data for the hybrid lattice of sample ASI43, in Orientation 3, with a square of a cosine function, attempting to fit to the background AMR curve – the red data is experimental and runs from -120mT up to +120mT – the blue curve is an attempted fit to the background curve caused by the AMR of the bars not parallel to the field - the inset panel showing how the current (red) and the applied magnetic field (blue) are orientated in relation to the hexagons of the lattice

The quality of the fit to the data is once again strong, albeit again in the negative field direction there is a discrepancy at the higher applied field in the negative direction. This offset does not appear to be as large as in the case for Orientation 4. Interestingly as well, the data fit appears to be strongest with the maximum resistance shifted away from zero by 10mT. This shows evidence from the fit and within the data of the hysteresis evident at low fields.

Once again, the fitted curve to the data was subtracted from it to remove the AMR effect from the magnetisation reversal data, and the result is displayed below in Figure 6.20.

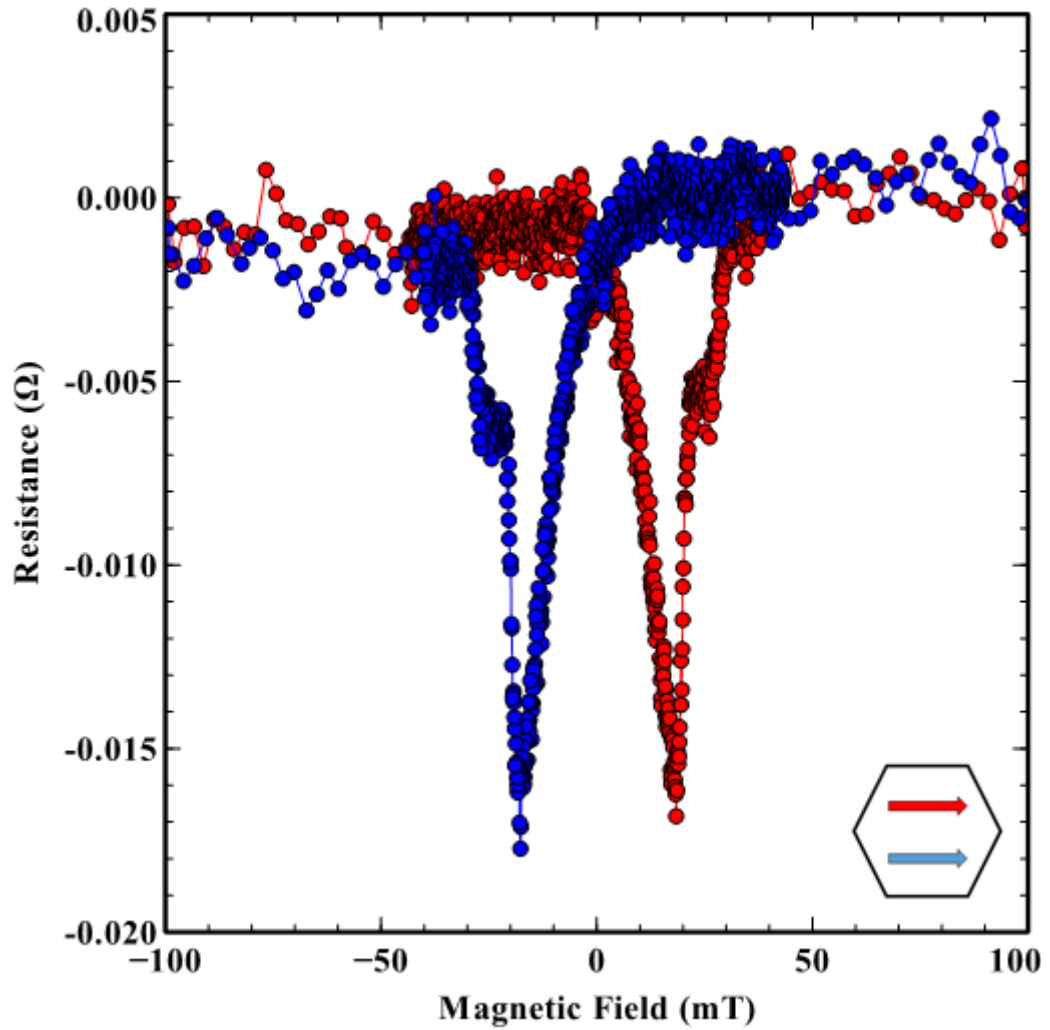


Figure 6.20: The remaining data for the Orientation 3 measurement of the hybrid lattice on sample ASI43, when the fitted curve is subtracted from the data - the inset panel showing how the current (red) and the applied magnetic field (blue) are orientated in relation to the hexagons of the lattice

This graph also presents clear evidence for the ice rules being obeyed in the hybrid lattice, and therefore confirms that the three magnetic bars at each vertex are categorically interacting with one another and not merely isolated wires, and this will be explained here.

As shown in the diagrams within Figure 6.12, the result of the interactions is that one of the diagonal bars of each vertex will switch at the same magnetic field as the bars parallel to the field.

In the Orientation 3 geometry, approximately 50% of the current path is bars parallel to the field, while there are 25% each of the two diagonal bars. Given the interaction shown in Figure 6.12, this means 75% of the bars reverse magnetisation at a lower

field, and 25% switch magnetisation at a higher field. This is borne out in the data of Figure 6.18, where the first AMR signal is 3 times larger in magnitude than the second AMR signal.

The high-field AMR effect is still very appreciable in this measurement, however it is certainly larger in Orientation 4 than it is in Orientation 3. This is due to there being significantly more of the 60 degrees diagonal bars included in this measurement than Orientation 3. The bending of the magnetisation to favour the magnetic field and away from the easy axis and the current, takes place over more of the magnetic bars, resulting in the greater decrease in resistance seen.

This can be compared with simulation, of a single vertex, where the magnetisation reversal behaviour is the same as seen in the hybrid lattice. The bars in the simulated vertex were set to be 1 μm in length and 120nm in width. One of the three bars was set to be parallel to the magnetic field which was applied, with the other two bars orientated at 60 degree angles to that field, thus replicating those conditions of Orientation 3.

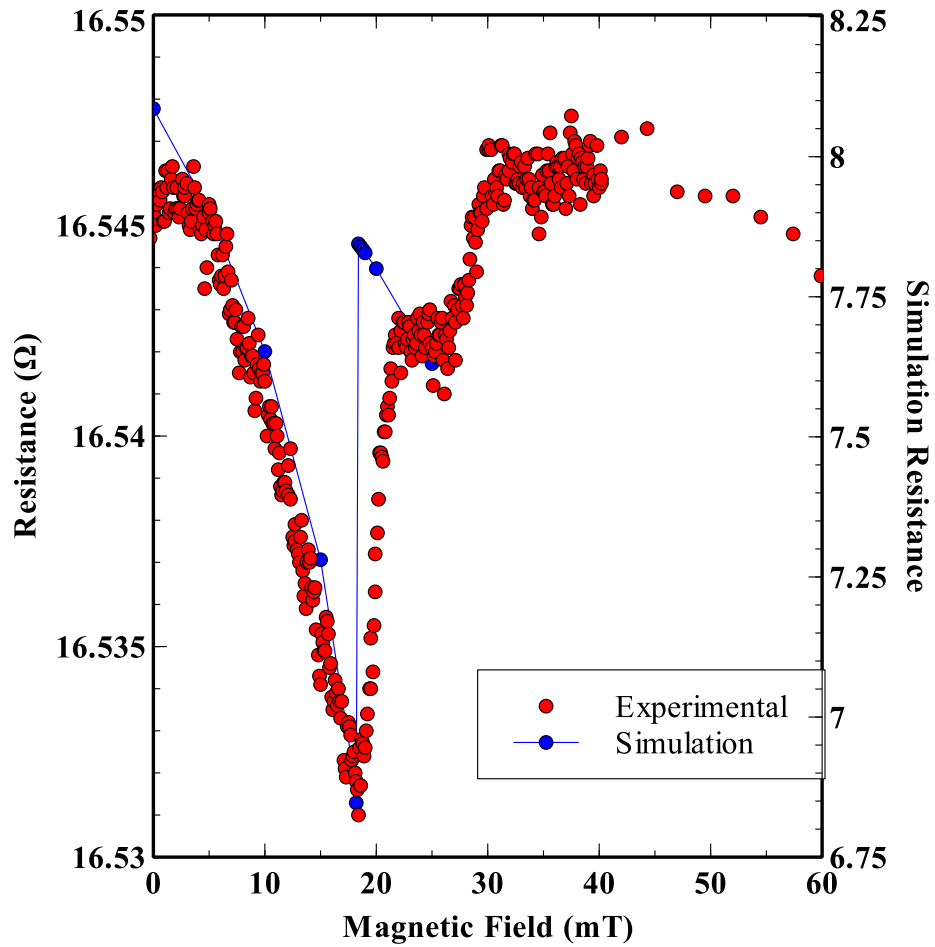


Figure 6.21: Comparing the magnetisation reversal of the hybrid lattice in Orientation 3 both experimentally and through OOMMF simulation of a single vertex

Two of the bars at the vertex are reversing their magnetisation at the same applied magnetic field. The profile of the magnetisation reversal for the data was compared to the same reversal in the simulation of the vertex, and this is shown in Figure 6.21.

The difference in the shape between the two different measurements is due to a minor discrepancy in the calibration of the simulation data compared with what is measured in the experimental setup. The difference in the coercive field values between the bar parallel to the field, and the bar lying at a diagonal angle, is not consistent. In the experimental data a second shoulder can be seen at 28mT, which corresponds to the second magnetisation reversal. It is not evident as a clear resistance drop followed by abrupt increase, as per the other magnetisation reversal events in the hybrid lattice. This is due to the data between 20mT and the second minimum at 28mT being influenced by more than one reversal process.

This results, firstly, in the abrupt increase in the resistance during the first magnetisation process being less abrupt, and occurring over a broader field range, in comparison with the sharp increase seen in the simulated data. This is due to the simultaneous decrease in the resistance from the second process, and so the profile of the data is actually a summation of the two competing influences on the resistance level of the measurement as a whole.

This also means that the nucleation of the DW in the second reversal process is obscured by the increase in resistance from the first process. Considering that the first process is responsible for the reversal of 75% of the measurement in the hybrid lattice, this dominates over the second reversal process. The final two Orientations both feature very distinct AMR data, beginning next with Orientation 2, shown below in Figure 6.22:

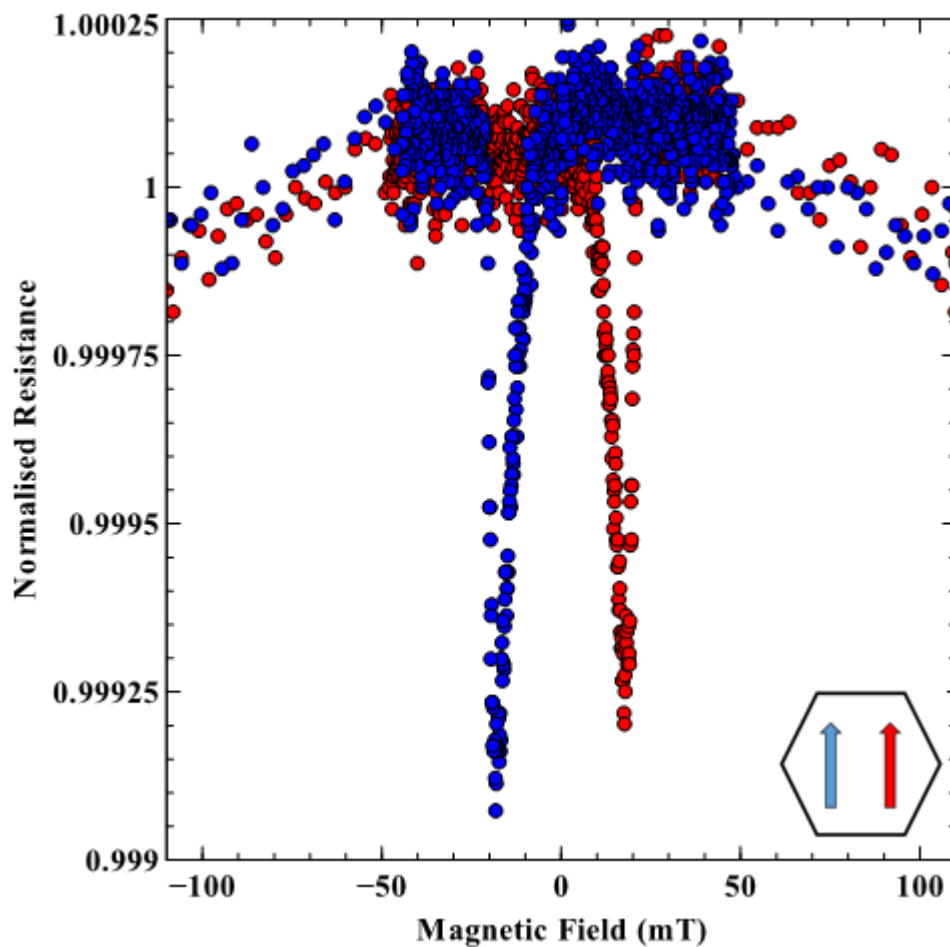


Figure 6.22: The AMR for the Orientation 2 measurement for the hybrid hexagonal ASI lattice at room temperature - the inset panel showing how the current (red) and the applied magnetic field (blue) are orientated in relation to the hexagons of the lattice

A subtraction of the background AMR for this data set was considered not worthwhile as this would barely have an impact on the visibility and clarity of the switching signal seen for this measurement. In this measurement orientation it is clearly apparent that the switching signal far exceeds the high-field AMR up to the 100mT measurement, which is significantly reduced on the level of high-field AMR seen in Orientations 3 & 4. This high-field AMR would eventually become larger in size than the switching signal, however with this measurement geometry it would require a field far in excess of 100mT.

The data gives the impression of an especially large switching signal, however when considered on the normalised scale, the signal is seen to be approximately 0.1% the size of the overall measurement resistance, which is similar to that which has been seen in the previous orientations, such as in Orientation 4, where the signal was shown to be fractionally in excess of 0.1%. What is also different for this measurement in comparison with the previous orientations is that, in Orientations 3 and 4 there can be seen to be two distinct large switching signals in the AMR data, whereas in Orientation 2 there is only one.

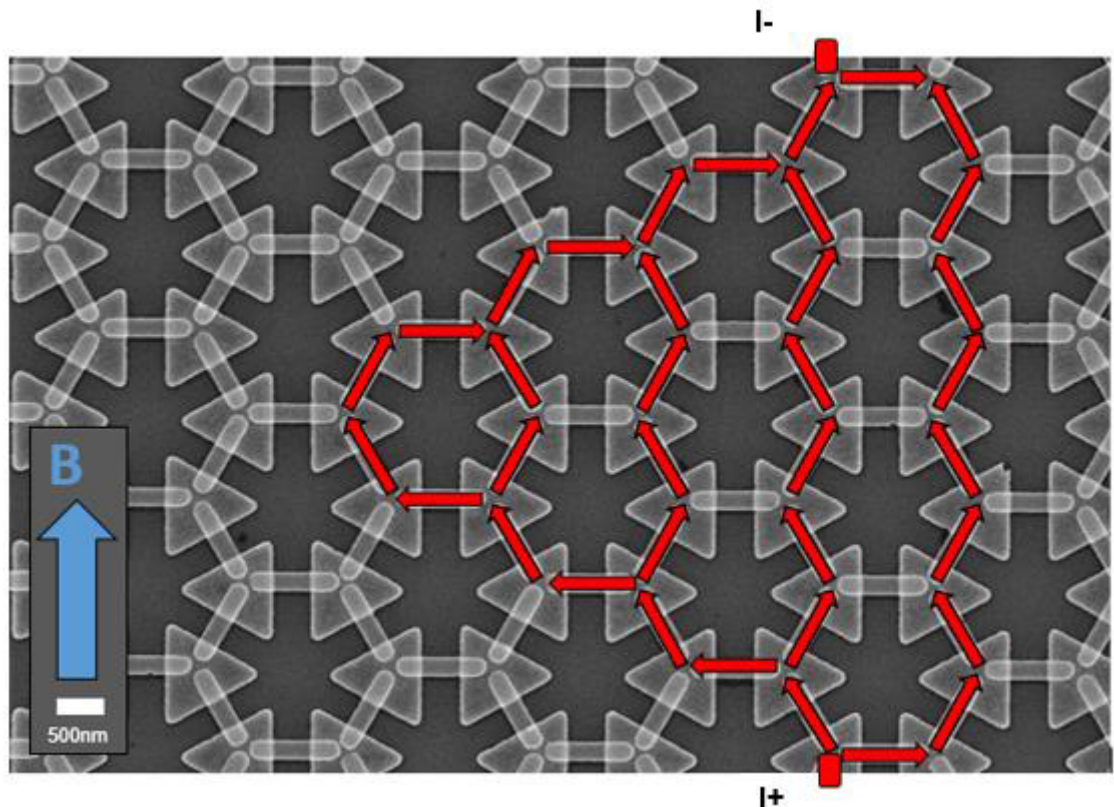


Figure 6.23: SEM image, highlighting the direction of the applied magnetic field (Blue) and the direction of the current path through the hybrid lattice (Red) during measuring of Orientation 2 flowing from the positive end to the negative end. This is a simplified representation as, given the size of the contacts relative to these wires, there are likely to be several start and end points of the current path

Orientation 2 is measured entirely over the diagonal bars, and features very few of the bars which are perpendicular to the field in its current path. The angle between the applied field and the diagonal bars is only 30 degrees for Orientations 1 and 2, and this results in the effect of the rotation of the magnetisation in the wires to be relatively small in its impact on the resistance, as the maximum the magnetic moments are forced away from the easy axis is 30 degrees.

In this Orientation, the two diagonal bars both lie at 30 degrees to the magnetic field, and therefore require equal switching fields for their magnetisation reversal.

This is borne out in the data for Orientation 2, as there is only one large switching event at $(19.0 \pm 0.2) \text{ mT}$, at which all of the diagonal bars sampled during the measurement switch over a very narrow field range. The perpendicular bars would only reverse their magnetisation under a significantly high field, which has not been sampled in this measurement due to the effect of current paths through the hexagonal network.

The switches observed in the AMR data once again are in agreement with what would be expected for a hexagonal lattice obeying the ice rules. In the case of Orientation 2, the two diagonal bars at the angle of 30 degrees to the field will switch at the same field as one another, and the bar which is perpendicular to the applied field will not experience a strong enough switching field to reverse its magnetisation.

If both of the diagonal bars align with the magnetic field when it is large enough for them to switch, then the geometry of the sample dictates that one of the magnetisation directions will point in towards the vertex, and the other will point away from the vertex. This means that in this measurement cycle there will not be a scenario where the ice rules will come into play in dictating the status of the magnetisation, as the sample seldom wants to be in a 3-in or a 3-out situation, with the exception of in monopole defect situations.

Like Orientation 2, Orientation 1 also sees one switching event, in the trace below in Figure 6.24. The single switching event is again due to the same two diagonal bars, even though in this measurement geometry the current path does include sampling of bars at each vertex in all three orientations. However, as these bars are perpendicular to the applied field, the magnetisation is not reversed within them by the effect of this field.

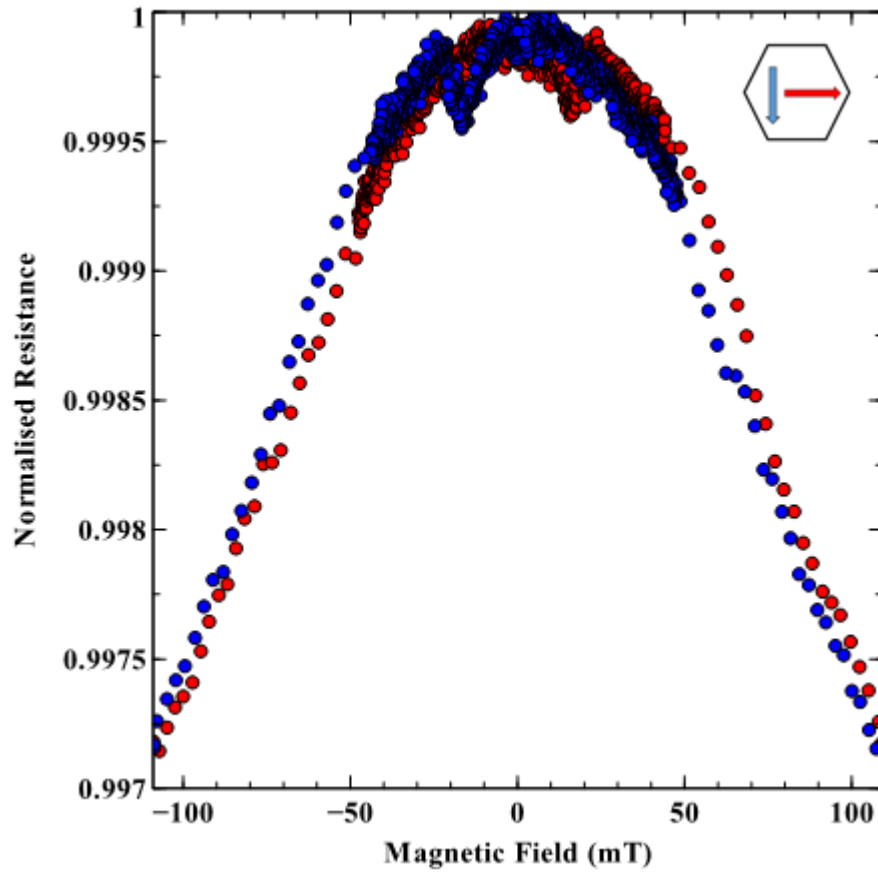


Figure 6.24: AMR of the Orientation 1 measurement for the hybrid hexagonal ASI lattice, of sample ASI43, at room temperature - the inset panel showing how the current (red) and the applied magnetic field (blue) are orientated in relation to the hexagons of the lattice

The measurement taken in Orientation 1 stands out for having both a weak switching signal and a particularly large high-field AMR effect. The weak switching signal is borne out of the fact that approximately half of the measurement is taken from bars which will not experience switching, based on the applied field direction, as shown below in Figure 6.25.

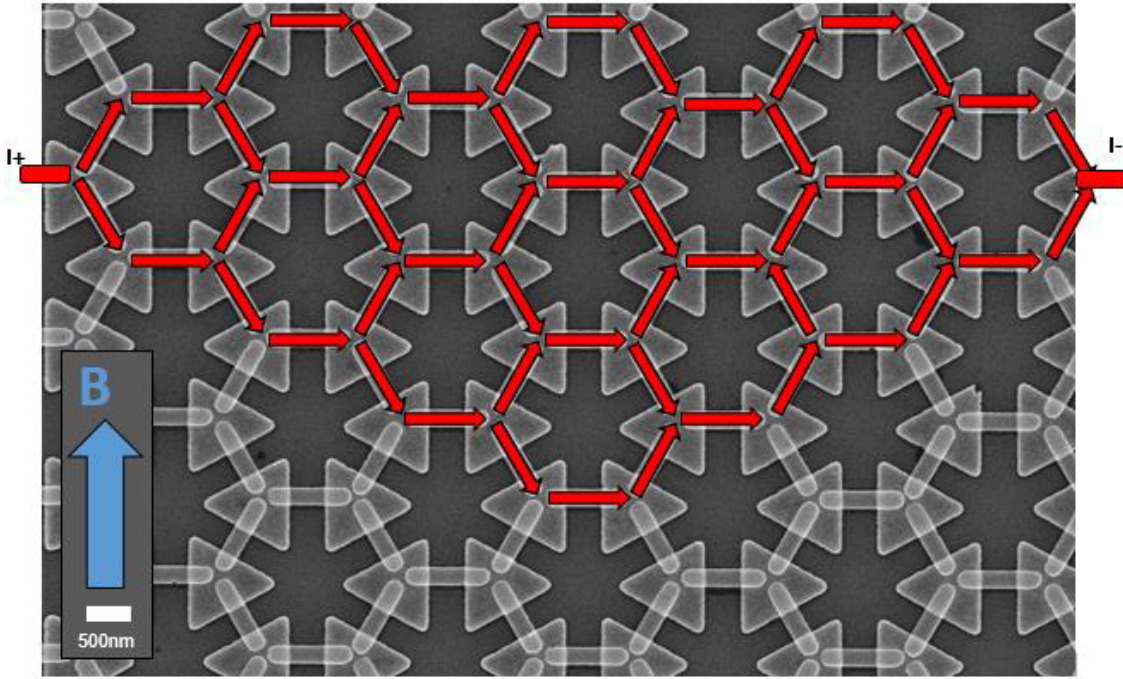


Figure 6.25: SEM image, highlighting the direction of the applied magnetic field (Blue) and the direction of the current path through the hybrid lattice (Red) during measuring of Orientation 1 flowing from the positive end to the negative end. This is a simplified representation as, given the size of the contacts relative to these wires, there are likely to be several start and end points of the current path

As shown in Figure 6.25, the current path is made up of all three angles of bar from within the lattice, and 50 percent of the measurement is on bars which are perpendicular to the field direction. These bars will not be forced to switch by the perpendicular field, as it would need to be significantly stronger to influence the bar at that large angle. Therefore the switching signal shown in the graph for Orientation 1 features only those diagonal bars, and the large switching signal associated with the 50 percent of bars which are parallel is not present in the data, by comparison with the others which have larger signals owing to the larger proportion of the current path that experiences a switch.

The high-field AMR, by contrast, is a particularly large effect at this orientation, because every single bar within the measurement path is contributing to that effect, by virtue of not being parallel to the applied field. In fact, 50% of the bars are perpendicular to the field, so the rotation of the bars associated with the high-field should be larger here than in any other bar for other geometries measured. As none of the bars are parallel to the applied field, this does ensure that the high-field AMR is particularly strong in this measurement, and this is also clearly shown by the drop in resistance at higher fields.

The switching signal is not very clear in this case, however, because it is significantly reduced in size compared with the background AMR. This makes the data a prime candidate to attempt to fit a curve to the background and remove this, yielding simply the switching signals on a flat background.

For the particular shape of the background in this case, this proved to be more challenging than previous data, with there being not a strong fitting to the data at higher fields. However, the main intention for this was to be able to extract the data regarding the switching signal, and so with the fit being more suitable at those lower fields, this was still valid as a means to extracting this information.

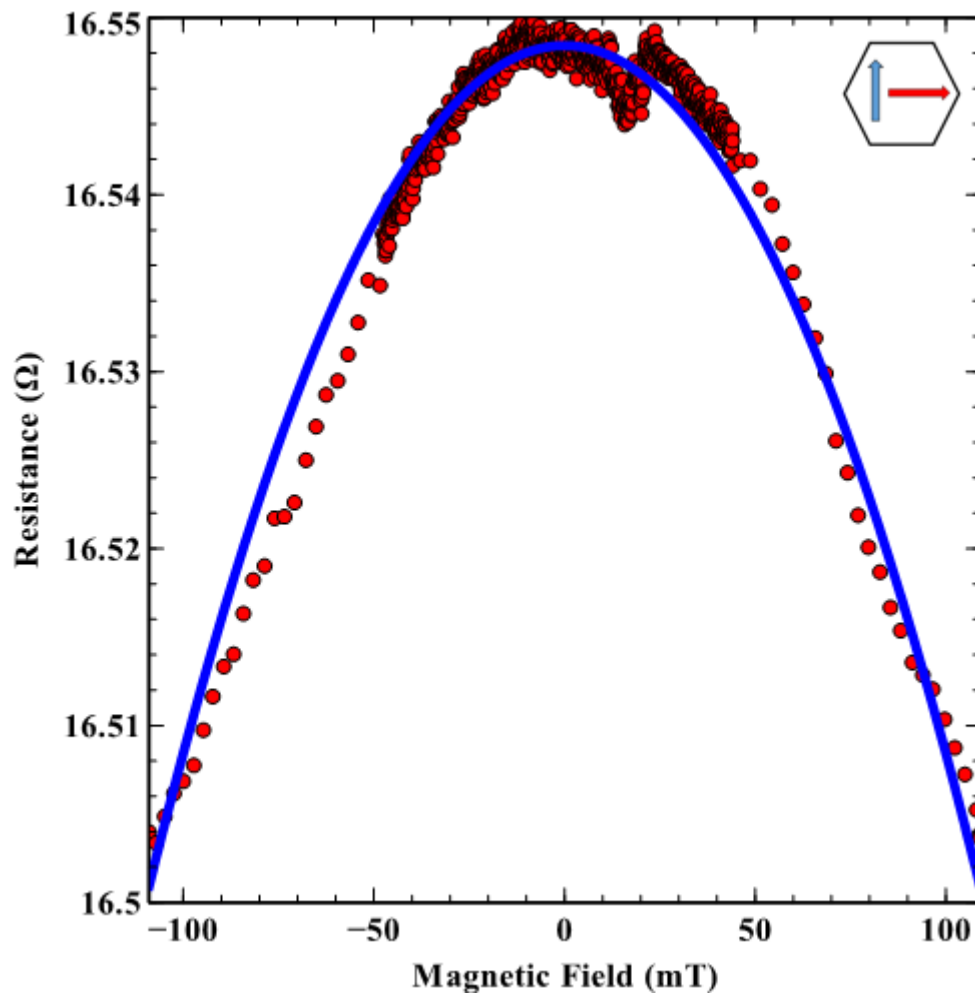


Figure 6.26: Fitting a curve to the AMR data obtained for Orientation 1 of the hybrid hexagonal lattice, on sample ASI43 – the blue curve is an attempt to match the background AMR effect but is not physically representative - the inset panel showing how the current (red) and the applied magnetic field (blue) are orientated in relation to the hexagons of the lattice

Using this fit, the switching signal has been extracted, with the graph focussing on the low-field data, due to the unsuitability of the fit at higher fields and its lesser significance by comparison.

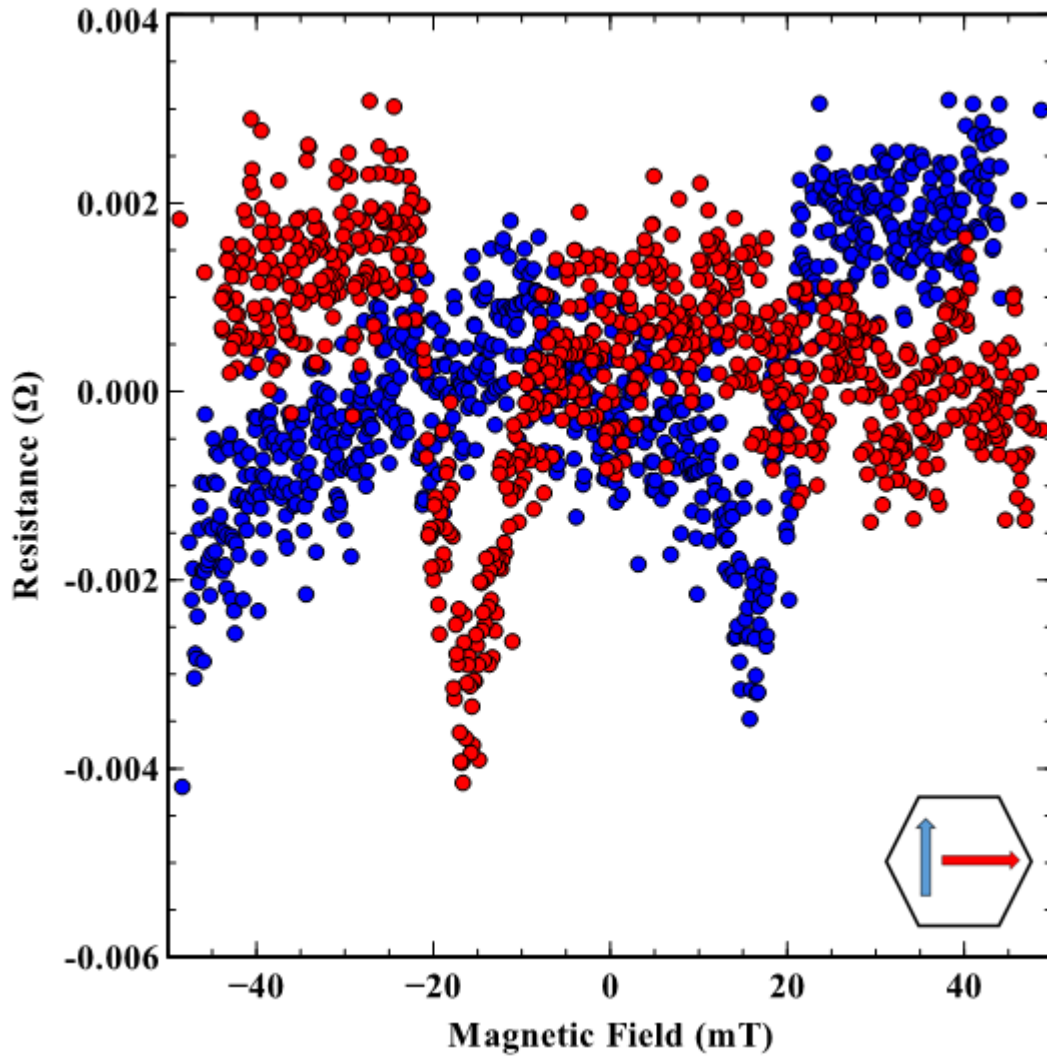


Figure 6.27: The resulting difference when subtracting the curve fitted to the data for Orientation 1 of the hybrid lattice from the data itself - the inset panel showing how the current (red) and the applied magnetic field (blue) are orientated in relation to the hexagons of the lattice

This resulting difference between the raw data and the fit to account for the background AMR results in the switching signals bearing a strong resemblance to those signals observed in the other orientations previously, and certainly makes these features appreciably clearer. Again the gradual decrease in resistance caused by the nucleation of the DWs is followed by an abrupt increase in the resistance as these DWs propagate along their nanowires.

6.3.2 Comparing Hybrid Lattice with OOMMF Simulations

The hybrid lattice data can be monitored and examined in comparison with OOMMF simulation data of the single vertex of the hexagonal lattice. The hybrid lattice is considered to be the electrical measurement of the hexagonal lattice where the bars at the vertices are not physically connected, but are in such close proximity to one another as to interact with one another. This was assessed for three different lattice configurations within OOMMF, and the expected AMR data compiled based on the method outlined previously for the single bar and other single vertex investigations in Chapter 0.

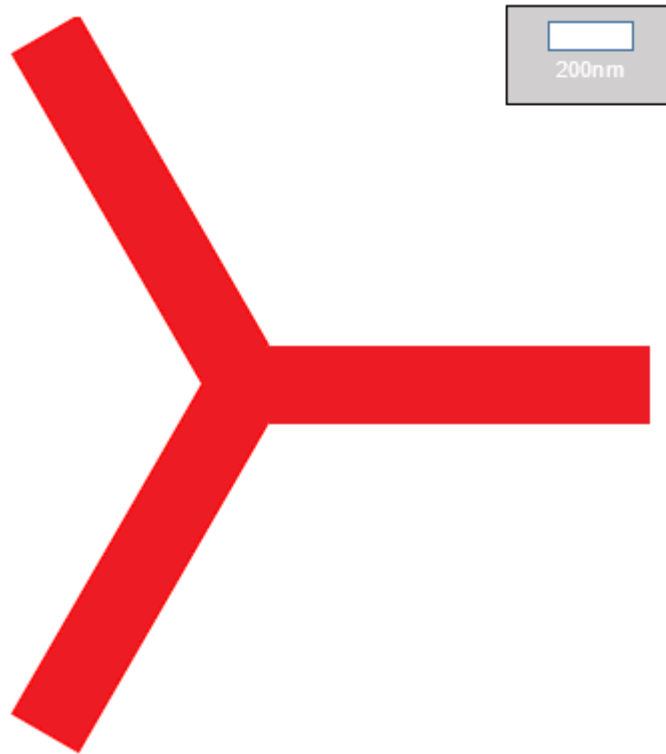


Figure 6.28: Base image created and inputted into OOMMF to simulate the AMR of a single vertex of Artificial Spin Ice, with scale bar inset

It was hoped that there would be a different behaviour between the two unconnected lattices, as this would show the interaction taking place between the unconnected bars like that which has been observed in the hybrid lattice. The three AMR calculations are shown below in Figure 6.29.

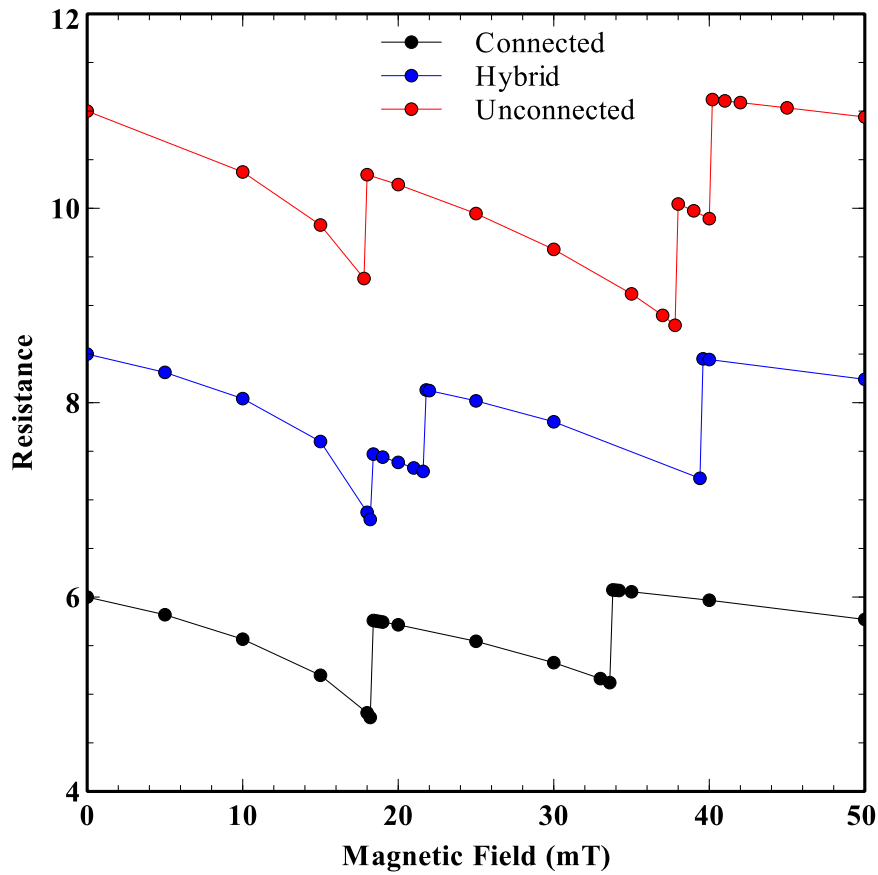


Figure 6.29: AMR data extracted from OOMMF simulations of a hexagonal vertex with varying levels of connection and proximity between the bars – an offset has been assigned to the y-axis measurements such that they do not overlap one another and thus readability is improved

This graph is mainly a clearly useable demonstration of the variation and number of magnetisation reversal events for the three different instances. The first switching event takes place at (18 ± 0.2) mT in all three simulations, and corresponds to the switching of the bar parallel to the field. In the connected lattice example, this also leads to the reversal of the magnetisation in one of the diagonal bars, as the DW is free to propagate along both wires sequentially. This is why there are only two switching events on this data set – as two of the bars switch at the same magnetic field.

In the connected example, the parallel bar has switched at the low field and this is followed by the two diagonal bars having magnetisation reversal. In an ideal system, these two bars are both orientated 60 degrees from the magnetic field, and therefore should reverse their magnetisation at the same field. This does not occur, likely due to minor asymmetries in the base image used in the simulation. It does however, show

that the switching field of the two bars is similar, with one switching at 38mT and the other at 40mT.

In the hybrid example, the proximity of the bars is closer than in the case of the unconnected lattice, albeit the bars are not physically connected. This does not allow the propagation of the DWs from one bar to the next, as in the connected. However, there is still an interaction which is observed in the data for the hybrid, as noted that the second magnetisation reversal occurs at roughly 22mT in this case, rather than the 38mT in the previous unconnected case.

6.3.3 Comparing Hybrid & Connected Lattice

A comparison was collected of an identical set of measurements across both the connected lattice and the hybrid lattice.

The first comparison, detailed earlier in this chapter, was that which discovered that the RRR of a connected Permalloy lattice is higher than a hybrid structure consisting of a combination of Permalloy with gold vertices. This can be attributed to the fact that the measured region of the spin ice contains a large number of interfaces within a hybrid lattice, compared with no interfaces in the measured region of a connected lattice. The interface resistance between a ferromagnet and a normal metal is larger than in the surrounding materials, with literature equating the interface resistance between Permalloy and silver to be 50m Ω . [101]

For the next study, a comparison of the switching mechanisms involved in both lattices, a consistent measurement type was chosen, to ensure that similar elements of the lattices were being investigated in both devices.

The connected and hybrid samples were measured for all orientations, with the comparison below initially focussing on Orientation 4.

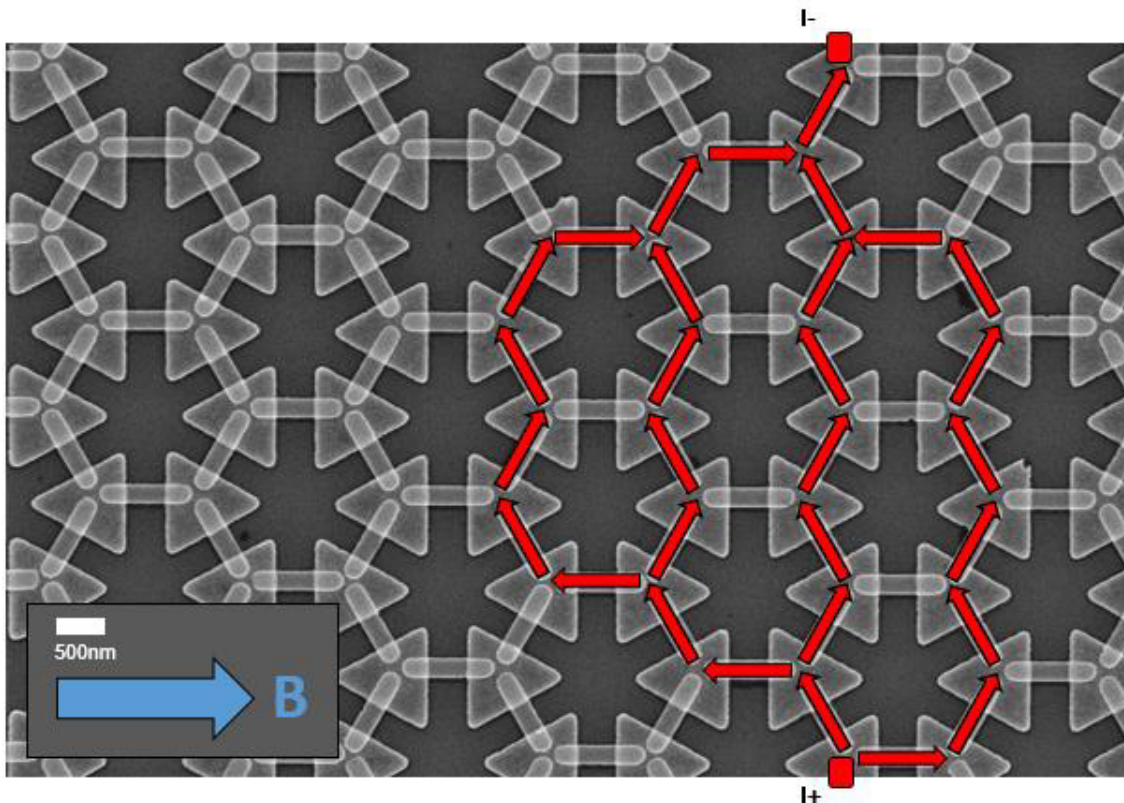


Figure 6.30: SEM image, highlighting the direction of the applied magnetic field (Blue) and the direction of the current path through the hybrid lattice (Red) during measuring of Orientation 4 flowing from the positive end to the negative end. This is a simplified representation as, given the size of the contacts relative to these wires, there are likely to be several start and end points of the current path

Figure 6.30 shows the measurement in Orientation 4, in which only the diagonal bars are being measured, and so only 2 of the 3 bars of each vertex are measured in the case of measuring the magnetotransport. As is therefore clearly seen, Orientation 4 sees the current path primarily running through bars which are neither parallel nor perpendicular to the external magnetic field. In fact only a small number of bars parallel to the field are registered in this measurement.

The AMR at large applied field values stems from the minor rotation of magnetic moments to align more closely with that field, and, by definition, this will have a stronger effect in regions where the easy magnetisation direction is not already parallel to the field. As Orientation 4 has few bars parallel to the field sampled in the measurement, the high-field AMR effect is proportionately large as the field increases, and the resistance drops significantly. An approximation of the current path through Orientation 4 in comparison with Orientation 3 is that the current path in Orientation 4

consists of almost 100% diagonal bars, while in Orientation 3 the measurement includes only approximately 50% bars which are diagonal.

As stated in the previous chapters, the AMR is an effect which is dependent on the angle between the magnetisation and the current, and so in the diagonal bars, where the magnetisation is slowly forced to align more closely to the applied field, its angle to the current increases slowly and forces the displayed decrease in resistance.

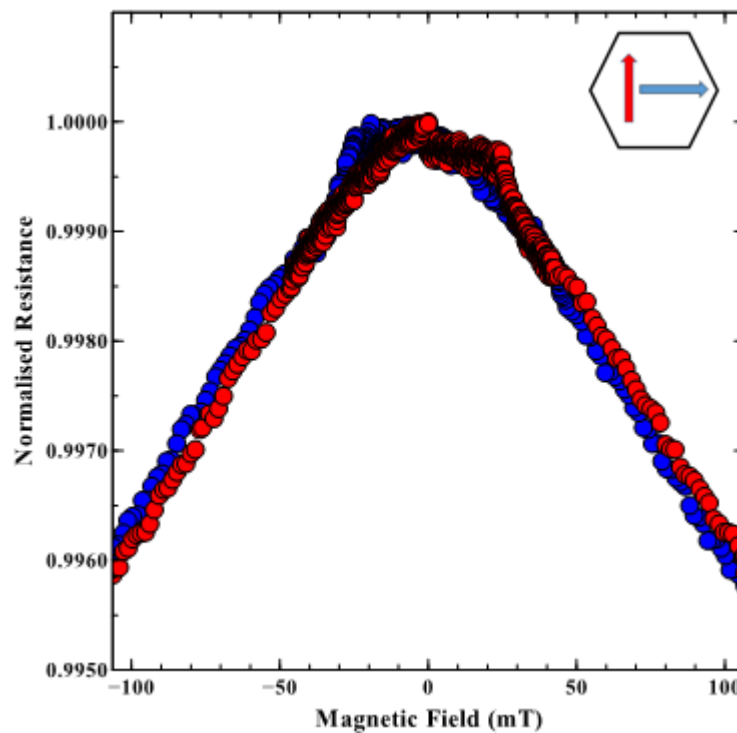


Figure 6.31: The AMR signal for Orientation 4 measurement of a connected ASI hexagonal lattice, on sample ASI46, at Room Temperature - the inset panel showing how the current (red) and the applied magnetic field (blue) are orientated in relation to the hexagons of the lattice

This means that the effect of the large field on the gradual turning of the magnetic moments away from the bars' easy axes will result in a greater decrease in the resistance, owing to the magnetisation and the current path being in directions not parallel to one another. The effect seen at +22mT of the blue sweep, and -22mT of the red sweep shows the switching of the magnetic bars, through a combination of the domain walls propagating through the network, and the rapid reversal mechanisms of the individual bars.

This can be set alongside the following figure, taken from the hybrid lattice and consisting of a measurement of the same orientation.

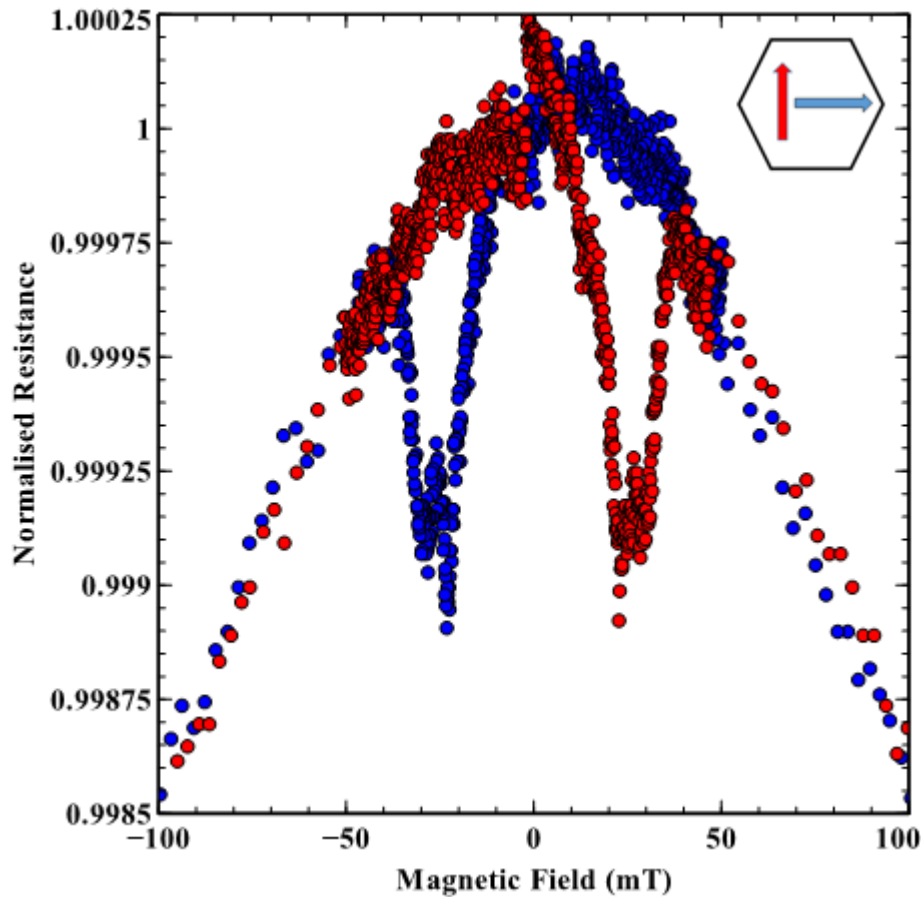


Figure 6.32: The AMR signal for Orientation 4 measurement of a hybrid ASI hexagonal lattice, on sample ASI43, at Room Temperature - the inset panel showing how the current (red) and the applied magnetic field (blue) are orientated in relation to the hexagons of the lattice

Figure 6.32 features the same steep AMR curve at higher fields, owing again to the diagonal bars present in both the hybrid and connected lattice. What is immediately apparent is the completely different switching event present from the hybrid sample. Whereas in the connected structure there is a minor effect present overlaying the AMR curve, in the hybrid sample this switch has manifested itself as two large decreases in resistance as a function of field.

The hybrid structure was designed so as to eliminate the possibility of DWs propagating from vertex to vertex and being the mechanism by which the nanomagnetic elements are reversing. Eliminating this effect, results in the nucleation of a DW within each individual bar, which leads to the magnetisation reversal of each bar separately, instead of simply a single domain wall causing many bars to reverse.

In the connected structure, DWs nucleated at the edges of the lattice can propagate through the network of bars and reverse the magnetisation within them. Each DW can

reverse the magnetisation of several bars. The propagation of the DWs through the network results in a far smaller change in the magnetisation at any one time than seen in the hybrid lattice. Being a series of unconnected nanoislands, every bar in the hybrid lattice will nucleate its own domain wall which will then reverse the magnetisation. So the accumulated decrease in resistance brought about by the individual DWs being nucleated, is far larger in the hybrid lattice than the connected lattice.

These results show, through the magnitude of the effect in the hybrid structures by comparison with the effect in the connected structures, that the predominant effect in conventional connected spin-ice structures is the propagation of DWs through the vertices of the samples. This is due to the lower energy requirements of such a mechanism by comparison with the rapid reversal.

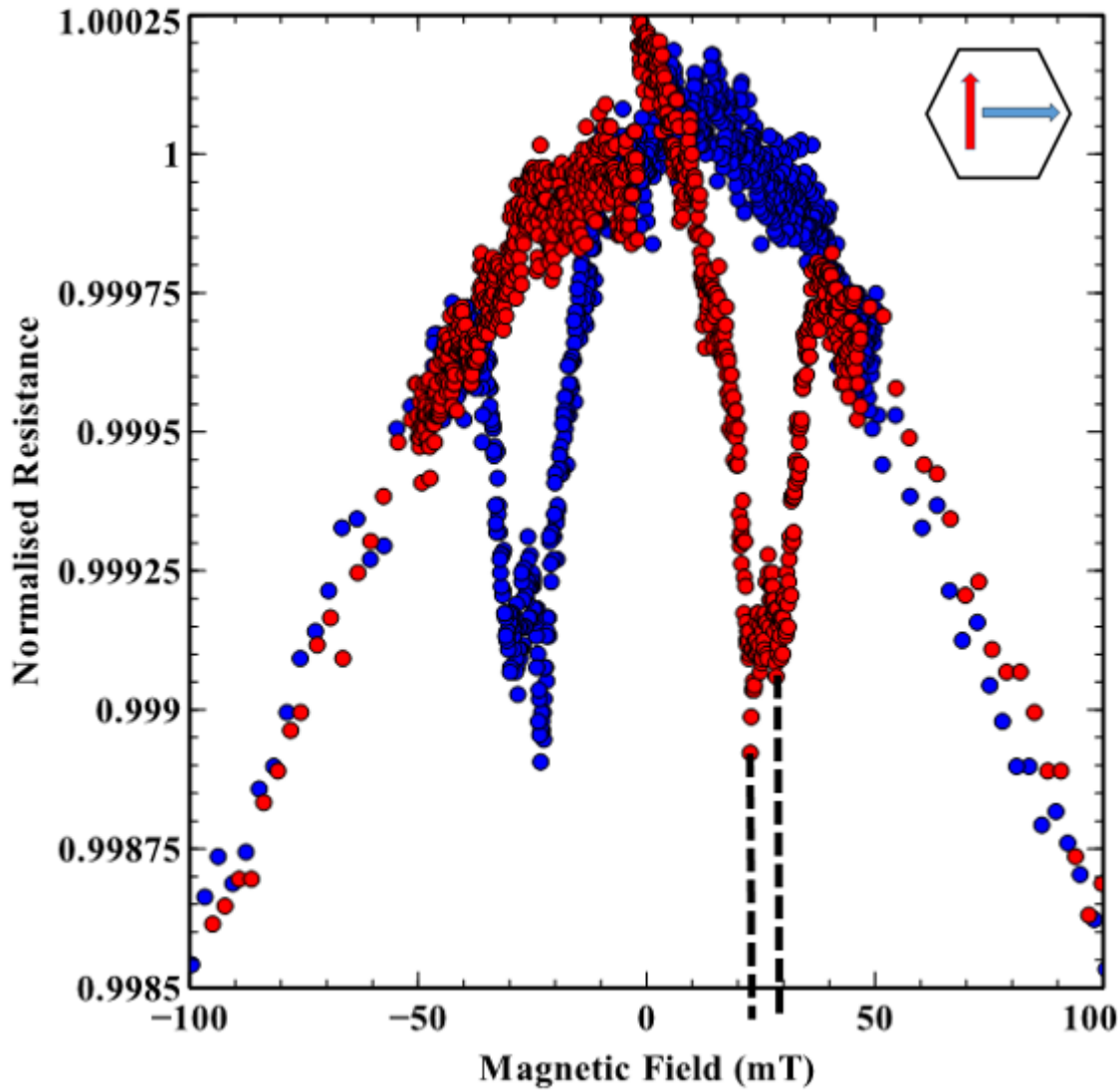


Figure 6.33: Low-field range data for Orientation 4 of a hybrid hexagonal ASI lattice, on sample ASI43, at room temperature, with two dashed black lines showing the two resistance minima and the fields at which they occur - the inset panel showing how the current (red) and the applied magnetic field (blue) are orientated in relation to the hexagons of the lattice

Figure 6.33 shows the same plot but focussed on the low-field range and on the switching of the bars as opposed to the AMR curves.

It can be seen clearly that in both the red and the blue field sweeps, there are two switching events separated by approximately 8mT in absolute field, as marked by the two black lines on the red data. These two AMR signals correspond to the two diagonal bars at any one vertex, alongside the third bar which in my measurements is situated either parallel or perpendicular to the external magnetic field.

6.3.4 Comparison of the hybrid AMR curves for different orientations

A key difference in the data of the two Orientations, aside from the nature of the low-field switches from the overall magnetisation reversal of the bars, is the higher-field effect of the rotation of the magnetisations in the diagonal bars of the lattice.

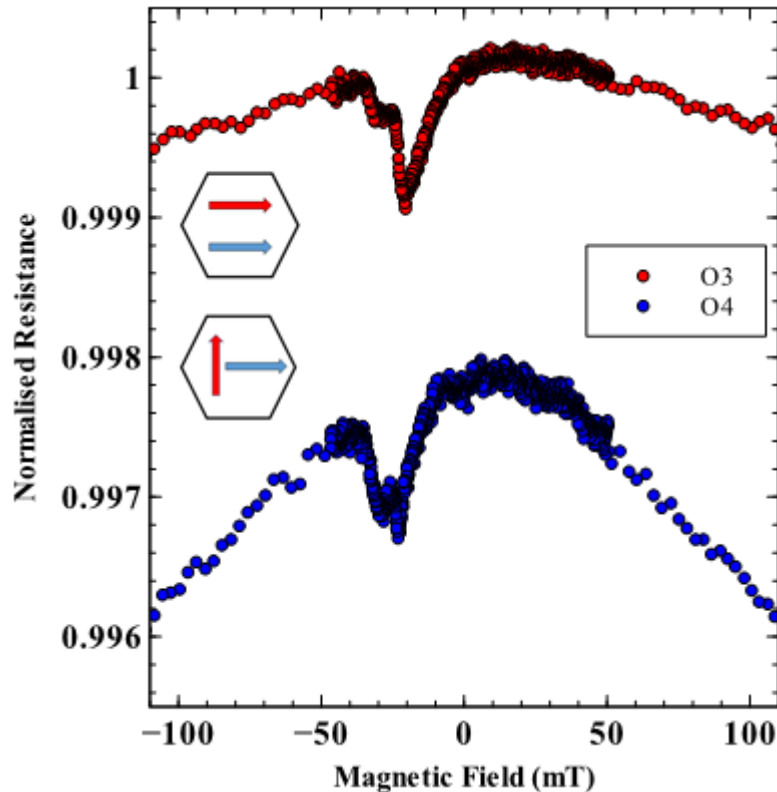


Figure 6.34: Comparing the normalised resistances measured through the hybrid lattice, on sample ASI43, through Orientations 3 & 4 – the offset on the y-axis between the two measurements is deliberate and not significant in the data - the inset panels correspond to the two sets of data, and show how the current (red) and the applied magnetic field (blue) are orientated in relation to the hexagons of the lattice in each instance

There is a stark contrast in the high-field AMR for the two orientations, as is clearly demonstrated in the above figure. This can be again explained through the number of diagonal bars being sampled for each measurement, with Orientation 4 being composed almost entirely of these bars, which results in the stronger high-field effect from the magnetisation in these bars being rotated by the external field away from the easy axis of the bars.

6.3.5 Hybrid Temperature Dependence

The investigation into the temperature dependence of the two different lattices, connected and hybrid, and also the different switching signals within them brought about a range of interesting similarities and distinctions between the two.

Comparing both the data from Orientation 3 of both the longitudinal measurements and the Hall geometry signals, for both the hybrid and connected lattice, the intention was to establish whether the switching mechanisms in these lattices had the same or different temperature dependence on cooling.

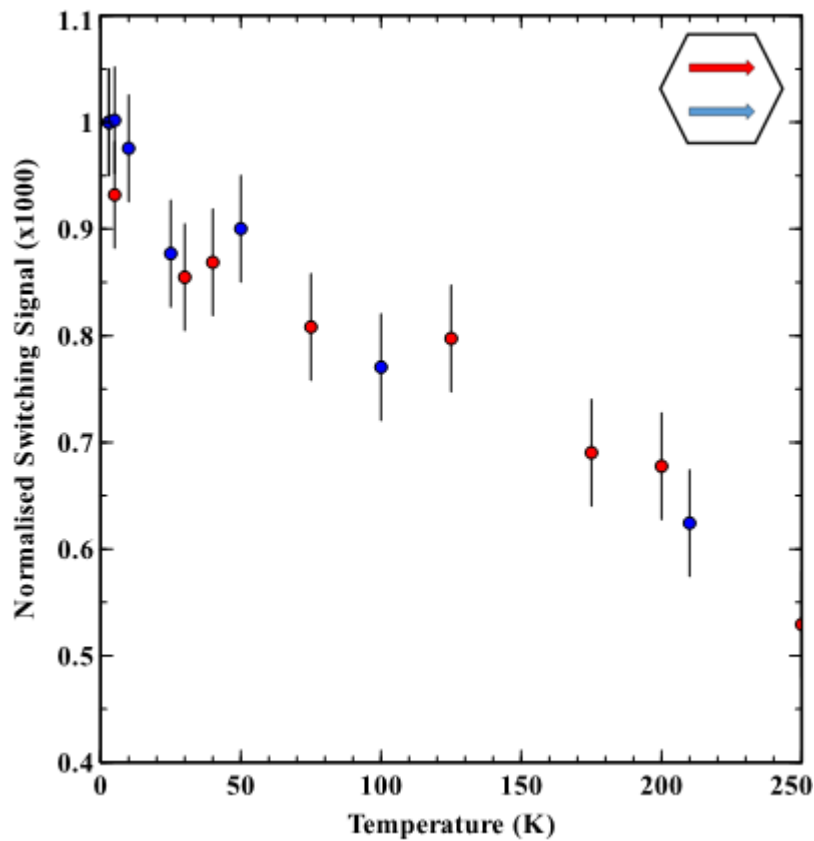


Figure 6.35: The normalised sizes of the switching signals of a hybrid lattice in Orientation 3, on sample ASI43, as a function of temperature – the two different colours refer to data sets taken several months apart, although they contribute to one set of data - the inset panel showing how the current (red) and the applied magnetic field (blue) are orientated in relation to the hexagons of the lattice

Figure 6.35 shows the normalised data compared to the switching signal size, and a pair of measurement sets taken in February 2015 and July 2015, the retaking of measurements being for confirmation of the reliability and integrity of the data, and for comparison with other measurements performed at the later date. The normalisation

method was to give the signal size at 3 kelvin a value of 1, and to adjust the other data accordingly.

The key finding is that of the increase in signal size as the sample is cooled towards 3 kelvin. The signal size doubles as the temperature decreases from 250 kelvin down to 3. The switching signal therefore undergoes a relatively predictable change in its size as the temperature is changed.

Moving on, the next point of consideration was any change that is observed in the coercive field of the structures at the different temperatures.

Table 6: List of the switching fields of hybrid lattices at different measurement temperatures

Temperature (± 0.003 K)	Switching Field (± 0.5 mT)
3	39.0
30	36.5
250	34.0

Little can be discerned from this measurement, except for a gradual increase observed in the switching field as the temperature increases.

This is as expected, given that at lower temperatures the system generally has a lower level of energy, and therefore for the same magnetisation reversal event to occur when the system is at these lower temperatures, a greater amount of energy needs to be added to the system. This is added in the form of the externally applied field.

6.4. Design and creation of the Restricting Lattice

The measurement and results obtained for the hybrid lattice and the connected lattice show the two different effects, as dependent on whether or not the DWs within the lattice are able to propagate through the network between wires, and not be confined to one. Between these two situations, of the connected lattice and the unconnected hybrid lattice, a point of interest is how the behaviour of the system reverts from one to the other. This has led to the study of an intermediary state of samples, which I have called a “restricting lattice”. This is a connected lattice in the sense that it has the continuous network of magnetic material, however around the vertices of the lattice, the magnetic

channel is restricted in width. An example of a vertex in a restricting lattice is shown below in Figure 6.36, showing the form by which the level of restriction in the lattice is defined.

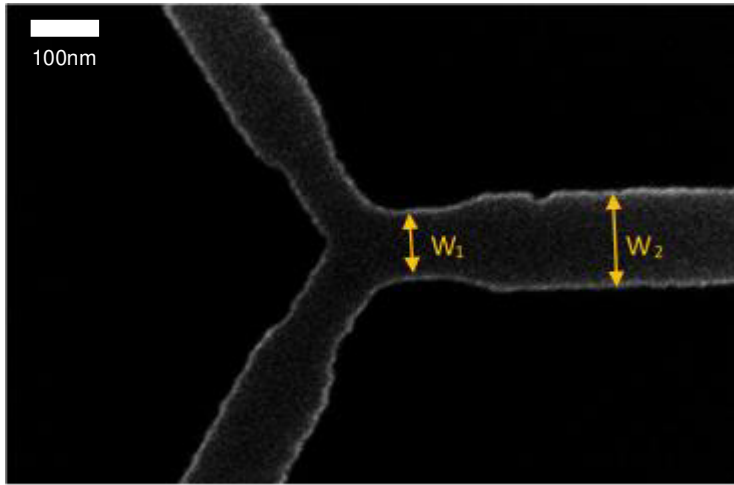


Figure 6.36: SEM image of a vertex within the restricting hexagonal lattice, with the two different widths of the lattice channels labelled – W_2 is the width of the normal hexagonal lattice, while W_1 is a reduction on this, in an attempt to obstruct the propagation of DWs across vertices in the lattice

As shown in Figure 6.36, the lattice's restriction is defined based on two parameters - the widths of the two different sections of the bars, at the vertex and along the bars connecting them. With w_1 being the width of the channel at the vertex, and w_2 the width along the bar, the calculation to determine the lattice restriction is as follows:

$$\frac{(w_2 - w_1)}{w_2} \times 100 \quad (9)$$

So each restricting lattice is defined in terms of the percentage of restriction – a low percentage would mean that the lattice is more closely comparable to a normal connected lattice, with a high percentage meaning that the bars are almost entirely unconnected.

Restricting the dimensions of nanowires to assess the effect it has on DWs and their propagation has been studied before [102], although not in the context of ASIs.

The intention with this design is to inhibit the propagation of the DWs through the sample to different extents – of course this is not as complete a solution to that issue as the hybrid lattice, where the vertices are non-magnetic and therefore the

propagation of DWs is completely prevented. At some level of restriction it will require equivalent magnetic field applications to propagate the DWs through the narrow vertex, and also to nucleate DWs in the bars which are at large angles to the field. This can be determined by considering the angle of adjacent wires in the lattice to these restricted sections, and consider whether the component of the field needed to nucleate the DW is stronger or weaker than the field required to propagate a different DW through the section of restricted width.

This places an onus on the quality of the lithography to be high and to be equivalent across all three bars of each vertex, as it is the intention for the lattice to behave uniformly – so that the entire lattice is either behaving like a connected lattice or like a hybrid.

A series of studies was performed making similar measurements to those for the connected and hybrid lattices previously measured. The measurement orientations used were defined in the same manner, as outlined in Section 4.2.3, and again were performed in both the longitudinal and planar Hall geometries of magnetotransport measurements. By considering the size and nature of the signals obtained in lattices of different restriction, an attempt was carried out to outline the level of restriction beyond which the DWs do not propagate between bars. The situation where the DW propagates until reaching the restricted vertex, and the increase in field required to overcome this, has strong similarities with the addition of notches to nanowires in existing publications. [103] Particularly the manner in which the structure varies from one wire width to the other can influence the propagation of the walls – whether there is an abrupt change in the width or whether there is a more gradual transition from one width to the other.

6.4.1 AMR Signal size for different lattice forms

Initial measurements of the restricting lattice saw the return to the standard longitudinal magneto-transport measurements, which also offer the opportunity to compare this with the other two lattice forms studied earlier, the connected and the hybrid. The measurements compared initially are all of the Orientation 4 longitudinal magneto transport measurement. The signals produced are all of a similar form, with a fairly sharp decrease in resistance followed by an abrupt increase back to the level of the high-field AMR. However, these signals have different amplitudes for the different lattices, as was already shown for the connected and hybrid lattices, where the signal

from the hybrid is larger than the connected. The measurement of Orientation 4 for a lattice with a 30% level of restriction is shown below in Figure 6.37.

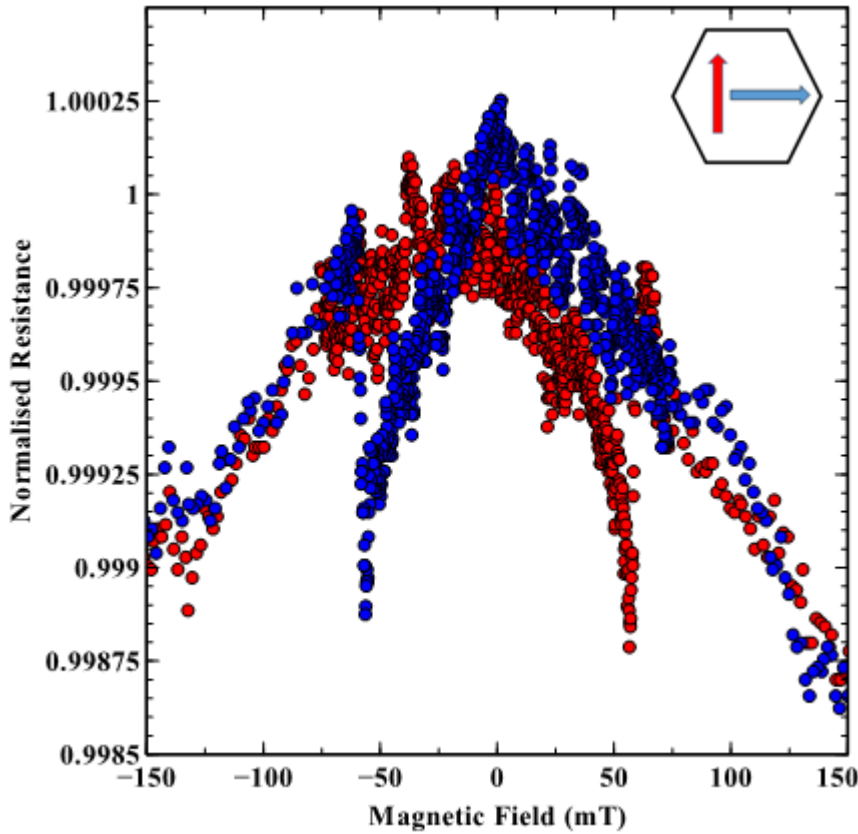


Figure 6.37: The AMR signal for a 30% restricting hexagonal lattice on sample ASI51, carried out in the Orientation 4 measurement geometry - the inset panel showing how the current (red) and the applied magnetic field (blue) are orientated in relation to the hexagons of the lattice

The switching signals observed in Figure 6.37, appearing at 55mT for this particular restricting lattice, are of a similar shape to those observed in other lattices. They feature the same gradual decrease in resistance as the magnetisation is rotated to form a DW within the magnetic bars, followed by an abrupt increase in resistance as the DW has propagated along the wire, reversing its magnetisation. This process is found in all three types of lattice, but their amplitude varies depending on the lattice type. The relative sizes of the signals compared to the overall resistance of the samples is shown below in Table 2, and reveals that the lattice with 30% restriction has a signal similar to that for the hybrid sample, and significantly larger than the connected lattice.

The other repeating feature is the decrease in the resistance observed as the external field is increased, caused by the rotation of the magnetisation in the diagonal nanowires and the difference between the angle of the current and the magnetisation. In the case of this restricting lattice, it is interesting to note the apparent asymmetry in the size of the high-field AMR effect, as in one field direction the resistance decreases by more than in the other. Proof that this is not caused by a field offset can be seen by the switching signals appearing at the same magnitude of applied field in both application directions. The restricting lattice represents a challenge in that the wire widths at the vertices are particularly narrow, in some cases less than 100nm. This can present a challenge in terms of ensuring that the entirety of the sample, particularly the narrower regions, are able to remain in contact with the substrate during lift-off.

Considering the relative sizes of the effects observed in the different lattices, the table below documents the size of the switching signal in Orientation 2 measurements, including this first example of the restricting lattice.

Table 7: Table showing the signal size of AMR measurements in Orientation 2 for a range of different hexagonal lattices

Lattice Type	$\Delta R/R$ ($\times 10^{-3}$)
Connected	0.35 ± 0.10
Restricting (19%)	0.29 ± 0.10
Restricting (30%)	1.10 ± 0.10
Hybrid	1.05 ± 0.10

These preliminary results on the restricting lattices led to the pursuit of another avenue of investigation, namely to understand the manner in which the signal changes across the range from connected lattice to unconnected lattice. Thus far, the data from the longitudinal AMR geometries of the different lattices has appeared to suggest that there are two different regimes, one in which the connected lattices lies and one containing the unconnected, hybrid lattice. It was my intention to ascertain whether there is a gradual change in signal between the two ranges, or whether there is an abrupt boundary at a given amount of restriction, and that there are two fundamentally different types of signal.

Using the lattices of various restrictions which had been created and measured, all considered in Orientation 4 for consistency, the size of the signal as a function of the level of restriction was considered. When comparing the size of the longitudinal AMR geometry signals relative to the magnitude of the resistance, for different lattice

restrictions, and doing likewise for the earlier data for conventional AMR, the results gathered are shown below in Figure 6.38.

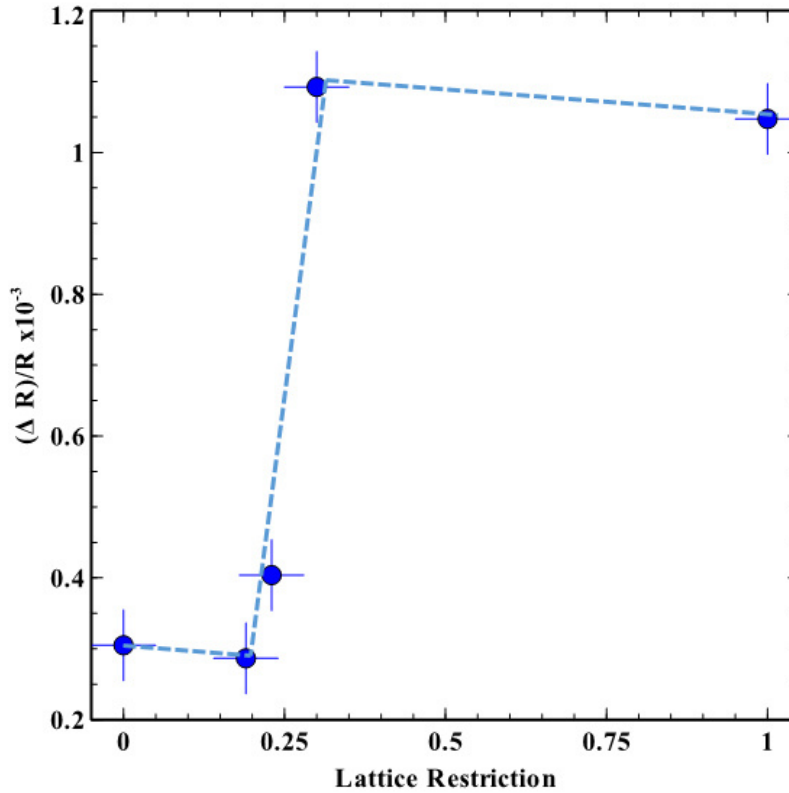


Figure 6.38: The size of the AMR switching signal for hexagonal lattices of different levels of restriction – the blue dotted line is a guide to the eye

The grouping of data points around similar values and, particularly, on the same side of the x-axis, implies a reproducibility of mechanisms occurring on both sides of the transition between reversal mechanisms, appearing at between 20% and 30% lattice restriction. This transition shows the level of restriction required for the lattice to no longer allow the propagation of DWs from one wire of the lattice to the next, as a result of their being no longer able to pass through the vertices. Therefore each wire requires its magnetisation to reverse independently.

Using micromagnetic simulations in OOMMF an attempt can be made to confirm the prediction of at what level of restriction the lattice behaviour changes. This was attempted by considering the case of a single restricted nanowire of both different widths and different levels of restriction. For each of these sets of dimensions, the magnetic field required to propagate a DW through the restriction was measured. These structures were compared to the instance of a nanowire orientated at 60

degrees to the applied field, and the magnetic field required to nucleate a new DW in one of these wires. By comparing the fields, it could be determined, for a given nanowire width, the level of restriction such that the two required applied fields would be equal. It would also reveal the importance of the wire width in this situation and whether a unique level of restriction is required for different wire widths.

Immediately it became apparent that the width of the wire did play a role in determining the necessary restriction for the transition between the two opposing DWs propagating at the lower field. This is immediately evident in Figure 6.39, which focusses on lattice with wire widths of 200nm and 300nm.

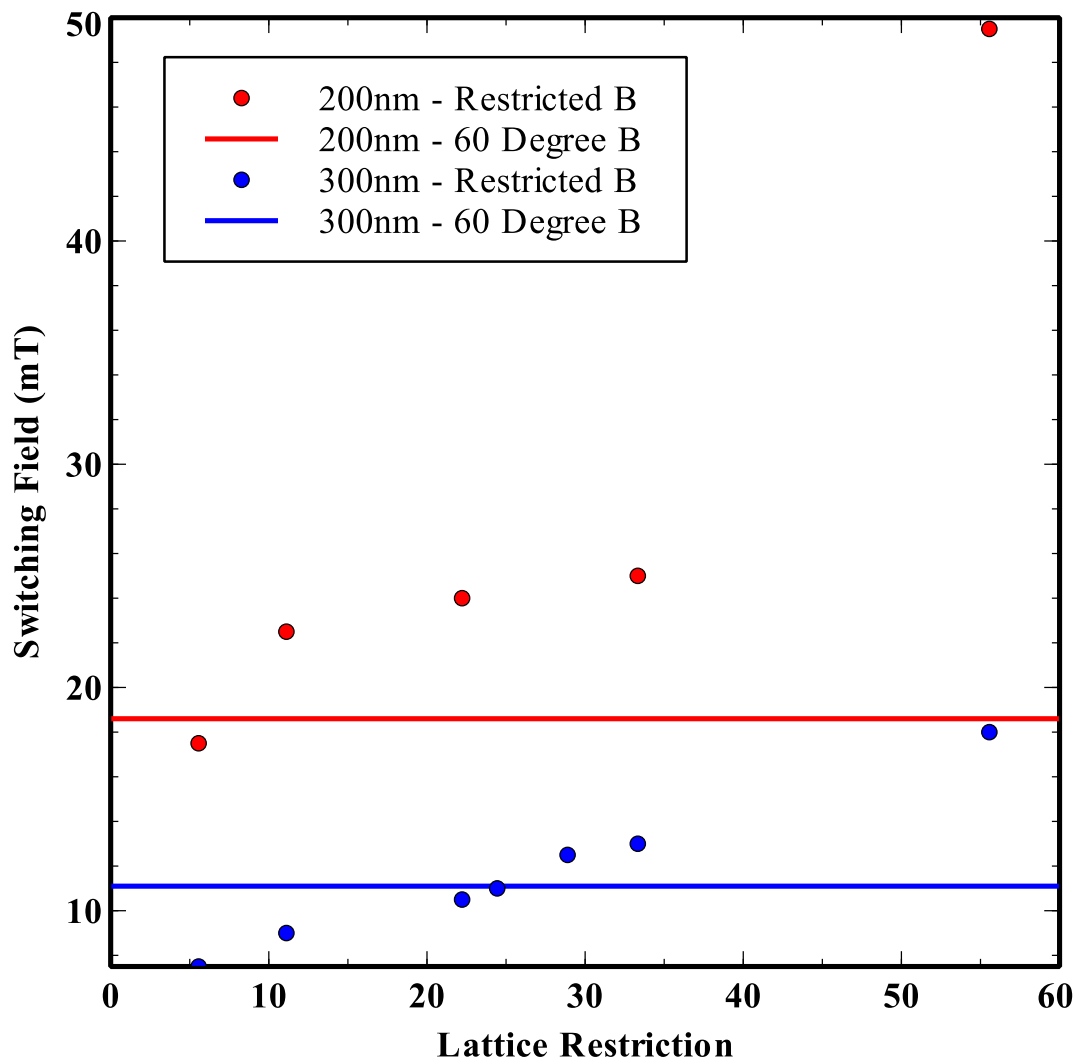


Figure 6.39: Simulating the competing magnetic fields within a restricting lattice to determine the nature of DW propagation – the red data refers to a lattice of wire width 200nm, the blue data for a lattice of wire width 300nm – the solid horizontal lines are the fields required to nucleate a new DW in a wire with 60° to the applied magnetic field

The points at which the data points corresponding to a certain wire width cross over the horizontal line of the same colour, can be read as showing the level of restriction required in the lattice structure, such that the magnetic fields required to propagate a DW through the restricted region, and to nucleate a new DW in the bar orientated at 60° , are equal. This marks the crossover point where, if the restriction was any greater, then the DW propagation between bars would not be responsible for the reversal over the lattice, and instead the sample would behave like a set of unconnected bars, thus replicating a physically unconnected lattice of nanoislands.

Alternatively, any decrease in this level of restriction would ensure that the lattice still behaves like a connected lattice, with the propagation of DWs between neighbouring wires being the governing mechanism for magnetisation reversal. It must also be clarified that this threshold level of lattice restriction varies depending on the width of the bars in the lattice.

This threshold level of restriction is markedly different for the two wire widths investigated here, with the 200nm-wide wires having a critical restriction of just 8%, whereas for a wire width of 300nm that restriction increases to 25%. So the level of restriction required appears to depend strongly on the standard dimensions of the lattice.

To further evaluate this, the manner in which the critical restriction is affected by the width of the wire was analysed for a greater number of different wire widths.

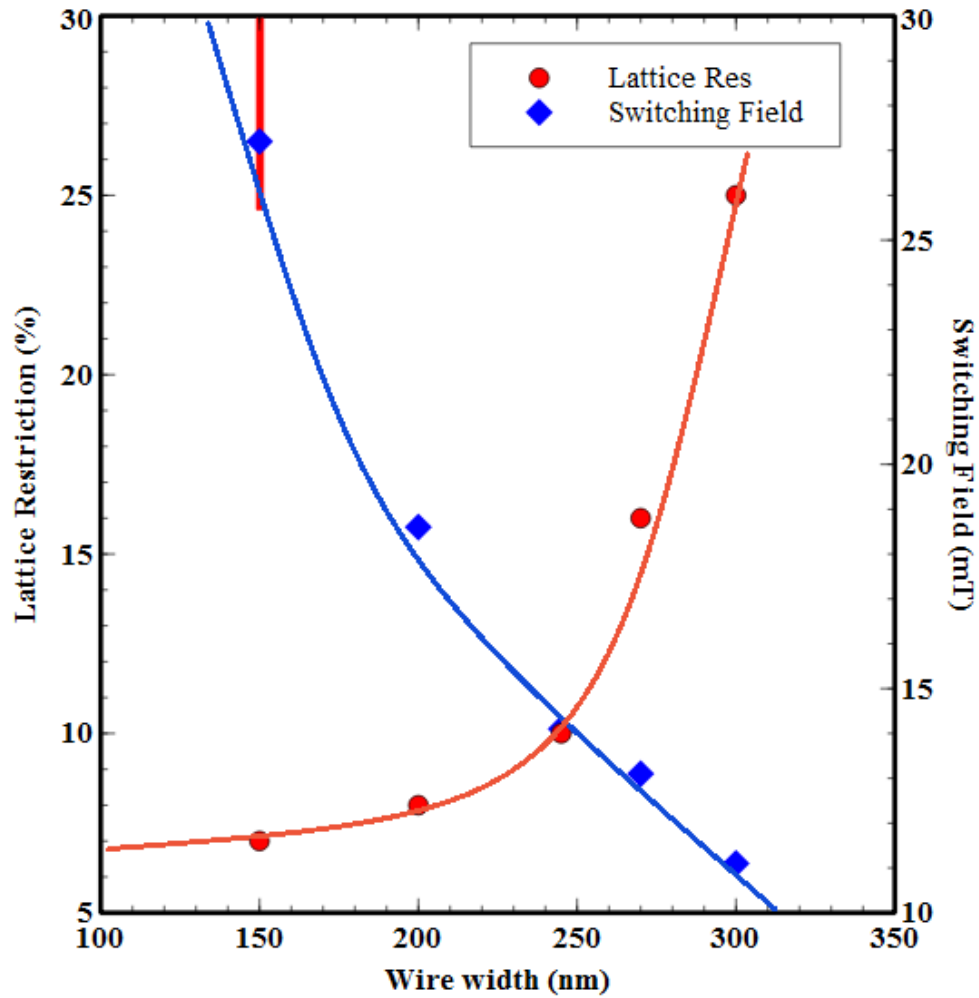


Figure 6.40: How the critical restriction of the hexagonal lattice varies as a result of the width of the wires within the lattices, and the corresponding switching field at the critical restriction – the blue trace shows how a reduction in the width of the wires results in an increase in the threshold restriction level at which the propagation of the DWs ceases to be the dominant reversal mechanism. The red trace shows the applied magnetic field required in order for a new DW to be nucleated in a wire, of widths as shown on the x-axis, angled at 60 degrees to that field – the narrow red rectangle represents the experimentally suggested approximate critical lattice restriction for a lattice with width 150nm – the red and blue lines are guides to the eye

The gradual result of this is that the critical restriction increases as the standard wire width in the lattice increases. This means that in a wider lattice, the DW propagation through the restricted region of the lattice is easier than nucleating a DW within the 60° wires, and the restriction needs to be greater before the nucleation is the favourable outcome. This is because, as the wires get wider, the restriction needs to be greater for it to be significant. In the previous studies on how the wire width affects the coercive field of the nanowires, there has been evidence of diminishing returns – that is to say that the change in coercive field is reduced with increased wire width.

All of which means that a restriction on the nanowire needs to be more sizeable for it to have an effect on the propagation of the DWs, and therefore the critical restriction is greater for wider wires.

The samples used in the experimental measurements are actually narrower than most of those which have been simulated, with the widths of the wires being 150nm. Therefore, on the basis of the simulations, the critical restriction should be lower than the 25-30% region suggested by the experimental data, as represented by the red ellipse on Figure 6.40. The reason for the discrepancy can be explained by the nature of the transition between the normal wire and the restricted portion of the wire.

In the simulations to this point the wire has seen a very abrupt change in the width into the region of restriction, with an immediate change from the regular width to the restricted width. This contrasts with the SEM images shown of the typical restricted samples experimentally measured so far, where the lithography has created a more gradual transition between the two wire widths. This makes the restriction less effective at halting the DW propagation, and so this will result in an increase in the critical restriction, which is what has happened in the experimental data for these lattices.

To prove this, a series of further simulations sought to confirm the effect of making the restriction more gradual, instead of simply an abrupt transition from the normal wire width. This immediately showed promising results. In the abrupt case, the 150nm wire had a 7% critical restriction, and this had a switching field of 27mT. When dramatically increasing the restriction to 36%, the expectation is that this would increase the required field considerably, and indeed, in this case the switching field is increased to 36.6mT.

However, by making the transition less abrupt and more gradual, the switching field was reduced to 23.5mT, despite the restriction being more than 5 times greater.

Another way to assess this is to see how the critical restriction changes considerably when the nature of the restriction is changed. The critical restriction for the lattice with a wire width of 150nm and abrupt transitions is 7%, whereas when these transitions are made gradual, the critical restriction is 52%. Of course this is now significantly higher than the critical restriction found experimentally for a lattice with this wire width. This does, however, support the suggestion that the reason for the experimental samples not having strong agreement with the initial simulations concerns the manner in which the restrictions are depicted.

A final evaluation of this theory is to attempt to design the simulated wire to have as similar an appearance as possible to that of the experimental wire. For this, the SEM images are required to be able to make a note of the manner in which the wire width is gradually restricted, to best mimic this in the simulation. As was mentioned above, the critical restriction for where the transition has been more gradual, is significantly greater than what was experimentally measured. This should be because the transition in the experimental sample, while not being abrupt, is less gradual than these simulations. Accurate measuring of the SEM images of the experimental sample will confirm or deny this.

Table 8: Detailing how the nature of the transitions within a restricting lattice affect the DW propagation and, therefore, the critical restriction

Exp/Sim	Wire width (nm)	Res Rate (%nm⁻¹)	Critical Res (%)
Simulation	150	Abrupt (∞)	7
Experiment	150	0.45	27*
Simulation	150	0.13	52

In Table 8, “Exp” and “Sim” are the abbreviations for Experiment and Simulation, and “Res” is the abbreviation for Restriction. Table 8 reveals that the experimental data is in keeping with what is expected based on the simulations carried out thus far, and the samples’ measured physical dimensions. The simulation where the transition is abrupt can be considered in theory as having an infinite rate of restriction. Clearly, the critical restriction is smaller when the transition is more abrupt, as this is the characteristic changing within the wires for these different measurements – with the materials and the wire widths remaining consistent.

This suggests further that the simulations of these samples are in agreement with the early measurements of restricted samples, and that determining a restricting lattice’s critical restriction is a complex mixture of the width of the wires and the nature of the transition between the regular wires and the restricted vertices.

6.5. Conclusions

This second results chapter builds on the results of the first, where the hexagonal ASI lattice was investigated in terms of both the signal vertex instance and the connected

lattice of these single vertices. The connected lattice is one of the two common forms of ASI, along with the lattice of physically unconnected nanoislands. A means of electrically measuring these unconnected islands, the hybrid lattice was derived, which attempted to form a connected network to enable the performing of electrical measurements on a lattice, while still maintaining the fact of the nanoislands being unconnected, preventing the propagation of the domain walls within the lattice through multiple bars.

This produced novel and interesting data when magneto-transport measurements were performed on this lattice. Observed was a clear difference between connected and hybrid lattices in terms of the profile of their switching signals, based on the fact that the DWs don't propagate through the network and each bar has to rotate its magnetisation individually. The single clearest effect this had on the AMR data for the hybrid sample was an increase in the signal size, which varies for different magnetic orientations, but leads to the conclusion that the DWs, which could each propagate through large numbers of nanowires in the connected lattice, are confined to a single wire in the hybrid case.

From this, and considering the connected and hybrid lattices as the two extremes on a scale of lattice "restriction", came the invention of the restricting lattice, whereby the lattice is fully connected single material, but where the vertices are narrower than the connecting nanowires. It was hoped to be able to map out the transition between the two switching conditions, with the free propagation of the DWs through the lattice and the narrow vertices preventing this.

7. Studying the interactions of magnetic Domain Walls (DWs) in adjacent nanostructures

Previously in this thesis, the focus has been on the hexagonal lattice, but this chapter takes a different focus. It consists of an investigation into the interactions between magnetic domain walls in adjacent nanostructures, be it through the horizontal or vertical separation of the wires (with respect to the substrate).

Firstly, there is a focus on the interaction between Domain Walls (DWs) which are situated in pairs of magnetic nanowires. The experiment intended to monitor interactions between the DWs in these neighbouring nanowires, and to establish the potential of causing the two DWs to pin each other in place within uniform wires, such that it cannot be attributed to other effects.

Secondly this chapter considers the case of vertical interactions, where the possibility exists for the creation of two magnetic layers, separated vertically by a non-magnetic layer, allowing for the magnetic interactions to be monitored. This approach would also provide two different investigations to be carried out through the same experiment.

It allows for the possibility of the DW interactions of adjacent nanowires to be investigated in a situation vertical to the substrate. But it also opens the possibility of an interesting variation of the square lattice Artificial Spin Ice (ASI).

One element of a hexagonal lattice which is not true of a square lattice, is that all of the interactions between pairs of nanowires around a vertex have identical magnitudes, so the lattice is designed with no inherent bias.

This initial section focusses on work which ultimately will look to achieve a square lattice which will feature equal interactions at each vertex throughout its geometry. This can be achieved by designing the lattice to consist of two layers, each one containing only parallel-orientated magnetic bars. If designed carefully then a lattice can be created with equal interactions across all sets of neighbouring bars.

Once again, any measurements of the Anisotropic MagnetoResistance (AMR) in this chapter are displayed in the same format as those previously, with the denoting of the field progression following the same as in previous chapters, shown below in Figure 7.1.

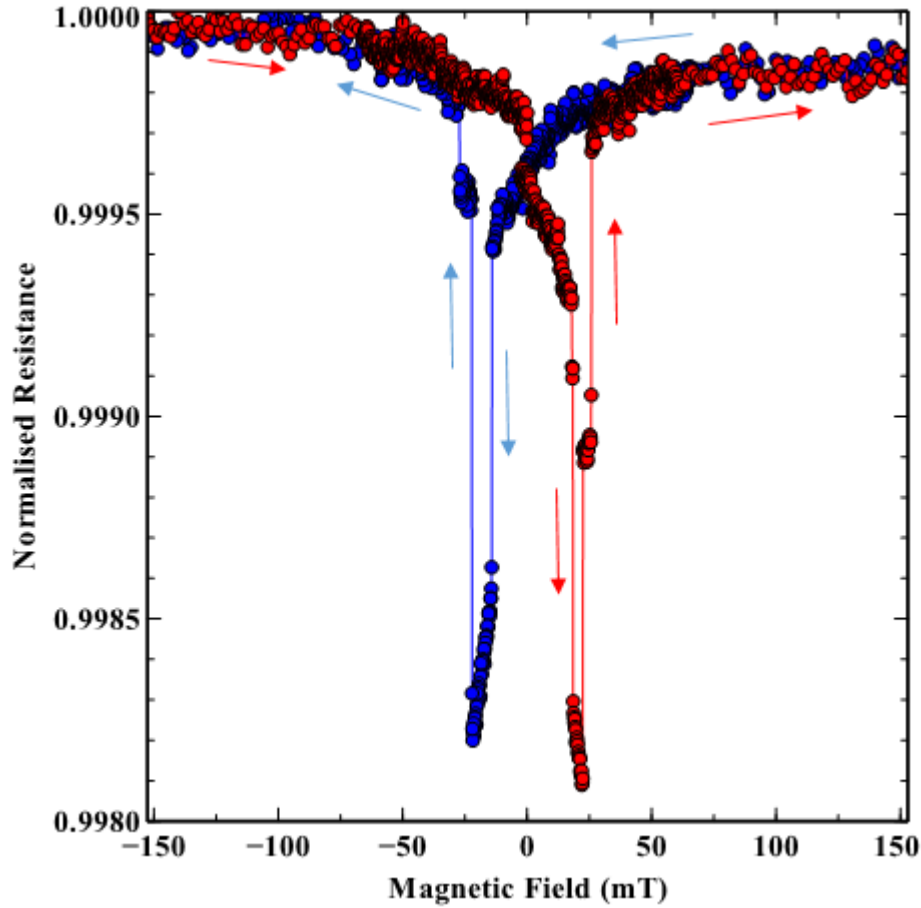


Figure 7.1: Example of a magnetotransport measurement dataset, with coloured arrows demonstrating the way in which the magnetic field is changing between data points of the corresponding colours

7.1. Samples for investigating DW-DW interactions

The earlier chapters of my results have focussed on the hexagonal lattice of ASI. In this chapter other nanomagnetic structures are considered, with the intention of investigating how DWs in these structures interact with one another, in different planes relative to the structures. The chapter features a variety of samples and different geometries. In all cases, however, the ferromagnetic section of the sample is made from Permalloy.

7.1.1 DW Pinning in adjacent magnetic nanowire

The first focus of in this chapter regards the interactions between DWs in pairs of horizontally-adjacent magnetic nanowires, created using the sample fabrication process outlined in Section 4.1. The design intends to ensure that, when orientated correctly with respect to an external magnetic field, any DWs nucleated in the wires will not be lost from the ends of the wires. The design is shown below in Figure 7.2.

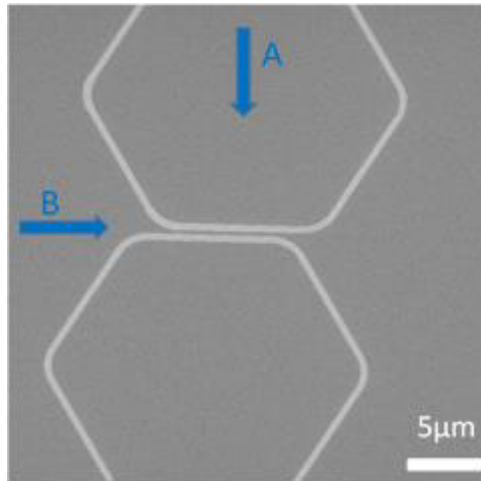


Figure 7.2: SEM image of a pair of magnetic nanowires, designed such that two different DW types can be nucleated into the wires and brought together through magnetic field applications – the arrows labelled A and B show the directions of applied magnetic field pulses during the experiment, required to nucleate and then propagate DWs through the wires

Samples were created such that a DW could be nucleated in each of the two nanowires given a particular application of magnetic field along arrow A, but also the two DWs would be different forms – i.e. the top wire containing a head-to-head DW, and the bottom wire will house a tail-to-tail DW. The importance of this is that the application of magnetic fields along arrow B can cause the two DWs to propagate in opposite directions to each other, thus creating the possibility that they can interact with one another as they pass.

7.1.2 A two-layer variation of the square ASI lattice

One area of high interest to this project is the potential to adapt the conventional square lattice of ASI such that the interactions between all pairs of bars across a vertex are equivalent. Therefore samples of differing complexity were created to build up to

the final sample attempt, beginning with conventional square lattices, both connected network and an unconnected array of nanoislands.

This then proceeds to samples with which studies can be compiled as to the possibility of measuring two distinct layers of magnetic structure in one measurement. Finally, two layer structures are created with the intention of the structures on the two layers interacting with each other. This would provide a key test immediately before creating an ASI across two layers.

7.2. Reproducible pinning and depinning of DW-DW pairs

7.2.1 Outline

An investigation was designed to assess the viability of the use of magnetic nanowires and their domains as magnetic data storage devices, to potentially replace the contemporary method of hard disc drives. The main benefit of the proposed use of these nanowires is the reduction in the physical space required to store a single bit of data. This therefore requires that an important aspect of this is the proximity that these magnetic wires can be positioned alongside each other. The limit on this is that the system needs to operate without the threat of corruption of data through the interaction of domain walls in adjacent nanowires.

My study has investigated pairs of ferromagnetic nanowires, such that their design would allow the DWs which form within them to pin to each other. This will depend on the particular geometry and proximity of the wires. An evaluation of the possibility of pinning and depinning the same pair of DWs will be completed. It will also assess the effect this pinning has on the structure of the DWs, making use of X-Ray Magnetic Circular Dichroism (XMCD) and PhotoEmission Electron Microscopy (PEEM) imaging technique at the Diamond Light Source synchrotron in Oxfordshire, UK.

7.2.2 Experimental

The structures were nanowires of the same cross-sections as those used in the Artificial Spin Ice samples discussed in Chapters 0 & 0. The length of the edges of the hexagons in this instance was $7\mu\text{m}$, with the corners being curved in profile compared with the abrupt corners of the lattices in the ASI cases.

The structures were similar in their basic design, but key elements such as the thickness of the deposited Permalloy, or the distance of separation between the two parallel nanowires, meant that there was a wide variety of different potential pinning strengths, including the prospect of the wires being separated by far enough a distance that pinning will not occur at all.

A magnetic field applied perpendicular to the central axis of the wires, denoted in Figure 7.2 by the letter A, creates the pair of DWs due to the design of the structures. One head-to-head and one tail-to-tail DW are created in this arrangement – this means that they respond oppositely to the same applied field, and so can potentially be brought together to interact with one another.

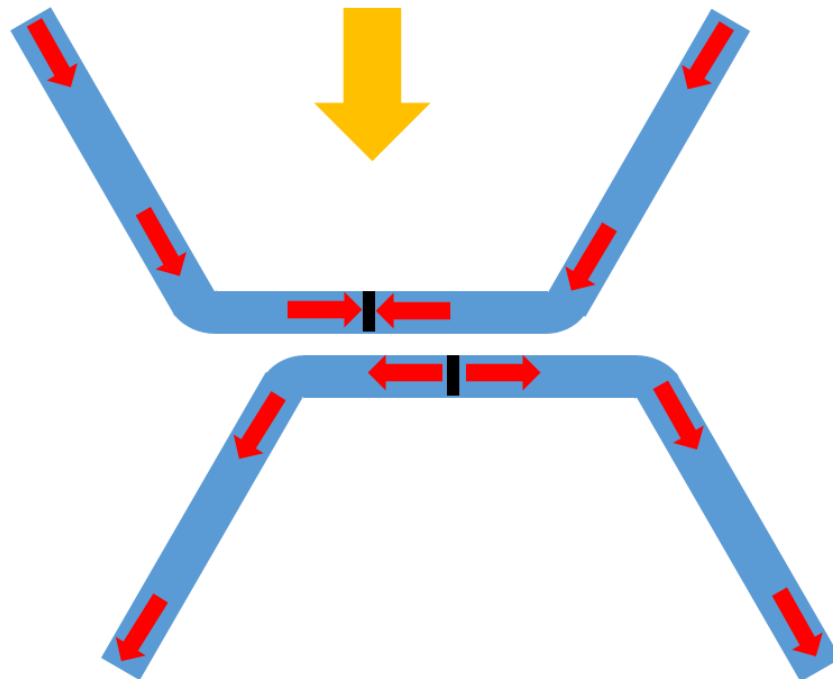


Figure 7.3: Schematic showing the manner in which magnetisation (red) in the sample is directed as a result of the external magnetic field (yellow arrow), resulting in the formation of one head-to-head and one tail-to-tail DW in the two wires

This can be achieved by applying another magnetic field, labelled B, in a direction parallel to the two regions of the wires in closest proximity to each other. This is further illustrated in Figure 7.3.

The image shows the response of the magnetisation to the initial field application along direction A in Figure 7.2 which results in the creation of a DW in each of the nanowires as a result of the geometry. The shape of the DW in the schematic diagram is not representative and the black rectangle is purely an indicator of the DW location, not its

form. This is because the DWs could be transverse, or vortex, depending on the width and thickness of the containing wires. In the case of the samples created for this investigation, the nanowires contained Vortex Domain Walls (VDWs).

The magnetisation is directed along the easy axes of the wires and results, in this case, in there being a head-to-head DW in the top wire, and a tail-to-tail DW in the bottom wire.

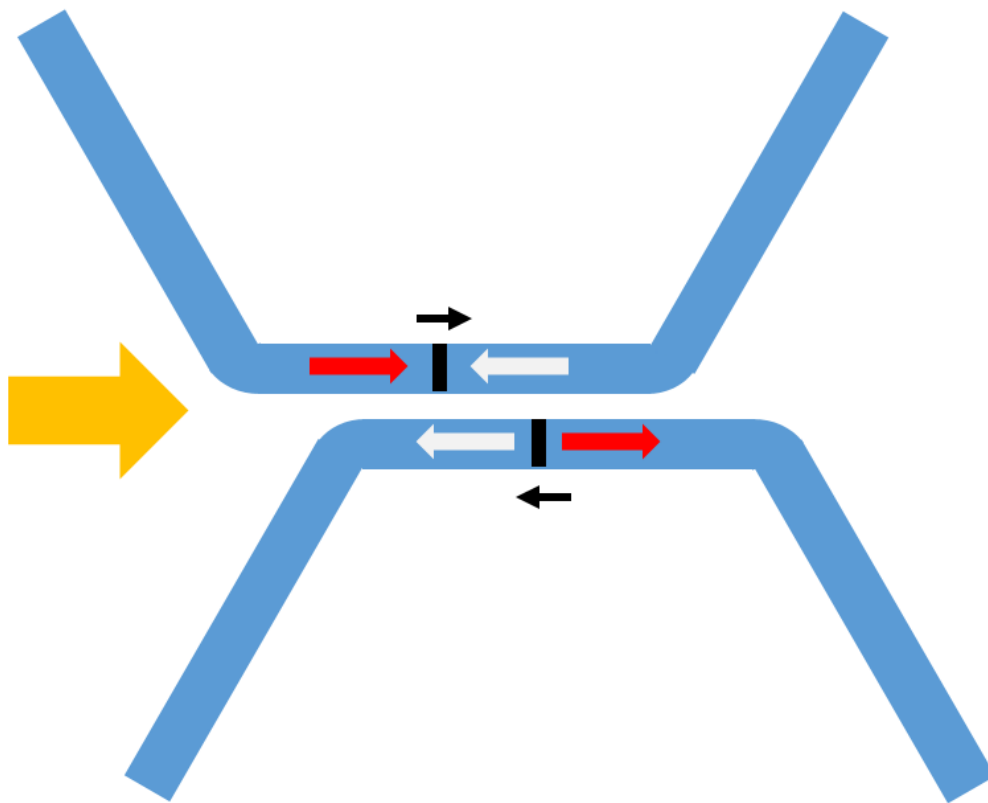


Figure 7.4: Schematic diagram showing the effect of the external field on the two types of DW, with the red and grey arrows showing the two magnetisation directions, and the black arrows the direction of DW propagation caused by the external field (yellow)

When the magnetic field is applied at the angle perpendicular to the initial nucleation angle, then the DWs will propagate along the wires in such a way as to increase the size of the domains parallel to the field, and reduce the domains which are antiparallel. As can be seen from the image, this will result in the propagation of the two DWs being opposites to one another, and under certain conditions, this will result in the DWs passing in close proximity to one another, and potentially interacting.

A high level of magnetic contrast was obtained from XMCD through the PEEM setup at DLS, such that the different domains and DWs within the structures are instantly clear. Such contrast can be seen in Figure 7.5 below:

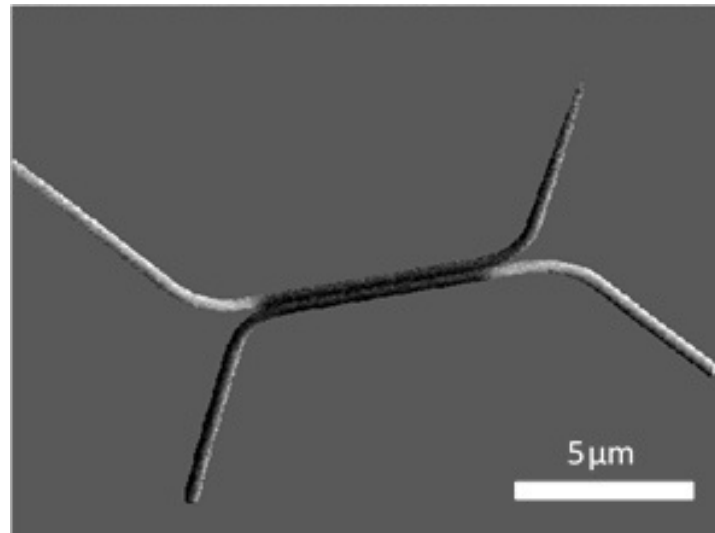


Figure 7.5: XMCD-PEEM image of a pair of nanowires, showing the magnetic contrast of magnetic domains and highlighting the DWs on the wires – the black and white regions of the wires are opposing directions of magnetic contrast

Figure 7.5 is an example of the high quality of images that can be obtained through the PEEM system. Here it is very clear to observe the difference in magnetisation direction between the opposite arms of this pair of wires. Although not shown clearly shown to be the case in Figure 7.5, higher magnification images of the structures reveal that the two wires are completely separate at all points, as is the requirement for the investigation.

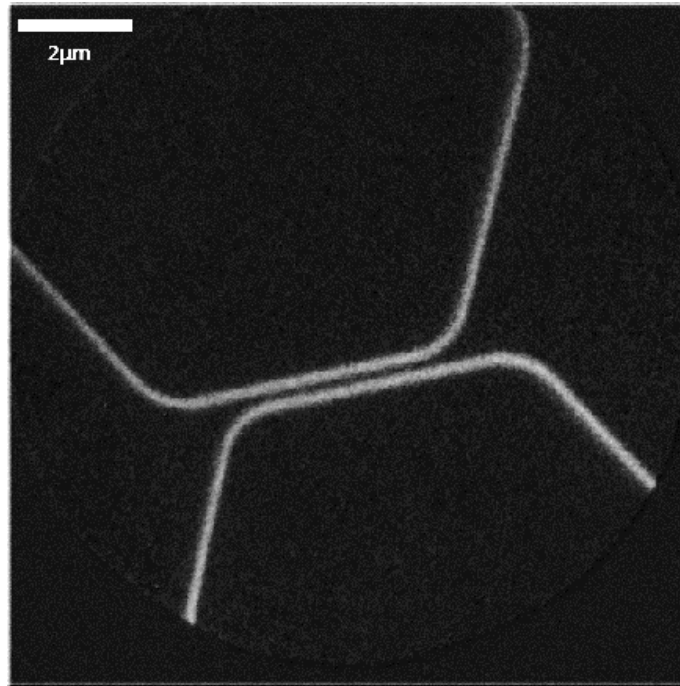


Figure 7.6: Image showing the clear separation of two nanowires used in the DW pinning experiment at Diamond Light Source

In some other structures, where an attempt has been made to maintain as close a proximity as possible between the wires, this has led to the merging of some features through the proximity effect. [9]

This setup of a head-to-head and a tail-to-tail DW at opposite corners of the two nanowires is the ideal starting position to enable the bringing together of the two, and observe their interaction. The sample was thoroughly evaluated for all of the pairs of nanowires deposited onto it, and a list of pairs suitable for the exhibition of DW pinning was created, with one such example being highlighted in Figure 7.7 below.

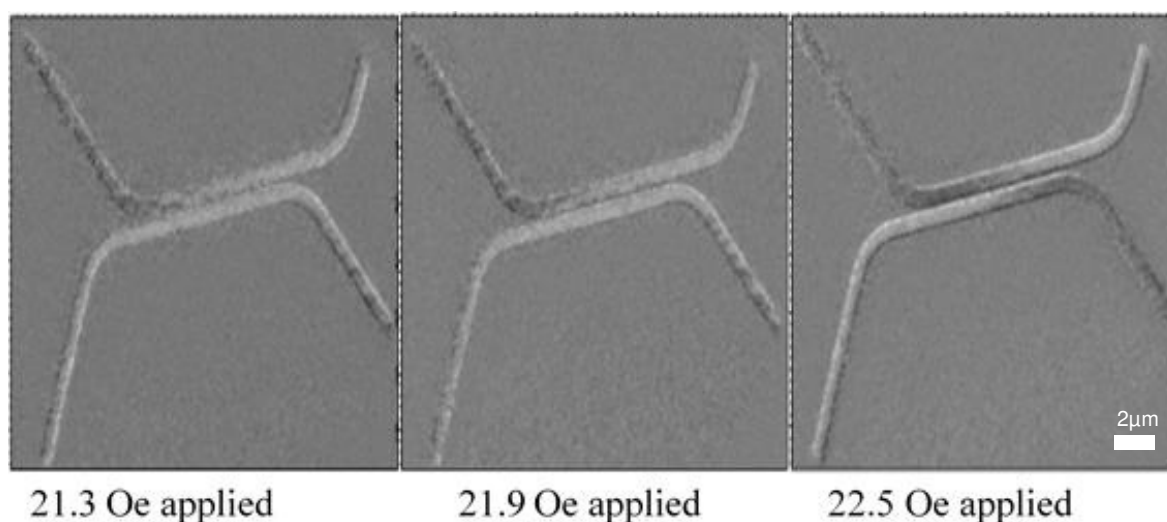


Figure 7.7: XMCD-PEEM images of pinning of DWs in the adjacent nanowires, and the strengths of the magnetic pulses at each different image shown above. The lighter and darker contrast within the nanowires show the two opposing magnetisation directions of the material

By applying short pulses of current across the sample to act as an external magnetic field, it was possible to move the DWs along the wires – in reality this means the growth of the domain that aligns parallel to the field direction, and the diminishing of the antiparallel domain.

In the central section of the two nanowires, where the long axis of the wire runs parallel to the direction of the externally applied magnetic field, the two DWs are brought together and are observed to ‘pin’ in position adjacent to one another.

Due to the straight nature of the wires at these points, a DW moving in either direction would continue to propagate along the wire until it reached an extremity (a far corner) of its wire, such that there was no possible further distance along the wire that it could travel along, with a component parallel to the magnetic field.

Just as the pinning of two DWs can have useful applications in the maintenance of stored data, then the depinning of two previously pinned DWs can also have applications. This could be carried out in two ways, either pulling the DWs apart, or applying a strong enough magnetic field to be able to push the two walls past one another. Figure 7.8, imaging a pair of nanowires at a field-of-view size of $15\mu\text{m}$, shows a variety of magnetic pulses applied along the central region of the nanowires, with the intention to ‘grow’ the magnetic domain shown by the white contrast, and in doing so, separate the DWs.

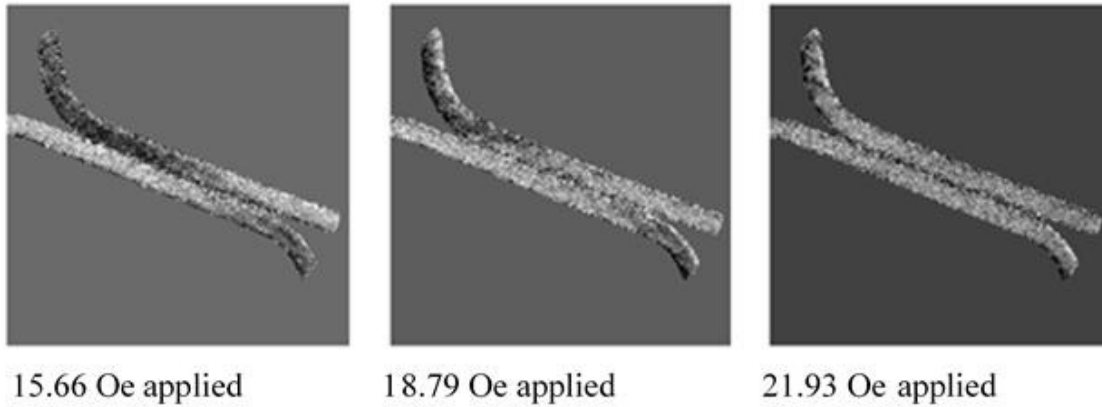


Figure 7.8: XMCD-PEEM imaging showing the depinning of a pair of DWs and the fields (magnitude) necessary for this. The lighter and darker contrast within the nanowires show the two opposing magnetisation directions of the material

The fields shown in this set of images are lower than those in the case in Figure 7.7.

This is a result of a number of different factors, notably the difference in the wire widths, of which more will be explained shortly.

It can also be seen in Figure 7.7, when the smaller magnetic pulses have been applied and the DWs have yet to be moved, they have still be moved around the corner of the wire. As such, their component of the magnetic field is not completely parallel, and so a higher external field is required, in order to have the same effect of moving the DW.

This is a similar situation to that which has been shown previously relating to hexagonal ASI in chapters 0 & 0.

7.3. Quasi 3-D ASI

7.3.1 Introduction

This investigation endeavours to develop the square lattice, introducing a method by which a square lattice of equal interactions can be created. It also sees the attempt to consider the vertical, out-of-plane interactions of DWs in adjacent magnetic nanostructures.

7.3.2 Square Lattice Theory

The hexagonal lattice has been the ASI I have focussed on in my work to this point. However there are other forms of ASI which have been investigated in a variety of other geometries. This has also led to more complex being discussed theoretically, and recently created and measured experimentally. Another commonly used lattice is the square lattice, albeit mostly the investigations previously have focussed on unconnected square lattices. [104]–[106]

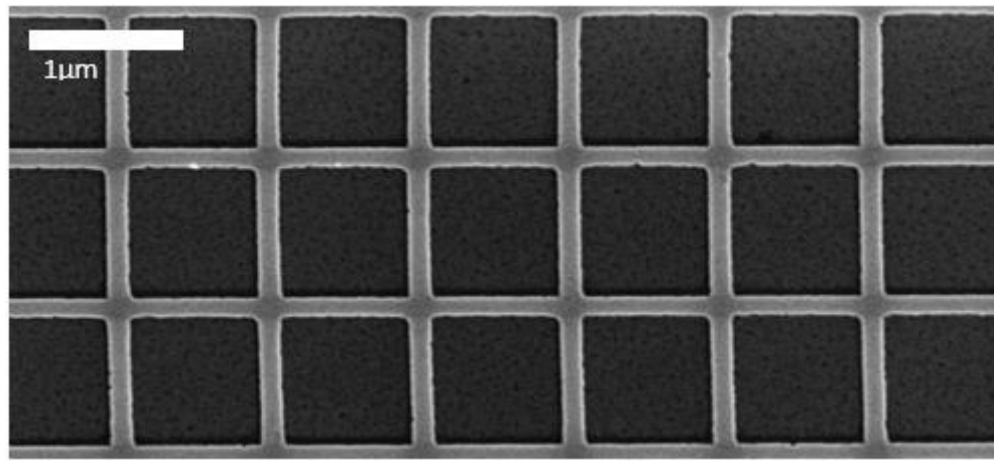


Figure 7.9: SEM image of a connected ASI square lattice produced during a single fabrication process – the bars consist of Permalloy

Here, the lattice consists of 4-vertices, points at which 4 nanomagnetic bars meet and interact with one another, in much the same way as the 3-vertices found in the hexagonal lattice. Below in Figure 7.10 the four bars of a single magnetic vertex are shown in an SEM image.

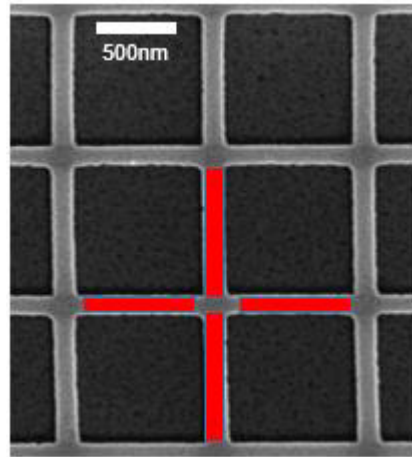


Figure 7.10: Close up of the SEM image of a connected ASI square lattice, with the red lines showing the four bars of a single vertex

Due to the geometry of the square lattice and the relative positions of the bars, there should be at most only two distinct coercive fields to the lattice, irrespective of the angle of the applied magnetic field to the bars of the vertex. If the applied field is parallel to one of the sets of wires, then it will also be perpendicular to the other set, so in this case there would be expected to be only one coercive field, as those bars which are perpendicular to the field would not reverse in their magnetisation. A rotation of the magnetisation to align with the applied field would be expected.

However there is an inherent and important difference between the various pairs of interactions in this lattice to those in the hexagonal lattice. This derives from an inherent asymmetry in the square lattice, where the distances between the different pairs of bars are not equal.

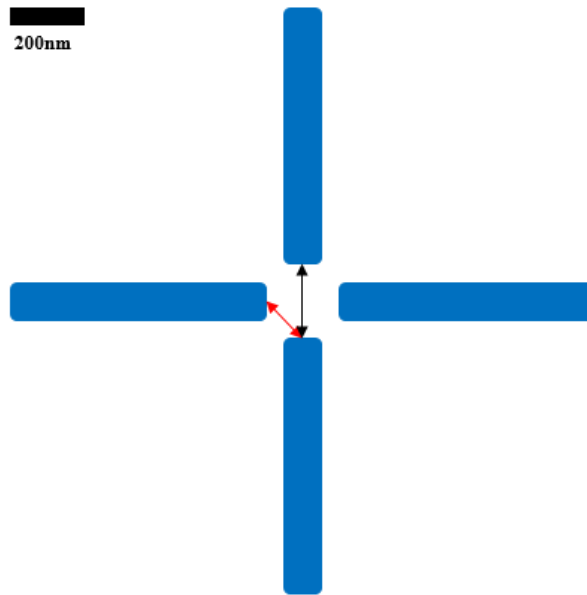


Figure 7.11: Schematic image showing the two varieties of interaction in a square lattice – the red arrow, showing the distance between the ends of a perpendicular pair of bars, is shorter than the black arrow indicating the separation of parallel bars

Figure 7.11 represents the two different types of nearest neighbour pairs which are to be found in a square lattice, and through the geometry of the lattice, these two types of nearest neighbour pair do not have equivalent interactions, so each individual bar experiences three interactions with neighbours across the vertex, which have two different magnitudes, based on the separation distances between the pairs of wires. The geometry dictates that those pairs of bars which are perpendicular to one another are in closer proximity than those which are parallel. This leads to these interactions being inequivalent, leading to the inclusion of a level of asymmetry into the square lattice which is hoped to be minimised within a true spin ice.

This analysis compares with the 3-vertex of the hexagonal lattice, where any pair of bars at each vertex are separated by an angle of 60° , and therefore it can be seen that there is an equivalency in all the interactions of nearest neighbours throughout the lattice. For the square lattice to feature equal interactions for all nearest neighbour pairs of nanowires, as is the case in the hexagonal lattice, an adjustment in the design of the lattice was required. This would also allow for a valid comparison between the hexagonal and square lattices with each containing equal interactions about their vertices.

The interactions between nanowires at 90° to one another are stronger than those at 180° , for a basic square lattice. This is due to the difference in the relative distances

between these two different pairs. A proposal to eradicate this inequality is to intentionally weaken the interaction between the perpendicular bars. This can be achieved by creating the lattice out of two separate sub-lattices. Each sub-lattice contains parallel nanowires, and the two wires of each sub-lattice orientated perpendicular to each other. The inclusion of a layer to lie between these two sub-lattices was proposed, as this should enable for the different pairs of interacting nanowires at each vertex to interact equally with all neighbours.

7.3.1 Experiment Outline

Ultimately, the intention is to be able to produce a square lattice ASI across two-layers such that the interactions between all pairs of nearest neighbours are equivalent, and that there isn't any inherent bias in the lattice which can lead to the lattice being deterministic.

There are different aspects which need to be considered, and which are key to this experiment's success. One aspect is to have the ability to accurately control the vertical displacement between the two layers of the lattice. The non-magnetic layer between the two magnetic lattices, with a controlled and determined thickness, should enable for the creation of the two-layer structure such that the interactions are equal to one another. It will also need to have a suitably low surface roughness, such that the ferromagnetic layer sat atop it will be able to behave in a manner similar to the one lying directly on the substrate.

With the layers (and the individual bars) being separate and unconnected, these samples will be investigated using MOKE. As a result of this, it is imperative that the spacer layer is one through which it is possible to obtain the MOKE signal from the first layer of the quasi-3D structure, as the intention is to interrogate both layers of ferromagnet.

This necessitates preliminary investigations into the ease of measuring through these spacer layers and any complications which may arise. It also immediately places limitations on the types of materials which will be suitable as spacer layers.

Ultimately the decision was taken to use thinner PMMA of the same specification as that which was used in the spinning and Electron Beam Lithography (EBL) processes for the ASI lattices from the first results chapter. This was chosen as it is easily tuneable in terms of its thickness, is transparent and can be simply inverted in order to prevent it being removed by acetone.

While the ultimate goal is to create a two-layer ASI, there are a variety of preliminary investigative samples and measurements which must be produced to attempt to glean information which can be used to guarantee the success of future samples.

The first preliminary exercise required the successful inversion of the PMMA resist achieved through the prolonged overexposure of the resist to the electron beam used in lithographic processes. This enables it to become resistant towards the acetone in the lift-off stage and the MIBK in the development stage.

Measurements could be carried out to establish the feasibility of measuring a sample through the layer of inverted PMMA. It was hoped that MOKE could prove effective at measuring through the PMMA, and any potential challenges which can arise out of this would then need to be considered in more complex measurements.

A simple two-layer sample was created to identify the ease with which both layers can be measured with MOKE simultaneously but also be distinguishable from one another. This was an important test to confirm the size of the relative signals for structures being measured through inverted PMMA, and also for a structure on top of a layer of PMMA, which is also not the normal measuring condition.

The reason for the choice of simple two-layer structure is that this has a level of tolerance for any misalignment in the lithographic process, whereas the Quasi 3-D lattice places a high importance on the alignment being correct in the order of tens of nanometres.

7.3.2 Initial PMMA Inversion

The first step was to perform a successful inversion of the PMMA resist. On a silicon substrate coated in the PMMA resist, two separate patterns were exposed: one at a standard exposure dosage, essentially with the intention of carrying out a routine lithographic and exposure process, the second pattern consisting of 10µm squares in a 10 x 10 grid, with each subsequent square in each direction having an incrementally increased dose.

The intention was to determine the dose at which the PMMA was inverting, that is to say that it was converted into a form where it would not be removed by the Acetone in the final lift-off process. A Permalloy deposition would be performed on the sample, and it was hoped to identify two different thicknesses of the Permalloy in the two different patterns, one where the Permalloy has been deposited directly onto the

substrate, and the other where the Permalloy is situated atop an inverted region of PMMA.

Following on from the attempted deposition of 20nm of Permalloy, the sample was tested for thickness using the Dektak Profilometer [107], a machine designed to map out the height profile of a region atop a sample through the physical interaction of a mounted stylus which passes across the top of the surface of the sample.

The measurement revealed that the standard sample pattern was revealing a height of 20nm, while the region believed to consist of inverted PMMA with a layer of Permalloy on top, had a thickness reading of 150nm. This was measured several times for additional verification, and the discrepancy between these two values was sufficiently large to conclude that this was a genuine result and that the dose applied during the lithographic process had been sufficient as to invert the PMMA.

7.3.1 Preliminary MOKE measurements

The MOKE setup which had been created for the measurement of the ferromagnetic structures required calibration and initial measurement tests, beginning with a large area of Permalloy on a silicon wafer. The amount of intersection between the ferromagnet and the laser spot dictates the potential size of the MOKE signal, and so a thin film will produce a far stronger signal than any ferromagnet. Below in Figure 7.12 is a run of 10 loops measuring the MOKE signal from a region within the thin film.

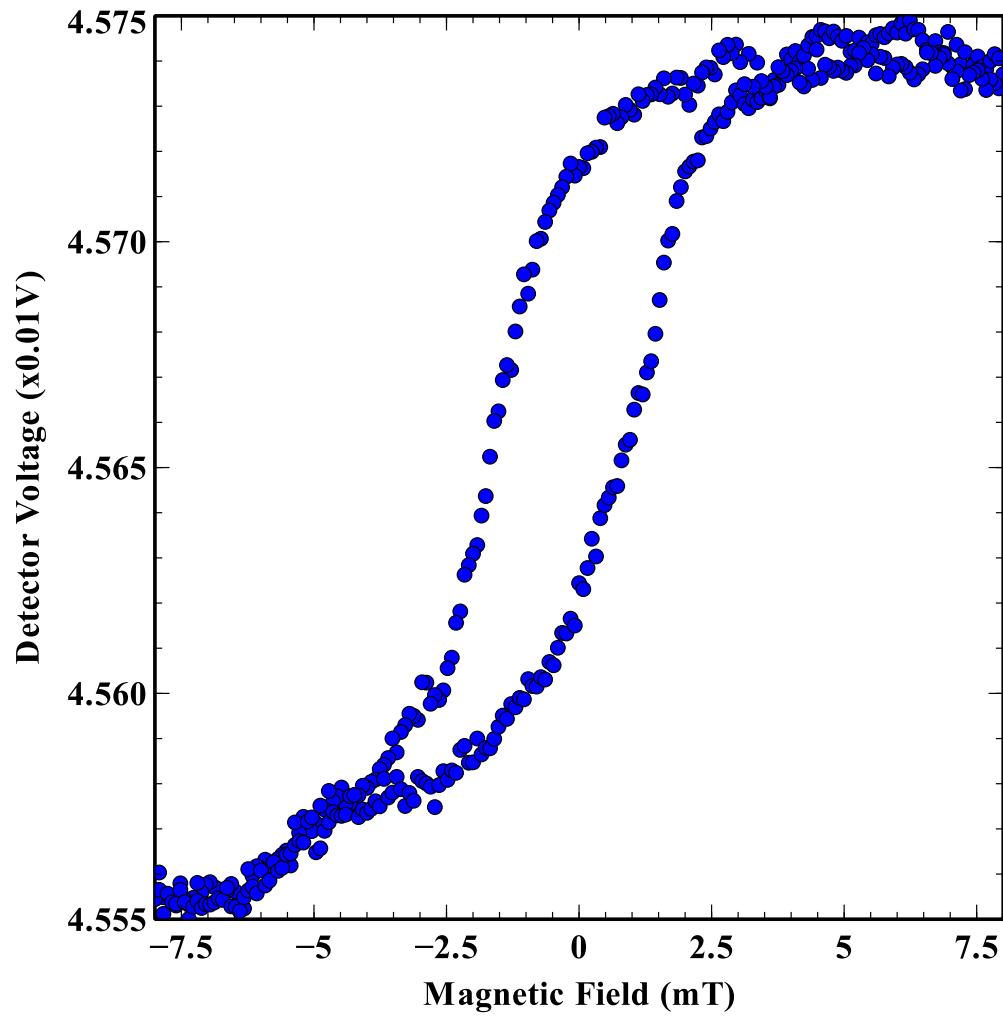


Figure 7.12: Hysteresis loop taken from a MOKE magnetometer measurement of a thin film of Nickel

The gradual nature of the MOKE signal is typical of Nickel, which is known to have its magnetisation reverse across the whole structure more progressively than compared with Permalloy, which has a more abrupt reversal of its magnetisation. This is well illustrated in the hysteresis loop obtained for a Permalloy thin film, seen in Figure 7.13.

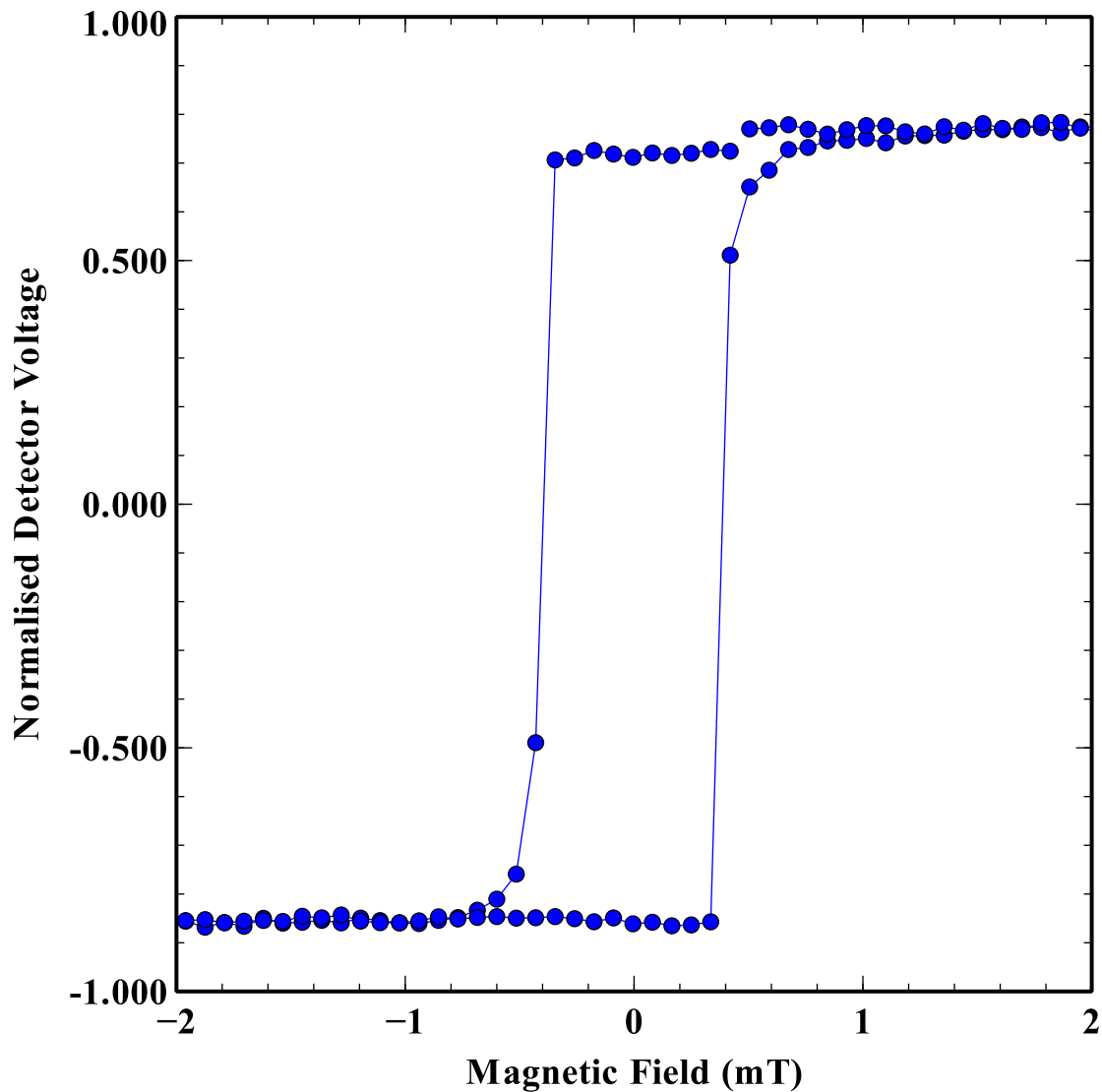


Figure 7.13: Hysteresis loop taken from a MOKE magnetometer measurement of a thin film of Permalloy, with the hysteresis occurring in the measured laser intensity by a detector following the reflection of the laser light off of the magnetic material being exposed to the magnetic field

7.3.2 Square lattice MOKE measurements

Following the first MOKE measurements, a pair of hexagonal lattices of ASI, typical of the ones measured in my other experiments, was investigated in the MOKE setup. The difference between these two lattices was that one was a connected lattice, with the other being unconnected. These two lattices have been measured along their hard axis – which means that of the three nanowires at each vertex, one of these is orientated perpendicular to the external magnetic field, and the other two lie at an angle of 30 degrees to the field.

Initially a connected square lattice was created, as this served to work alongside my previous work on Magneto-transport measurements in the hexagonal connected lattice, and to begin the preliminary investigations which would enable me to confirm the validity of the proposed plan. Tests were completed on this connected square lattice, in the form of magneto-optic measurements akin to those completed on the hexagonal lattice at the beginning of this chapter. A variety of measurements was taken with the applied field in the plane of the sample and at angles of either 0° or 45° . What these two angles are in reality is shown below in Figure 6.2.



Figure 7.14: Scanning Electron Microscope image of the square lattice Artificial Spin Ice, showing the angles that the externally applied magnetic field was directed across the sample, and what these angles refer to in respect to the lattice

The main difference between these two measurements is the angle of the easy axis of the bars in the lattice, relative to the applied magnetic field. In the case of an angle of 0° , for each vertex there is one pair of bars which are lined parallel to the field, and the other pair of bars positioned exactly perpendicular to the field. This should result in only two of the bars switching their orientation as a result of the field. By comparison the measurement at 45° has all four bars at an equivalent angle of 45° to the applied field, and therefore all four of these bars are expected to switch at the same field.

The intention of the test was to evaluate the relative ease with which a MOKE measurement can be obtained through a layer of inverted PMMA. Initially a measurement was taken of the square lattice prior to the application of the layer of PMMA. This measurement was taken at an angle of 45° .

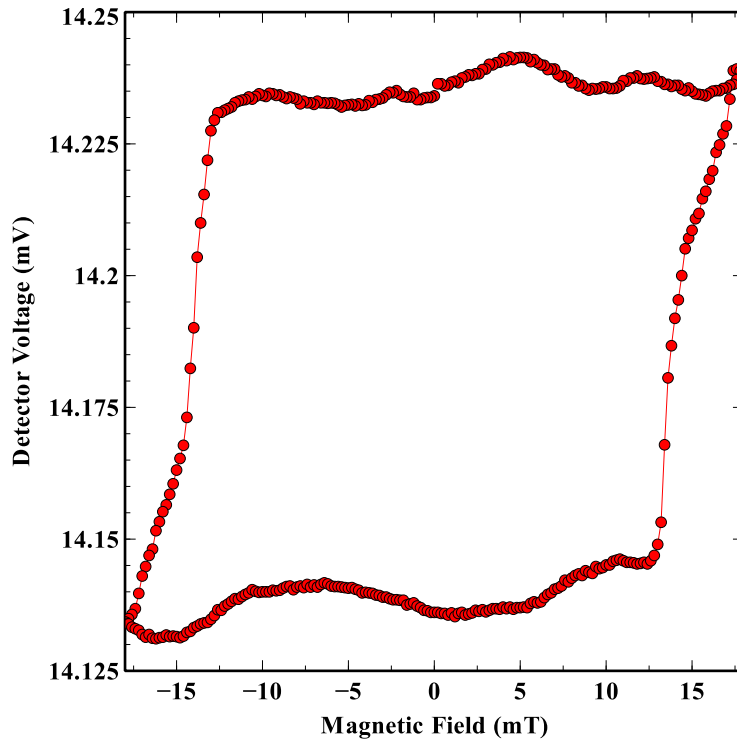


Figure 7.15: Graph showing the hysteresis loop of a square lattice Artificial Spin Ice, for an applied field of angle 45° obtained via MOKE

Immediately apparent when comparing the figures for the two different angles of magnetic field application, is that the MOKE signal at 45° is twice that at 0° . This is confirmation of the anticipated outcome, whereby at 0° the field is only able to affect two of the four bars, as the other two are perpendicular, whereas in the case of an angle of 45° , all four bars are affected, and equally. This ensures that there is twice as big a change in the sample when the field angle is 45° as opposed to 0° .

Another comparison shows that the switch in Figure 7.15 is almost instantaneous in terms of field.

7.3.3 MOKE through photoresist layer

The data shown in Section 7.3.2 was for the square lattice, plain, atop the silicon substrate. In the case of the intended Quasi 3-D ASI, one of the layers of the two-layer magnetic sample will be positioned underneath a layer of PMMA resist. So a measurement was required to ensure the feasibility of measuring magneto-optically through a layer of resist, both in terms of the potential signal size, and also the effect of laser light potentially scattering while propagating through the resist.

The connected square lattice measured in the previous section, was coated in a layer of photoresist and MOKE measurements were carried out at an angle of zero degrees to the easy axis.

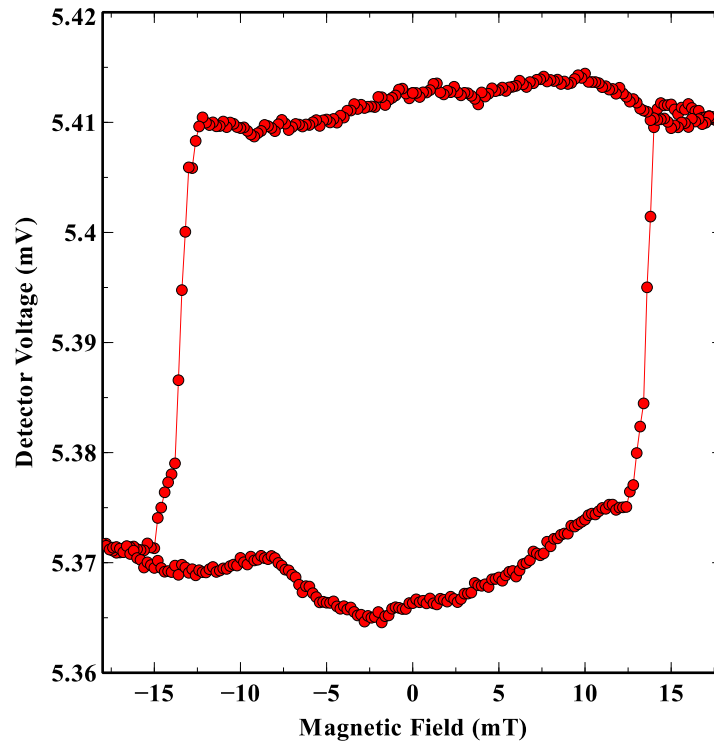


Figure 7.16: Graph showing the size and quality of the MOKE signal obtained from a square lattice of ASI through a layer of inverted PMMA, with the magnetic field at an angle of 0 degrees to the easy axis of the lattice – also taken with the laser's temperature controller turned off

As part of the process of refining and improving the capabilities of the MOKE, a temperature controller was implemented into the system, controlling the temperature of the laser, to ensure that the power emitted is as consistent as possible. In order to understand fully the benefits of this, a pair of measurements were made one after the other. Above in Figure 7.16, the first of these measurements is performed without the use of the temperature controller.

The graph above in Figure 7.16 shows the MOKE signal for the square lattice which has been measured from the shining of the laser light through the layer of inverted PMMA atop the substrate and lattice. The graph clearly shows that the strength of the MOKE signal is still significantly greater than any background features of the MOKE signal. There is a bending of the signal at higher applied fields than was the case in the measurements with no PMMA atop the lattice. This can therefore be attributed to the

PMMA's presence, and is not a major concern as in the cases with no PMMA the high-field effect was negligible and so this is not obstructing any key information about the square lattice.

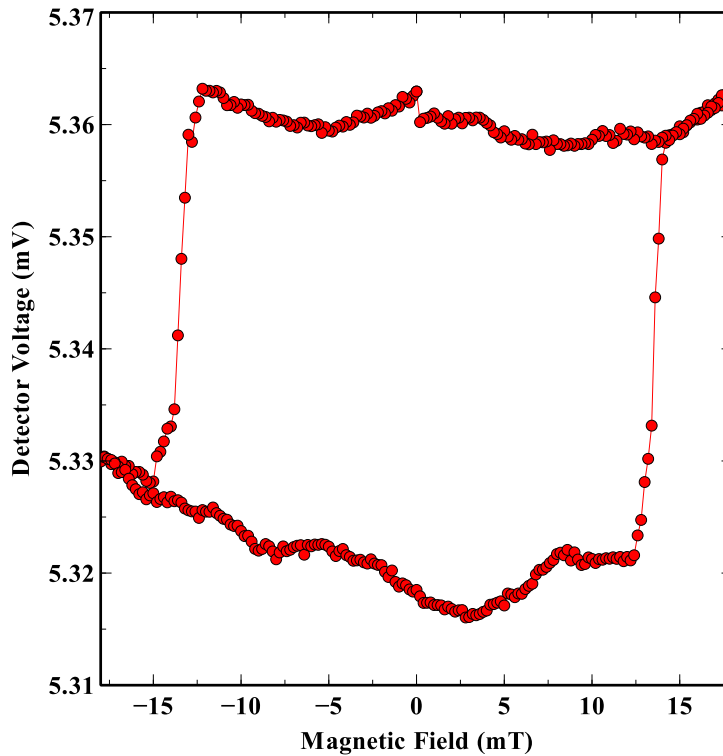


Figure 7.17: Graph showing the size and quality of the MOKE signal obtained from a square lattice of ASI through a layer of inverted PMMA, with the magnetic field at an angle of 0 degrees to the easy axis of the lattice – for comparison, the laser's temperature controller was turned on

This is the second part of the back-to-back study of the effects of the temperature controller on the quality of the MOKE signal detected. Figure 7.17 shows the signal measured through the inverted PMMA when the temperature controller is turned on. It can be seen that there is a limited improvement in the quality of the signal seen when the temperature controller is included or not.

7.3.4 Simple Two-layer structure

Prior to attempting to produce a two-layer ASI structure, it was determined to produce a series of far simpler samples to obtain preliminary measurements of a sample produced using the same two-layer process as that which will ultimately be used. A series of pairs of magnetic bars was created. These pairs of bars were a mixture of

parallel and perpendicular to one another, and also contained a variety of distances between one another, with some containing regions where the second nanowire was directly vertically above the first.

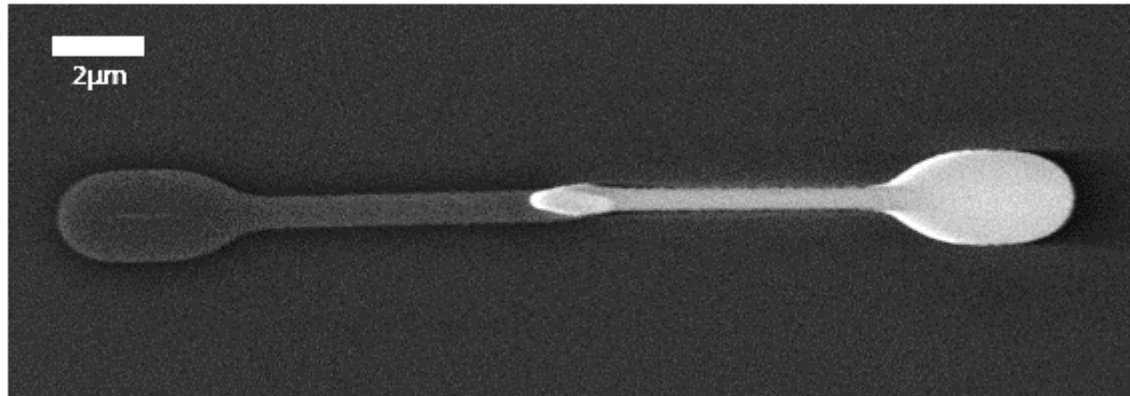


Figure 7.18: SEM image of a simple two-layer structure with the two layers separated by a transparent layer of inverted PMMA

This was made possible by the inversion of the layer of PMMA photoresist between the two halves of the magnetic samples. Inverting the layer of PMMA results in the reversal of the usual behaviour, where normally any resist which has been exposed to the electron beam has its structure changed such that it becomes soluble, and is removed by the developer following the exposure. The remainder of the PMMA, which has not been exposed, remains as originally. The reverse is true with inverted PMMA. The inverted region remains following exposure, and the remainder is removed after being placed in Acetone.

The optimum thickness of this photoresist layer such that the fabrication is as straightforward as possible, whilst still being able to observe an interaction between the magnetic layers, was not immediately obvious and so a number of samples will need to be created in order to optimise this. For this first measurement the primary objective was to observe two switching signals, one for each magnetic layer, within MOKE data.

Due to the challenge posed by measuring the MOKE signal not just from two structures simultaneously, but also needing to measure one signal through a layer of the inverted PMMA, a range of different samples were created, including structures with larger dimensions. This of course limits their use in terms of comparisons with nanostructures but served as an opportunity to test the potential of measuring a signal through the PMMA by having a far larger surface area of the magnetic regions.

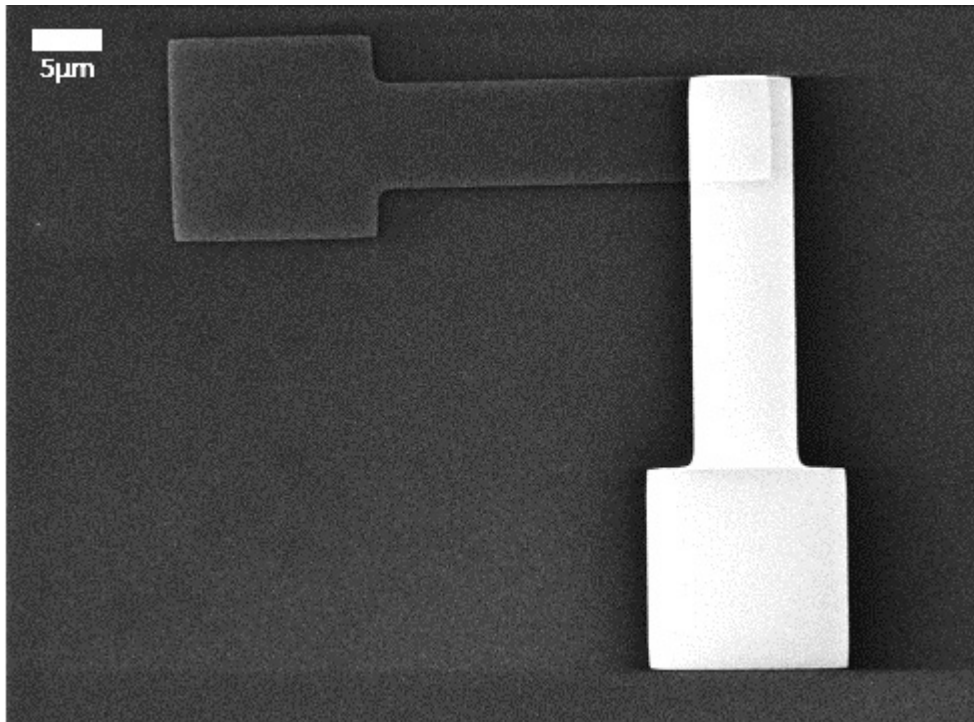


Figure 7.19: SEM image of a larger two-layer structure with the two layers separated by a transparent layer of inverted PMMA

This was made possible by the inversion of the layer of PMMA photoresist between the two halves of the magnetic samples. The optimum thickness of this photoresist layer such that the fabrication is as straightforward as possible, whilst still being able to observe an interaction between the magnetic layers, was not immediately obvious and so a number of samples will need to be created in order to optimise this. For this first measurement the primary objective was to observe two switching signals, one for each magnetic layer, within MOKE data.

There are some contrast changes within the structures, notably at boundaries between regions of different dimension. This appears also to be not present in the darker structures, which are the first deposited layer, directly atop the substrate.

For a visit to the Advanced Light Source synchrotron at Berkeley National Laboratory in California, samples were fabricated which included two-layer square lattice structures, for an experiment using soft X-Ray Microscopy to observe the magnetic contrast and to hope to visualise the interactions between the magnetic bars on two different layers.

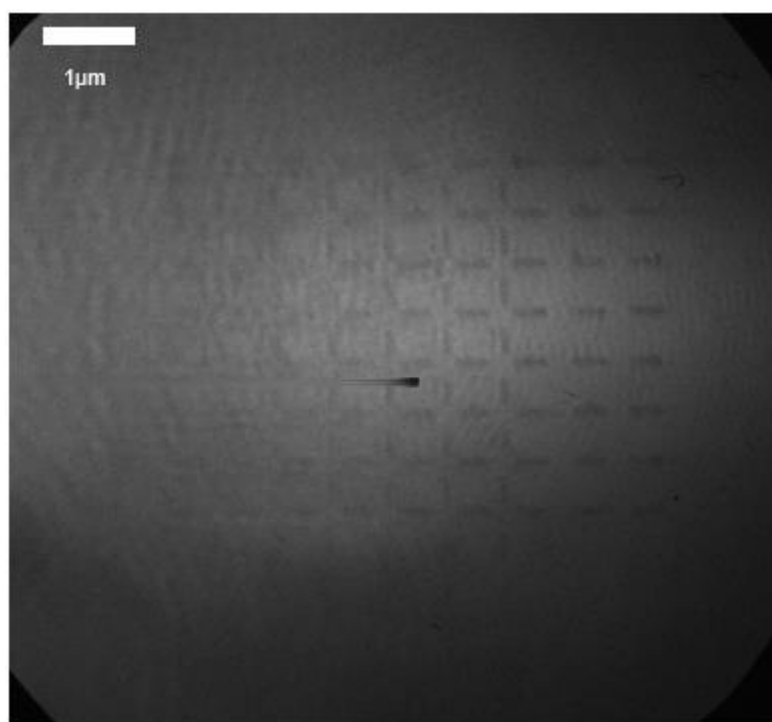


Figure 7.20: SEM Image of a Quasi 3D Square lattice - the line across the image along the centre, ending in a black dot, is a row of dead pixels on the image capturing camera

Figure 7.20 shows an SEM image of a two-layer square lattice, which has aligned nicely across the two layers. The vertically-orientated nanowires form the first lithographed layer, with the horizontal nanowires forming the second layer, with a layer of inverted PMMA between the two.

Upon attempting to obtain an image showing the magnetic contrast between two images of this structure, by combining two images of opposing magnetic field application, the sensitivity of the measuring instrument was marginally insufficient to get a good image of the contrast. Due to the narrow widths of the wires involved and, predominantly, their small thicknesses, there was not enough magnetic material in order to obtain a good magnetic signal. This has already been remedied in designs of further samples, which are due to be measured at a follow-up visit to the beamline at the Advanced Light Source.

A couple of the perceived challenges, however, were to successfully align the two magnetic layers so as to form a balanced lattice, and to be able to deposit a second layer successfully atop inverted PMMA. The first samples measured have shown that this is a valid method for realising the desired measurements.

7.4. Conclusions

This third and final results chapter has considered the interactions between DWs in adjacent magnetic nanostructures, both in the plane of a sample substrate and out of the plane, perpendicular to the substrate. This pair of studies has numerous applications, many of which can be attributed to both of the forms of interactions, most notably the manner in which DWs interfere with each other when situated in close proximity, and the implications this can have regarding the maximum viable density for these devices to sit within potential future data storage hardware.

Through the use of XMCD and PEEM on beamline I06 at Diamond Light Source synchrotron, images have been acquired which show the potential for DWs in adjacent nanowires to pin to one another repeatedly. This is to say that the DWs have been brought into close proximity through the application of an external magnetic field, at which moment they keep each other in place along the two nanowires. With the reversing of the magnetic field direction, the two walls can be separated, and then the process repeated multiple times. This is useful in terms of showing the potential reproducibility of this feature, should it be considered a useful factor in future technological devices.

The other benefit of this is to consider the separation between adjacent nanowires such that they will not interfere with one another. In the potential data storage devices that could one day be created using lithographed nanowires featuring DWs, the retention and integrity of the DWs in the nanowires is integral to the successful operation. So, this kind of experiment will enable an appreciation for the closest proximity that two DWs in adjacent nanowires can be stationed while not potentially corrupting the information encoded into neighbouring DWs in the structures.

The use of PMMA as the material between the two stages of the lithographic process for these quasi 3-D structures has proven to have merits, due to the fact that the strength and quality of the MOKE signal from an ASI lattice through the layer of inverted PMMA does not suffer greatly. This can be investigated more extensively, with aspects such as the surface smoothness of the inverted PMMA to be considered. Of course, the tendency would be to assume a similar smoothness between the substrate and the PMMA, but this is an aspect which definitely requires greater analysis.

8. Conclusion

Artificial spin ice (ASI) and domain walls (DWs) in magnetic nanowires were studied. Asymmetry in magnetotransport data of a connected lattice arises at low temperatures, specifically lower than 25K. This asymmetry is greatly reduced by the addition of a non-magnetic capping layer to the sample. This is in agreement with a recently published piece [14] suggesting likewise, and both of these findings appear to suggest an effect being played by exchange bias caused by an antiferromagnetic oxide layer forming in uncapped samples. A previously published work using uncapped Cobalt nanowires [15] witnessed the low temperature asymmetry and attributed it to the onset of the long range dipolar ice phase [15] in ASI systems.

The hybrid lattice has been created, which allowed for the first electrical measurements of an unconnected ASI lattice, previously only magnetically imaged. The lack of propagation of DWs through the lattice leads to a far larger signal within the anisotropic magnetoresistance (AMR) data, with a like-for-like measurement showing a normalised AMR switching signal of 0.01% in a connected lattice, compared to 0.1% in the hybrid lattice. This results from a DW being nucleated in every single nanowire.

The restricting lattice was conceived, as a lattice between the two extremes of the connected and unconnected variations – so where there are physical connections at the vertices, but these are narrower than the nanowires between them. As this restriction in the lattice becomes greater, so it becomes more favourable for new DWs to nucleate within every nanowire individually, than for DWs to propagate between wires. This results in the lattice behaving like it is unconnected. Simulations and experiments have shown that the required restriction for this change to occur is dependent on the dimensions of the wires in the lattice, and also the nature of the restriction. For instance a comparison can be made in the case of a lattice of an abrupt narrowing of the wire. In this instance when the lattice has nanowires which are 150nm wide, the required restriction is just 7%, meaning that the vertices need to be 7% narrower than the nanowires. Whereas when the lattice has nanowires 300nm wide, the required restriction rises to 25%. This was the situation when the wires narrow immediately at the vertex, so in this case for a wire width of 150nm, the required restriction is 7%. By contrast, still at a wire width of 150nm, but when the restriction occurs more gradually – the wire's width reducing by just 0.13% for every nanometre sideways along the wire - this increases the required restriction up to 52%.

The study has considered the interactions between magnetic DWs in a variety of nanostructures, including ASI, and this has included the design and creation of a square lattice of ASI, fabricated over two vertical layers, in order to balance the interactions across vertices between neighbouring nanowires.

8.1. Future restricting lattices and quasi 3-D ASI

The investigation into the effects of reducing the widths of vertices within ASI lattices, through the creation of the restricting lattice, has been shown to have potential for understanding the propagation of DWs through ASI lattices. Further instances of these samples can be fabricated to ensure a more diverse range of these lattices, in terms of the widths of the nanowires involved, and also the nature of the transition from the wider nanowire to the narrower vertex.

The initial discovery of the amount of lattice restriction required to prevent the DW propagation, as a function of nanowire width, can be further investigated with a variety of simulations. These simulations could include more complex transitions between the nanowires and the narrow vertices. Of particular note is that thus far samples with an abrupt transition between the nanowire and the vertex have only been simulated, and this will be an interesting sample to measure experimentally. The restricting lattice can also be applied to other common ASI lattices, such as the square lattice.

The hybrid lattice has been shown to be highly effective at measuring the AMR of an unconnected ASI lattice, in the hexagonal geometry. From this, there is a clear possibility of being able to extend this to other ASI lattices such as the square lattice, to attempt to better understand the variations between unconnected nanoislands and connected lattice.

A key feature of interest is that of continuing the work into quasi 3-D ASI, which has the potential lead to further ASI systems which are constructed on multiple layers such as this. The manner in which the spacer layer between the ferromagnetic arrays responds to the two layers is integral to the understanding of the effectiveness of the PMMA as a suitable spacer layer. This has numerous potential applications, such as the opportunity to create more densely populated storage devices, through vertical offsetting of adjacent nanowires to avoid interactions. A further application of this form

of nanostructure is the potential to create samples with multiple levels and multiple separating layers, such as a quasi 3D-style lattice in 3 dimensions.

9. References

- [1] S. S. P. Parkin, M. Hayashi, and L. Thomas, "Magnetic Racetrack Memory," *Science*, vol. 320, no. 5873, pp. 190–194, 2014.
- [2] M. Hayashi, L. Thomas, R. Moriya, C. Rettner, and S. S. P. Parkin, "Current Controlled Magnetic Domain Wall Nanowire Shift Register," *Science*, vol. 320, no. 5873, p. 209–211, 2008.
- [3] D. A. Allwood, "Magnetic Domain-Wall Logic," *Science*, vol. 309, no. 5741, pp. 1688–1692, 2005.
- [4] B. D. Terris, T. Thomson, and G. Hu, "Patterned media for future magnetic data storage," *Microsyst. Technol.*, vol. 13, no. 2, pp. 189–196, 2007.
- [5] T. Thomson, B. Lengsfeld, H. Do, and B. D. Terris, "Magnetic anisotropy and reversal mechanisms in dual layer exchanged coupled perpendicular media," *J. Appl. Phys.*, vol. 103, no. 7, pp. 251–254, 2008.
- [6] R. L. Scheir, "New storage technologies to deal with the data deluge," *Computer World*, 2013. [Online]. Available: <http://www.computerworld.com/article/2495700/data-center/new-storage-technologies-to-deal-with-the-data-deluge.html>. [Accessed: 02-Aug-2016].
- [7] E. R. Lewis, D. Petit, L. Thevenard, a. V. Jausovec, L. O'Brien, D. E. Read, and R. P. Cowburn, "Magnetic domain wall pinning by a curved conduit," *Appl. Phys. Lett.*, vol. 95, no. 15, pp. 131–134, 2009.
- [8] D. Atkinson, D. S. Eastwood, and L. K. Bogart, "Controlling domain wall pinning in planar nanowires by selecting domain wall type and its application in a memory concept," *Appl. Phys. Lett.*, vol. 92, no. 2, pp. 0–3, 2008.
- [9] T. H. P. Chang, "Proximity effect in Electron Beam Lithography," *J. Vac. Sci. Technol.*, vol. 12, no. 6, p. 1271, 1975.
- [10] C. Vieu, "Electron Beam Lithography: Resolution limits and applications. Applied Surface Science," *Appl. Surf. Sci.*, vol. 164, no. 1–4, pp. 111–117, 2000.
- [11] R. F. W. Pease, "Electron Beam Lithography.," *Contemp. Phys.*, vol. 22, no. 3, pp. 265–290, 1981.
- [12] A. Kaiser, C. Wiemann, S. Cramm, and C. M. Schneider, "Influence of magnetocrystalline anisotropy on the magnetization dynamics of magnetic microstructures.," *J. Phys. Condens. Matter*, vol. 21, no. 31, p. 314008, 2009.
- [13] A. Pushp, T. Phung, C. Rettner, B. P. Hughes, S.-H. Yang, L. Thomas, and S. S. P. Parkin, "Domain wall trajectory determined by its fractional topological edge defects," *Nat. Phys.*, vol. 9, no. 8, pp. 505–511, 2013.
- [14] B. L. Le, D. W. Rench, R. Misra, L. O'Brien, C. Leighton, N. Samarth, and P. Schiffer, "Effects of exchange bias on magnetotransport in permalloy kagome artificial spin ice," *New J. Phys.*, vol. 17, no. 2, p. 023047, 2015.

- [15] W. R. Branford, S. Ladak, D. Read, K. Zeissler, and L. F. Cohen, "Emerging Chirality in Artificial Spin Ice," *Science*, vol. 335, no. 6067, pp. 1597-1600, 2012.
- [16] I. S. Grant and W. R. Phillips, *Electromagnetism*. 2nd edn. Chichester: John Wiley 1990, pp. 175-180.
- [17] D. Jiles, *Introduction to Magnetism and Magnetic materials*. 2nd edn. London: Chapman & Hall, 1998.
- [18] J. M. D. Coey, *Magnetism and Magnetic Materials*. Cambridge: CUP 2010.
- [19] L. Landau and E. Lifshitz, "On the Theory of the Dispersion of Magnetic Permeability in Ferromagnetic Bodies," *Phys. Zeitsch. der Sow.*, vol. 8, pp. 153-169, 1935.
- [20] A. Hubert, R. Schäfer, *Magnetic Domains: The Analysis of Magnetic Nanostructures*. Berlin: Springer 1998.
- [21] V. Gehanno, A. Marty, B. Gilles, and Y. Samson, "Magnetic domains in epitaxial ordered FePd(001) thin films with perpendicular magnetic anisotropy," *Phys. Rev. B*, vol. 55, no. 18, pp. 12552–12555, 1997.
- [22] J. D. Livingstone, *Driving Force: The natural magic of magnets*. London: Harvard University Press 1996.
- [23] R. Cowburn, A. Adeyeye, and M. Welland, "Configurational Anisotropy in Nanomagnets," *Phys. Rev. Lett.*, vol. 81, no. 24, pp. 5414–5417, 1998.
- [24] L. W. McKeehan, *Magnets*. Van Nostrand 1967.
- [25] T. Koyama et al, "Observation of the intrinsic pinning of a magnetic domain wall in a ferromagnetic nanowire," *Nature Materials*, vol. 10, pp. 194-197, 2011.
- [26] O. A. Tretiakov et al, "Dynamics of domain walls in magnetic nanostrips," *Phys. Rev. Lett.*, vol. 100, no. 12, p. 127204, 2007.
- [27] M. Kläui, "Head-to-Head domain walls in magnetic nanostructures," *J. Phys. Condens. Matter*, vol. 20, no. 31, p. 313001, 2008.
- [28] M. Kläui, "Head-to-Head domain-wall phase diagram in mesoscopic ring magnets," *Appl. Phys. Lett.*, vol. 85, no. 2004, pp. 5637–5639, 2011.
- [29] Y. Nakatani, A. Thiaville, and J. Miltat, "Head-to-head domain walls in soft nanostrips: A refined phase diagram," *J. Magn. Magn. Mater.*, vol. 290–291 PA, pp. 750–753, 2005.
- [30] G. H. Wannier, "Antiferromagnetism, The triangular Ising net.," *Phys. Rev.*, vol. 79, p. 357, 1950.
- [31] R. Moessner, "Magnets with strong geometric frustration." *Can. J. Phys.*, vol. 79, nos. 11-12, p. 1283-1294, 2001.

- [32] J. Cumings, L. J. Heyderman, C. H. Marrows, and R. L. Stamps, "Focus on artificial frustrated systems," *New J. Phys.*, vol. 16, p. 075016, 2014.
- [33] S. T. Bramwell, "Spin Ice State in Frustrated Magnetic Pyrochlore Materials," *Science*, vol. 294, no. 5546, pp. 1495–1501, 2001.
- [34] M. Tanaka, E. Saitoh, H. Miyajima, T. Yamaoka, and Y. Iye, "Domain structures and magnetic ice-order in NiFe nano-network with honeycomb structure," *J. Appl. Phys.*, vol. 97, no. 10, pp. 2003–2006, 2005.
- [35] R. F. Wang, C. Nisoli, R. S. Freitas, J. Li, W. McConville, B. J. Cooley, M. S. Lund, N. Samarth, C. Leighton, V. H. Crespi, and P. Schiffer, "Artificial 'spin ice' in a geometrically frustrated lattice of nanoscale ferromagnetic islands," *Nature*, vol. 439, no. 7074, pp. 303–306, 2006.
- [36] K. Zeissler, S. K. Walton, S. Ladak, D. E. Read, T. Tyliczszak, L. F. Cohen, and W. R. Branford, "The non-random walk of chiral magnetic charge carriers in artificial spin ice," *Sci. Rep.*, vol. 3, p. 1252, 2013.
- [37] S. Ladak, S. K. Walton, K. Zeissler, T. Tyliczszak, D. Read, W. R. Branford, and L. F. Cohen, "Disorder-independent control of magnetic monopole defect population in artificial spin-ice honeycombs," *New J. Phys.*, vol. 14, p. 045010, 2012.
- [38] E. De Ranieri, A. W. Rushforth, K. Výborný, U. Rana, E. Ahmad, R. P. Campion, C. T. Foxon, B. L. Gallagher, A. C. Irvine, J. Wunderlich, and T. Jungwirth, "Lithographically and electrically controlled strain effects on anisotropic magnetoresistance in (Ga,Mn)As," *New J. Phys.*, vol. 10, p. 065003, 2008.
- [39] T. R. McGuire and R. I. Potter, "Anisotropic Magnetoresistance," *IEEE Trans. Magn.*, vol. 11, pp. 1018–1038, 1975.
- [40] H. Corte-León, V. Nabaei, A. Manzin, J. Fletcher, P. Krzysteczko, H. W. Schumacher, and O. Kazakova, "Anisotropic Magnetoresistance State Space of Permalloy Nanowires with Domain Wall Pinning Geometry," *Sci. Rep.*, vol. 4, pp. 1–10, 2014.
- [41] J.-E. Wegrowe, D. Kelly, A. Franck, S. Gilbert, and J.-P. Ansermet, "Magnetoresistance of Ferromagnetic Nanowires," *Phys. Rev. Lett.*, vol. 82, no. 1, pp. 3681–3684, 1999.
- [42] D. A. Allwood, G. Xiong, M. D. Cooke, and R. P. Cowburn, "Magneto-optical Kerr effect analysis of magnetic nanostructures," *J. Phys. D. Appl. Phys.*, vol. 36, no. 18, pp. 2175–2182, 2003.
- [43] Z. Q. Qiu and S. D. Bader, "Surface magneto-optic Kerr effect (SMOKE)," *J. Magn. Magn. Mater.*, vol. 200, no. 1, pp. 664–678, 1999.
- [44] C. Daboo, J. A. C. Bland, R. J. Hicken, A. J. R. Ives, M. J. Baird, and M. J. Walker, "Vectorial magnetometry with the magneto-optic Kerr effect applied to Co/Cu/Co trilayer structures," *Phys. Rev. B*, vol. 47, no. 18, pp. 11852–11859, 1993.

- [45] H. W. F. Sung and C. Rudowicz, *A closer look at the hysteresis loop for ferromagnets - A survey of misconceptions and misinterpretations in textbooks*. Hong Kong: City University of Hong Kong, Department of Physics and Materials Science 2002.
- [46] D. A. Allwood, G. Xiong, and R. P. Cowburn, "Domain wall diodes in ferromagnetic planar nanowires," *Appl. Phys. Lett.*, vol. 85, no. 14, pp. 2848–2850, 2004.
- [47] C. Nisoli, R. Moessner, and P. Schiffer, "Colloquium: Artificial spin ice: Designing and imaging magnetic frustration," *Rev. Mod. Phys.*, vol. 85, no. 4, pp. 1473–1490, 2013.
- [48] M. Tanaka, E. Saitoh, H. Miyajima, T. Yamaoka, and Y. Iye, "Magnetic interactions in a ferromagnetic honeycomb nanoscale network," *Phys. Rev. B - Condens. Matter Mater. Phys.*, vol. 73, no. 5, pp. 3–6, 2006.
- [49] P. Mellado, O. Petrova, Y. Shen, and O. Tchernyshyov, "Dynamics of magnetic charges in artificial spin ice," *Phys. Rev. Lett.*, vol. 105, no. 18, pp. 1–4, 2010.
- [50] S. A. Daunheimer, O. Petrova, O. Tchernyshyov, and J. Cumings, "Reducing disorder in artificial kagome ice," *Phys. Rev. Lett.*, vol. 107, no. 16, pp. 2–5, 2011.
- [51] A. Libál, C. Reichhardt, and C. J. O. Reichhardt, "Hysteresis and Return Point Memory in Artificial Spin Ice Systems," *Phys. Rev. E.*, vol. 86, p. 5, 2011.
- [52] G. Möller and R. Moessner, "Magnetic multipole analysis of kagome and artificial spin-ice dipolar arrays," *Phys. Rev. B - Condens. Matter Mater. Phys.*, vol. 80, no. 14, pp. 2–4, 2009.
- [53] S. Zhang, I. Gilbert, C. Nisoli, G.-W. Chern, M. J. Erickson, L. O'Brien, C. Leighton, P. E. Lammert, V. H. Crespi, and P. Schiffer, "Crystallites of magnetic charges in artificial spin ice.," *Nature*, vol. 500, no. 7464, pp. 553–557, 2013.
- [54] Y. Qi, T. Brintlinger, and J. Cumings, "Direct observation of the ice rule in an artificial kagome spin ice," *Phys. Rev. B*, vol. 77, no. 9, p. 094418, 2008.
- [55] E. Mengotti, L. J. Heyderman, a. Fraile Rodríguez, A. Bisig, L. Le Guyader, F. Nolting, and H. B. Braun, "Building blocks of an artificial kagome spin ice: Photoemission electron microscopy of arrays of ferromagnetic islands," *Phys. Rev. B - Condens. Matter Mater. Phys.*, vol. 78, no. 14, pp. 1–7, 2008.
- [56] S. Ladak, D. Read, T. Tyliczszak, W. R. Branford, and L. F. Cohen, "Monopole defects and magnetic coulomb blockade," *New J. Phys.*, vol. 13, p. 023023, 2011.
- [57] I. Gilbert, G.-W. Chern, B. Fore, Y. Lao, S. Zhang, C. Nisoli, and P. Schiffer, "Direct visualization of memory effects in artificial spin ice," *Phys. Rev. B*, vol. 92, no. 10, p. 104417, 2015.

- [58] J. P. Morgan, A. Stein, S. Langridge, and C. H. Marrows, "Thermal ground-state ordering and elementary excitations in artificial magnetic square ice," *Nat. Phys.*, vol. 7, no. 1, pp. 75–79, 2011.
- [59] S. Ladak, D. E. Read, W. R. Branford, and L. F. Cohen, "Direct observation and control of magnetic monopole defects in an artificial spin-ice material," *New J. Phys.*, vol. 13, p. 063032, 2011.
- [60] D. M. Burn, M. Chadha, and W. R. Branford, "Dynamic dependence to domain wall propagation through artificial spin ice," *Phys. Rev. B.*, vol. 95, p. 104417, 2017.
- [61] O. Sendetskyi, L. Anghinolfi, V. Scagnoli, G. Möller, N. Leo, A. Alberca, J. Kohlbrecher, J. Lüning, U. Staub, and L. J. Heyderman, "Magnetic diffuse scattering in artificial kagome spin ice," *Phys. Rev. B - Condens. Matter Mater. Phys.*, vol. 93, no. 22, pp. 1–8, 2016.
- [62] G. W. Chern, M. J. Morrison, and C. Nisoli, "Degeneracy and criticality from emergent frustration in artificial spin ice," *Phys. Rev. Lett.*, vol. 111, no. 17, pp. 1–7, 2013.
- [63] I. Gilbert, G.-W. Chern, S. Zhang, L. O'Brien, B. Fore, C. Nisoli, and P. Schiffer, "Emergent ice rule and magnetic charge screening from vertex frustration in artificial spin ice," *Nat. Phys.*, vol. 10, no. 9, pp. 670–675, 2014.
- [64] I. Gilbert, Y. Lao, I. Carrasquillo, L. O'Brien, J. D. Watts, M. Manno, C. Leighton, A. Scholl, C. Nisoli, and P. Schiffer, "Emergent reduced dimensionality by vertex frustration in artificial spin ice," *Nat. Phys.*, vol. 12, pp. 162–165, 2015.
- [65] V. S. Bhat, J. Sklenar, B. Farmer, J. Woods, J. B. Ketterson, J. T. Hastings, and L. E. De Long, "Ferromagnetic resonance study of eightfold artificial ferromagnetic quasicrystals," *J. Appl. Phys.*, vol. 115, no. 17, 2014.
- [66] A. Farhan, A. Scholl, C. F. Petersen, L. Anghinolfi, C. Wuth, S. Dhuey, R. V. Chopdekar, P. Mellado, M. J. Alava, and S. van Dijken, "Thermodynamics of emergent magnetic charge screening in artificial spin ice," *Nat. Commun.*, vol. 7, p. 12635, 2016.
- [67] E. R. Lewis, D. Petit, A. V. Jausovec, L. O'Brien, D. E. Read, H. T. Zeng, and R. P. Cowburn, "Measuring domain wall fidelity lengths using a chirality filter," *Phys. Rev. Lett.*, vol. 102, no. 5, pp. 1–4, 2009.
- [68] E. R. Lewis, D. Petit, L. O'Brien, a Fernandez-Pacheco, J. Sampaio, a-V. Jausovec, H. T. Zeng, D. E. Read, and R. P. Cowburn, "Fast domain wall motion in magnetic comb structures," *Nat. Mater.*, vol. 9, no. 12, pp. 980–983, 2010.
- [69] D. Petit, A. V. Jausovec, H. T. Zeng, E. Lewis, L. O'Brien, D. Read, and R. P. Cowburn, "High efficiency domain wall gate in ferromagnetic nanowires," *Appl. Phys. Lett.*, vol. 93, no. 16, pp. 131–134, 2008.
- [70] L. O'Brien, D. Petit, E. R. Lewis, R. P. Cowburn, D. E. Read, J. Sampaio, H. T. Zeng, and a. V. Jausovec, "Tunable remote pinning of domain walls in magnetic nanowires," *Phys. Rev. Lett.*, vol. 106, no. 8, pp. 1–4, 2011.

- [71] L. O'Brien, D. Petit, H. T. Zeng, E. R. Lewis, J. Sampaio, a. V. Jausovec, D. E. Read, and R. P. Cowburn, "Near-field interaction between domain walls in adjacent permalloy nanowires," *Phys. Rev. Lett.*, vol. 103, no. 7, pp. 1–4, 2009.
- [72] D. Thonig, S. Reißaus, I. Mertig, and J. Henk, "Thermal string excitations in artificial spin-ice square dipolar arrays," *J. Phys. Condens. Matter*, vol. 26, no. 26, p. 266006, 2014.
- [73] D. Thonig and J. Henk, "Pinning of thermal excitations at defects in artificial dipolar arrays: A theoretical investigation," *J. Magn. Magn. Mater.*, vol. 386, pp. 117–124, 2015.
- [74] G. A. Prinz, "Magnetoelectronics applications," *J. Magn. Magn. Mater.*, vol. 200, no. 1, pp. 57–68, 1999.
- [75] T. J. Hayward, M. T. Bryan, P. W. Fry, P. M. Fundi, M. R. J. Gibbs, D. A. Allwood, M. Y. Im, and P. Fischer, "Direct imaging of domain-wall interactions in Ni80Fe 20 planar nanowires," *Phys. Rev. B - Condens. Matter Mater. Phys.*, vol. 81, no. 2, pp. 1–4, 2010.
- [76] T. J. Hayward, M. T. Bryan, P. W. Fry, P. M. Fundi, M. R. J. Gibbs, M. Y. Im, P. Fischer, and D. a. Allwood, "Pinning induced by inter-domain wall interactions in planar magnetic nanowires," *Appl. Phys. Lett.*, vol. 96, no. 5, pp. 251–254, 2010.
- [77] M. Kläui, C. A. F. Vaz, J. Rothman, J. A. C. Bland, W. Wernsdorfer, G. Faini, and E. Cambril, "Domain wall pinning in narrow ferromagnetic ring structures probed by magnetoresistance measurements," *Phys. Rev. Lett.*, vol. 90, no. 9, p. 097202, 2003.
- [78] M. Kläui, H. Ehrke, U. Rüdiger, T. Kasama, R. E. Dunin-Borkowski, D. Backes, L. J. Heyderman, C. a F. Vaz, J. a C. Bland, G. Faini, E. Cambril, and W. Wernsdorfer, "Direct observation of domain-wall pinning at nanoscale constrictions," *Appl. Phys. Lett.*, vol. 87, no. 10, pp. 1–3, 2005.
- [79] C. C. Faulkner, M. D. Cooke, D. A. Allwood, D. Petit, D. Atkinson, and R. P. Cowburn, "Artificial domain wall nanotraps in Ni81Fe19 wires," *J. Appl. Phys.*, vol. 95, no. 11, pp. 6717–6719, 2004.
- [80] T. C. Chen, C. Y. Kuo, A. K. Mishra, B. Das, and J. C. Wu, "Magnetic domain wall motion in notch patterned permalloy nanowire devices," *Phys. B. Condens. Matter*, vol. 476, pp. 161–166, 2015.
- [81] D. Petit, A. V. Jausovec, H. T. Zeng, E. Lewis, L. O'Brien, D. Read, and R. P. Cowburn, "Mechanism for domain wall pinning and potential landscape modification by artificially patterned traps in ferromagnetic nanowires," *Phys. Rev. B - Condens. Matter Mater. Phys.*, vol. 79, no. 21, pp. 1–9, 2009.
- [82] D. Petit, H. T. Zeng, J. Sampaio, E. Lewis, L. O'Brien, A. V. Jausovec, D. Read, R. P. Cowburn, K. J. O'Shea, S. McVitie, and J. N. Chapman, "Magnetic imaging of the pinning mechanism of asymmetric transverse domain walls in ferromagnetic nanowires," *Appl. Phys. Lett.*, vol. 97, no. 23, pp. 2010–2013, 2010.

- [83] A. Manzin, V. Nabaei, H. Corte-Leon, O. Kazakova, P. Krzysteczko, and H. W. Schumacher, "Modeling of Anisotropic Magnetoresistance Properties of Permalloy Nanostructures," *IEEE Trans. Magn.*, vol. 50, no. 4, pp. 1–4, 2014.
- [84] G. M. Wysin, W. A. Moura-Melo, L. A. S. Mól, and A. R. Pereira, "Dynamics and hysteresis in square lattice artificial spin ice," *New J. Phys.*, vol. 15, p. 045029, 2013.
- [85] M. Tanaka, E. Saitoh, H. Miyajima, and T. Yamaoka, "Asymmetric field variation of magnetoresistance in Permalloy honeycomb nanonetwork," *J. Appl. Phys.*, vol. 99, no. 8, pp. 2004–2007, 2006.
- [86] L. O'Brien, D. Read, D. Petit, and R. P. Cowburn, "Dynamic propagation and nucleation in domain wall nanowire devices," *IOP Sci.*, vol. 024222, 2012.
- [87] Clean Air Technology Inc, "What is a cleanroom?" [Online]. Available: <http://www.cleanairtechnology.com/cleanroom-classifications-class.php>. [Accessed: 27-Feb-2016].
- [88] U. of Pennsylvania, "PMMA Data Sheet," *Microchem.* [Online]. Available: https://www.seas.upenn.edu/~nanosop/documents/PMMA_Data_Sheet.pdf. [Accessed: 27-Feb-2016].
- [89] A. A. Tseng, K. Chen, C. D. Chen, and K. J. Ma, "Electron beam lithography in nanoscale fabrication: Recent development," *IEEE Trans. Electron. Packag. Manuf.*, vol. 26, no. 2, pp. 141–149, 2003.
- [90] A. N. Broers, A. C. F. Hoole, and J. M. Ryan, "Broers 1996 Electron beam lithography Resolution limits," *Microelectron. Eng.*, vol. 32, nos. 1-4, pp. 131–142, 1996.
- [91] M. Yan, S. Choi, K. R. V. Subramanian, and I. Adesida, "The effects of molecular weight on the exposure characteristics of poly(methylmethacrylate) developed at low temperatures," *J. Vac. Sci. Technol. B Microelectron. Nanom. Struct.*, vol. 26, no. 6, p. 2306, 2008.
- [92] National Institute of Standards and Technology, "OOMMF," 2006. [Online]. Available: <http://math.nist.gov/oommf/>. [Accessed: 01-Oct-2015].
- [93] J. Nogués and I. K. Schuller, "Exchange bias," *J. Magn. Magn. Mater.*, vol. 192, no. 2, pp. 203–232, 1999.
- [94] M. Fitzsimmons, T. Silva, and T. Crawford, "Surface oxidation of Permalloy thin films," *Phys. Rev. B*, vol. 73, no. 1, p. 014420, 2006.
- [95] A. Fert and L. Piraux, "Magnetic nanowires," *J. Magn. Magn. Mater.*, vol. 200, no. 1, pp. 338–358, 1999.
- [96] D. M. Burn, M. Chadha, S. K. Walton, and W. R. Branford, "Dynamic interaction between domain walls and nanowire vertices," *Phys. Rev. B*, vol. 90, no. 14, p. 144414, 2014.

- [97] K. Nielsch, R. B. Wehrspohn, J. Barthel, J. Kirschner, U. Gösele, S. F. Fischer, and H. Kronmüller, "Hexagonally ordered 100 nm period nickel nanowire arrays," *Appl. Phys. Lett.*, vol. 79, no. 9, pp. 1360–1362, 2001.
- [98] K. Zeissler, M. Chadha, E. Lovell, L. F. Cohen, and W. R. Branford, "Low temperature and high field regimes of connected kagome artificial spin ice: the role of domain wall topology," *Sci. Rep.*, vol. 6, p. 30218, 2016.
- [99] M. Poniatowski and A. Wirths, "Improving the residual resistivity of pure gold," *Gold Bull.*, vol. 10, no. 4, pp. 104–107, 1977.
- [100] W. R. Branford, "Emergent magnetic monopoles in frustrated magnetic systems.," *Philos. Trans. A. Math. Phys. Eng. Sci.*, vol. 370, no. 1981, pp. 5702–4, 2012.
- [101] T. Kimura and Y. Otani, "Large spin accumulation in a permalloy-silver lateral spin valve," *Phys. Rev. Lett.*, vol. 99, no. 19, pp. 1–4, 2007.
- [102] D. Petit, A. V. Jausovec, D. Read, and R. P. Cowburn, "Domain wall pinning and potential landscapes created by constrictions and protrusions in ferromagnetic nanowires," *J. Appl. Phys.*, vol. 103, no. 11, 2008.
- [103] T. Komine, H. Murakami, T. Nagayama, and R. Sugita, "Influence of notch shape and size on current-driven domain wall motions in a magnetic nanowire," *IEEE Trans. Magn.*, vol. 44, no. 11 PART 2, pp. 2516–2518, 2008.
- [104] R. C. Silva, R. J. C. Lopes, L. A. S. Mól, W. A. Moura-Melo, G. M. Wysin, and A. R. Pereira, "Nambu monopoles interacting with lattice defects in a two-dimensional artificial square spin ice," *Phys. Rev. B - Condens. Matter Mater. Phys.*, vol. 87, no. 1, pp. 1–7, 2013.
- [105] L. A. S. Mól, W. A. Moura-Melo, and A. R. Pereira, "Conditions for free magnetic monopoles in nanoscale square arrays of dipolar spin ice," *Phys. Rev. B - Condens. Matter Mater. Phys.*, vol. 82, no. 5, pp. 1–6, 2010.
- [106] C. Phatak, A. K. Petford-Long, O. Heinonen, M. Tanase, and M. De Graef, "Nanoscale structure of the magnetic induction at monopole defects in artificial spin-ice lattices," *Phys. Rev. B - Condens. Matter Mater. Phys.*, vol. 83, no. 17, pp. 1–5, 2011.
- [107] Gatech, "Dektak 150 Profilometer Instructions," 2014 [Online]. Available: https://cleanroom.iem.gatech.edu/media/resources/equipment/instructions/Dektak%20150_instructions.pdf [Accessed: 04-Sept-2016].